Investigating Continental Deformation using PS-InSAR

Victoria A. Nockles

Thesis submitted to the University of Oxford
for the degree of Doctor of Philosophy
in
Earth Sciences

Department of Earth Sciences
and St Cross College,
University of Oxford

Trinity, 2015

Supervised by Prof. B. Parsons, Prof. T. Wright and Dr. R. Holley

Declaration

The contents of this thesis are all my own work, except where otherwise stated. The views and opinions expressed herein are mine and not necessarily those of any other person or body unless so attributed.

Citation: Nockles, V. A. (2015), Investigating Continental Deformation Using PS InSAR, D.Phil. thesis, University of Oxford, Department of Earth Sciences, Oxford, UK.

Keywords: InSAR, PS InSAR, Coseismic, Interseismic, Earthquake, Faulting, Numerical Modelling, Kunlun, Tibet, ERS, ENVISAT, Sliprate, Afterslip, Rheology.

This thesis has been typeset using LaTeX 2_ε and references were compiled using BibTeX. Most of the figures were produced using the open source Generic Mapping Tools (GMT) software and Matlab. Interferometric SAR processing was performed using ROI_PAC, copyright 2002–2008 Caltech/Jet Propulsion Laboratory and StAMPS copyright *Hooper et al.* (2012).

Printed in the United Kingdom.

To OUMC; .

Abstract

I use Persistant Scatterer Interferometric Synthetic Aperture Radar (PS InSAR) to measure interseismic strain accumulation across the Kunlun Fault, observe and model the postseismic signal associated with the Mw 7.8 2001 Kokoxili earthquake, and map strain in Western Turkey. PS InSAR selects pixels whose echo is dominated by a single scatterer in a series of interferograms (*Hooper et al.*, 2004). To date most tectonic signals measured with InSAR have used Differential InSAR (DifSAR) rather than PS InSAR. I compare PS InSAR and DifSAR across the Kunlun Fault to obtain equivalent slip rates of 9.5 mm/yr and 10.5 mm/yr, respectively. I show that regions which are incoherent in DifSAR, are coherent using PS InSAR.

Knowledge of slip rates along faults has important implication in terms of seismic hazard and is key to our understanding of the mechanical behaviour of the crust and mantle; for example they can be used to test the prediction of various models (*Van Der Woerd et al.*, 2002). I show slip rate variability on the eastern Kunlun Fault in Tibet with rates reducing eastwards by ∼9 mm/yr over a region of ∼80 km to a slip rate of 2.4 mm/yr towards the fault tip.

To date both afterslip and viscoelastic relaxation have been proposed as plausible mechanisms (*Wen et al.*, 2012) for the Kokoxili earthquake. I model afterslip across the Kunlun Pass Fault using rate and state friction to create a series of models with various preseismic slip rates and frictional parameters. I then perform a parameter space search to find the best fitting models to ENVISAT data from 2003-2010. I compare the best fit afterslip model with viscoelastic relaxation to show that viscoelastic relaxation gives a better fit to the data.

A number of studies have looked at interseismic strain accumulation across the North Anatolian and East Anatolian faults, e.g. *Walters et al.* (2014); *Yamasaki et al.* (2013), but relatively little work has been done on a fault scale across the grabens in Western Turkey. GPS data for the region shows fairly uniform strain (*Aktug et al.*, 2009). I compare PS InSAR with GPS data to see whether the spatial resolution of the GPS is too low to resolve strain localisation. I then combine the two data sets to generate velocity and strain rate maps, which can be used for seismic hazard assessment, and to distinguish between different dynamic models of continental deformation.

Extended Abstract

Investigating continental deformation using PS InSAR

Victoria A. Nockles
St Cross College, Oxford

Trinity 2015

Many, fatal earthquakes occur within the continental interiors where large populations are located in close proximity to faults (*Jackson*, 2006); such as the recent Nepal earthquake, which initial estimates suggest resulted in 8,126 fatalities http://earthquake.usgs.gov/regional/world/world_deaths.php. The Tibetan Plateau and Western Turkey are examples of two such areas, with high rates of continental deformation. Persistent Scatterer Interferometric Synthetic Aperture Radar (PS InSAR) is a space geodetic technique that can be used to measure and monitor the relationship between tectonic forces, stress and strain throughout the lithosphere. Such measurements can be used to improve our understanding of the earthquake cycle and contribute to seismic hazard assessment.

Study of the earthquake cycle using standard Differential Synthetic Aperture Radar (DifSAR) is becoming more widespread. However, PS InSAR studies have largely been constrained to measuring landslides, volcanic deformation, mining subsidence and acquifer recharge rather than tectonic processes. Whilst a wealth of literature is available on coseismic events using InSAR, there are still relatively few studies that measure postseismic and interseismic displacements. This is largely

because the signals are comparatively small. This study will use PS InSAR to measure interseismic strain accumulation across the Kunlun Fault in Tibet, postseismic signals related to the 2001 Kokoxili earthquake on an offshoot from this main fault (the Kunlun Pass Fault), and strain accumulation in Western Turkey.

To date most tectonic signals measured with InSAR have used Differential InSAR (DifSAR) rather than PS InSAR. Measuring accurate slip rates across the Tibetan Plateau using DifSAR has proved to be a difficult task (see *Garthwaite*, 2011), as the region is remote with high levels of erosion, steep topography, snow covered regions, and irregularly spaced satellite passes. This all contributes to regions of decorrelation across interferograms, difficulty with co-registration, and compounds unwrapping problems. Consequently, the area lends itself well to PS InSAR, where the selection of a subset of the data with good signal to noise ratio helps provide data in regions where decorrelation is high. It also enables constraints on perpendicular baselines (applied for standard InSAR) to be relaxed, so more satellite passes can be used in a region where there are already gaps in the time series of up to four years and many swaths are limited to at most two passes a year.

I compare for a single track of data measurements of satellite Line-of-sight (LOS) velocity obtained using DifSAR with those obtained using PS InSAR. I apply the PS selection process developed by *Hooper et al.* (2007) and implemented in the Stanford Method for Persistent Scatterers (StAMPS) software. The StAMPS framework is a series of spatial and temporal filtering routines used to estimate the different terms that compose the phase of an INSAR image to select pixels with high signal to noise ratio or Persistent Scatterers. In order to get accurate measurements the best parametrisations for PS selection in the region are explored and explained.

Satellite radar interacts with the dipole moments of gas molecules in the atmosphere, resulting in an increase in the apparent path length between the satellite and

the ground. Changing atmospheric conditions between SAR acquisitions (controlled primarily by pressure, temperature and water vapour content) vary the phase delay, in space and time, causing an atmospheric component that can be difficult to distinguish from deformation. To estimate the atmospheric LOS contribution to the radar delay (for each scene relative to a master scene), I use the European Centre for Medium Range Weather Forecasting (ECMWF) ERA interim re-analysis data. This was done following the approach of *Jolivet et al.* (2011). I show that, using this technique, estimates of the atmospheric contribution to phase delay spatially reflect variability in the real data, but often have an incorrect amplitude. I demonstrate that much better results can be obtained by applying a scaling factor based on the amplitude of the measured data to the atmospheric component.

The PS InSAR technique is then applied to 109 scenes of ENVISAT data from 2003-2010 covering a 750 km by 400 km region across the Kunlun Fault. The resulting data is used to estimate the variability in slip rate across this fault. Whilst a number of geological studies have used a combination of dating techniques and offset measurements, notably *Kirby et al.* (2007a) and *Van Der Woerd et al.* (2002), relatively few geodetic studies have mapped strain across the Kunlun Fault (*Zhang et al.*, 2004; *Li et al.*, 2005; *Wang et al.*, 2001; *Bell et al.*, 2011). In fact this is the first PS InSAR study measuring interseismic strain accumulation in Tibet.

The slip rates across major faults on the Eastern Tibetan Plateau are poorly constrained and vary significantly in different tectonic models. A number of studies have suggested variability in slip rate along the Altyn Tagh (*Taylor and Peltzer*, 2006) and Karakoram faults (*Chevalier et al.*, 2005; *Brown et al.*, 2002); However, the debate is split in the case of the Kunlun Fault. Some authors, including *Van Der Woerd et al.* (2002), have argued that slip rates are spatially uniform, based on offset measurements along a 600 km central section of the fault. Other authors,

including *Kirby et al.* (2007a), who focus more on the eastern end (towards the fault tip), suggest that slip rates systematically decrease towards the east.

Knowledge of slip rates along faults is key to our understanding of the mechanical behaviour of the crust and mantle beneath the plateau; for example they can be used to test the prediction of various models (*Van Der Woerd et al.*, 2002). The two main competing models are eastward rigid block translation and distributed deformation. The block model approach is analagous to plate tectonics applied by breaking up the major plates into microplates. The continnuum approch treats the lithosphere as a viscous fluid which flows under the influence of external boundary forces and internal buoyancy forces. We would expect the slip rates for distributed deformation to be lower than for rigid-block-translation (*England and Houseman*, 1986; *Avouac and Tapponier*, 1993; *England and Molnar*, 1997; *Meyer et al.*, 1998). This debate has important implications for the mechanisms of stress transfer and seismic risk in Tibet. GPS sites in the region are sparse, so InSAR is uniquely positioned to provide spatially dense data across the fault to help answer some of these questions.

Firstly, for a test track across the Kunlun Fault, I compare the results obtained using PS InSAR with those obtained using standard DifSAR for a small baseline subset of the data (SBAS). I show that in regions that are decorrelated in standard InSAR, or where there are few satellite passes, PS InSAR can maximise the information available in a given dataset, and measure signals that could not reliably be detected using DifSAR. I show velocity maps together with atmospheric estimates, tectonic models, and residuals for 5 tracks of data. Finally, I discuss why significantly lower slip rates are observed at the fault tip compared with the central section of the fault, and where this slip deficit is being transferred to beyond the Kunlun Fault.

The westernmost track of the processed data measured a postseismic signal related to the M_w 7.8 2001 Kokoxili earthquake. Previous InSAR studies for this event all use standard InSAR rather than PS InSAR and focus on the main fault strand over the earthquakes epicentre. Here, InSAR data is incoherent along the fault and there is very little data covering the peaks of the postseismic signal. By using PS InSAR on a track at the end of the Kokoxili rupture, 380km from the epicentre location, I show good coherence across the entire track with data connecting both sides of the fault and clearly defined peaks. Coseismic geodetic studies, notably *Lasserre et al.* (2005), suggest that the rupture continues to the east on the Kunlun Pass Fault rather than the main Fault strand. I analysed the measured surface displacements for this earthquake using the processed ENVISAT data to see whether the postseismic signal is localised across the Kunlun Fault, the Kunlun Pass Fault or a combination of both.

To date both afterslip and viscoelastic relaxation have been proposed as plausible mechanisms (*Wen et al.*, 2012) for this event. I show whether the deformation after the earthquake is due to one or more postseismic mechanisms. I model afterslip using the hot-friction approximation of the rate and state frictional laws to create a series of models with various preseismic slip rates and frictional parameters. I then perform a parameter space search to find the best fitting models to the Envisat data. I create a series of viscoelastic relaxation models with a Maxwell rheology using: PSGRN to prepare the green's functions that describe the model response; and PSCMP to calculate the surface displacements, using a discrete number of rectangular fault planes (*Wang et al.*, 2006). I then compare my results for rate and state friction models for the Kokoxili earthquake to those for the 1997 M 7.6 Manyi earthquake, taken from *Bell* (2013).

A number of studies have looked at interseismic strain accumulation across the

North Anatolian and East Anatolian faults, e.g. *Walters et al.* (2014); *Yamasaki et al.* (2013); *Cavalié and Jónsson* (2014), but relatively little work has been done on a fault scale across the grabens in Western Turkey. I use PS InSAR to look at this problem both due to the interest in regional tectonics and as a consequence of questions that have been raised by continous GPS monitoring. *Aktug et al.* (2009) argue that GPS results show largely uniform strain accumulation across the region and it is not known why this should be. I aim to see whether GPS data are too sparsely located to measure strain localisation or if the GPS data accurately show tectonic deformation in the region.

I use a combination of PS InSAR and GPS measurements to measure strain accumulation in Eastern Tibet from the Envisat satellite. I compare the PS InSAR data with GPS data in the region, to see whether the spatial resolution of the GPS is too low to resolve strain localisation across the grabens, or whether deformation is more distributed. I then combine the two data sets to generate high resolution velocity and strain rate maps, which can be used for seismic hazard assessment, and to distinguish between different dynamic models of continental deformation.

Acknowledgements

This research was funded by a tied Natural Environment Research Council studentship with Fugro NPA, bank of mum and dad, and the Department of Earth Sciences at Oxford University (with particular thanks to David Pyle and Chris Ballentine). All the data in this thesis were provided free from the European Space Agency. I would like to thank all those who have written code used in this thesis, in particular Andy Hooper for StAMPS, Rongjiang Wang for PSGRN/PSCMP and Marcus Bell.

Thank you to my supervisors Barry Parsons, Tim Wright and Rachel Holley for their helpful comments and constructive criticism. Many friends have also helped to proof read a number of the chapters. Particular thanks go to Jenny Southern, Kerry Mellor, Bethan White and Stefan Lachowycz. I also wish to thank my parents, big sister, Marion Marland, Jon Rollason, Kate Booys, Rachel Cassidy, Helen Burns, Ginny Howells, and OUMC for their support and encouragement.

Contents

List of Figures

List of Tables

Chapter 1

Introduction

Many, fatal earthquakes occur within the continental interiors where large populations are located in close proximity to faults (*Jackson*, 2006); such as the recent Nepal earthquake, which initial estimates suggest resulted in 8,126 fatalities http://earthquake.usgs.gov/regional/world/world_deaths.php. The Tibetan Plateau and Western Turkey are examples of two such areas, with high rates of deformation. Persistent Scatterer Interferometric Synthetic Aperture Radar (PS InSAR) is a space geodetic technique that can be used to measure and monitor the relationship between tectonic forces, stress and strain throughout the lithosphere. Such measurements can be used to improve our understanding of the earthquake cycle and contribute to seismic hazard assessment.

Study of the earthquake cycle using standard Differential Synthetic Aperture Radar (DifSAR) is becoming more widespread. However, PS InSAR studies have largely been constrained to measuring landslides, volcanic deformation, mining subsidence and acquifer recharge rather than tectonic processes. This is because early PS selection algorithms were not optimised for large areas, in remote regions , resulting in insufficient PS being selected to unwrap data. Whilst a wealth of literature is

available on coseismic events using InSAR, there are still relatively few studies that measure postseismic and interseismic displacements. This is largely because the signals are comparatively small. This study will use PS InSAR to measure interseismic strain accumulation across the Kunlun Fault, in Tibet, postseismic signals related to the 2001 Kokoxili earthquake on an offshoot from this main fault (on the Kunlun Pass Fault), and strain accumulation in Western Turkey.

1.1 Seismic hazard

Seismic hazard assessment used by government organisations and insurance companies typically combines: historical seismicity, knowledge of regional plate tectonics, fault locations and slip rates, paleoseismology, peak ground accelerations (PGA), and strain rates to generate seismic hazard maps. A number of regions that were assigned low seismic hazard using existing techniques have subsequently been the location of damaging earthquakes; for example, the 1995 Kozani-Grevna (*Goldsworthy and Jackson*, 2001) and 2011 Tohoku earthquakes (*Geller*, 2011). InSAR measurements can be directly used to generate strain rate maps (as shown in chapter 5 for Western Turkey) to improve existing seismic hazard maps.

In the last century over 2 million people in the world have died in earthquakes. Approximately 60% of these deaths have occurred in the Alpine Himilayan belt. This is the semi-continuous mountain chain that runs from the Meditteranean to China, for an extent of 10,000 km, and includes Tibet and Western Turkey, which form the focus of this study. In fact, the most damaging earthquake of the last century is the 1976 M 7.5 Tangshan earthquake, East of Beijing, which killed ∼255,000 people. Figure 1.1 shows global deaths from earthquakes above 10,000, since 1900.

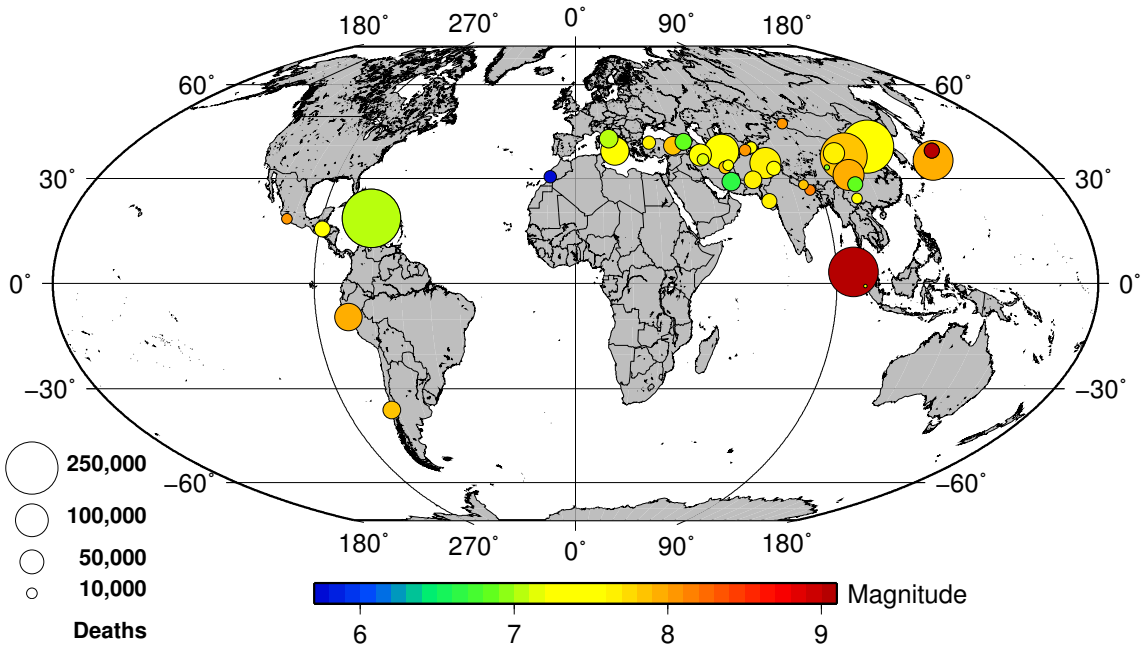

Figure 1.1: Distribution and scale of earthquake related deaths from 1900–2015 (May) with fatalities greater than 10,000 updated from *Elliott* (2008b). The area of the circles is proportional to the number of deaths and the colour to the earthquake magnitude. Data is taken from the USGS compilation (http://earthquake.usgs.gov/regional/world/world deaths.php). The earthquakes are mostly clustered along the Alpine-Himalayan orogen, with Italy, Turkey, Iran, Pakistan, India and China suffering a large number of fatal events. With the exception of the Sumatra earthquake with its many tsunami related deaths, the vast majority of deaths have occurred in earthquakes with a magnitude range of M 6.5–8 ($\sim 1 - 100 \times 10^{19}$ Nm), including the recent Nepal earthquake.

In recent years, earthquake fatalities have increased due to increasing concentration of population centres in close proximity to major faults (*Jackson*, 2006). Figure 1.2 shows a map of earthquakes that caused >1000 deaths in China and population density relative to the major fault systems. The most populated areas are located around the Ordos block, Beijing and the Sichuan Basin; these are also the regions where the highest number of deaths have occurred due to earthquakes. In the last century, three of the ten most destructive earthquakes in the world occurred in China, and three of the ten mostly deadly earthquakes in China occurred around the Sichuan Basin.

Furthermore, the most fatal earthquake in recorded history is believed to be

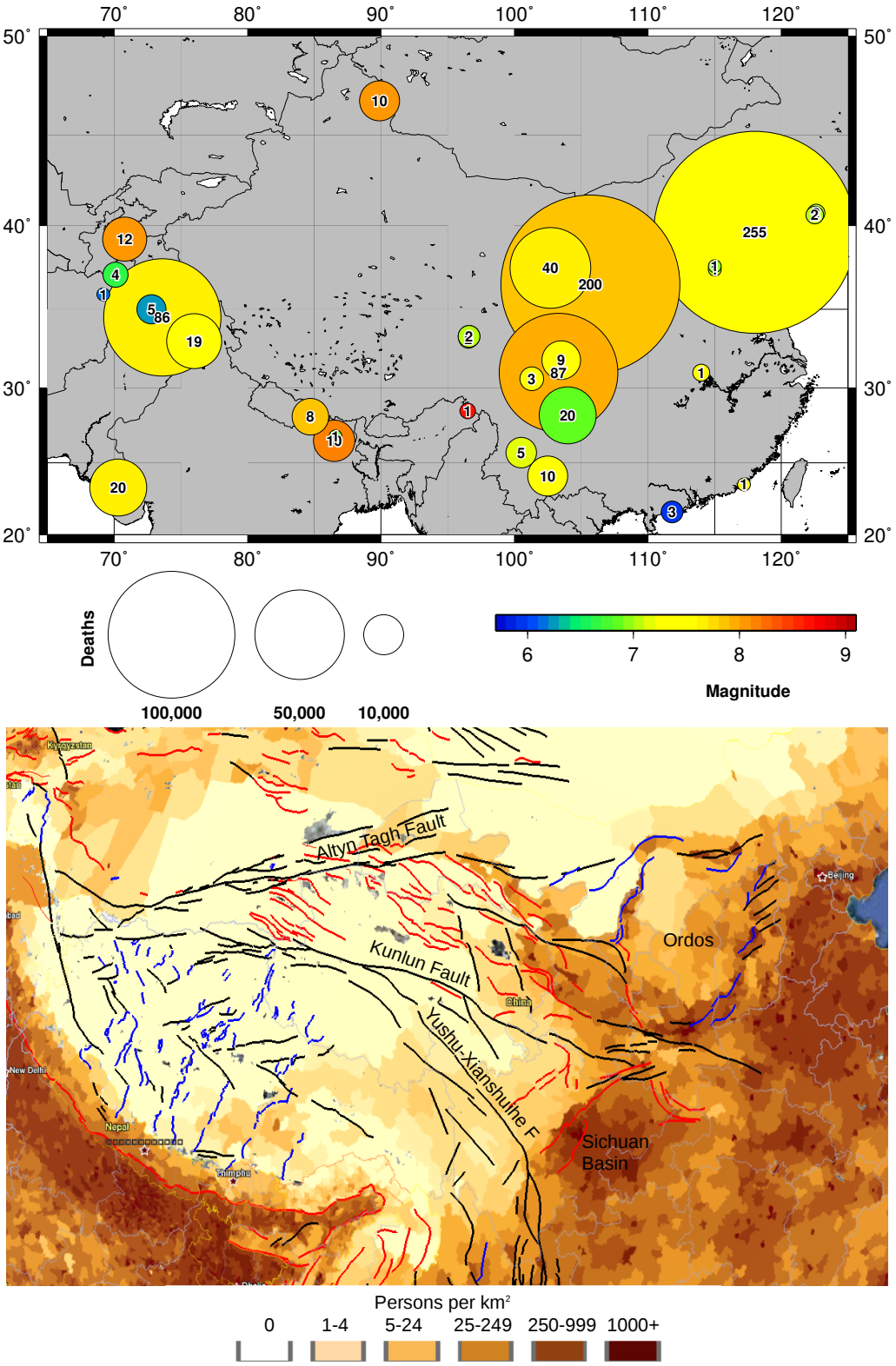

Figure 1.2: Earthquake related deaths of 1,000+ people in China 1900-2015 (May) (above) and a map showing the location of major fault systems relative to population density centres (below). Strike-slip faults are shown in black, thrust faults in red, and normal faults in blue (*Taylor and Yin*, 2009).

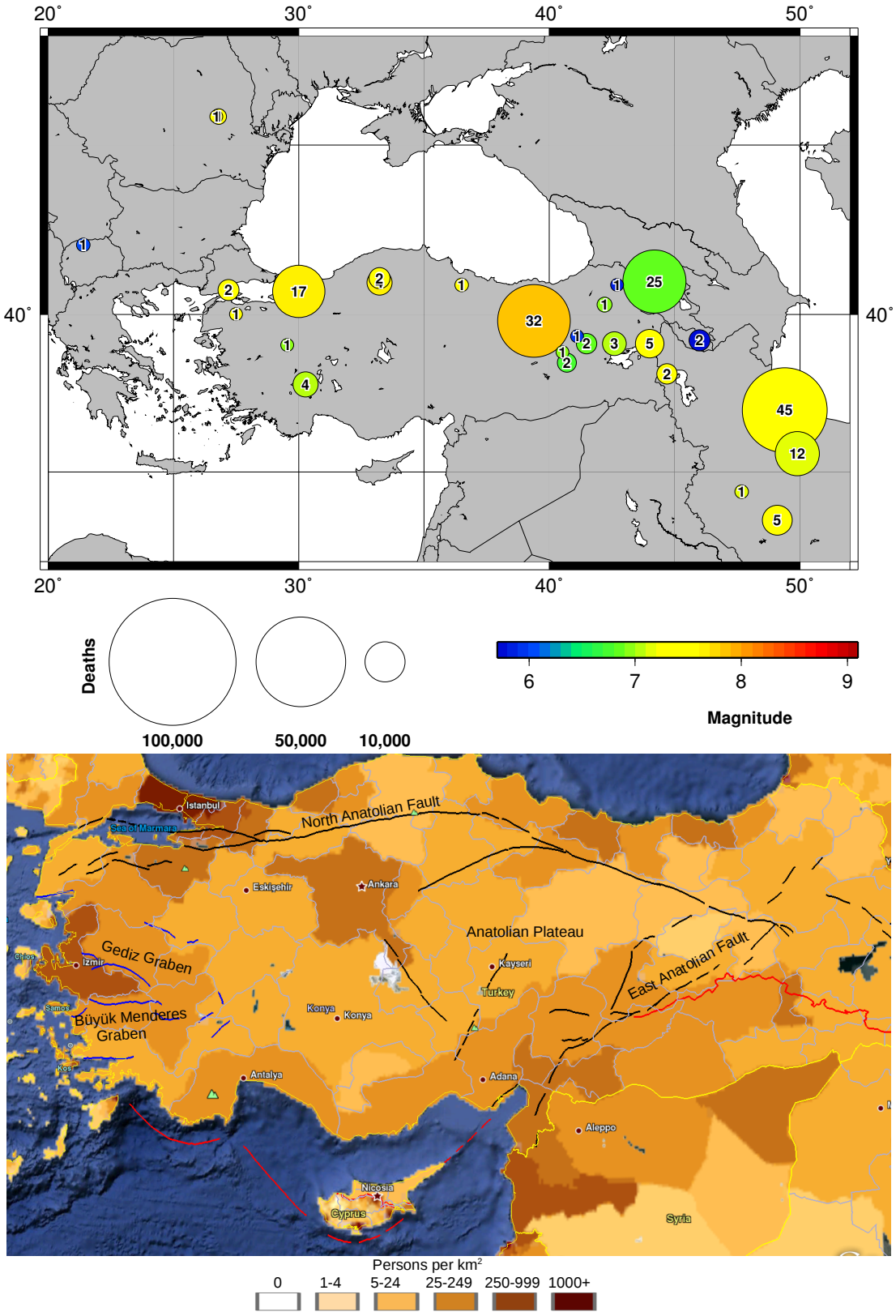

Figure 1.3: Earthquake related deaths 1,000+ in Turkey 1900-May 2015 compared to a map showing where the major fault systems are in Turkey (*Saroglu et al.*, 1992) (above) relative to population density centres.

Earthquake Deaths in China 2005–2015 (May)

Date yyyy mm dd	Location	Latitude	Longitude	Deaths	Magnitude
2008 05 12	Sichuan	31.0°N	103.3°E	87,587	7.9
2010 04 14	Qinghai	33.3°N	96.6 °E	2,968	6.9
2014 08 03	Ludian County	27.2°N	103.4°E	617	6.1
2013 04 20	Lushan County	30.3°N	103°E	193	6.6
2013 07 22	Gansu	34.5°N	104.2°E	95	5.9
2012 09 07	Yunnan Province	27.6°N	104°E	81	5.6
2008 08 30	Panzhihua	26.0°N	101.9°E	43	6.1
2011 03 10	Myanmar	24.7°N	98 °E	26	5.5
2006 07 22	Yanjin	28.0°N	104.2°E	22	4.9
2005 11 26	Jiangxi	29.7°N	115.7°E	16	5.2
2008 10 06	Damxung	29.8°N	90.3°E	10	6.4
2005 07 25	Heilongjiang	48.8°N	125.0°E	1	5.0
2005 10 16	Guangxi	23.6°N	107.8°E	1	4.2

Table 1.1: Earthquake fatalities from 2005–2015 (May) in China from the USGS compilation (http://earthquake.usgs.gov/regional/world/world_deaths.php), listed in order of the number of deaths. The total number of deaths resulting from these earthquakes is ∼91,660.

the 1556 M 8 Huaxian earthquake, in the Shaanxi Province of central China, which killed or injured up to 830,000 people (*Hou et al.*, 1998). In the last decade alone, 91,660 people in China have been killed by earthquakes. A table listing each of the events together with earthquake magnitudes and fatalities is shown in table 1.1. The most damaging of these earthquakes was the 2008 M 7.9 Sichuan earthquake, which left ∼87,000 people dead, many hundreds of thousands injured and many millions homeless (*Elliott*, 2008b). This is followed by the M 6.9 Yushu earthquake in 2010, which killed 2,968 people and injured over 12,000.

The Yushu earthquake is a good example of the advantages of InSAR compared to more traditional techniques. *Li et al.* (2011) measured surface displacements using InSAR to reveal a maximum slip of 1.5 m at a depth of 4 km, a fault dip of 70° and a rupture distance of almost 80 km. This rupture length is much longer

Earthquake deaths in Turkey of 1000+ during 1900–2015 (May)

Date yyyy mm dd	Location	Latitude	Longitude	Deaths	Magnitude
1939 12 26	Erzincan	39.80°N	39.38°E	32,700	7.8
1999 08 17	Doğantepe	40.70°N	30.00°E	17,118	7.6
1976 11 24	Çaldiran	39.10°N	44.00°E	5,000	7.3
1943 11 26	Ladik	40.97°N	33.22°E	4,000	7.6
1914 10 03	Burdur	37.82°N	30.27°E	4,000	7.0
1903 04 28	Malazgirt	39.10°N	42.60°E	3,500	7.0
1912 08 09	Murefte	40.75°N	27.20°E	2,800	7.4
1944 02 01	Gerede	41.11°N	33.22°E	2,790	7.4
1966 08 19	Varto	39.10°N	41.48°E	2,529	6.8
1975 09 06	Diyarbakir Province	38.50°N	40.70°E	2,300	6.7
1983 10 30	Erzurum and Kars	40.30°N	42.20°E	1,342	6.9
1946 05 31	Ustukran	39.33°N	41.10°E	1,070	5.9
1942 12 20	Urbaa	40.90°N	36.50°E	1,100	7.3
1970 03 28	Gediz	39.06°N	29.54°E	1,086	6.9
1953 03 18	Yenice Gonen	40.01°N	27.49°E	1,070	7.3
1971 05 22	Bingol	38.83°N	40.52°E	1,000	6.9
1903 05 28	Gole Malazgirt	40.90°N	42.70°E	1,000	5.8

Table 1.2: Earthquake fatalities 1,000+ from 1900–2015 (May) in Turkey from the USGS compilation (http://earthquake.usgs.gov/regional/world/world_deaths.php), listed in order of the number of deaths. The total number of deaths resulting from these earthquakes is ∼84,405.

than that estimated using initial seismological and field estimates of the fault length. Similarly, in Turkey, *Elliott et al.* (2013) used InSAR to measure surface displacements related to the M_w 7.1 Van earthquake. They estimated for this event 9 m of reverse and oblique slip on a pair of en-echelon NW40° − 54° dipping fault planes. This was the most damaging earthquake in Turkey in the last decade, it killed 604 people, injured 4,152 and left homeless an estimated 60,000 people.

Figure 1.3 shows earthquakes in Turkey, during the last century, causing >1,000 deaths. Table 1.2 lists these events together with fatalities. The most damaging earthquake in the last century in Turkey occurred in 1939, killing an estimated 32,700 people. It had a magnitude of M 7.8, 3.7 m of horizontal displacement, 2 m

of vertical offset, and resulted in over 300 km of surface rupture along the North Anatolian Fault between Erzincan and Niksar (http://earthquake.usgs.gov).

In Western Turkey, interseismic surface displacements have primarily been measured using GPS data, which is much more sparsely located than InSAR. The focus of this thesis, in measuring interseismic strain accumulation in Western Turkey, is from a longitude of ∼26°E to ∼31°E across the major grabens which are the most densely populated regions in Turkey, with the exception of Istanbul (see figure 1.3). There are also relatively few InSAR studies covering interseismic strain accumulation in Tibet, with the majority focusing on the Altyn Tagh (*Elliott et al.*, 2008a; *Jolivet et al.*, 2008; *Wright et al.*, 2004), the Karakoram (*Wang and Wright*, 2012; *Wright et al.*, 2004) and the Haiyuan faults (*Cavalié et al.*, 2008; *Jolivet et al.*, 2012). In contrast to Western Turkey, the Kunlun Fault, in Tibet, covers a region of low populations compared to the more densely populated Sichuan Basin and Ordos block (see figure 1.2). However, Tibet has formed a major role in the formulation of modern ideas on continental tectonics; in particular the debate on whether rigid blocks or distributed deformation (refer to section 1.2 and figure 1.5) are a more appropriate model for continental deformation processes (*Tapponnier et al.*, 1986; *England and McKenzie*, 1982).

1.2 Continental Tectonics

The theory of plate tectonics was developed in part to explain the occurence and location of earthquakes (*McKenzie and Parker*, 1967; *Morgan*, 1968). It states that the Earth's lithosphere is divided into a series of discrete rigid plates, separated by narrow boundaries of deformation (on the order of a few km) that are approximated as faults. Little internal deformation was permitted to occur within the plate, and

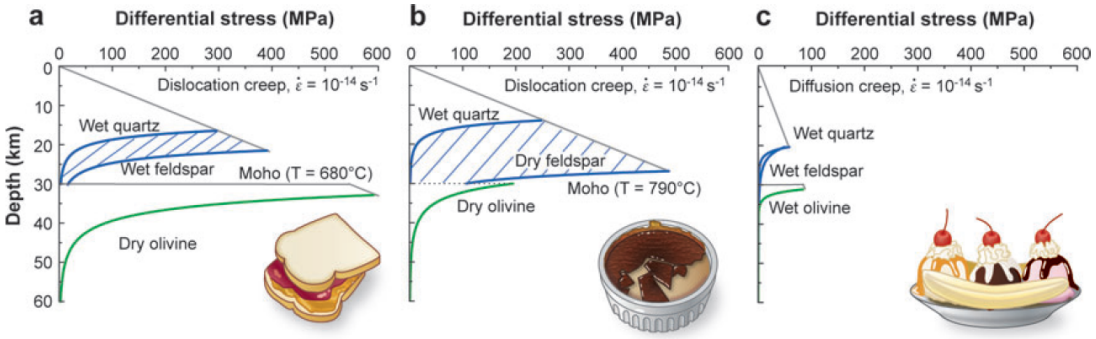

Figure 1.4: Schematic view of models of strength through continental lithosphere. All three models show an initial increase in strength with depth and pressure. The two left most models have a higher coefficient of friction due to lower pore pressure. Model a), the jelly sandwich, shows a low strength lower crust due to the presence of water. Model b), the crème brûlée, has a strong lower crust but weak upper mantle. The strength in this model lies in the brittle, dry crust. Model c), the banana split, considers faults as weak due to strain weakening and feedback processes. Taken from *Bürgmann and Dresen* (2008).

the relative motion of plates was described by rotations about Euler poles. This theory is shown to be a good representation of what occurs in oceanic lithosphere, but is a poor description of what happens in the continents.

In the case of oceanic lithosphere, earthquakes are shown to be localised at the plate boundaries; at the mid-ocean ridges, transform faults and subduction zones. However, on the continents, the regions of deformation that occur when continents converge are observed to extend over regions of over 1000 km and earthquakes are regularly observed to occur away from major plate boundaries.

This difference in behaviour between continental and oceanic lithosphere is a consequence of their distinct rheology (*Chen and Molnar*, 1983). The strength of oceanic lithosphere lies mainly within a single layer, most of which is within the mantle (*Wiens and Stein*, 1983). Oceanic lithosphere exhibits brittle behaviour as it is largely composed of olivine and is mostly anhydrous (*Byerlee*, 1978).

Models of continental lithospheric strength all show an initial increase in

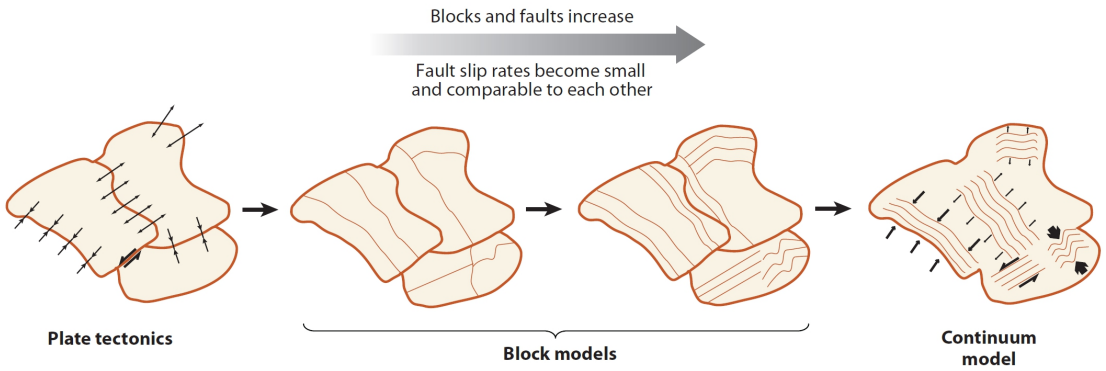

Figure 1.5: Image showing the transition from global plate kinematics of block models to continuum driven models. Fault slip rates become comparable to each other over the course of the transition. Bold lines denote major block boundary faults. Thin lines are faults separating smaller blocks. Reproduced from *Thatcher* (2009).

strength with depth. However, beyond a depth of 20 km the rheological and strength profiles are less certain, with three main structures suggested. These are summarised by *Bürgmann and Dresen* (2008) using analogies to a jelly sandwich, crème brûlée and banana split, as shown in figure 1.4. In the jelly sandwich model, a weak mid-to-lower crust is sandwiched between a strong upper crust and a strong upper mantle, with the latter composed dominantly of dry olivine. In the crème brûlée model, the strength of the lithosphere lies in the dry and brittle crust; the upper mantle is weak due to a higher geotherm. In the banana split model, there is weakness in major crustal fault zones throughout the lithosphere, due to strain weakening and feedback processes.

The observation that continental behaviour was inconsistent with the plate tectonic model resulted in a move to break up the major plates into microplates (*Meade and Hager*, 2005; *Thatcher*, 2009), i.e. the development of block model theory. *England and McKenzie* (1982) suggested that a more appropriate model would be a continuum model based on distributed deformation. This opened a debate between the proponents of block models and those of continuum models,

which remains today. The transition from global plate kinematics of block models to continuum models is illustrated in figure 1.5. In the context of Tibet, this debate centres around whether convergence between India and Asia is accommodated mostly by lateral expulsion of a rigid Tibetan microplate (*Tapponnier et al.*, 1986), or by thickening of the Tibetan Plateau (*England and Molnar*, 1997).

1.3 The Earthquake Cycle

The concept of the earthquake cycle was first developed by *Reid* (1910), following observations made before and after the San Francisco earthquake in 1906. He measured ground motions using triangulation on monuments, and noticed that before an earthquake the ground is moving fastest far away from the fault, and during an earthquake velocities were highest closest to the fault. He suggested that elastic strain accumulated on the fault due to continuous far-field motion either side of the fault, during the period before an earthquake (the interseismic period) and that as slip started, the frictional stress on the fault decreased, resulting in an earthquake (the coseismic). In this simple model, the sum of the interseismic and coseismic resulted in a step function across the fault that reflected permanent displacements. Elastic rebound theory had been conceived, together with the idea of a characteristic earthquake cycle with the build up and subsequent release of stress on characteristic recurrence timescales.

Although a good initial approximation of the earthquake cycle, Reid's elastic rebound theory omits later observations of large displacements after an earthquake, which decrease exponentially over time (the postseismic). It also fails to account for continuous creep and slow slip events such as at the Cascadia subduction zone

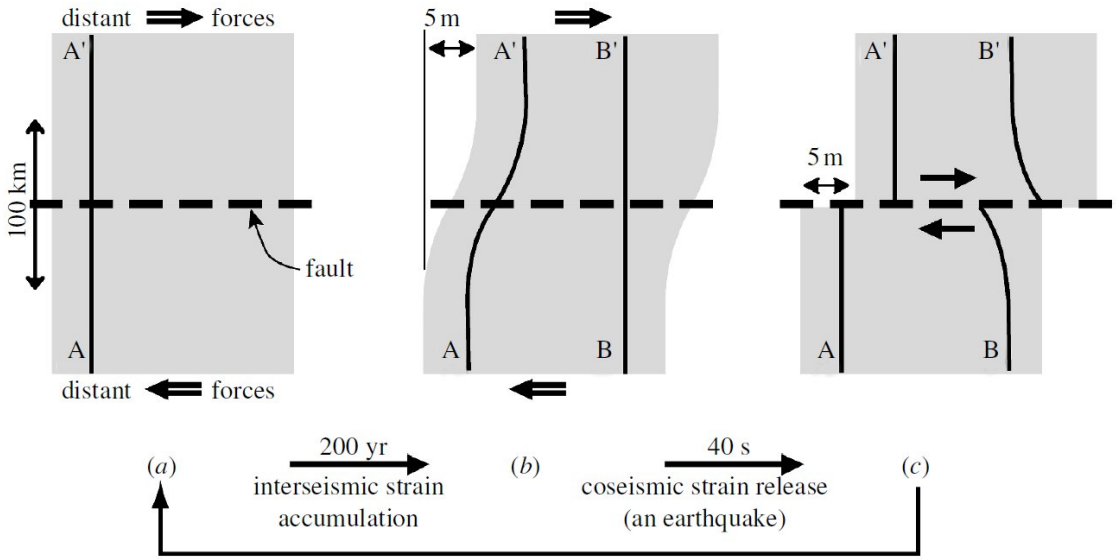

Figure 1.6: Adapted from *Wright* (2002). Elastic rebound model of *Reid* (1910) for the earthquake cycle. (a) shows a locked linear fault cutting through the elastically straining portion of the lithosphere the instant after the last earthquake (A-A'). (b) The same region is shown after interseismic displacements and shear strain accumulation in the region either side of an infinitely long strike-slip fault. Offset of the Earth's surface is observed in the far field as shown by profile A-A'. A second profile B-B' is marked just prior to the coseismic event. (c) Release of accumulated strain in the coseismic period returns the profile A-A' to being straight, but with right lateral offset equivalent to the coseismic slip. Profile B-B' is curved in the opposite sense to the interseismic strain and has the coseismic offset at the fault. There is no net accumulation of finite strain in either block after completion of the cycle.

(*Wang et al.*, 2003; *Rogers and Dragert*, 2003). The current model consists of three distinct phases; coseismic, interseismic and postseismic, all of which can be measured using InSAR (*Wright*, 2002).

1.3.1 Coseismic deformation

Coseismic deformation can be on the order of cm to m, occurs over a time period of seconds to minutes and has a lengthscale of tens of km. Eventually the build-up of strain below a locked fault overcomes friction, resulting in the onset of slip. Friction then decreases, causing an earthquake and consequent stress drop. There are two

main observations from the coseismic period: (i) seismic waves radiate from the fault rupture, which can be detected on seismometers, and (ii) permanent displacement is observed, which can be measured using offsets, InSAR and GPS.

Each of the techniques available for the observation of earthquakes have distinct advantages. Seismology measures waves emitted by the earthquake that can be detected at fixed locations globally. It has high temporal resolution, but uncertainties arise in precisely locating an earthquake as its position needs to be triangulated. GPS provides very precise continuous measurements at fixed locations. InSAR provides high spatial resolution images of deformation at the surface, but has poorer temporal resolution limited by satellite trajectories.

The first earthquake to be measured using InSAR was the Landers earthquake (*Massonnet et al.*, 1993). Measuring the coseismic signal with InSAR can provide the fault geometry and slip distribution, and enables us to calculate the seismic moment release (*Elliott*, 2008b). Knowledge of moment release is critical for seismic hazard assessment and for calculating regional strain rates (*Kostrov*, 1974; *Jackson and McKenzie*, 1988; *Ekström and England*, 1989).

The scaling laws that relate the slip and stress drop in an earthquake to fault rupture dimensions allow us to calculate earthquake moment release (*Scholz*, 1982). The earthquake moment release M_0 for an elastic dislocation of a halfspace with rigidity μ, with average slip of $\bar{u}$, for a rectangular fault of length L and width W is given by:

$$M_o = \mu L W \bar{u} \tag{1.1}$$

The average stress drop $\Delta\tau$ is given by:

$$\Delta\tau = C\mu\frac{\bar{u}}{L} \tag{1.2}$$

where C is a geometric constant and L a characteristic length scale. The characteristic length scale can either be the fault length or width. Combining equations 1.1 and 1.2 gives:

$$M_o = \alpha \mu L W^2 \tag{1.3}$$

where $\alpha = \frac{\Delta\tau}{C}$ and the length scale is assigned the fault width, W, and:

$$M_o = \alpha \mu L^2 W \tag{1.4}$$

where the length scale is assigned the fault length, L.

Average slip has been shown to increase with rupture length, but *Scholz* (2002) has shown that the earthquake magnitude remains proportional to L^2 regardless of earthquake size. This raises the question, which InSAR can help answer: to what extent are small earthquakes a model for large earthquakes?

1.3.2 Interseismic deformation

The interseismic signal is on the order of mm of motion per year, spread over a lengthscale of tens to hundreds of km. This signal has only recently become regularly measured using GPS and InSAR; there are still relatively few measurements using InSAR, as the signal is very small and noise within the data (particularly from atmospheric effects *Jolivet et al.* (2011)) is comparatively high. *Wright* (2002) was the first to measure interseismic strain accumulation using InSAR. Such measurements are incorporated to develop strain rate maps which may be used for seismic hazard assessment. From interseismic studies using InSAR we can estimate fault locking depths, compare slip rates of different faults, look at slip variability along strike and identify regions of creep and locked portions of faults. The different mod-

els that we use for interseismic signals are described in detail in chapter 3.

Initial interseismic studies using InSAR generated velocity maps using individual tracks, collapsing data onto a single profile across individual faults for example *Wright et al.* (2001) (North Anatolian Fault), *Taylor and Peltzer* (2006)(central Tibet), *Cavalié et al.* (2008) (Haiyuan Fault), and *Wang et al.* (2009) (Xianshuihe Fault). Then contiguous tracks were processed to retrieve spatial variations of interseismic coupling for example *Jolivet et al.* (2012) (Haiyuan Fault), *Thomas et al.* (2014) (Longitudinal Valley Fault, Taiwan), and *Cetin et al.* (2014) (North Anatolian Fault). More recent studies have focused on identifying temporal variations in coupling of creep for example *de Michele et al.* (2011); *Jolivet et al.* (2014); *Khoshmanesh et al.* (2015); *Turner et al.* (2015) (San Andreas Fault).

1.3.3 Postseismic deformation

The 1906 San Francisco earthquake provided some of the earliest studies that observed continuing, time-decaying displacements immediately after an earthquake (*Thatcher*, 1975). It is now widely accepted that large earthquakes are followed by transient postseismic deformation that occurs in response to stress variations in an earthquake (*Segall*, 2010).

The magnitude and wavelength of postseismic signals are generally on the order of mm to cm, and tens to hundreds of km, respectively. These wavelengths are much larger than for equivalent coseismic signals. The physical mechanisms behind postseismic signals have been modelled using a variety of techniques; the main models are viscoelastic relaxation, transient fault slip within the rupture zone (or below it on the downdip extension of the fault), known as afterslip, and poroelastic rebound (*Perfettini et al.*, 2005). InSAR and GPS can contribute towards discriminating between these different mechanisms by measuring the time evolution of surface dis-

placements after earthquakes.

Measuring and modelling postseismic signals provides us with constraints on the rheology of the lower crust and the upper mantle lithosphere (*Bürgmann and Dresen*, 2008). Accurate modelling of postseismic signals is also crucial for reliable assessment of seismic moment using InSAR, as the first satellite passes can be days, weeks or even months after an earthquake. The coseismic response would therefore incorporate a postseismic signal that needs to be removed before assessing seismic moment. We also need to account for postseismic signals when measuring interseismic rates; for example, the Manyi (*Bell*, 2013) and Kokoxili earthquakes (see chapter 3) need to be accounted for when measuring slip rates across the Kunlun Fault.

1.4 PS InSAR

InSAR is a geodetic technique that uses the difference in the phase of radar returns between two satellite passes to measure ground motion on the order of millimeters with spatial resolution on the order tens of meters. To obtain images with a coherent signal, standard InSAR is limited to satellite passes with similar trajectories (low perpendicular baselines) and short time spans (small temporal baselines). Persistent Scatterer (PS) InSAR is a later adaptation that selects pixels from a standard InSAR image with high signal to noise ratio. This enables constraints on temporal and perpendicular baseline to be relaxed and reduces decorrelation and noise.

PS InSAR was developed by *Ferretti et al.* (2001) and piloted in urban areas. Two different algorithms for the selection of PS were originally developed. The first uses temporal correlation to identify bright pixels that are stable across a number of interferograms and is expected to work better in urban environments. The second

technique uses spatial correlation across neighbouring pixels and is expected to work better in non-urban areas. Both techniques used amplitude to select PS. *Hooper et al.* (2004) later adapted the technique to work better in natural terrains, using a probabilistic approach to PS selection based on phase stability. It is the first PS InSAR method designed to select a network of self-consistent PS in the absence of bright scatterers that does not require an assumed deformation model as an input. I apply this probabilistic approach to regions of normal faulting in Western Turkey and the Kunlun Fault in China. In carrying out this study it is anticipated that contributions will be made to our understanding of the kinematics (describes the deformation) and dynamics (considers the underlying forces that account for deformation using initial conditions and physics) of faulting.

1.5 Thesis structure

The rest of this thesis looks at the application of PS InSAR to the earthquake cycle in Tibet and Western Turkey, organised as follows:

Chapter 2 introduces the basic theory behind PS InSAR. I start with a description of the process used to filter and isolate different components of the phase. I then explain the probabilistic PS selection process and how different selection parameters alter the results. I compare PS selection results produced using StAMPS with those from GAMMA. I outline the techniques for orbital phase error removal, the correction of atmospheric errors, and the unwrapping of data to obtain a continuous deformation field. Finally I demonstrate the result of inverting for an amplitude scaling factor whilst correcting the phase for atmospheric effects using ECMWF data.

Chapter 3 looks at slip rate variability across the Kunlun Fault using PS InSAR.

I start with a basic review of Tibetan tectonics, then describe seismic activity and slip rates across strike-slip faults, measured primarily using GPS and geological techniques. I review the modelling of interseimic strain accumulation across strike-slip faults using the Kunlun Fault as an example. I use a test track to compare line-of-sight velocity maps generated using standard DifSAR with those produced using PS InSAR, during the interseismic period. I show velocity maps for five tracks of data across the Kunlun Fault, generated using PS InSAR. Finally, I invert the observed data to obtain slip rates along subsections of the Kunlun fault, and compare the results to estimates from other techniques.

Chapter 4 is a study of the postseismic displacements following the 2001 Kokoxili earthquake towards the end of the coseismic rupture. I show whether the signal is localised across the Kunlun Fault, the Kunlun Pass Fault or a combination of both. Models are then produced of rate and state frictional afterslip, and viscoelastic relaxation. These are tested against observations from PS InSAR to distinguish between plausible mechanisms. I compare the results to the best fit models and observed surface displacements from the Manyi earthquake.

Chapter 5 shows the results of an interseismic PS InSAR study across the major grabens in Western Turkey. I use five overlapping tracks for both ascending and descending satellite passes, that cover a region 400 km $\times$ 300 km: from the North Anatolian Fault in the north to the Mediterranean Sea in the south, and from Antalya in the east to the Aegean Sea in the west. I combine these data with a compilation of GPS data to generate a velocity field and strain rate map for the region.

Chapter 6 summarises the findings of the previous chapters, discusses the tectonic and technical implications of these findings, and explores further work that could be undertaken.

Chapter 2

PS InSAR

To date most tectonic signals measured with InSAR have used DifSAR rather than PS InSAR. In this chapter I discuss the PS selection process developed by *Hooper et al.* (2007) and implemented in the Stanford Method for Persistent Scatterers (StAMPS) software. I then explain and show some examples of the parameters that are altered to optimise the processing chain. I describe the post processing data analysis techniques and the modelling appropriate to each phase. I also discuss and show examples of different atmospheric noise removal techniques and illustrate the benefit of using amplitude scaling on ECMWF data models, when applying them to InSAR.

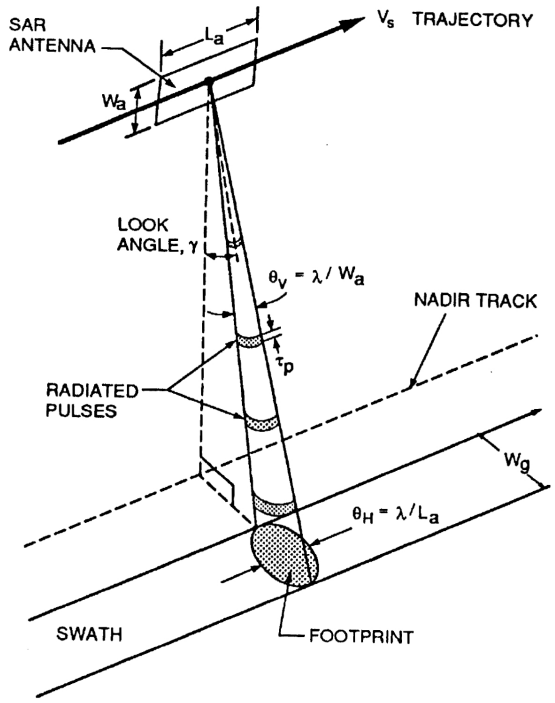

Figure 2.1: SAR configuration, antenna and swath parameters, reproduced from *Curlander and McDonough* (1991). V_s - satellite velocity (∼6 km/s), L_a - antenna length (∼10 m), W_a - antenna width (∼1 m), λ - wavelength (∼60 mm) θ_V - beam width, τ_p - radar pulse duration (∼ 37μs), θ_H - azimuth beam width, W_g - swath width (∼100 km).

2.1 InSAR

Many authors have described in detail the theory of InSAR and the methodology behind processing data up to the point of generating an interferogram. This detail is therefore omitted here and the author refers the reader to the following references for background information on these techniques, *Rosen et al.* (2004), *Curlander and McDonough* (1991), *Hanssen* (2001), *Buckley* (1998), *Zebker et al.* (1994). All of the data processed in this thesis comes from the ENVISAT satellite launched by ESA in 2002. The acquisition geometry is shown in figure 2.1 as a quick reference for error terms that are discussed in the following sections.

PS InSAR and DifSAR have been largely used for different applications as they have distinct advantages. PS InSAR can extend the available data by using pairs

of scenes with larger perpendicular distances between satellite passes, known as the perpendicular baselines. This enables us to dispense with the common assumption of rates of uniform deformation and generate a time series. Uniform deformation rates are often assumed as data are routinely stacked, in order to reduce noise levels sufficiently to accurately measure ground motions. PS InSAR involves using a select subset of the data spatially with improved signal-to-noise ratio(SNR). To date it has been shown to be good at delineating short wavelength features and works well in urban environments *Hooper et al.* (2004). The main challenge is to extend the technique to work in natural terrains by ensuring sufficient PS are selected to successfully unwrap data over larger areas. DifSAR exploits the large volume of data by spatially averaging. It is good at delineating long wavelength deformation and works well in natural terrains. Whilst DifSAR is an established technique for measuring tectonic deformation, PS InSAR has been mostly applied for monitoring localised patterns of subsidence related to mining, geothermal plants, landslides and volcanic activity (*Ferretti et al.*, 2000; *Hooper et al.*, 2004). Very little research has focused on using PS InSAR for measuring long-wavelength tectonic processes.

2.1.1 Contributions to phase delay

In this section I explain the different components of the measurement included in our data when we generate an interferogram. Subsequent sections detail how errors are mitigated or removed within StAMPS using the PS InSAR technique.

The interferometric phase at a given pixel p, located at position (k, l), in an unwrapped interferogram n, generated between a master image i and slave image j, is composed of a geometric phase component $\delta\phi^{\epsilon}_{n,p}$, a phase error due to errors in the satellite orbits $\delta\phi^{orb}_{n,p}$, a tectonic signal $\delta\phi^{def}_{n,p}$, an atmospheric phase error $\delta\phi^{atm}_{n,p}$, a noise component due to variability in scattering from the ground, thermal noise

and coregistration errors $\delta\phi_{n,p}^{noise}$, and an offset from the reference pixel $\delta\phi_{n,p}^{ref}$ which can be written as:

$$\delta\phi_{n,p} = \delta\phi_{n,p}^{\epsilon} + \delta\phi_{n,p}^{orb} + \delta\phi_{n,p}^{def} + \delta\phi_{n,p}^{atm} + \delta\phi_{n,p}^{noise} + \delta\phi_{n,p}^{ref} \tag{2.1}$$

The removal of the contributions due to topography and imaging geometry is referred to as the flattening of interferograms. This process involves two key stages: removal of the phase component due to earth curvature, and removal of topographic errors due to DEM error and sub-pixel position error.

2.1.2 Geometric phase error

To remove effects due to earth curvature we assume that all scatterers lie on the WGS-84 ellipsoid. A DEM in radar coordinates is used to compute the topographic phase component. Using an approximate DEM can introduce systematic errors resulting in a topographic error $\delta\phi_{ij}^{top}$ at a given pixel (k, l) given by:

$$\delta\phi_{ij}^{top}(k,l) = \frac{4\pi}{\lambda}\frac{B_{\perp}\Delta H(k,l)}{r\sin\theta} \tag{2.2}$$

where λ is the radar wavelength, $B_{\perp}$ is the perpendicular baseline between the slave and master scene, $\Delta H(k,l)$ is the DEM error, r is the distance between the radar antenna and the target, and θ is the incidence angle.

If the dominant scatterer in a SAR pixel is not centered on the pixel location, we get a range sub-pixel position error that introduces a corresponding phase offset given by *Kampes* (2006):

$$\delta\phi_{range} = \frac{4\pi}{\lambda}B_{\perp}\frac{\epsilon\cos(\theta)}{r} \tag{2.3}$$

where ϵ is the distance of the dominant scatterer from the SAR pixel centre. From the equations above it can be seen that the range sub-pixel error has the same relationship to phase as the topographic error so the two components are indistinguishable.

Similarly if the squint angle between each of the scenes used to generate an interferogram is different, we get a sub pixel azimuth error due to an offset of the dominant scatterer from the SAR pixel centre, which is given by:

$$\delta\phi_{azi} = \frac{2\pi}{\nu} \cdot \Delta F_{DC} \cdot \eta \tag{2.4}$$

where ν is the velocity of the SAR platform, ΔF_{DC} is the difference in doppler centroid frequency between the master and slave, and η is the offset in azimuth of the dominant scatterer from the SAR pixel centre. The azimuth offset makes a very small contribution and can be indistinguishable from deformation so is ignored.

2.2 PS InSAR

Ferretti et al. (2000) developed a technique to mitigate decorrelation effects that they referred to as Permanent Scatterers. They identified resolution elements whose echo is dominated by a single scatterer. If a pixel contains only one scatterer, then there is no cancellation of the echo as the imaging geometry changes. This eliminates spatial decorrelation and temporal decorrelation due to the random motion of small scatterers over time (*Ferretti et al.*, 2000). Figure 2.2 illustrates a pixel that is dominated by a signal from a single scatterer and one that has more distributed scattering. Their corresponding variability in phase is shown in the scatter plot below. Echoes from dimmer distributed scatterers are referred to as clutter and contribute to $\delta\phi_{i,j}^{noise}$ in equation 2.1.

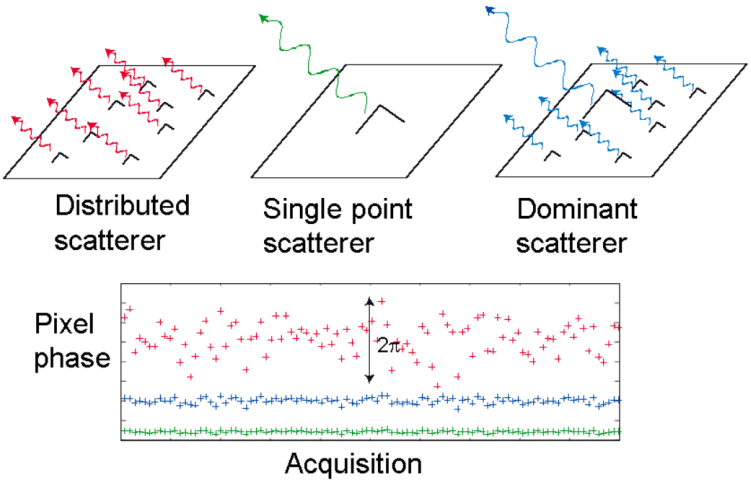

Figure 2.2: Models showing the scattering mechanisms for a SAR resolution element for a distributed scattering pixel (red), an ideal single point scatterer (green) and a pixel with a single dominant persistent scatterer (blue). Scatter plots below show the PS pixel has a much smaller phase variation than the distributed scatterer, *Zebker et al.* (2007).

Prior to the development of StAMPS, two key techniques were used to identify PS: amplitude dispersion (explained in section 2.3.1) and the signal-to-clutter ratio (SCR). The SCR is defined as the ratio of the reflected energy from the dominant scatter to the reflected energy from the rest of the resolution cell. It is evaluated using the power of a PS candidate to that of its neighbouring pixels (*Kampes and Adam*, 2005; *Kampes*, 2006). In general, a high SCR, ∼8, indicates low interferometric phase variation, ∼ 0.25 rads (*Zebker et al.*, 2007).

The SCR selection technique has been shown to work well for monitoring short wavelength deformation in urban areas. Figure 2.3 shows examples of PS selected with this technique using GAMMA near Izmir, in Turkey. However, in natural terrain PS pixels with low SCR often have stable phase characteristics but would not be identified using this technique. *Hooper* (2006) introduced a technique for identifying PS with stable phase rather than amplitude. This was shown to work well in natural environments and has the added advantage that no assumed deformation

Figure 2.3: Examples of PS selected using a combination of Signal-to-Clutter Ratio and amplitude dispersion in an urban environment using GAMMA. Here the corners of buildings in a housing development and a central reservation barrier along a motorway are the source of PS clusters. This data is taken from track 14 in the region surrounding Izmir in Western Turkey.

Spectral phase characteristics

	Component	Spatial Properties	Temporal Properties
$\delta\phi^{\epsilon}$	Geometric	High frequency	Correlated with baseline
$\delta\phi^{atm}$	Atmosphere	Low frequency	High frequency
$\delta\phi^{orb}$	Orbital error	Low frequency	Low frequency
$\delta\phi^{n}$	Scatterer noise	High frequency	High frequency
$\delta\phi^{def}$	Deformation	Low frequency	Low frequency

Table 2.1: Spectral phase characteristics of each of the terms in equation 2.1 for a PS pixel *Hooper* (2006)

model is required (*Hooper*, 2006).

2.3 StAMPS

In the case of StAMPS, PS pixels are defined as those pixels in a series of SAR images with very little variation in the scatterer noise term, ϕ^{noise}, and other noise such as that due to the atmosphere. The StAMPS framework is a series of spatial

and temporal filtering routines used to estimate the first five terms in equation 2.1: the phase error due to inaccuracies in the DEM, the phase error due to orbit inaccuracies, the deformation, the atmospheric phase component, and the scatterer noise term; and thereby identify PS. This is done by assuming a given spectral structure for each of the phase components, as shown in table 2.1 taken from *Hooper* (2006).

This section summarises the techniques used by the StAMPS software (downloadable from http://homepages.see.leeds.ac.uk/ earahoo/stamps/) and the author refers the reader to *Hooper* (2006), *Hooper et al.* (2007), *Hooper et al.* (2004), *Ferretti et al.* (2001), *Colesanti et al.* (2003), *Zebker et al.* (2007) and *Shankar and Zebker* (2011) for a more in depth analysis of the subroutines incorporated in this software. Where there are parameters explained in the text that are user-controlled in the software, I have highlighted them in bold and used the same terminology as the Matlab scripts.

The StAMPS software has a range of parameter options for the filtering of data, the selection of PS candidates, the weeding out of noisy candidates and the unwrapping of data. I explain here the theory behind the StAMPS method alongside how these parameters control each aspect of the processing chain.

PS analysis is done using a set of interferograms generated with respect to a master scene. This master is chosen to minimise decorrelation effects and atmospheric effects. I also try to pick a scene that is central in the time series, and that maximises the number of interferograms with small perpendicular baselines. I oversample the Single Look Complexes (SLC) by a factor of 2 to carry out the analysis at the highest possible resolution. I produce interferograms using the DORIS software and divide them into square patches to carry out PS selection. For each track approximately 12 patches are used.

2.3.1 Amplitude analysis

To improve computational efficiency, a preliminary selection of PS candidates is made on a pixel by pixel basis, using **amplitude dispersion** which is a measure of their stability. It is defined as the ratio between the standard deviation, σ_b, and the mean of the SAR amplitude, μ_b:

$$D^A = \frac{\sigma_b}{\mu_b} \tag{2.5}$$

This technique was first developed by *Ferretti et al.* (2001) and is used here with a high threshold value of 0.4 to 0.45. This first pass is intended to reduce the processing time for later selection stages by removing only those points in the sea, and in decorrelated areas affected by high levels of vegetation or snow. The pixels are then weighted by the inverse of the dispersion amplitude.

2.3.2 Phase stability

To assess phase stability StAMPS uses a temporal coherence measure developed by *Hooper et al.* (2007). This measure is defined as the temporal coherence of our noise term, $\delta\phi^{noise}_{n,p}$, so is independent of variability in phase of the other terms that compose our measured signal in equation 2.1. To separate out these components it is assumed that $\delta\phi^{def}_{n,p}$, $\delta\phi^{atm}_{n,p}$ and $\delta\phi^{orb}_{n,p}$ are spatially correlated over distances of a given length scale L (user-defined), and that $\delta\phi^{\epsilon}_{n,p}$ and $\delta\phi^{noise}_{n,p}$ are uncorrelated over the same length scale with a mean of zero.

Shankar (2010) showed that if the positions of all PS are known, the mean phase of all those within a circular patch, centred on a pixel p, with radius L is given by:

$$\delta\bar{\phi}^{PS}_{n,p} = \delta\bar{\phi}^{orb}_{n,p} + \delta\bar{\phi}^{def}_{n,p} + \delta\bar{\phi}^{atm}_{n,p} + \delta\bar{\phi}^{noise}_{n,p} \tag{2.6}$$

where $\delta\bar{\phi}^{noise}_{n,p}$ is the sample mean of the uncorrelated noise terms and the remaining terms are the sample means of the correlated components, $\delta\phi^{def}_{n,p}$, $\delta\phi^{atm}_{n,p}$ and $\delta\phi^{orb}_{n,p}$. The uncorrelated noise terms are assumed to be small and are given by collecting the phase noise component and the geometric phase error, $\delta\phi^{noise}_{n,p} + \delta\phi^{\epsilon}_{n,p}$. Subtracting the mean of the sample, $\delta\bar{\phi}^{PS}_{n,p}$, in equation 2.6 from the measured phase data, $\delta\phi_{n,p}$, defined in equation 2.1 then gives:

$$\delta\phi_{n,p} - \delta\bar{\phi}^{PS}_{n,p} = \delta\phi^{\epsilon}_{n,p} + \delta\phi^{noise}_{n,p} - \delta\bar{\phi}^{noise\prime}_{n,p} \tag{2.7}$$

where

$$\delta\bar{\phi}^{noise\prime}_{n,p} = \delta\bar{\phi}^{noise}_{n,p} - (\delta\phi^{atm}_{n,p} - \delta\bar{\phi}^{atm}_{n,p}) - (\delta\phi^{orb}_{n,p} - \delta\bar{\phi}^{orb}_{n,p}) - (\delta\phi^{def}_{n,p} - \delta\bar{\phi}^{def}_{n,p}) - \delta\phi^{ref}_{n,p} \tag{2.8}$$

The azimuth offset that forms a part of the geometric phase error, $\delta\phi^{\epsilon}_{n,p}$ makes a very small contribution to the error terms and can be confused with deformation so is ignored. The geometric phase error is therefore reduced to the sum of the phase error due to DEM errors and the subpixel position error in range, given by equations 2.2 and 2.3, respectively. This component is proportional to the perpendicular baseline so can be represented by:

$$\delta\phi^{\epsilon}_{n,p} = B_{\perp n,p} K^{\epsilon}_{p} \tag{2.9}$$

where K^{ϵ}_{p} is the proportionality constant. This constant is estimated on a pixel by pixel basis with a least squares inversion using all available interferograms. Substi-

tuting equation 2.9 into equation 2.7 then gives:

$$\delta\phi_{n,p} - \delta\bar{\phi}^{PS}_{n,p} = B_{\perp n,p}K^{\epsilon}_{p} + \delta\phi^{noise}_{n,p} - \delta\bar{\phi}^{noise\prime}_{n,p} \tag{2.10}$$

The temporal coherence, γ_p is then measured on a pixel by pixel basis using (*Hooper et al.*, 2007):

$$\gamma_p = \frac{1}{N}\left|\sum_{n=1}^{N}\exp\{j(\delta\phi_{n,p} - \delta\bar{\phi}^{PS}_{n,p} - \delta\hat{\phi}^{\epsilon}_{n,p})\}\right| \tag{2.11}$$

where N is the number of interferograms and $\delta\hat{\phi}^{\epsilon}_{n,p}$ is our estimate of the geometric error. This estimate is obtained using equation 2.10 to estimate K^{ϵ}_{p} in a least squares sense, as this is the only term that correlates with baseline. For small values of $\delta\bar{\phi}^{noise\prime}_{n,p}$ the temporal coherence is a measure of the phase stability so can be used to select PS. However, $\delta\bar{\phi}^{noise\prime}_{n,p}$ is dominated by the spatially correlated phase components: orbital phase error, deformation and atmospheric phase error, making it difficult to identify scatterers. To minimise $\delta\bar{\phi}^{noise\prime}_{n,p}$ we therefore first estimate the spatially correlated components using a combined lowpass adaptive phase (CLAP) filter. We then remove them before evaluating the temporal coherence. Our estimate of the phase stability is then refined in an iterative process described in subsection 2.3.3.

2.3.3 Estimation of temporal coherence

Hooper et al. (2007) show that PS can be identified using the temporal coherence provided that we have prior knowledge of other PS locations as this is required to calculate the mean phase of the PS for each patch, as shown in equation 2.11. Initially, we have no knowledge of the location of any PS. *Hooper et al.* (2007) therefore

developed an iterative process to identify PS in all locations simultaneously. For a first pass the starting PS candidates could be all available data, but to improve computational efficiency I use only those remaining after the removal of points with **amplitude dispersion** below the chosen threshold (see section 2.3.1).

For each PS candidate, at each iteration, we: subtract the mean of other local candidates as shown in equation 2.7, estimate K_p^{ϵ}, and calculate the temporal coherence. All PS with low temporal coherence are temporarily rejected as those with higher values are statistically more likely to be PS. The means of each patch are then recalculated using only the remaining candidates.

At each iteration each pixel amplitude is weighted by an estimate of the signal to noise ratio (SNR). For the first pass the SNR is calculated using the amplitude dispersion only. For all subsequent steps a combination of the amplitude dispersion and our noise estimate are used to calculate the SNR.

Weighting pixels by SNR

The SNR is given by (*Hooper et al.*, 2007):

$$SNR = \frac{\hat{g}_p^2}{[\hat{\sigma}_p^{noise}]^2} \tag{2.12}$$

where our estimate of the amplitude of the signal $\hat{g}_p$ is given by:

$$\hat{g}_p = \frac{1}{N} \sum_{n=1}^{N} A_{n,p} \cos \delta\phi_{n,p}^{noise} \tag{2.13}$$

and the estimate of the noise variance for a gaussian distribution is given by:

$$[\hat{\sigma}_p^{noise}]^2 = \left[\frac{\sum_{n=1}^{N} A_{n,p}^2}{N} - \left(\frac{\sum_{n=1}^{N} (A_{n,p} \cos \delta\phi_{n,p}^{noise})}{N} \right)^2 \right] \tag{2.14}$$

At each iteration we re-estimate the temporal coherence for every candidate with the new weighting applied. At each new iteration $\delta\bar{\phi}_{n,p}^{n}{}'$ is generally smaller than previously until gradually the temporal coherence is dominated by the noise term, $\delta\phi_{n,p}^{noise}$. A limit for convergence is chosen using **gamma change convergence**. The iteration ceases when the difference in the mean value of the temporal coherence(γ_p) between the current iteration and the previous iteration is less than the chosen threshold. We now have estimates of the phase stability of each pixel. Next we select those most likely to be PS.

2.3.4 PS selection

Any pixel with random phase has a finite chance of having high temporal coherence resulting in the selection of false positives. PS candidates are therefore selected based on those statistically most likely to be true PS using a threshold value for the fraction of false positives that we decide are acceptable. We then reject pixels based on three main criteria: those that are only PS in a subset of the interferograms, those that are noisy, those with energy leaking from surrounding pixels.

Random phase sequences

We statistically assess the estimate of our noise term using probabilities to keep the fraction of incorrectly identified PS below a specified value, q (*Hooper et al.*, 2007). In StAMPS q can either be specified in terms of a maximum percentage or in terms

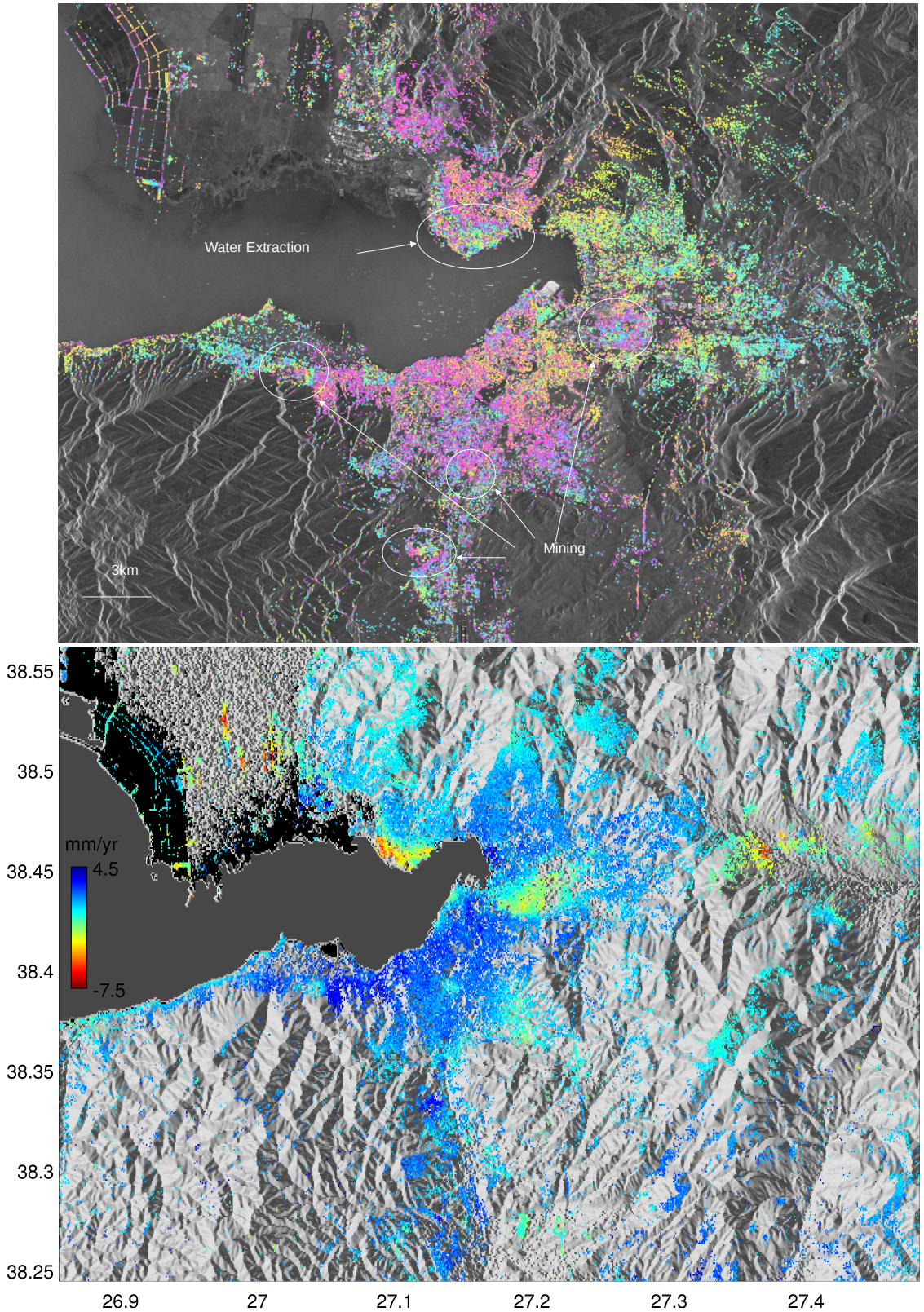

Figure 2.4: Wrapped interferogram showing PS selection (in Izmir, Western Turkey) using the GAMMA software (above) and unwrapped for the StAMPS software (below). Insufficient PS were found in non-urban areas using GAMMA to unwrap the data. This resulted in jumps in velocity at patch boundaries. Sufficient PS are selected using the StAMPS algorithm where PS are found particularly in the bottom left hand corner and the bottom right hand corner. Wrapped data is superimposed on an amplitude image in the radar co-ordinate geometry. Unwrapped data is superimposed on a DEM in geographic co-ordinates.

of a maximum density of pixels with random phase using the parameters **density random** and **percentage random** and by changing the **select method**.

We could assess the probability of a pixel being a PS based solely on phase stability. However, *Hooper et al.* (2007) show that there is correlation between phase stability and the variance in amplitude. The probability of a pixel being a PS is therefore calculated more accurately using the amplitude dispersion and temporal coherence simultaneously. The probability density function (PDF) of the temporal coherence and amplitude dispersion for the data, $f(\gamma_p, \hat{D}_p^A)$, is the weighted sum of the PDF for the simulated random phase pixels, f^{ran}, and the PDF for the (non-random) PS pixels, f^{PS}, (so that $f(\gamma_p, \hat{D}_p^A)$ is weighted by the proportion of PS pixels, α, and f^{ran} is weighted by the proportion of non-PS pixels, $1-\alpha$):

$$f(\gamma_p, \hat{D}_p^A) = (1 - \alpha(\hat{D}_p^A))f^{ran}(\gamma_p) + \alpha(\hat{D}_p^A)f^{PS}(\gamma_p, \hat{D}_p^A) \tag{2.15}$$

where $\alpha(\hat{D}_p^A)$ is the proportion of pixels that are PS and $0 \leq \alpha \leq 1$. We then seek a temporal coherence threshold, γ^{thresh}, such that:

$$\frac{(1 - \alpha(\hat{D}_p^A)) \int_{\gamma^{thresh}}^1 f^{ran}(\gamma_p)d\gamma_p}{\int_{\gamma^{thresh}}^1 f(\gamma_p, \hat{D}_p^A)d\gamma_p} = q \tag{2.16}$$

where, γ^{thresh}, depends on the estimated amplitude dispersion, $\hat{D}_p^A$.

To get the probability distribution $f(\gamma_p, \hat{D}_p^A)$ of our observed data we bin the pixels by $\hat{D}_p^A$ and the temporal coherence values in increments of 0.01. In order to derive $f^{ran}(\gamma_p)$ 300,000 pseudo pixels are simulated with random phase. The temporal coherence and amplitude dispersion are then evaluated for each simulated pixel. These are then used to estimate $f^{ran}(\gamma_n)$ as for the observed data.

All temporal coherence estimates less than 0.3 are assumed to be noisy non-PS

pixels (i.e. they have $f^{PS}(\gamma_p, \hat{D}_p^A) \approx 0$) so equation 2.15 can be rewritten:

$$\int_0^{0.3} f(\gamma_p, \hat{D}_p^A) d\gamma_p = (1 - \alpha(\hat{D}_p^A)) \int_0^{0.3} f^{ran}(\gamma_p) d\gamma_p \tag{2.17}$$

The integral on the left hand side is evaluated from the data and the integral on the right hand side from the simulation. This then gives us a minimum estimate for the number of PS pixels, $\alpha(\hat{D}_p^A)$. The probability that a pixel p is a PS is then given by:

$$P(p \in PS) = 1 - \frac{(1 - \alpha(\hat{D}_p^A)) f^{ran}(\gamma_p)}{f(\gamma_p, \hat{D}_p^A)} \tag{2.18}$$

We can define a random pixel acceptance rate RPAR (*Agram*, 2010) based on the observed and simulated probability measures which corresponds to a given coherence threshold:

$$RPAR(\gamma^{thresh}) = \frac{\int_0^{0.3} f^{ran}(\gamma_p) d\gamma_p}{\int_0^{0.3} f(\gamma_p, \hat{D}_p^A) d\gamma_p} \frac{\int_{\gamma^{thresh}}^1 f^{ran}(\gamma_p) d\gamma_p}{\int_{\gamma^{thresh}}^1 f(\gamma_p, \hat{D}_p^A) d\gamma_p} \tag{2.19}$$

The histograms of the observed and simulated coherence values are normalised by the assumption all coherence values less than 0.3 are for non PS.

All pixels with temporal coherence thresholds greater than the estimated threshold which depended on the chosen selection criteria (**density random** or **percentage random**) are identified as PS. If the threshold is too high (equivalent to low **density random** or **percentage random**), many potential PS pixels are not included and the resulting PS network may be too sparse to unwrap. If the threshold is set too low, too many non-PS pixels are included, resulting in poor quality points that are noisy.

PS weeding

The identified PS are then weeded on the basis of their noise characteristics, dropping those that are too noisy. The time series for the phase of each pair of neighbouring pixels is smoothed using a Gaussian weighted piecewise linear fit (*Hooper et al.*, 2004). The standard deviation of the Gaussian is specified by **weed time window** in days. The noise is then given by the original phase minus the smoothed phase. For each pixel, the phase noise standard deviation for all combinations of pixel pairs is calculated. If the minimum standard deviation is greater than the threshold set by **weed standard deviation** then the pixel is dropped.

We can combine the **weed standard deviation** together with **density random** or **percentage random** to ensure we are selecting good quality PS where they are available, but balancing it with sufficient lower quality PS in regions with high phase variability. Figure 2.5 shows how using a high phase standard deviation results in sufficient pixels being selected to the south of the Kunlun Fault that it is possible to unwrap the data. To minimise the number of noisy PS selected I used a low density random per km^2. This limits the selected PS, in particular to the north of the fault (where the number of PS dropped based on standard deviation alone would be low), to those with higher temporal coherence values. This is explained in more detail in section 2.3.6.

Whenever adjacent pixels are identified as PS the less coherent of these pixels is rejected as being affected by energy leaking from the sidelobes of the brighter PS. This step can be switched on or off be setting **weed neighbours** to y or n.

2.3.5 Combined Lowpass Adaptive Phase (CLAP) filter

Low pass filtering is combined with adaptive phase filtering to remove the correlated noise terms. This technique was adapted for PS InSAR by *Hooper et al.* (2007) to

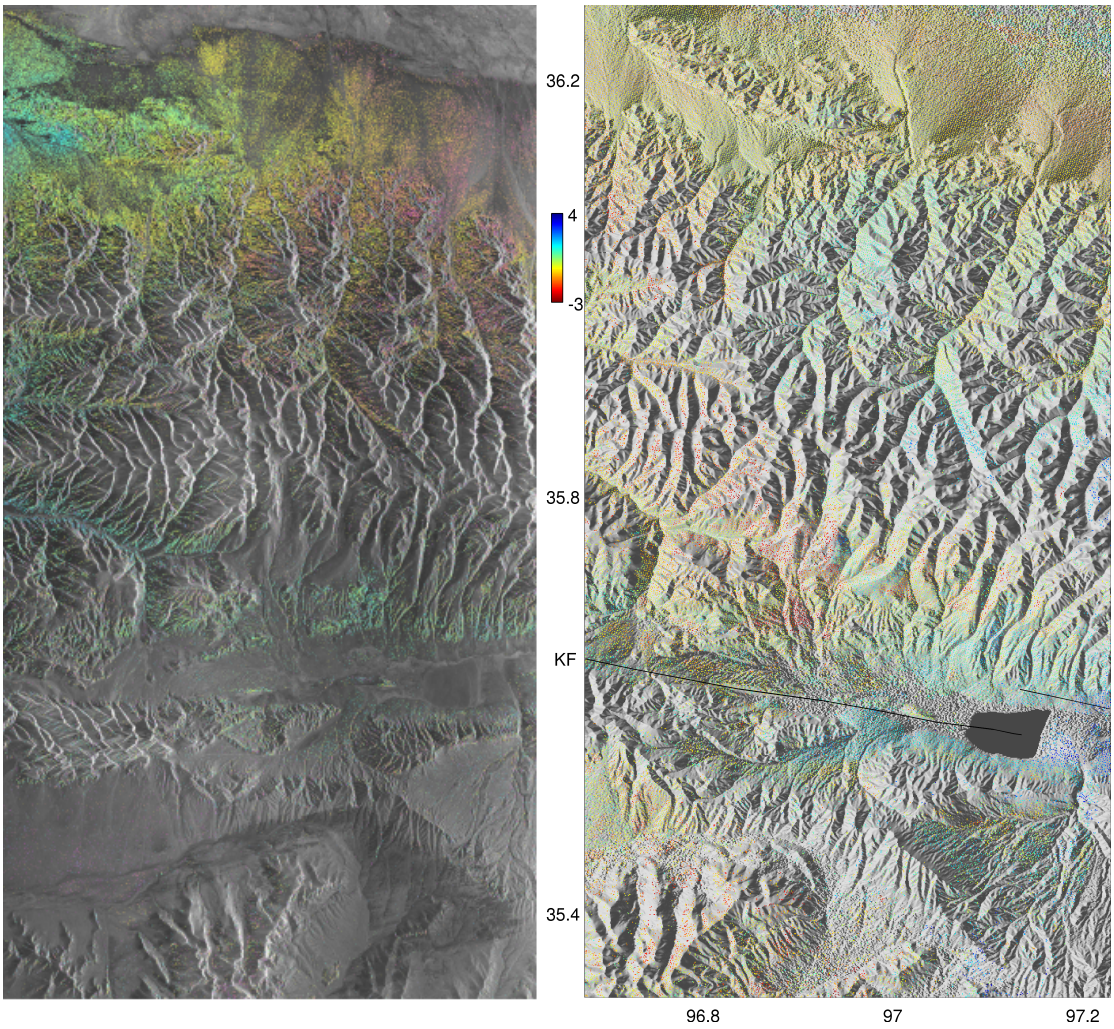

Figure 2.5: Wrapped interferogram showing PS selection using the GAMMA software (left) and unwrapped for the StAMPS software, with the LOS velocity shown in mm, (right). PS selection is performed in GAMMA using SCR and amplitude dispersion, and in StAMPS primarily using **density random** and **weed standard deviation** of the phase of pixels. Insufficient PS were found to the south of the Kunlun Fault (KF) using GAMMA to unwrap the data. Using the StAMPS algorithm for PS selection, I set the maximum allowed phase standard deviation relatively high at 0.9, and specified a low density random of 20 PS per km^2. This resulted in sufficient points being selected to the south of the fault that it was possible to unwrap the data.

preserve interferometric fringes, as interferograms are wrapped at the point of PS identification. Before filtering, all candidate pixels are resampled to a grid specified by the **filter grid size** in meters typically 50 to 100 m.

The adaptive component of the filter uses the dominant frequencies in the phase

of the pixels to estimate the pass band at each loop refinement. A Finite Impulse Response (FIR) filter is designed using a 7 pixel by 7 pixel Gaussian as the impulse response to smooth the data. This filter is then combined with a Butterworth filter to introduce the low pass component and applied to the data. The Butterworth filter has a cutoff frequency determined by the **Clapeyron low pass wavelength** in meters (wavelengths longer than this are passed) and a sampling frequency calculated from the **filter grid size** and the number of windows specified by **Clapeyron window**. **Clapeyron** α and **Clapeyron** β determine the relative contributions of the low pass and adaptive phase elements typically 1 for α and 0.3 for β.

The filter response, G(u,v) is defined by *Hooper et al.* (2007) as:

$$G(u,v) = L(u,v) + \beta \left(\frac{H(u,v)}{\bar{H}(u,v)} - 1 \right)^{\alpha} \tag{2.20}$$

where $L(u,v)$ is the narrow low pass filter response from a fifth order Butterworth filter, $H(u,v)$ is the adaptive phase filter response, α and β are adjustable weighting parameters and $\bar{H}(u,v)$ is the median value of $H(u,v)$. $H(u,v)$ is given by:

$$H(u,v) = |Z(u,v)| \tag{2.21}$$

where $Z(u,v)$ is the smoothed intensity of the 2D FFT after convolution with the Gaussian.

The resulting filtered phase value is a wrapped estimate of the correlated parts of the deformation, atmospheric component, orbital phase error and geometric component. The uncorrelated parts of these signals are left to be removed later. The phase error due to the error in DEM is estimated on a pixel by pixel basis using the baselines of the stack of interferograms. This relationship was demonstrated previously in equation 2.2 and the implementation is shown by equation 2.9. This

leaves the phase residuals that are the assumed scatterer noise.

2.3.6 PS selection examples

Figure 2.4 compares PS selection using the StAMPS software with results obtained using GAMMA. Using the StAMPS algorithm I am able to select many more pixels in natural terrain enabling the unwrapping of data across regions where no points are available using more traditional techniques. In Izmir in Western Turkey I was not able to successfully unwrap data using GAMMA without getting jumps in phase at patch boundaries. In contrast in StAMPS I obtained sufficient PS in natural terrain to generate a continuous velocity field.

In Figure 2.5 to the north of the Kunlun Fault I identify an abundance of PS but insufficient points are shown to the south of the fault to reliably model the deformation across the fault using GAMMA PS selection. Ideally, we want to keep good points where they are available but need to balance this with having sufficient points to reliably unwrap the data.

In StAMPS I changed the **density random** of selected pixels with random phase to a much lower value of 20 per km^2, compared to a more standard value of 40, which as the only parameter altered would result in fewer PS being selected. I then increased the **weed standard deviation** to 0.9, compared to a more standard value of 0.8, which alone would result in more PS being selected. The combined result of changing both parameters together is that the reduced maximum spatial density per km^2 dominates to the north resulting in pixels with high signal to noise ratio where coherence is high, but increased threshold standard deviation dominates to the south enabling poorer points to be selected where the coherence of interferograms is much lower. This provides enough PS in more incoherent regions to the south of the fault enabling the unwrapping of data to produce a continuous deformation field. As a

consequence I found much better results using the StAMPS software than those obtained using GAMMA as illustrated in figure 2.5.

2.3.7 Unwrapping

After selecting and weeding the most likely PS we reject all other pixels and return to the original wrapped interferogram phase for our selected data. To generate a continuous velocity field we now need to unwrap our data. In order to do so we generally require the difference in phase between neighbouring pixels to be less than π (*Shankar*, 2010). We therefore correct for the estimated spatially uncorrelated geometric error, calculated when evaluating the temporal coherence of each PS. We then merge the patches together and resample to a grid size specified by **merge resample size**.

The data is then unwrapped using a 3-D cost function phase unwrapping algorithm (*Hooper and Zebker*, 2007b) on a resampled grid specified by **unwrap grid size**. The noise distribution of the phase for each pair of neighbouring pixels is then estimated using a Gaussian window to smooth the time series for each pair. The standard deviation of the Gaussian is specified by the **unwrap time window** in days. The assumed noise is given, as was the case earlier for the wrapped phase, by the original phase minus the smoothed phase. This assumed noise is used to estimate the probability of a phase jump between each pair of pixels.

The spatially correlated noise is then estimated for the unwrapped phase by low pass filtering pixel pairs in time and low pass filtering in space. The time window and wavelength are specified by **scn time window** and **scn wavelength** respectively. We are then left with our unwrapped deformation and spatially uncorrelated error terms that can be modelled as noise.

2.4 Atmospheric phase delay

Atmospheric effects are caused by changes in the wave speed of the satellite radar due to interactions of the electromagnetic waves with the dipole moments of gas molecules in the atmosphere. Changing atmospheric conditions controlled primarily by pressure, temperature and water vapour content vary the phase delay in space and time causing an atmospheric component that can be difficult to distinguish from deformation. The most significant factor influencing interferograms is the water content of the troposphere. A number of approaches to atmospheric noise removal including the use of GPS, direct measurements of water vapour from satellite instruments such as MERIS and MODIS, and numerical modelling techniques, have been employed to reduce atmospheric effects with varying degrees of success. The author refers the reader to *Jolivet et al.* (2011) and *Hanssen* (2001) for a more in-depth analysis of atmospheric noise removal techniques.

On the Tibetan Plateau, MERIS data is no longer available in the archive above 4000 m. This excludes the use of this approach across the Kunlun Fault. GPS data in the region are too sparse to be useful. Therefore, I explore the following three techniques for the reduction of atmospheric effects: (i) an empirical linear relationship with topography; (ii) the estimation of the atmospheric phase delay from ERA-Interim ECMWF numerical weather model reanalysis data; and (iii) weighting of inversions with a 1d covariance function that explores the magnitude and spatial scale of atmospheric errors.

2.4.1 Topographically correlated phase correction

In the case of a stratified atmosphere over flat terrain, for an infinite number of atmospheric layers each with a constant refractivity, there would be no horizontal

phase delay differences. In the presence of topography, a difference in the vertically integrated refractivity between two acquisitions would result in a difference between any pixels with different heights (*Hanssen*, 2001). Because the tropospheric thickness decreases with increasing surface topography, a change in water vapour content between any pair of satellite passes would result in a phase change that correlates with topography.

On the Tibetan plateau, residual atmospheric noise is seen to strongly correlate with topography in individual interferograms. This is shown in figure 2.6 where, 200 km along the profile, a strong positive correlation is seen with an inteferogram generated using 040724 as the master (1st satellite pass), and a negative correlation with an interferogram generated using this date as the slave (2nd satellite pass). This reversal in correlation reflects the fact that a strong atmospheric effect must dominate the SLC for 040724. A number of approaches have been used by various authors to estimate the relationship between a change in phase associated with atmospheric effects and topography empirically: a linear relationship with height (*Elliott et al.*, 2008a), an exponential relationship (*Socquet et al.*, 2005), and the use of correlation windows to account for spatial variability (*Taylor and Peltzer*, 2006). I demonstrate the approach of *Elliott et al.* (2008a) on individual interferograms for track 462 after the removal of an initial orbital ramp as shown later, in section 2.5.

The change in phase due to atmospheric topographical effects is given by inverting for the difference in correlation of phase with elevation:

$$\delta\phi_{n,p}^{atm}(k,l) = a_n \cdot [(\Delta h(k,l))] + c_n \tag{2.22}$$

where $\delta\phi_{n,p}^{atm}(k,l)$ is the estimated change in phase for interferogram n and pixel p at location (k,l), $\Delta h(k,l)$ is the change in elevation for each pixel with respect

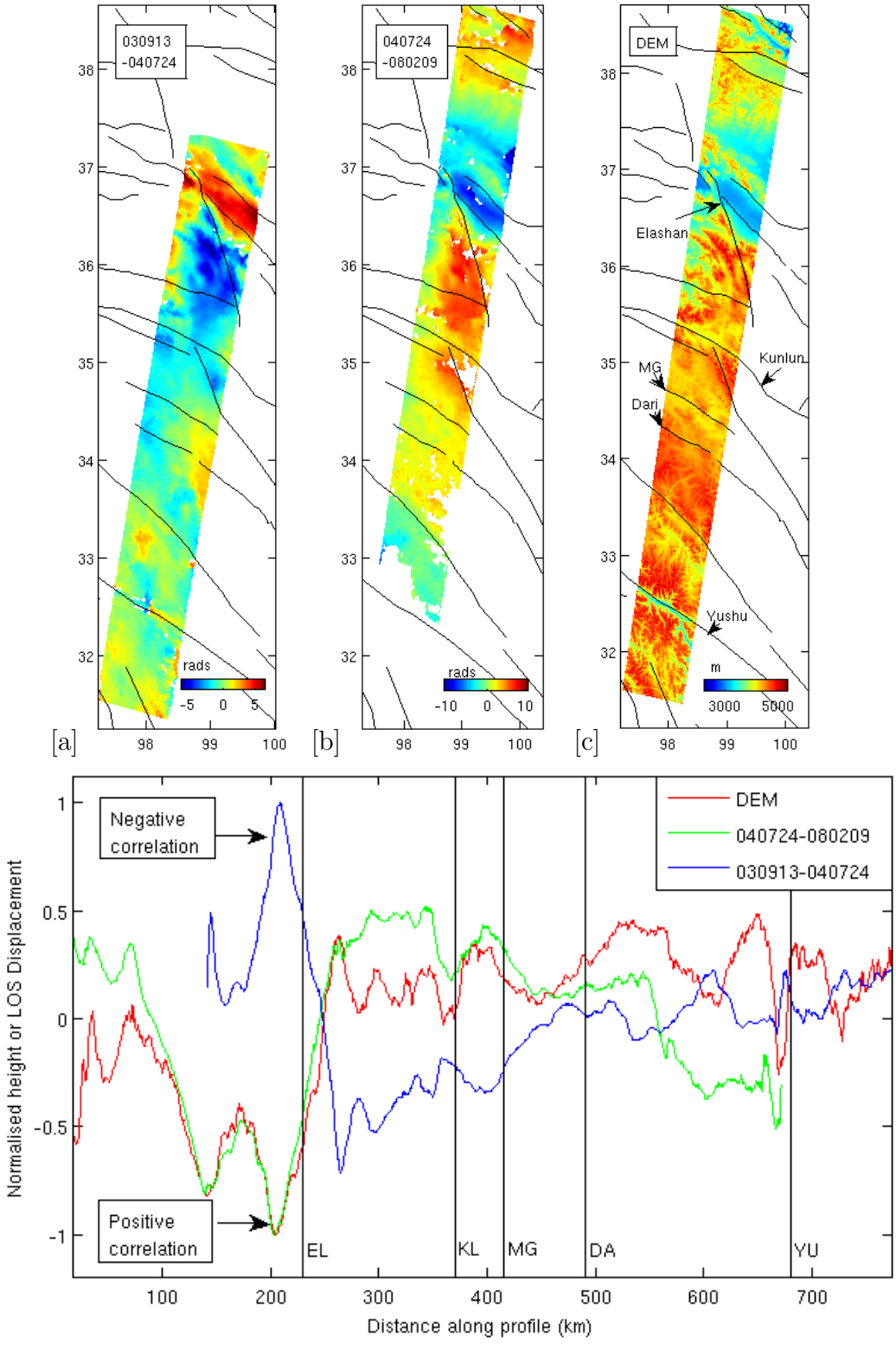

Figure 2.6: Strong correlations are seen between the phase of interferograms and topography. [a] An interferogram generated using 040724 as the slave, [b] an interferogram with 040724 as the master, [c] the DEM, [d] average profiles taken perpendicular to the Kunlun fault from north to south for the region shown in the DEM. These profiles have been normalised by the absolute value of the maximum or minimum depending on which is greater. Correlations of peaks and troughs in the interferograms with the DEM are shown to reverse due to atmospheric effects when 040724 is changed from being the slave to the master scene. Locations of the Elashan Fault (EL), Kunlun Fault (KL), Maduo-Gande Fault (MG), Dari Fault (DA) and Yushu-Xianshuihe Fault (YU) are shown with vertical black lines.

to a reference pixel (x, y) in mm, c_n are the offsets, and a_n are the atmospheric parameters for each interferogram n. $\Delta h(k, l)$ in equation 2.22, above is then given by:

$$\Delta h(k,l) = \left[\frac{h(k,l) - h(x,y)}{1000}\right] \tag{2.23}$$

where $h(k, l)$ is the DEM height in meters at pixel (k, l) for interferogram n, and $h(x, y)$ is the DEM height in meters at the reference pixel (x, y).

$$\mathbf{A}\ \mathbf{x}\ =\ \mathbf{b}$$

$$\begin{pmatrix} \Delta h_{1,1} & 0 & \cdots & 0 & 1 & 0 & \cdots & 0 \\ \vdots & \vdots & \vdots & \vdots & \vdots & \vdots & \vdots & \vdots \\ \Delta h_{k,l} & 0 & \vdots & \vdots & 1 & 0 & \cdots & \vdots \\ 0 & \Delta h_{1,1} & \vdots & \vdots & 0 & 1 & \vdots & \vdots \\ \vdots & \vdots & \vdots & \vdots & \vdots & \vdots & \vdots & \vdots \\ \vdots & \Delta h_{k,l} & \vdots & \vdots & \vdots & 1 & \vdots & 0 \\ \vdots & \vdots & \cdots & \Delta h_{1,1} & \vdots & 0 & \vdots & 1 \\ \vdots & \vdots & \vdots & \vdots & \vdots & \vdots & \vdots & \vdots \\ 0 & 0 & \cdots & \Delta h_{k,l} & 0 & 0 & \cdots & 1 \end{pmatrix} \begin{pmatrix} a_1 \\ \vdots \\ a_n \\ c_1 \\ \vdots \\ c_n \end{pmatrix} = \begin{pmatrix} \phi^T_{1j,1l} \\ \vdots \\ \phi^T_{1j,kl} \\ \vdots \\ \phi^T_{ij,1l} \\ \vdots \\ \phi^T_{ij,kl} \end{pmatrix} \tag{2.24}$$

A design matrix $\mathbf{A}$ is constructed from columns of changes in elevation at each pixel (k, l), with respect to a reference pixel, and columns of ones to account for an offset. A column vector $\mathbf{b}$ is constructed of the observed interferometeric phase between the master i and each slave scene j. I invert the data using least squares to obtain $\mathbf{x}$, which gives the correlation factor a_n for each interferogram between phase and elevation, and the offsets c_n. This is done by reformulating the forward problem $\mathbf{Ax} = \mathbf{b}$ as an inverse problem $\mathbf{A}^T\mathbf{Ax} = \mathbf{A}^T\phi$, so that:

$$\mathbf{x} = (\mathbf{A}^T\mathbf{A})^{-1}(\mathbf{A}^T\phi) \tag{2.25}$$

Topographically correlated phase correction results

Although improvements can be seen in some individual interferograms after removing the estimated phase change due to atmosphere using equation 2.22, they are generally very small. Figure 2.7 shows the results of applying this technique to a selection of interferograms from track 462 across the Kunlun Fault, in Tibet. The variation in phase reduces from 53.9 mm to 36.6 mm for 030809-031122, from 55.4 mm to 49.9 mm for 040619-050604, and from 36.6 mm to 34.4 mm for 080209-090509. I assume reductions in phase variation to be an improvement in signal to noise ratio, as interseismic displacements would be small, smoothly varying, and of long wavelength.

Plots showing the relationship between phase and elevation for each interferogram forming track 462 are shown in figure 2.8. Whilst linear relationships can be seen for some interferograms, for example 041106-080209, many show no obvious linear relationship, for example 040515-080209. This method also assumes that the same relationship between phase and elevation is applicable across the entire region of the swath, which is not the case for all interferograms.

Furthermore, in order to invert for a linear topographic relationship, it is necessary to resample data onto a regular grid and to reduce the resolution by multilooking. However, one of the main advantages of PS InSAR is selecting specific pixels with high signal to noise ratio, reduced atmospheric contamination, and stronger scatterers. I therefore explored the possibility of using the European Centre for Medium Range Weather Forecasting (ECMWF) interim reanalysis data to estimate atmospheric phase delay.

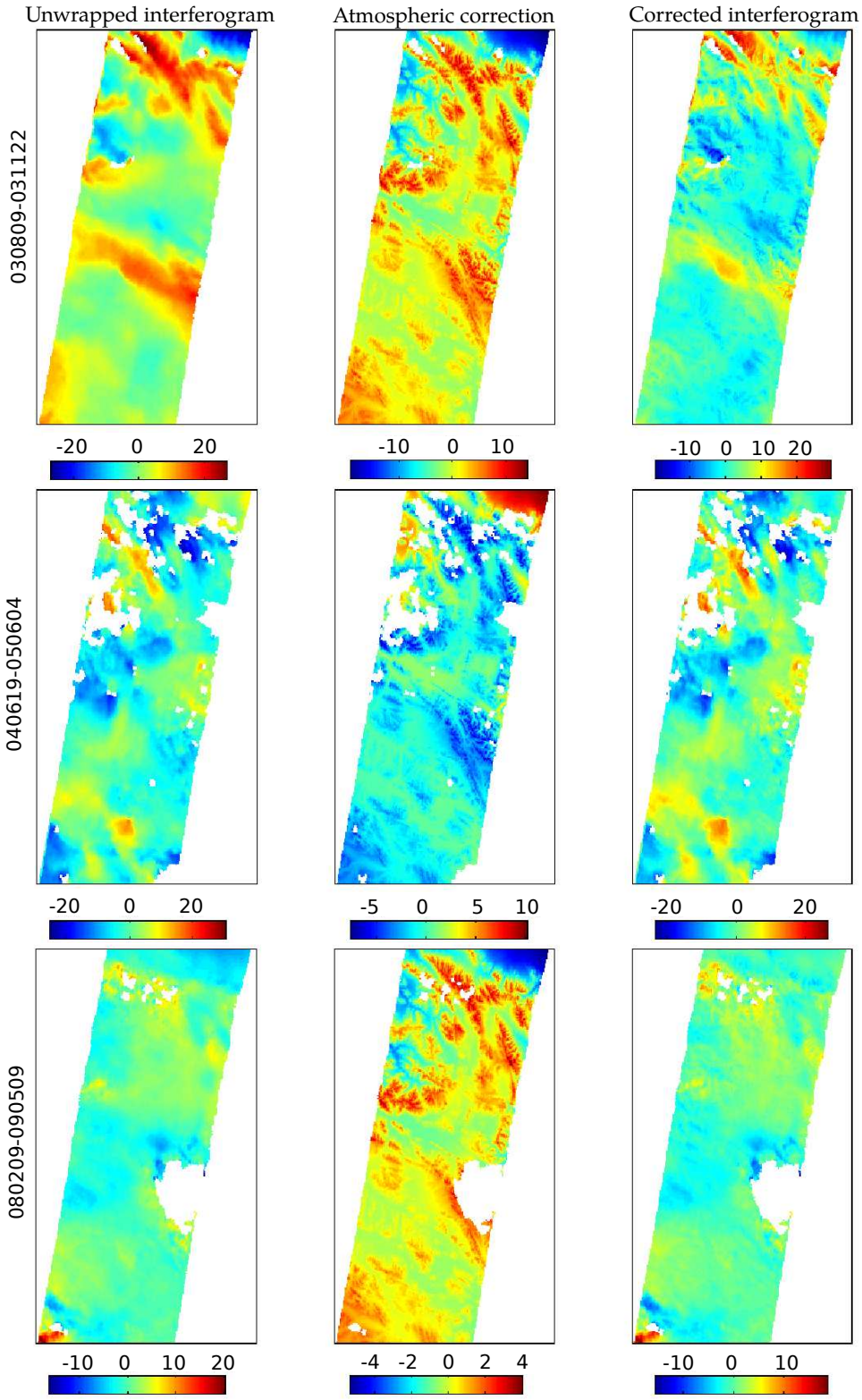

Figure 2.7: From left to right the unwrapped LOS displacement in mm prior to atmospheric noise removal, the estimated atmosphere using a linear relationship with topography and after atmospheric noise removal are shown for 3 example pairs of dates. Small improvements are seen, particularly in the top right hand corner to the north of the South Gonge Fault, where heights are much lower in the region of 3km.

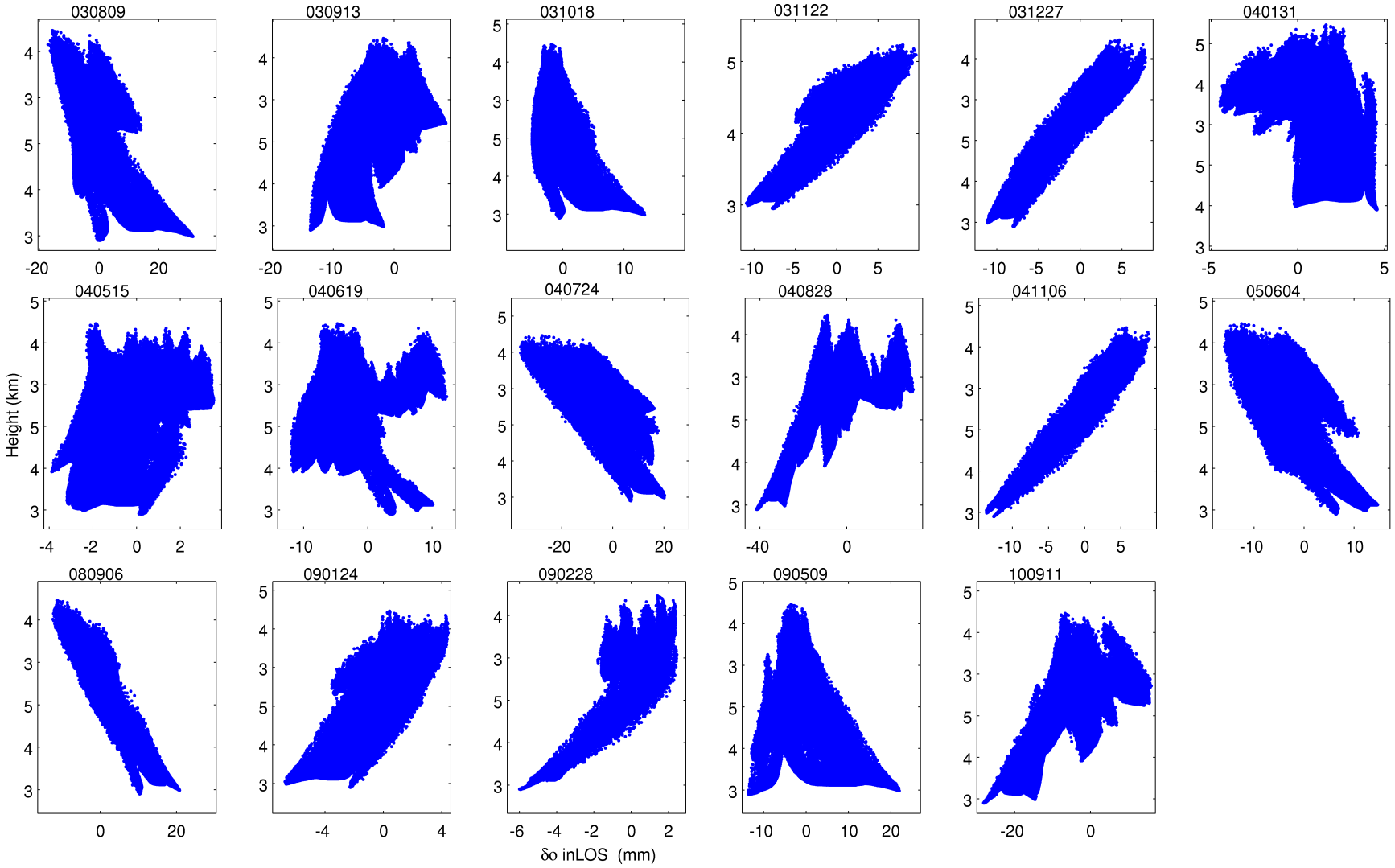

Figure 2.8: Plots showing the relationship between interferometric phase and elevation for track 462 for each slave with respect to the master date 080209

2.4.2 ERA-Interim ECMWF Numerical Weather Model

To estimate the atmospheric line of sight contribution to the radar delay for each scene relative to the master scene, I followed the approach of *Doin et al.* (2009) and *Jolivet et al.* (2011). *Hanssen* (2001) showed that the atmospheric path delay in the satellite line of sight for pixel (k, l) at acquisition time i is given by:

$$S^i_{k,l} = 10^{-6} \underbrace{\int_0^H \frac{N}{\cos\theta_{inc}} dh}_{S^i_{k,l,velocity}} + \underbrace{\int_0^H \frac{1}{\cos\theta_{inc}(h)} dh - R_k}_{S^i_{k,l,bending}} \tag{2.26}$$

where

$$N = 10^6 \left(\frac{c_0}{c} - 1\right) \tag{2.27}$$

where $n = \frac{c_0}{c}$ is the ratio of the speed of light in a vacuum to the speed of light through a medium, referred to as the refractive index, n. The first term in 2.26 arises due to a change in wave speed along the ray path and the second term from the bending of the ray path.

The change in path length is given by the vertically integrated refractivity, N from zero height to the height of the satellite above the scatterer, H. This is adjusted along the line of sight of the satellite using the known incidence angle, θ_{inc}. The ray path bending is given by the vertically integrated change in line of sight at height h relative to the true slant range (the distance measured along a straight line between the radar antenna and the target), R_k. *Hanssen* (2001) showed that for SAR data this component is negligible so the atmospheric component of the delay can be considered solely a function of propagation velocity. This reduces the above equation to the first term.

Equation 2.26 then becomes the sum of the vertically integrated hydrostatic

delay, wet delay, ionospheric delay, and liquid delay, respectively:

$$S_k^i = \frac{1}{10^6 \cos\theta_{inc}} \left\{ \int_0^H N_{hyd} dh + \int_0^H N_{wet} dh + \int_0^H N_{iono} dh + \int_0^H N_{liq} dh \right\} \quad (2.28)$$

Smith and Weintraub (1953) and *Kursinski et al.* (1997), showed that each of these refractive components making up the slant atmospheric delay can again be decomposed. The hydrostatic refractivity is a function of total atmospheric pressure P in hPa and atmospheric temperature T in Kelvin. The refractivity for the wet component is a function of the partial pressure of water vapour, e, in hPa and atmospheric temperature. The ionospheric refractivity depends on the radar frequency f and n_e, the electron density per m^3. Finally the liquid component is given by the liquid water content W in g/m^3. The total refractivity for satellite radar can therefore be reformulated as shown below:

$$N = \underbrace{k_1 \frac{P}{T}}_{N_{hyd}} + \underbrace{\left(k_2' \frac{e}{T} + k_3 \frac{e}{T^2}\right)}_{N_{wet}} - \underbrace{4.03 \times 10^7 \frac{n_e}{f^2}}_{N_{iono}} + \underbrace{1.4W}_{N_{liq}} \quad (2.29)$$

Where $k_1 = 77.6$, $k_2' = 23.3$ and $k_3 = 3.7510 \times 10^5$ are taken from *Smith and Weintraub* (1953).

The ECMWF weather model provides the temperature, relative humidity in percent, geopotential in m^2/s^2 and 37 pressure levels in hPa for latitudes and longitudes globally on a grid at 75 km intervals. We therefore need to convert relative humidity to water vapour partial pressure and geopotential to geometric height in order to apply equation 2.29 and spatially interpolate the data to finer resolution using a DEM. Following *Baby et al.* (1988), the relative humidity, RH can be converted to water vapour partial pressure given the saturated water vapour pressure svp, in

hPa:

$$e = \frac{RH}{100} svp \tag{2.30}$$

The saturated water vapour pressure is given by a mixing ratio that can be calculated from temperature using the ideal gas law (*Buck*, 1981). Here we use the WMO CIMO(2008) formulations over water, svp_w, and ice, svp_i, temperature ranges.

We use svp_w for temperatures greater than 0 °C and svp_i for temperatures less than -20°C:

$$\begin{aligned} svp_w &= 6.1121 \exp^{\frac{17.502(T-T_1)}{240.97+T-T_1}} && \text{for } T > T_1 \\ svp_i &= 6.1115 \exp^{\frac{22.542(T-T_1)}{273.48+T-T_1}} && \text{for } T < T_2 \end{aligned} \tag{2.31}$$

where $T_1 = 273.16$ K is the temperature bound 1 set at 0°C and $T_2 = 253.16$ K is temperature bound 2 set at -20°C. A mixing ratio is applied for ranges between these 2 bounds giving:

$$svp_i + b^2(svp_w - svp_i) \qquad \text{for } T_2 < T < T_1 \tag{2.32}$$

where the weighting, b, is given by:

$$b = (T(x, y, z) - T_2)/(T_1 - T_2) \tag{2.33}$$

The geometric height, Z can then be calculated from the geopotential, Φ, by converting this to geopotential height, H.

$$H = \frac{\Phi}{g_0} \tag{2.34}$$

To convert geopotential height to geometric height, corrections then need to be made for the change in gravity from mean sea level $g_0 = 9.80665$ and the variation in earth radius, R_e with latitude φ:

$$g(\varphi) = 9.80616(1 - 0.002637cos(2\varphi) + 0.0000059(cos(2\varphi))^2) \tag{2.35}$$

$$R_e = \sqrt{\frac{1}{\frac{(cos(\varphi))^2}{R_{max}^2} + \frac{(sin(\varphi))^2}{R_{min}^2}}} \tag{2.36}$$

The geometric height is then given by:

$$Z = \frac{HR_e}{\frac{R_e g}{g_0} - H} \tag{2.37}$$

where $R_{max} = 6378137$, $R_{min} = 6356752$. Pressure, water vapour partial pressure, and temperature can then be interpolated using a spline function onto height profiles for each pixel. The slant total delay can then be calculated using equation 2.29

2.4.3 Scaling the amplitude of ERA-Interim ECMWF phase delays

Individual interferograms with small temporal baselines should be dominated by atmospheric noise. We can therefore assess how well our ECMWF generated estimate of the atmosphere compares with our real data. The predicted atmospheric component from ECMWF data was found to have amplitudes that in some cases matched the real data remarkably well (e.g. for interferogram 040724-040828 which has an amplitude range of 20 mm for the real data and 20.1 mm for the ECMWF) but in others were significantly different (e.g. for interferogram 040828-041106 which has an amplitude range of 20 mm for the real data but only 12 mm for the predicted

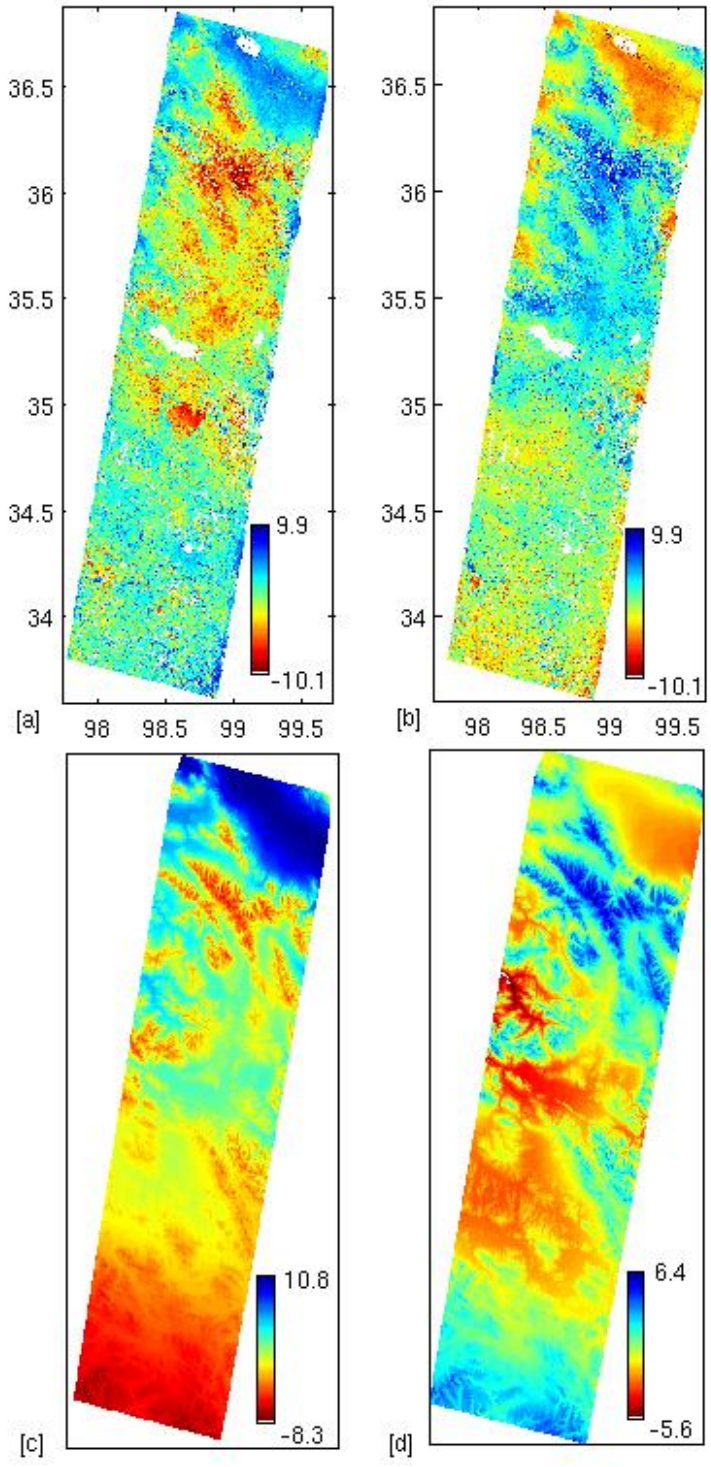

Figure 2.9: Predicted line of sight velocities are shown to match the amplitudes of real data for some interferograms with short time spans but not others [a] Real data for 040724-040828 gives an amplitude range of 20mm, [b] Real data for 040828-041106 given an amplitude range of 20mm, [c] Predicted LOS velocity from ECMWF for 040724-040828 gives an amplitude range of 20.1mm, [d] Predicted LOS velocity from ECMWF for 040828-041106 gives a much smaller amplitude range of 12mm

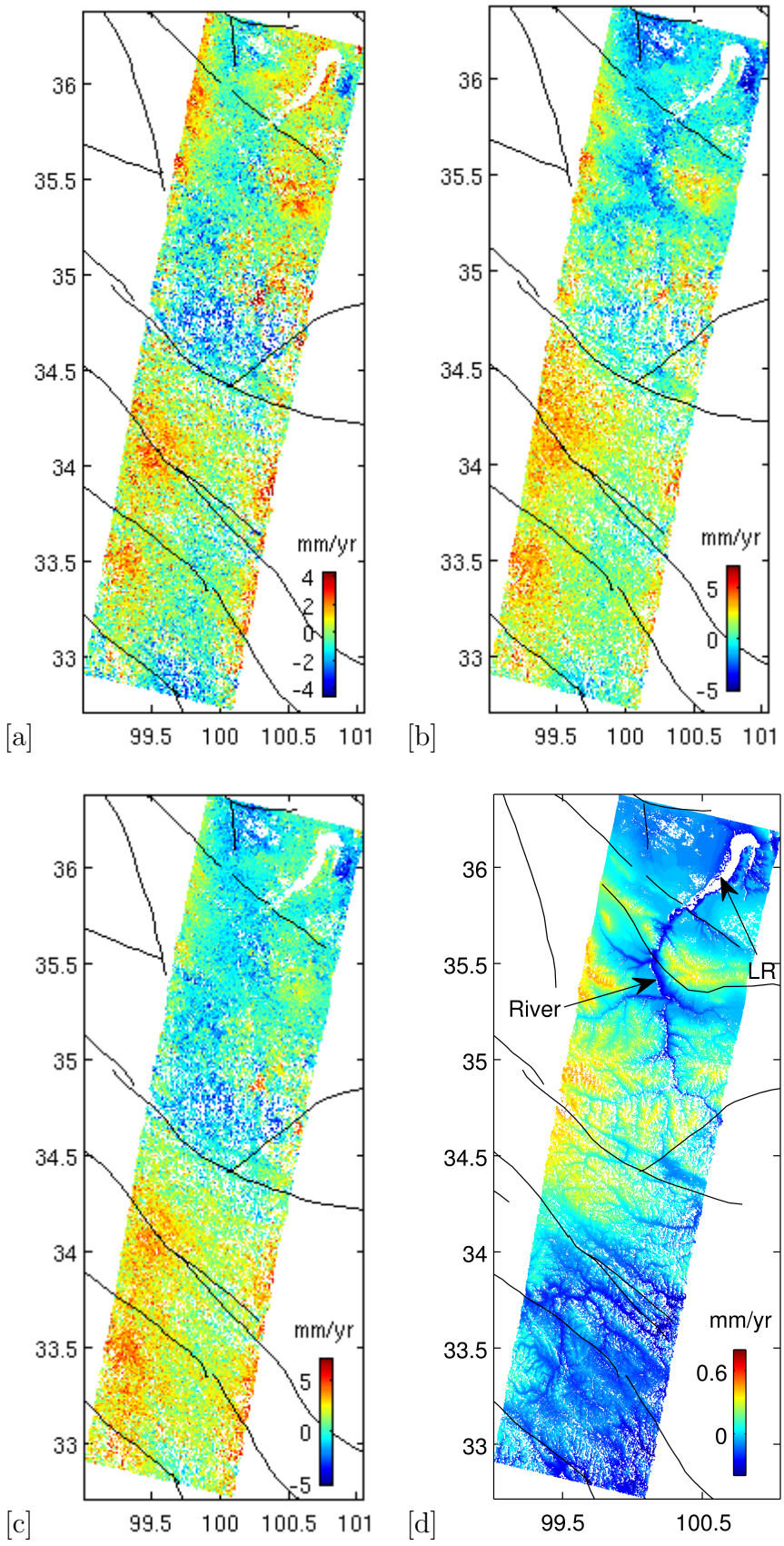

Figure 2.10: For track 419 (a) no atmospheric correction (b) unscaled atmospheric correction applied using ECMWF, (c) scaled atmospheric correction applied using ECMWF with a scaling factor of 0.3, (d) modelled atmosphere scaled by a factor of 0.3. Without applying a scaling correction we see features from an overcorrection of the atmosphere appearing in our data, for example, effects from the river running to the south of the Longyangxia Reservoir (LR).

ecmwf as shown in figure 2.9). This suggests that our estimate of the atmosphere for scene 041106 is inaccurate. Nevertheless, the spatial patterns are seen to be representative of the real signal. *Walters* (2012) demonstrated that in many cases applying an atmospheric correction using ECMWF data can give worse results than not applying any correction.

ECMWF interim data is provided at six hourly intervals and across the Kunlun fault the time stamps of satellite passes were found to be in the middle of the ECMWF data time-stamps introducing the largest possible temporal interpolation error. As the spatial patterns are seen to consistently representative of the real signal I used ECMWF, applying a scaling factor to correct for any inaccuracies in amplitude and to avoid applying any correction where the ECMWF data fails to match the real data. This was done by incorporating the ECMWF delay into a simultaneous inversion with fault models and an orbital model, introducing an additional parameter in order to enable scaling of the amplitude for the predicted atmospheric component.

Removing the predicted atmospheric effect using ECMWF without applying a scaling factor results in a velocity map that shows a strong anti-correlation with the atmosphere, suggesting an over correction as shown in 2.10. Applying the atmospheric correction without any scaling factor results in features that look very similar to the atmospheric component in particular around the lake and to the south along the river. After applying the amplitude correction with the scling factor a clear tectonic signal can be seen across the Kunlun fault and there are no clear features related to the atmospheric correction along the river.

The need for an amplitude scaling factor is attributed to widely publicised inaccuracies in water vapour concentrations in the lower troposphere (*Bao and Zhang*, 2013; *Oikonomou and O'Neill*, 2006) which are used to calculate the water vapour

partial pressure, e in equation 2.29. *Bao and Zhang* (2013) observe that comparisons between sounding data and the ERA-Interim show the smallest overall RMS error in Relative Humidity of the available products (23%-26%). Nevertheless, they conclude that the RMS errors between the reanalyses and the sounding observations are large, suggesting that the quality of the moisture analysis may be highly inaccurate (*Bao and Zhang*, 2013).

2.4.4 E-folding spatial variance covariance matrix

The closer two pixels are the more correlated their error. The correlation of errors is represented by functions that decrease with increasing distance between points. Therefore, in order to determine the atmospheric noise component we can use a 1-D covariance function to estimate the magnitude and spatial scale of the noise as shown by *Hanssen* (2001). This function can then be used to weight our data. *Parsons et al.* (2006) showed that the 1-D covariance function is found from the radial average of the 2-D auto-covariance function of the interferogram. This is calculated from the cosine Fourier transform of the power spectrum. A simple exponential function is used to characterise the covariance function as shown below:

$$c_{kl} = \sigma^2 e^{(-d_{kl}/\alpha)} \tag{2.38}$$

where d_{kl} is the spatial distance separating any two points with index k,l and alpha controls the spread or dispersion of the correlation function.

The spatial variance covariance matrix c_{kl} is then used to weight the model inversion in a similar way that the temporal variance covariance matrix is used to weight individual interferograms as shown later in section 3.5.

The disadvantage of using this approach is that the atmospheric noise is as-

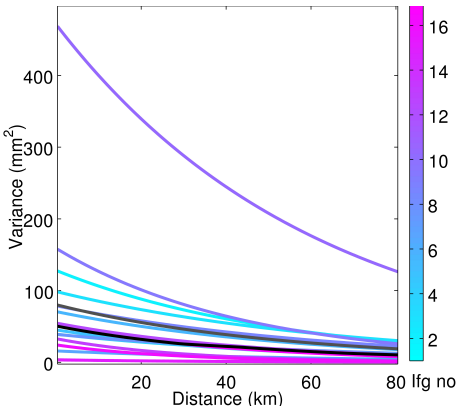

Figure 2.11: The 1 D covariance functions for the 17 interferograms across the Kunlun Fault for track 462 calculated from the radial average of the 2D autocovariance functions. The median variance is shown in black and the mean is shown in grey

sumed to be radially symmetric and homogeneous across the interferogram. However, higher noise levels would be expected for lower lying areas where the vertically integrated atmospheric component is greater (*Hanssen*, 2001; *Parsons et al.*, 2006). Figure 2.11 shows the 1D covariance functions for each of the interferograms from track 462. The decay distances, α, are 29-71 km and the variance,σ^2, is in the range 3 mm to 470 mm.

Whilst using this technique has been shown to work well by *Biggs et al.* (2007) for standard DifSAR, the higher resolution of PS data results in memory problems for computation of the spatial variance covariance matrix. The advantage of using PS over DifSAR is that the selection of pixels with higher signal to noise ratio results in a non uniform sampling grid with some regions having much higher spatial resolution than others. This is due to the presence of natural persistent scatterers or as consequence of lower atmospheric contribution. Spatially averaging the data prior to generating a rate map in order to resolve memory problems would counteract the major advantage of using PS in the first place. Consequently only inversions carried out for standard difsar are weighted by the spatial variance covariance matrix.

2.5 Orbital phase errors

We correct for this component after generating a rate map. The residual orbital error is modelled as a planar ramp in the x and y directions $\phi_{n,k} = (a_n)x_k + (b_n)y_k + c_n$ where $[x_k, y_k]$ is the pixel coordinate, (a_n) and (b_n) are gradient parameters and c_n is the intercept. The gradients for the best fitting plane are estimated using least squares on the generated rate map whilst simultaneously inverting for an atmospheric scaling factor and deformation.

2.6 Conclusions

I have demonstrated that the PS selection algorithm in StAMPS, which assesses the likelihood of a pixel being a PS using a probabilistic approach based on phase stability rather than amplitude, works much better in non-urban environments than GAMMA. Whilst GAMMA worked very well in cities there were insufficient points in remote areas in Western Turkey to unwrap the data and measure long wavelength deformation signals.

I have shown a new approach to applying ECMWF data that involves scaling the amplitude using our measured InSAR data. This technique has been shown to improve my results preventing overcorrection of atmospheric effects that degrade our signal. This is one approach that can be used to adjust for over-estimation of the water vapour content by ECMWF data in Tibet.

Chapter 3

Interseismic strain accumulation across the Kunlun fault

3.1 Introduction

The PS InSAR technique described in chapter 2 is applied here to estimate the variability in slip rate across the Kunlun Fault, Tibet. Whilst a number of geological studies have used a combination of dating techniques and offset measurements, notably *Kirby et al.* (2007a) and *Van Der Woerd et al.* (2002), relatively few geodetic studies have mapped strain across the Kunlun Fault (*Zhang et al.*, 2004; *Li et al.*, 2005; *Wang et al.*, 2001). This is the first PS InSAR study measuring interseismic strain accumulation in Tibet and covers an area 750 km by 400 km.

The slip rates across major faults on the Eastern Tibetan Plateau are poorly constrained and vary significantly in different tectonic models. A number of studies have suggested variability in slip rate along the Altyn Tagh (*Taylor and Peltzer*, 2006) and Karakoram faults (*Chevalier et al.*, 2005; *Brown et al.*, 2002); However, the debate is split in the case of the Kunlun Fault. Some authors, including *Van*

Der Woerd et al. (2002), have argued that slip rates are spatially uniform, based on offset measurements along a 600 km central section of the fault. Other authors, including *Kirby et al.* (2007a), who focus more on the eastern end (towards the fault tip), suggest that slip rates systematically decrease towards the east. This study provides much higher resolution data looking at slip rate variability along the Eastern Kunlun Fault, and the partitioning of slip between the Kunlun and surrounding faults, in particular the Kunlun Pass Fault.

Knowledge of slip rates along faults has been key to our understanding of the mechanical behaviour of the crust and mantle beneath the plateau; for example they have been used to test the prediction of various models (*Van Der Woerd et al.*, 2002). Historically the two main competing models were eastward rigid block translation and distributed deformation. Lower slip rates were expected for distributed deformation than for rigid-block-translation (*England and Houseman*, 1986; *Avouac and Tapponier*, 1993; *England and Molnar*, 1997; *Meyer et al.*, 1998). This debate had important implications for the mechanisms of stress transfer and seismic risk in the region.

Initial interseismic studies from InSAR produced velocity maps from isolated tracks, collapsed onto a single profile across a fault for example *Wright et al.* (2001) (North Anatolian Fault), *Taylor and Peltzer* (2006)(central Tibet), *Cavalié et al.* (2008) (Haiyuan Fault), and *Wang et al.* (2009) (Xianshuihe Fault). This progressed to the processing of contiguous tracks to retrieve spatial variations of interseismic coupling for example *Jolivet et al.* (2012) (Haiyuan Fault), *Thomas et al.* (2014) (Longitudinal Valley Fault, Taiwan), and *Cetin et al.* (2014) (North Anatolian Fault). More recent studies have focused on identifying temporal variations in coupling of creep for example *de Michele et al.* (2011); *Jolivet et al.* (2014); *Khoshmanesh et al.* (2015); *Turner et al.* (2015) (San Andreas Fault). With improved

spatial and temporal resolution there is a move towards dynamical models of the earthquake cycle, constrained by observations of different parts of faults at different stages in the cycle. InSAR can help contribute to our understanding of the role of fault segmentation, the partitioning of slip between faults, fault interactions, and variability in properties across a fault zone. GPS sites in the region are sparse, so InSAR is uniquely positioned to provide spatially dense data across faults to help answer some of these questions.

Measuring accurate slip rates across the Tibetan Plateau using InSAR has proved to be a difficult task (see *Garthwaite*, 2011), as the region is remote with high levels of erosion, steep topography, snow covered regions, and irregularly spaced satellite passes. This all contributes to regions of decorrelation across interferograms, difficulty with co-registration, and compounds unwrapping problems. Consequently, the area lends itself well to PS InSAR, where the selection of a subset of the data with good signal to noise ratio helps provide data in regions where decorrelation is high. It also enables constraints on perpendicular baselines (applied for standard InSAR) to be relaxed, so more satellite passes can be used in a region where there are already gaps in the time series of up to four years and many swaths are limited to at most two passes a year.

In this chapter I give a brief outline of Tibetan Plateau tectonics and provide a summary of existing estimates of slip rates. I then explain the process for the modelling and inversion of continental deformation. For a test track across the Kunlun Fault, I compare the results obtained using PS InSAR with those obtained using standard DifSAR for a small baseline subset of the data (SBAS). I show that in regions that are decorrelated in standard InSAR, or where there are few satellite passes, PS InSAR can maximise the information available in a given dataset, and measure signals that could not reliably be detected using DifSAR. I show veloc-

ity maps together with atmospheric estimates, tectonic models, and residuals for 5 tracks of data. Finally, I discuss why significantly lower slip rates are observed at the fault tip compared with the central section of the fault, and where this slip deficit is being transferred to beyond the Kunlun Fault.

This chapter examines interseismic strain accumulation only; where a strong postseismic signal is observed for the Kokoxili earthquake, it is modelled and removed in Chapter 4, and the interferograms are shown here with that signal removed. Throughout this chapter, left lateral motion is quoted as positive values of slip rate, and right lateral motion as negative values.

3.1.1 Tibetan Plateau tectonics

Approximately 90% of the relative motion between India and Eurasia (measured to be ∼38 mm/yr) is absorbed through deformation in Tibet and its margins (*Wang et al.*, 2001). A magnitude 6 earthquake or greater occurrs in the region on average every month according to the global CMT catalogue (http://www.globalcmt.org/). The distribution of earthquake mechanisms across Tibet and their contribution to convergence show underlying trends that can principally be explained by gradients in gravitational potential energy (*Elliott et al.*, 2010). North-south shortening is accommodated by thrust faulting that is largely confined to the lower lying regions in the north and south of Tibet, as shown in figure 3.1. Conversely, normal faulting across north-south striking grabens is confined mainly to regions above 4.5 km in elevation (*Elliott et al.*, 2010) towards the west. The notable exception to this is a series of east-west striking normal faults near the Eastern Syntaxis and the mechanically strong Sichuan Basin, which has largely resisted deformation (*Copley and McKenzie*, 2007).

In the southern and central plateau, eastwards motion is accommodated along a series of left-lateral strike-slip faults. Further east this motion is diverted north-east and south-east around the Sichuan Basin. West and south-west of the Sichuan Basin, southward motion of the upper crust is accommodated by clockwise rotation and left-lateral slip along a series of E-W striking faults (*England and Molnar*, 1990), including the Kunlun and Yushu-Xianshiuhe fault systems. A broad-scale map of the region and the major fault systems, together with seismic activity for earthquakes greater than M 6.0 is shown in figure 3.1.

The role that the Kunlun Fault plays in regional tectonics is determined by its relative slip rate compared to surrounding fault systems and the variability in slip along its strike. The Tibetan plateau is bounded to the north by three key strike-slip faults: the Altyn Tagh, with slip rates of up to 11 mm/yr (*Elliott et al.*, 2008a), the Kunlun, with slip rates documented as 1-16 mm/yr (shown in table 3.1), and the Haiyuan, with slip rates of up to 8 mm/yr (*Cavalié et al.*, 2008). The lateral extent and spatial relationship of these faults to high-angle thrust faults suggest that they play a major role in accommodating the convergence of India and Asia (*Tapponnier et al.*, 1990; *Meyer et al.*, 1998).

3.1.2 The Kunlun Fault

The Kunlun Fault runs east-west parallel to the Kunlun Shan mountain range for ∼1600 km on the northern Tibetan Plateau. The western end runs south of the Qaidam basin, through the Qimantag Shan at a height of 5500 km. The eastern end follows the Anyemaqen suture. The fault is typically subdivided into five sections from west to east: the Kusai Hu, the Xidatan-Dongdatan, the Alan Hu, the Donxi Co and the Maqen segments. A more detailed fault map showing these segmentsm,

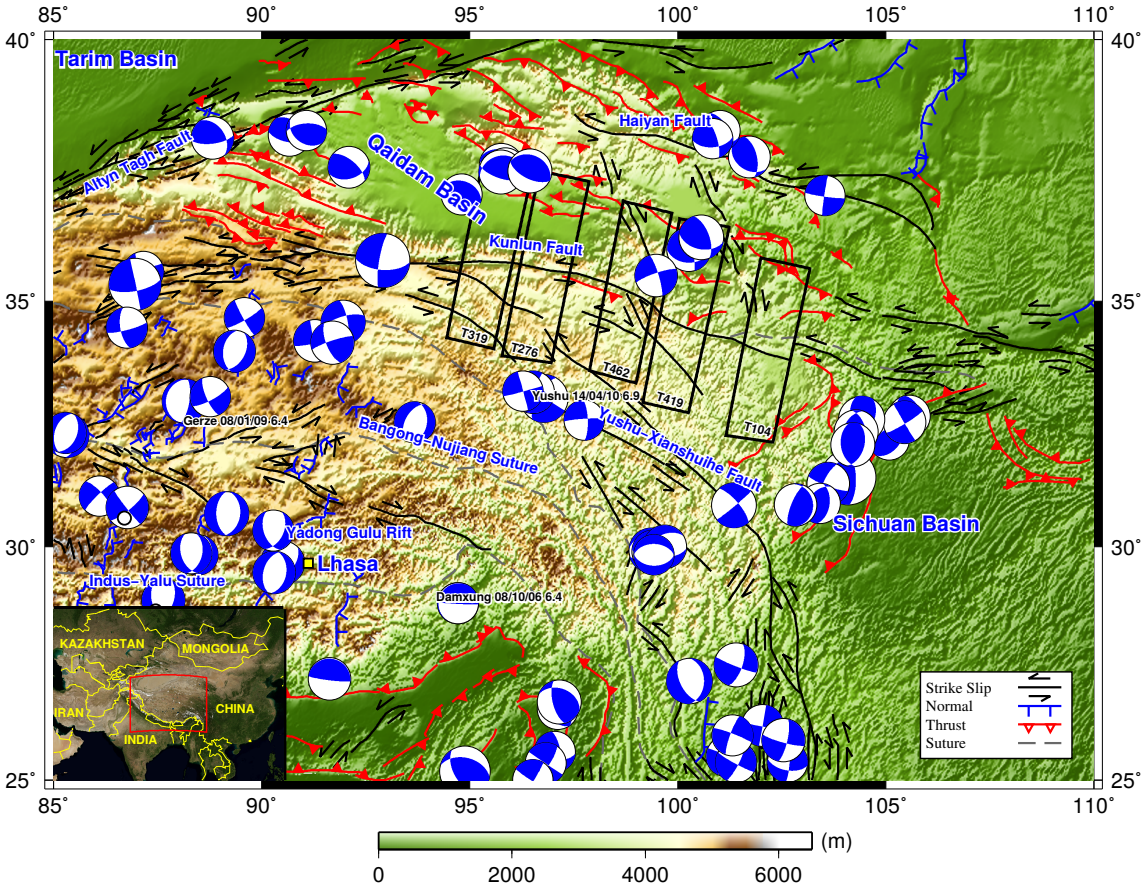

Figure 3.1: Geographic borders and locations of features in the region of Tibet. Earthquake locations for events greater than M 6, taken from the CMT catalogue, are shown with blue beachballs. Track locations for the processed InSAR data are shown as black boxes. Major strike-slip faults are shown in black, normal faults in blue and thrust faults in red, taken from the fault map of *Taylor and Yin* (2009). The inset map shows the region of Asia under study and surrounding countries.

the track locations of processed data and earthquake history is seen in figure 3.2.

The different segments of the Kunlun Fault are characterised by different magnitudes of earthquake, with different recurrence times and characteristic slip. This study covers the four easternmost segments, from the last 40 km of the Kokoxili rupture to the tip of the fault at Maqu. The four westernmost segments have been ruptured by major earthquakes in the last century, leaving the Maqen segment as the only section to have had no major earthquake ruptures in recorded history.

At its western end the Kunlun Fault splits into a number of splays. The Manyi

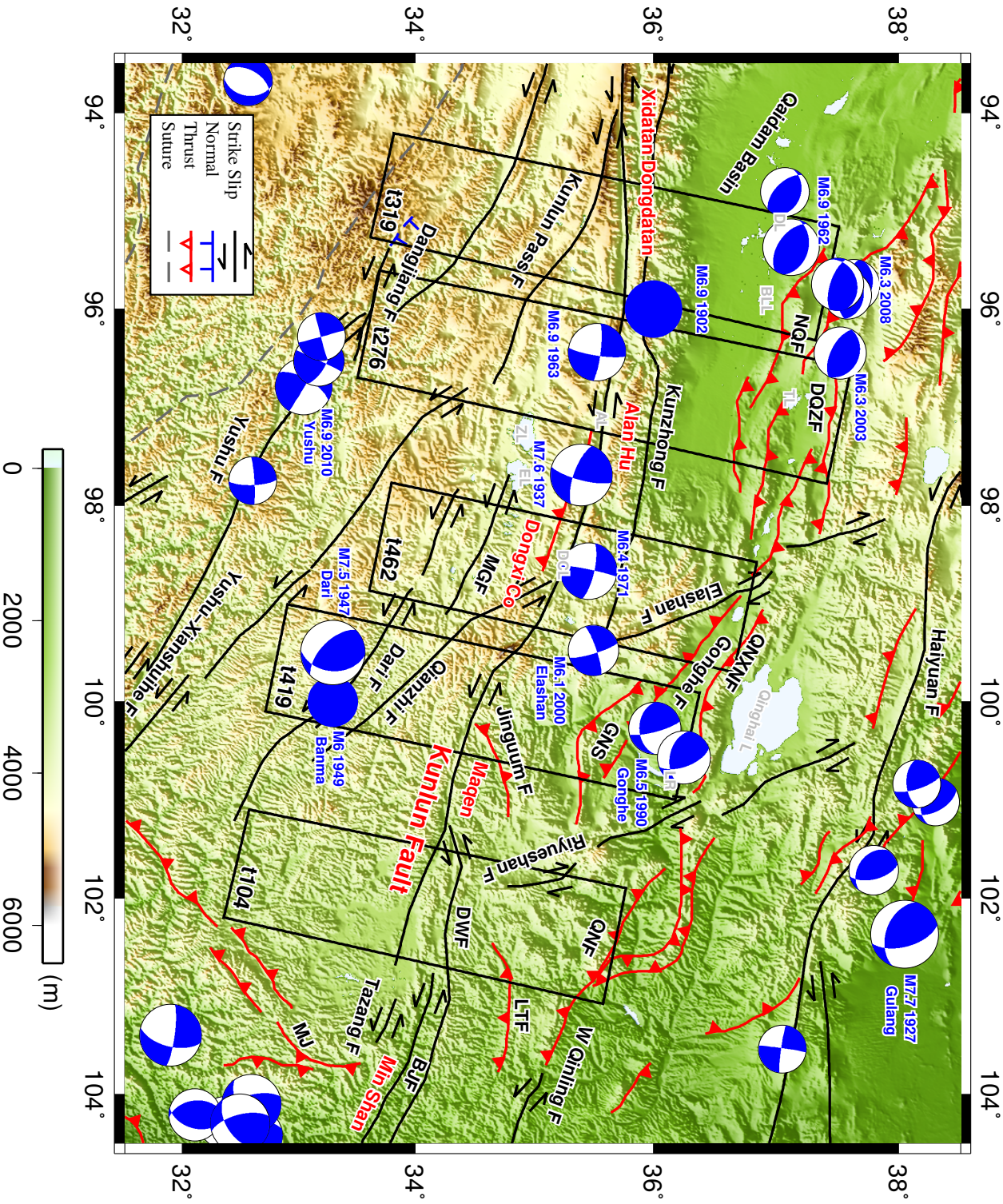

Figure 3.2: Relief map showing faults according to *Taylor and Yin* (2009) as black lines (with the addition of the Yushu mapped as per *Wang et al.* (2008) the Gonghe Fault as per *Craddock and Kirby* (2014) and *Deng et al.* (2007), and the Kunzhong as per *Deng et al.* (2007)), footprints of the processed ENVISAT tracks (from left to right 319, 276, 462, 419, 104) as black boxes, and earthquake history according to the USGS as beach balls and blue circles. Abbreviations: N=North, W=West, DQZ=Da Qaidam-Zongwulongshan, NQF=North Qaidam Fault, MGF=Maduo-Gande Fault, GNS=Gonghe Nan shan, QNXN=Qinghai Nanshan-Xunhua Nanshan, QNF=Qinghai Nanshan, LTF=Lintan Tanchang Fault, DWF=Diebu-Wadu Fault, BJF=Bailong Jiang Fault, MJ=Min Jiang Fault, DC=Donggei Cuona, TL=Tuoso Lake, DL=Dabuxun Lake, BLL=Beihuo Luxun Lake, ZL=Zhalingu, EL=Elinghu, AL=Alake Lake, LR=Longyangxia Reservoir

Comparison of Calculated Slip Rates for the Kunlun Fault

Method	Longitude	Slip rate (mm/yr)	Reference
Geological			
Alluvial fan, gully offsets & C14	93.8°E	16-17	*Lin et al.* (2006)
C14 dated offsets	102.5°E	3	*Lin and Guo* (2008)
Thermoluminescence of offsets	92.5°E	10±1.5	*Li et al.* (2005)
Terrace riser offsets & cosmogenic dating EH	94.2°E	13.5±1.8	*Van Der Woerd et al.* (2002)
Terrace riser offsets & cosmogenic dating EH	94.2°E	11.2 ±1.3	*Van Der Woerd et al.* (2002)
Terrace riser offsets & cosmogenic dating LH	94.7°E	11.3±1.9	*Van Der Woerd et al.* (2002)
Terrace riser offsets & cosmogenic dating LH	94.7°E	9.7±2.8	*Van Der Woerd et al.* (2002)
Terrace riser offsets & cosmogenic dating	94.4°E	12±2.6	*Van Der Woerd et al.* (2002)
Terrace riser offsets	99.2 ° E	10	*Van Der Woerd et al.* (2002)
Terrace riser offsets	99.5 ° E	9-10.5	*Van Der Woerd et al.* (2002)
Lateral moraine Offset	100.5°E	12.5±2.5	*Van Der Woerd et al.* (2002)
Moraine offsets	94°E	13.5 +6.5-3.5	*Kidd and Molnar* (1988)
Moraine glacier & post-glacial valley offsets	95°E (KP)	10+10-5	*Kidd and Molnar* (1988)
Terrace riser offsets	∼94°E	5-7.5	*Guo* (2006)
Offset landforms and fault outcrops	98.5-100°E	7	*Guo et al.* (2007)
Offset landforms and fault outcrops	102.3°E	2.5-4	*Guo et al.* (2007)
Terrace riser offsets	101.4°E	<5.0±0.4	*Kirby et al.* (2007a)
Terrace riser offsets	101.4°E	<6.0±1.2	*Kirby et al.* (2007a)
Terrace riser offsets	101.4°E	>4.1±0.3	*Kirby et al.* (2007a)
Terrace riser offsets	101.4°E	>4.1±0.4	*Kirby et al.* (2007a)
Terrace riser offsets	101.8°E	<2.0±0.4	*Kirby et al.* (2007a)
Terrace riser offsets	103.1°E (T)	<1.0	*Kirby et al.* (2007a)
Cosmogenic and ^{14}C dated offsets	99.8°E	6.1±1.3	*Harkins et al.* (2010)
Cosmogenic and ^{14}C dated offsets	100.6°E	3.7±2.0	*Harkins et al.* (2010)
Cosmogenic and ^{14}C dated offsets	100.9°E	4.4±1.9	*Harkins et al.* (2010)
Cosmogenic and ^{14}C dated offsets	101.6°E	3.4±1.0	*Harkins et al.* (2010)
Terrace riser offsets	94°E	10-15	*Ren et al.* (1999)
Offsets	∼94°E	10.4	*Zhao* (1996)
Offsets	∼98°E	11.7	*Zhao* (1996)
Displaced terrace risers	∼103°E (T)	1.4-3.2	*Ren et al.* (2013)
Cosmogenic dating of alluvial surfaces	Xidatan	12.1 ±2.6	*Ryerson et al.* (1998)
Geodetic			
GPS	∼95-99°E	8-11	*Zhang et al.* (2004)
INSAR	91-92.5°E	3.6-7	*Garthwaite* (2011)
GPS	94.2°E	8-18 ±4	*Wang et al.* (2001)
GPS	H	6±2	*Chen et al.* (2000)

Table 3.1: Published estimates of the slip rates on the Kunlun Fault using Dating, geological offsets, and geodetic techniques. EH stands for Early Holocene and LH Late Holocene. Measurements for offshoots and continuations of the Kunlun Fault are indicated in brackets after the longitude. KP represents Kunlun Pass, H for Haiyuan and T for Tazang.

Fault, which ruptured in 1997 in a M 7.6 earthquake and in 1973 in a M 7.4 event, was first identified as one of these splays by *Tapponnier and Molnar* (1977). It has the same orientation as the Kunlun Fault, so is widely considered to be its westward continuation. The 1997 event resulted in a 170 km surface rupture and a maximum

slip of 7 m (*Funning et al.*, 2007). This segment typically has an assumed earthquake recurrence time of 300 years (*Bell*, 2013).

The Kusai Hu segment and the western section of the Xidatan-Dongdatan segment, up until the intersection of the Kunlun Fault with the Kunlun Pass Fault, were ruptured in the 2001 Kokoxili earthquake (see 4.3 for the mapped rupture and earthquake location). At the intersection the rupture continued along the southeastern Kunlun Pass Fault rather than following the main fault strand (*Lasserre et al.*, 2005). This M_w 7.8 event resulted in a rupture greater than 400 km in extent. The locking depth has been widely documented as approximately 18 km, with the dip varying from 85° to 90° (*Li et al.*, 2005; *Lasserre et al.*, 2005). Recurrence times for large earthquakes along the Kusai Hu segment are believed to be 300 ± 50 years with a characteristic slip of 3 ± 0.5 m (*Li et al.*, 2005).

There is no historical event recorded as having its epicentre on the Xidatan-Dongdatan segment, but trenching and dated surface offsets suggest ∼Mw 8 earthquakes with an average slip of 10 ± 2 m and a recurrence time of 850 ± 200 years along this section (*Li et al.*, 2005).

The Alan Hu section of the fault covers a step-over occurring at 97.1°E, 35.61°N. It was ruptured in 1963 by a M 6.9 event with maximum slip of 8 m (*Li et al.*, 2005). Characteristic slip values and recurrence times for this segment are not available, other than those recorded for this single event.

The Donxi Co segment has had two major earthquakes in recorded history, a M7.6 in 1937 (known as the Tuoso lake earthquake) and a M6.4 in 1971. The earlier event produced a 180 km long rupture with up to 7 m of slip (*Li et al.*, 2005); no surface rupture has been identified for the second event. This segment typically has M 7.5 earthquakes with a characteristic slip of 4.4 ± 0.4 m and a recurrence time of 420 ± 60 years (*Li et al.*, 2005).

According to the paleoseismic record, the most recent event on the Maqen segment occurred ca. 1500 ka (*Lin and Guo*, 2008) with a slip rate of no greater than 3-5 mm/yr (*Harkins et al.*, 2010).

3.2 Data availability and processing

I processed a total of 109 SAR satellite acquisitions, on five tracks, from the ENVISAT mission using the open-source JPL/Caltech ROI_PAC software (*Rosen et al.*, 2004) for data from 2003 to 2011. Gaps between tracks are a reflection of insufficient data on the overlapping passes (generally less than six satellite acquisitions). I carried out an initial co-registration using the Gamma software and cropped the SLCs to cover identical areas. This is done to resolve issues created by trying to co-register SLCs with significant offsets.

3.2.1 DifSAR processing (track 462)

In the case of DifSAR, the remaining processing steps were carried out using ROI_PAC. These steps are not described here, instead the author refers the reader to the following references *Buckley* (1998), *Rosen et al.* (2000), *Funning* (2005), and *Biggs et al.* (2007). In order to detect deformation signals on the order of a few mm, I restricted interferograms to satellite passes with short perpendicular baselines and short time intervals. This approach is known as the small baseline subset approach (SBAS). I used a perpendicular baseline cutoff of 300 m. It was not possible to generate interferograms for all pairs with shorter perpendicular baselines due to incoherence, resulting in problems coregistering scenes. A plot of perpendicular baseline against time is shown in figure 3.3, with the successfully generated interferograms indicated by the connecting lines.

Twenty two interferograms were processed from sixteen independent dates (shown in table 3.2) between 2003-09. Topography was removed using a 90 m SRTM. The level of decorrelation was shown to be relatively high, so it was necessary to multilook the data to 64 looks, giving a resolution of approximately 1.5 km. The multilooked interferograms were unwrapped using a branch cut technique (*Goldstein et al.*, 1988). Unwrapping errors were then corrected using a phase closure method (*Biggs et al.*, 2007). To produce a ratemap, I use the $\pi-$RATE (Poly-Interferogram Rate and Time-series Estimate) Matlab-based software package of *Wang et al.* (2009) to combine interferograms into maps of LOS velocity. This implements the procedure of *Biggs et al.* (2007) for measuring interseismic deformation.

3.2.2 PS InSAR Processing

In the case of PS InSAR, after the initial SLC crop, I performed DEM assisted co-registration using the DORIS software. I selected an appropriate master scene using a central date in the time series, chosen to provide the maximum number of interferograms with baselines below 300 m. In the event of there being more than one possible master scene, I chose a master so as to minimise atmospheric effects. For many tracks, I generated interferograms for two or three possible masters and chose the scene providing the most coherent interferograms to continue on for PS selection.

I used a 90 m SRTM digital elevation model to make topographic corrections and Delft (ODR) orbits (*Scharroo and Visser*, 1998) to make orbital corrections. I then selected PS using StAMPS, following the procedure outlined in chapter 2. I applied a Goldstein filter (*Goldstein and Werner*, 1998) and regridded the data to enable unwrapping in 3D, using the SNAPHU software (*Chen and Zebker*, 2002). I

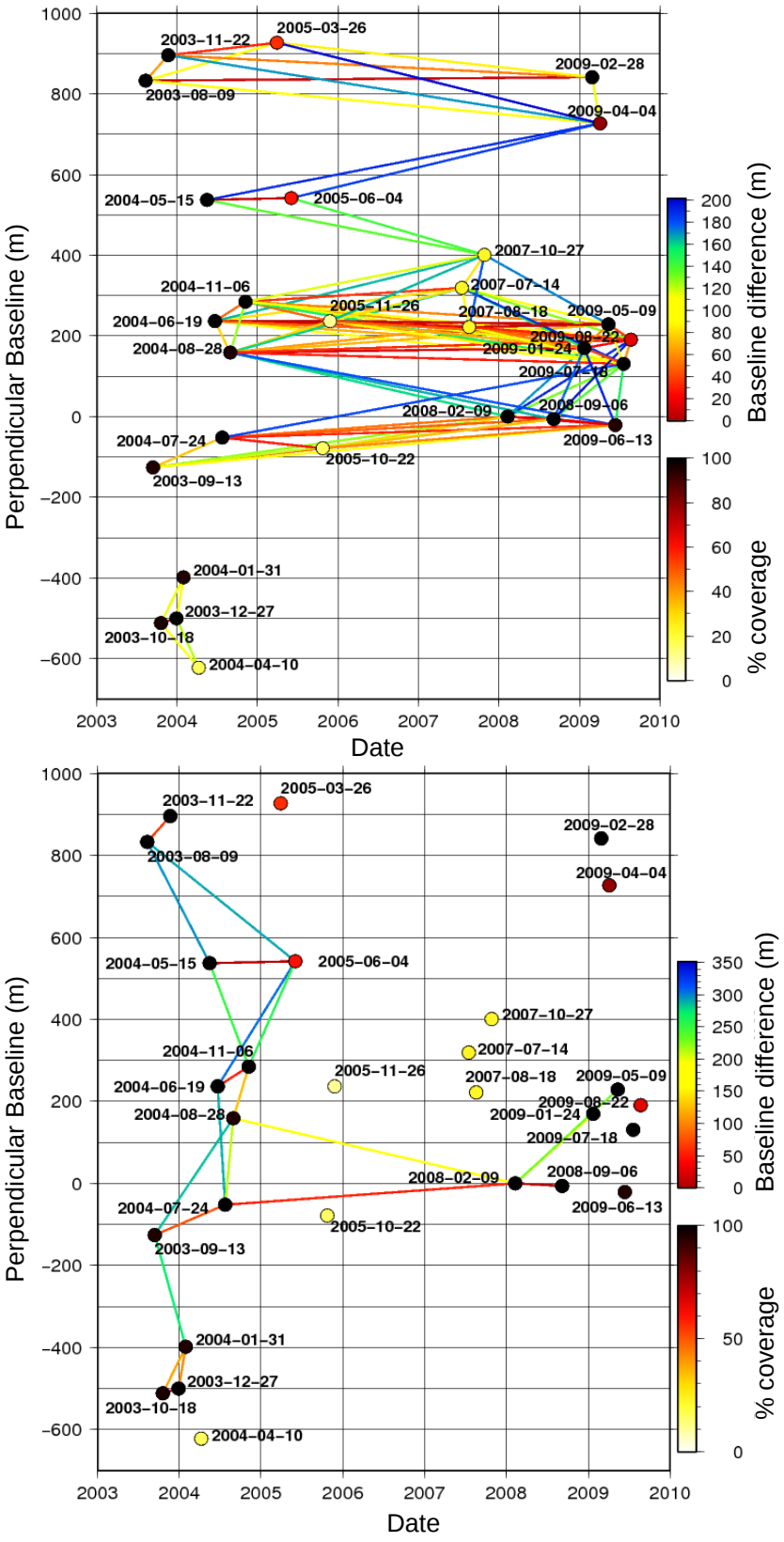

Figure 3.3: Perpendicular baselines for track 462 showing the available data (top) and the processed data (bottom) using DifSAR in ROI_PAC. A general perpendicular baseline cutoff of 300 m was applied. However, due to problems coregistering some scenes, it was not possible to produce interferograms for all pairs with perpendicular baselines below this cutoff.

Key showing the dates of satellite passes represented by the numbers in figure 3.4

No	Track 319	Track 276	Track 462	Track 419	Track 104
1	20030625	20030413	20030809	20031224	20030715
2	20031008	20030622	20030913	20040128	20031202
3	20040121	20031005	20031018	20041103	20040106
4	20040818	20031214	20031122	20070606	20040210
5	20041027	20041024	20031227	20080521	20040316
6	20041201	20050522	20040131	20080903	20040629
7	20061206	20080824	20040515	20081217	20041012
8	20070214	20080928	20040619	20090121	20041116
9	20070425	20081102	20040724	20090225	20050125
10	20070704	20081207	20040828	20090401	20050301
11	20070808	20090111	20041106	20090819	20080219
12	20070912	20090215	20050604	20100210	20080916
13	20071017	20090322	20080209	20100317	20081021
14	20071121	20090531	20080906	20100421	20090203
15	20080130	20090705	20090124	20100630	20090310
16	20081105	20090809	20090228	20100804	20090414
17	20081210	20091018	20090509	20100908	20090519
18	20090218	20091122	20100911	20101013	20090623
19	20090708	20100307			20090728
20	20090812	20100725			20091215
21	20090916	20100829			20100119
22	20091021				20100330
23	20091230				20100504
24	20100414				20100608
25	20100519				20100713
26	20100623				20100817
master	**20061206**	**20080824**	**20080209**	**20070606**	**20090519**

Table 3.2: Key showing the dates of satellite passes represented by the numbers in perpendicular baseline plots for Tibet.

attempted to use all available scenes; however, in some cases the baseline between some dates was too large to produce an interferogram of sufficient coherence.

Plots showing perpendicular and temporal baselines for each of the five main tracks are shown in figure 3.4, with excluded scenes indicated in grey. Table 3.3 shows the number of PS selected for each of the tracks. I tested a range of PS selection parameters for each of the tracks. For this region, similar parameterisations were found to consistently produce the highest levels of coherence. Consequently, I mainly kept the same parameterisations for each track (refer to chapter 2 for details of parameters), of a 365 day **unwrapping time window**, a 200 m **merge resample size**, a **Clapeyron low pass wavelength** of 800 m, a PS **phase standard deviation** of 0.8, and a 1000 m **unwrap grid size**. I changed the **density random**

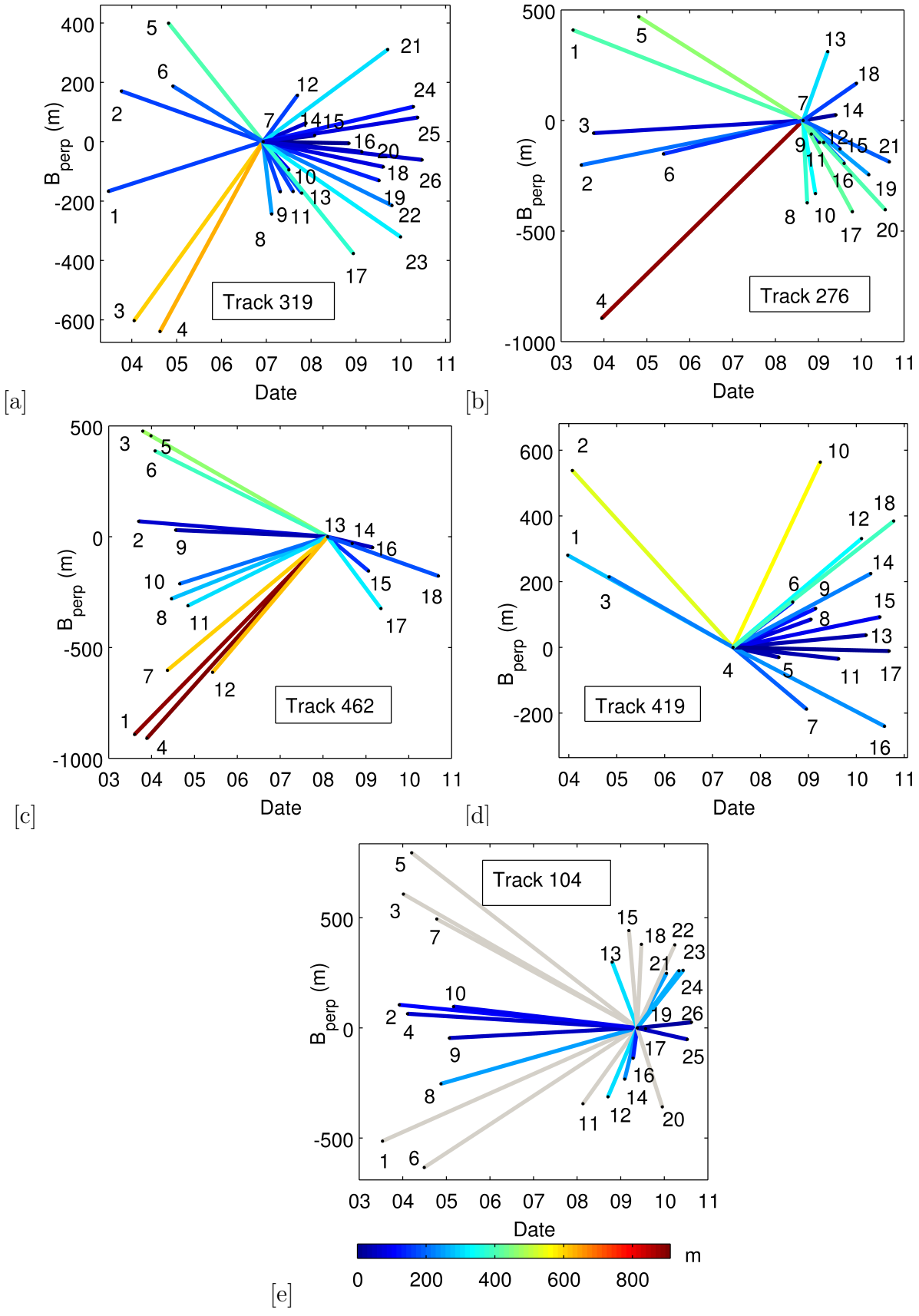

Figure 3.4: Perpendicular baselines in meters are shown for tracks [a] 319,[b] 276,[c] 462,[d] 419 and [e] 104. Lines are colour coded according to the perpendicular distance between each satellite pass; the master date is shown in table 3.2. Grey lines indicate those dates excluded from PS selection and stacking due to incoherence.

Number of PS points selected for each track	
Track number	Number of PS points
319	466513
276	623449
462	549411
419	457150
104	564281

Table 3.3: PS selection was performed using StAMPS with the same PS being used for each interferogram in the time series.

for the furthest east and furthest west tracks to address increased decorrelation to the south. Therefore, for tracks 462, 419, and 276 a **density random** of 40 per km^2 was used, whilst for track 319 and 104 a value of 20 per km^2 was used. Approximately half a million PS points were chosen for each track; precise numbers for each track are specified in table 3.3.

An average velocity map spanning the entire time series was then generated from the unwrapped PS InSAR data. I calculated the best fitting LOS velocity using a least squares inversion for each flattened interferogram on a pixel by pixel basis, as outlined in section 3.3.

3.2.3 Coherence

There is large variability in coherence across the region; coherence is generally lower in: (i) more vegetated areas towards the fault tip, (ii) regions with snow to the south of the Kunlun Fault (where heights are in the region of 4500 m), and (iii) areas where erosion rates associated with water run-off are particularly high (for example, where the Yellow River runs northwards through track 419, towards the Longyangxia Reservoir). Loss of coherence due to vegetation can be mapped by correlating Normalised Difference Vegetation Index (NDVI) with coherence. Coherence is lowest for track 104, so I used a small baseline subset of the 15 scenes with

the shortest perpendicular baselines for this track.

Coherence is seen to systematically decrease to the southern side of the Kunlun Fault, as shown in the previous chapter in figure 2.5. Consequently the PS selection criteria are chosen to increase the number of PS selected by using a relatively high standard deviation over the entire scene. This is balanced by reducing the density random parameter, to exclude points with lower standard deviation to the north where coherence is high, thereby selecting the best points. Where snow is seasonal, coherence can be improved by excluding passes in winter months. However in Tibet, snow is present all year round in many areas, and there are insufficient passes to exclude those from winter months in lower lying regions. I therefore use the same approach as for vegetation and change the standard deviation and density random parameters.

3.3 Formation of a rate map

To find the best fitting LOS velocity for PS InSAR, a least-squares inversion is carried out for each flattened interferogram on a pixel by pixel basis. This is weighted by the temporal variance covariance matrix. This gives greater weighting to interferograms with lower standard deviation and therefore lower noise levels. Before doing so, the unwrapped flattened phase is first converted from radians to millimetres. The inversion is then carried out to obtain a rate map, r_k, for each pixel, k, as

shown below:

$$\frac{4\pi}{\lambda}\mathbf{T}\mathbf{r}_k = \mathbf{\Phi} \tag{3.1}$$

$$\frac{4\pi}{\lambda}\mathbf{T}^T\mathbf{\Sigma}_\phi^{-1}\mathbf{T}\mathbf{r_k} = \mathbf{T}^T\mathbf{\Sigma}_\phi^{-1}\mathbf{\Phi} \tag{3.2}$$

$$\mathbf{r}_k = \frac{\lambda}{4\pi}\underbrace{\left[\mathbf{T}^T\mathbf{\Sigma}_\phi^{-1}\mathbf{T}\right]^{-1}}_{\mathbf{\Sigma_r}}\mathbf{T}^T\mathbf{\Sigma}_\phi^{-1}\mathbf{\Phi} \tag{3.3}$$

where $\mathbf{T}$ is a column vector of times in days with respect to the master scene, i, and ones to account for an offset, $[t_{1i}1, t_{2i}1...t_{ji}1]^T$, ϕ is a vector of phase for each slave with respect to the master image, $\mathbf{\Sigma}_\phi$ is the temporal variance covariance matrix. In the case of PS InSAR data, the temporal variance covariance is given by:

$$\Sigma_\phi = \mathbf{diag}\left(\sqrt{\frac{\Sigma\phi_{unw}^2}{N}}\right) \tag{3.4}$$

where ϕ_{unw} is the unwrapped phase of each PS for slave j (with respect to the master i), N is the number of PS points, and diag represents the diagonal matrix. The formal error in the rate map is then given by $\mathbf{\Sigma_r}$, shown in equation 3.3 above.

3.4 Tectonic model of interseismic strain accumulation

Two key models have been adopted for modelling interseimic strain accumulation, a deep fault model and a shear zone model. In the deep fault model, an infinite screw dislocation is extended from the bottom of the seismogenic layer to infinite depth. During the interseismic period, the fault is locked by friction from the surface to depth d, and aseismic strike slip motion occurs at a rate s below this locked seismogenic zone. In the shear zone model introduced by *Prescott and Nur* (1981),

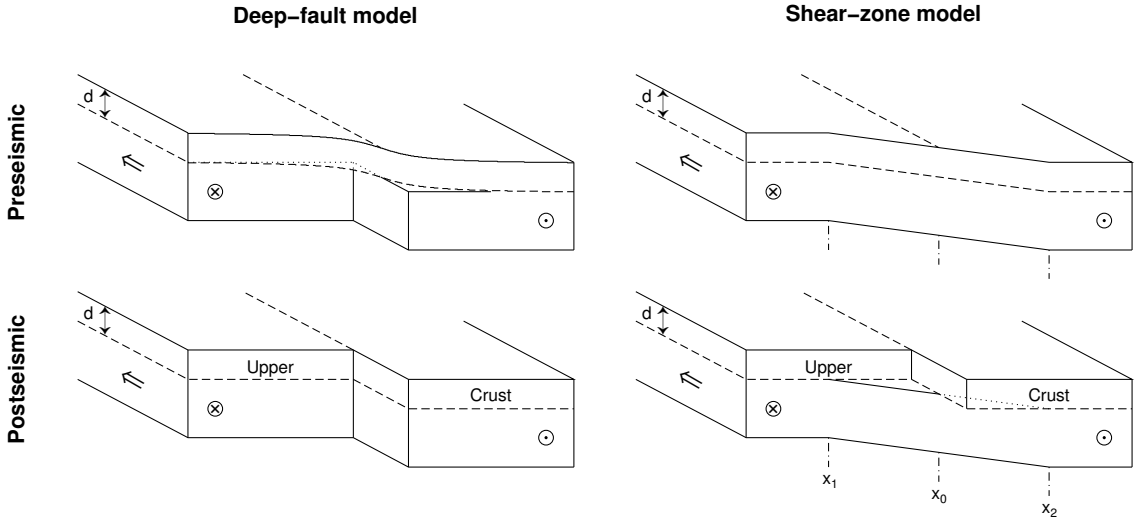

Figure 3.5: Two fault models for the distribution of crustal deformation at depth for the earthquake cycle. Left: deep-fault model with an upper crust of elastic thickness d; prior to an earthquake (top-left) which is strained above an offset lower crust and mantle, which slides by creep as aseismic slip on a discrete plane. Immediately after an earthquake (bottom-left), the elastic rebound occurs in the upper crust, restoring the offset between the layers. Right: shear-zone model in which the elastic upper crust is strained by shear traction above a ductile lower layer, with deformation distributed linearly across some finite width (top-right). The long-term motion of the upper crust is the same in both models, but the velocity of the lower crust in the shear-zone model (bottom-right) is half that of the upper crust immediately either side of the fault (e.g. x_o relative to x_1). In the shear-zone model, the deformation in the upper crust is not necessarily localised on a single fault plane. Adapted from *Molnar et al.* (1999) by *Elliott* (2008b).

viscous shear is distributed across a region of finite width at depth and concentrated onto localised fault planes in the upper crust. However, the two models become indistinguishable beyond a certain width, as deformation at depth is filtered through the locked elastic layer above the dislocation (*Bell*, 2013). *Wright et al.* (2001) calculated that this width is 75 km for the eastern North Anatolian Fault. *Savage and Burford* (1973) also showed that any shear zone can be matched by a distribution of deep dislocations. For ease of calculation I therefore use the approach of the deep fault model.

3.4.1 Deep fault model

To obtain slip rate estimates, I generate a synthetic forward model for the Kunlun Fault, assuming that all displacements are fault-parallel and horizontal. I model the Kunlun Fault as a buried infinite screw dislocation in an elastic half-space, where during the interseismic period, left-lateral aseismic slip occurs at a rate s below a locking depth d. The interseismic fault parallel displacement u at a perpendicular distance from the fault x is then given by (*Savage and Burford*, 1973; *Okada*, 1985, 1992):

$$u(x) = \frac{s}{\pi}\tan^{-1}\left(\frac{x}{d}\right) \tag{3.5}$$

Although there are just two unknowns, the locking depth and slip rate, variation in dip can also be incorporated as an apparent offset in the fault location. Figure 3.6 shows the effect of varying slip rate, locking depth, and dip on an average profile taken perpendicular to the fault location. Locking depth has been shown to trade off against slip and to be poorly constrained by a number of studies, such as *Cavalié et al.* (2008); *Walters* (2012). As the thickness of the seismogenic layer can be modelled directly or inferred from studies of coseismic displacements, I can validate the obtained locking depths and dips using track 319, which covers the Kokoxili earthquake. A number of coseismic studies have been carried out on this earthquake which could be used for this purpose, notably *Lasserre et al.* (2005).

3.5 Slip rate estimation and inversion for PS InSAR

I performed a least squares weighted inversion for the slip rate s, with a parameter search for the locking depth and dip. I searched over the ranges 10-38 km at 4 km

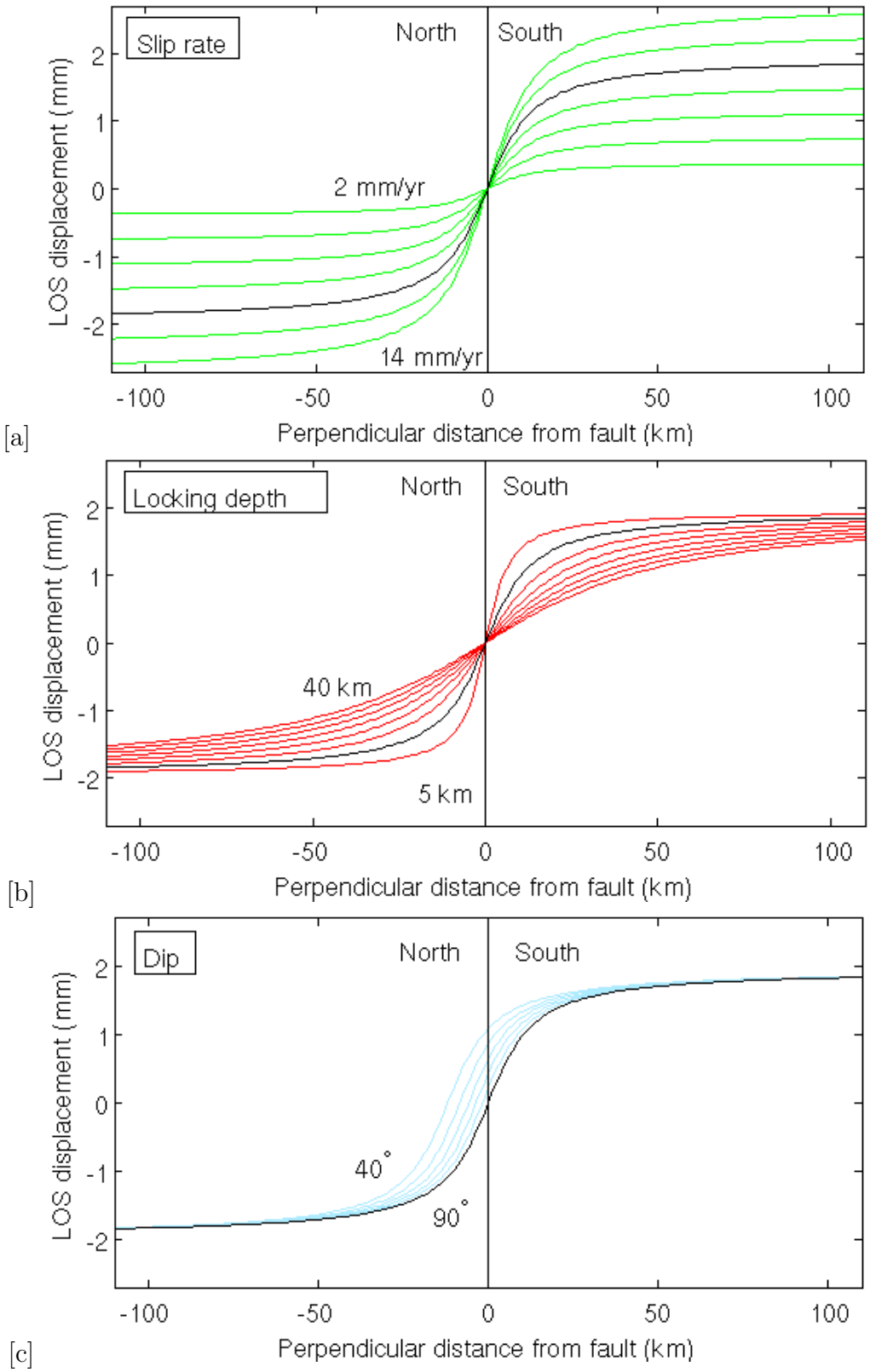

Figure 3.6: Change in length-scale, amplitude, and asymmetry of the deformation due to an infinitely long vertical strike-slip fault with (a) variable slip rate from 2 mm/yr to 14 mm/yr, at 2 mm/yr intervals; (b) variable locking depth from 5 km to 40 km, at 5 km intervals; (c) variable dip from 40° to 90°, at 10° intervals. The curve for a locking depth of 10 km, slip rate of 10 mm/yr, and dip of 90° is shown in black for comparison.

intervals for the locking depth, and over the range 70-110° at 5° intervals for the dip. For the forward model, I generated a design matrix **A** consisting of: the Green's function g_k for tectonic velocity, the x and y position of each pixel, the atmospheric model $\delta\phi^{ecmwf}$ (calculated in section 2.4.2), and a vector of ones. For each combination of dip and locking depth, I then inverted the rate map r (constructed in equation 3.7) to simultaneously find: an average slip rate s, an atmospheric amplitude scaling factor β (described in section 2.4.3), parameters in x of a and in y of b for a linear orbital trend (described in section 2.5), and a static offset in LOS rate c. I found the best fit model that minimised the total RMS misfit between the design matrix **A** and the data **b**:

$$\underset{\mathbf{A}}{\begin{pmatrix} g_1 & x_1 & y_1 & \delta\phi_1^{ecmwf} & 1 \\ g_2 & x_2 & y_2 & \delta\phi_2^{ecmwf} & 1 \\ \vdots & \vdots & \vdots & \vdots & \vdots \\ g_k & x_k & y_k & \delta\phi_k^{ecmwf} & 1 \end{pmatrix}} \underset{\mathbf{x}}{\begin{pmatrix} s \\ a \\ b \\ \beta \\ c \end{pmatrix}} = \underset{\mathbf{b}}{\begin{pmatrix} r_1 \\ r_2 \\ \vdots \\ r_k \end{pmatrix}} \tag{3.6}$$

In the case of the tectonic model, g_k, I simplified and fixed the fault positions and geometries to a single strike based on the fault map by *Taylor and Yin* (2009) with the addition of the Yushu Fault mapped as per *Wang et al.* (2008), the Gonghe Fault as per *Craddock and Kirby* (2014) and *Deng et al.* (2007), and the Kunzhong as per *Deng et al.* (2007). For standard DifSAR, I weighted the inversion by the spatial variance covariance matrix $\mathbf{\Sigma_S}$, to account for the spatial correlation between pixels. This is determined by the median e-folding wavelength calculated in section 2.4.4. In the case of PS InSAR I do not apply any spatial weighting to pixels, as a matrix

containing spatial correlations between pixels for approximately half a million points results in significant memory problems. However, each of the interferograms in the time series was previously weighted at the point of rate map generation, using a temporal covariance matrix, as shown earlier in section 3.3.

Re-arranging equation 3.6 above then gives the solution:

$$\mathbf{Ax} = \mathbf{b} \tag{3.7}$$

$$\mathbf{A}^T\Sigma_S^{-1}\mathbf{Ax} = \mathbf{A}^T\Sigma_S^{-1}\mathbf{b} \tag{3.8}$$

$$\mathbf{x} = \underbrace{\left[\mathbf{A}^T\Sigma_S^{-1}\mathbf{A}\right]^{-1}}_{\Sigma_x}\mathbf{A}^T\Sigma_S^{-1}\mathbf{b} \tag{3.9}$$

3.5.1 Synthetic tests of slip rate estimation

To test whether velocity maps are dominated by tectonic rather than atmospheric signal, I generated synthetic data sets for track 462 using an infinite screw dislocation for a characteristic slip rate for the Kunlun of 10 mm/yr. I superimposed on the tectonic signal a predicted atmospheric signal generated using ECMWF data. The velocity map is shown in figure 3.7 (a) to be dominated by the tectonic signal. Model inversions carried out without spatial weighting give a slip rate of 9.3 mm/yr close to the true value of 10 mm/yr, as shown in figure 3.7 (b).

3.5.2 Constructing profiles

For visualisation of the results, I constructed fault perpendicular mean profiles across the ratemaps, corrected for orbital and atmospheric errors. This was done by rotat-

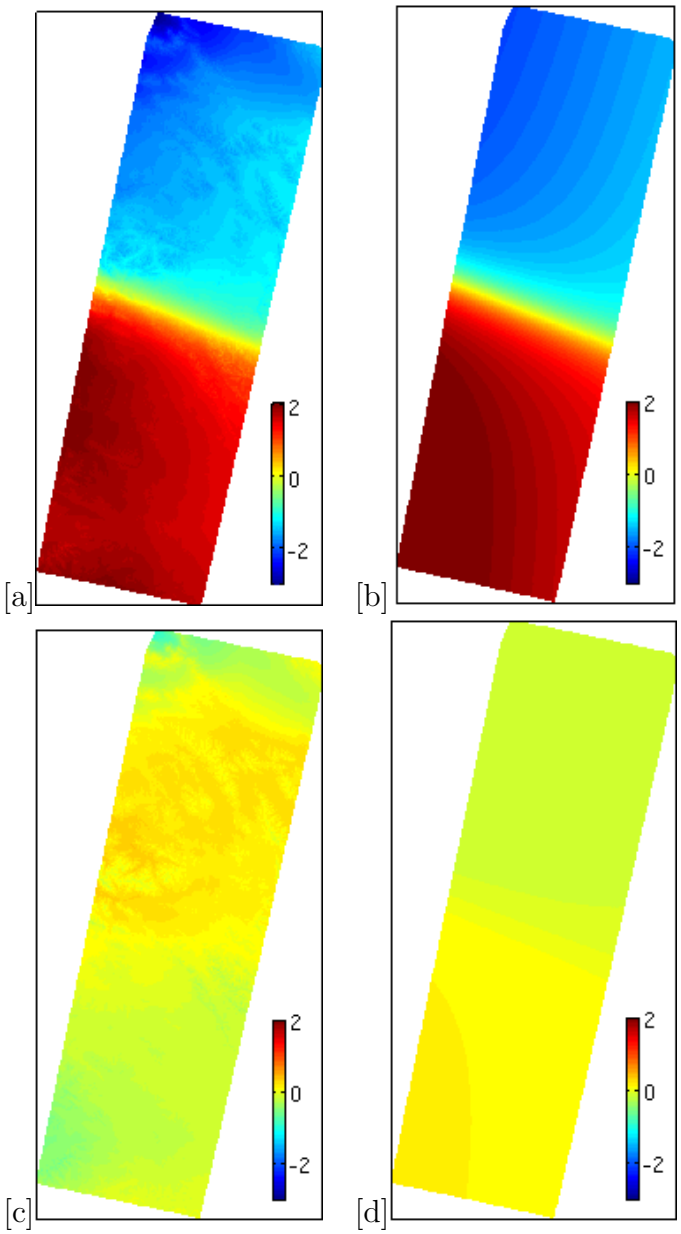

Figure 3.7: (a) Stacked velocity map for synthetic ECMWF data and modelled tectonic signal. (b) Forward modelled deformation using an infinite screw dislocation for a slip rate of 10 mm/yr. (c) Residual between stacked data and input model, equivalent to (d) plus the stacked atmospheric effect (d) residual between the inverted deformation of 9.3 mm/yr and the input deformation of 10 mm/yr.

ing the swath and averaging pixels across the swath, resampled to a grid of 0.0022°.

$$\mathbf{A} = [x_{kl} y_{kl} r_{kl}] \tag{3.10}$$

$$\theta = -\gamma(\pi/180) \tag{3.11}$$

$$\varphi = \begin{pmatrix} \cos(\theta) & -\sin(\theta) & 0 \\ \sin(\theta) & \cos(\theta) & 0 \\ 0 & 0 & 1 \end{pmatrix} \tag{3.12}$$

$$r_{rot} = [\varphi A^T]^T \tag{3.13}$$

where x and y is the pixel location, γ is the fault angle, r is the stacked rate map, r_{rot} is the rotated rate map, and φ is the rotation matrix. r_{rot} was then resampled on a coarser grid and an average profile calculated from the sum of each resampled row, scaled by the number of data points. I calculated the 1σ bounds for the standard error of each track, based on the standard deviation of the data within each profile bin (this will be a maximum estimate for the error in the measurement). Similarly average profiles are shown for the inverted atmospheric component, generally showing this component to be relatively small compared to the tectonic effect.

3.6 Comparison between PS InSAR and DifSAR

Results comparing the two techniques as 2-D images can be seen in figure 3.8 and as average profiles in figure 3.9. A clear tectonic signal consistent with left-lateral strike slip faulting is observed for both techniques across the Kunlun Fault. Inverting the data using an elastic dislocation model gives slip rates of 9.5 ±3.2 mm/yr for PS InSAR and 10.5 ±2.1 mm/yr for standard DifSAR. The data spread is seen to be much larger for PS InSAR (4 mm/yr in satellite LOS) than for DifSAR (2

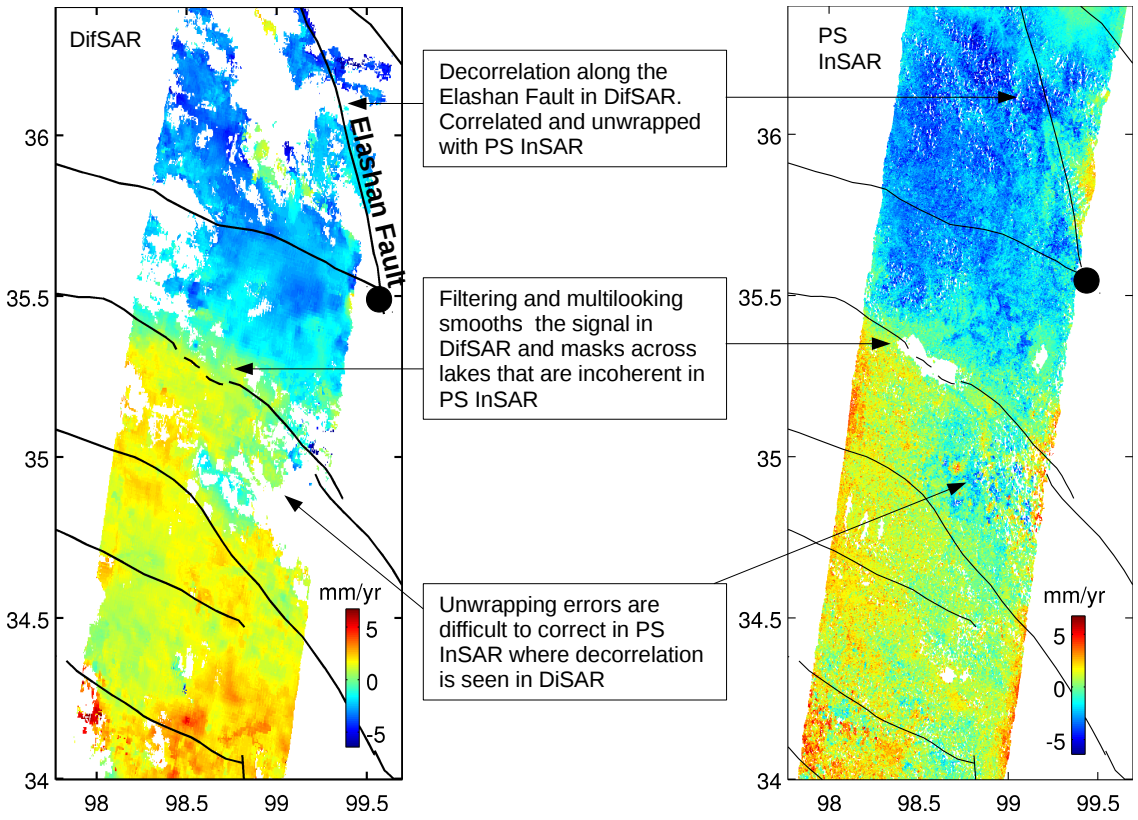

Figure 3.8: Unwrapped LOS velocity maps in mm/yr showing the main differences between data processed using DifSAR (left) in ROI_PAC and data processed using PS InSAR (right) in StAMPS for track 462.

mm/yr). This is in part due to the fact that the DiFSAR data have been filtered and multilooked to 64 looks.

In the north of the processed track, the region covering the Elashan Fault is decorrelated in DifSAR, so large portions of the data are missing in this region. The same is true to the south of the Kunlun Fault, on the western side of the track. We are able to see signal in the PS InSAR data related to the 2000 M_w 6.1 earthquake across the Elashan Fault. We do not see any signal related to this event in the DifSAR due to decorrelation. This event ocurred on the south-east tip of the fault, which is consistent with the signal observed in the PS InSAR.

I have shown that it is possible to measure long wavelength tectonic signals

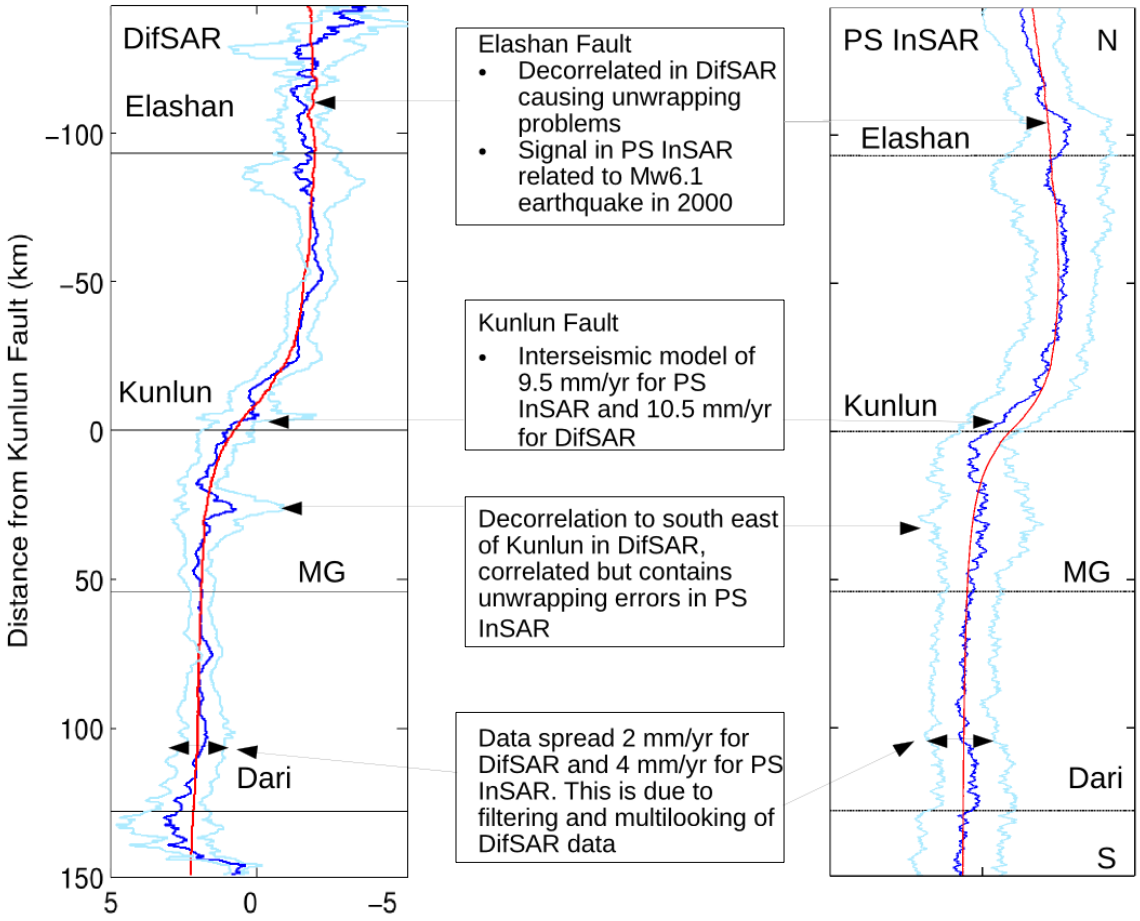

Figure 3.9: Profiles showing the main differences between data processed using PS InSAR in StAMPS (right) and data processed using DifSAR in ROI_PAC (left) for track 462. The average profile for the real data is shown in blue, with 1 sigma error bounds in the average profile shown in light blue, and the best fit inverted models shown in red. The best fit interseismic model across the Kunlun Fault is 10.5 mm/yr for DifSAR and 9.5 mm/yr for PS InSAR.

in natural terrain in a challenging environment using PS InSAR. I have demonstrated that the PS selection algorithm in StAMPS, which assesses the likelihood of a pixel being a PS using a probabilistic approach based on phase stability rather than amplitude, works much better in non-urban environments. The results for PS InSAR are consistent with those shown using more conventional DifSAR. Regions of the data that are decorrelated using DifSAR are also shown to be correlated and successfully unwrapped using PS InSAR. In particular, I have been able to measure

signals associated with the 2000 M_w 6.1 Elashan earthquake using PS InSAR, which were decorrelated in standard DifSAR. Therefore, from this point on I use PS InSAR rather than DifSAR for all measurements to obtain the most coherent signal possible.

3.7 Velocity maps across the Kunlun Fault, Tibet

Table 3.4 below summarises the slip rates, dips, and locking depths for each track. The highest slip rate is seen to be for the Kunlun Fault on track 419 where the fault strike changes direction at the intersection with the Jinguum Fault on the Dongxi Co segment. However, tracks 276, 462 and 419 have consistent slip rates to within error. Figures 3.10 to 3.14 show the measured line of sight velocity, the best fit model, the residuals between the best fit model and data, the scaled atmospheric component, the DEM, and LOS velocity profiles for each of the tracks. Throughout this section, average profiles for models are shown with the real data sampling applied. For synthetic models with uniformly sampled data, see figure 3.6.

3.7.1 The end of the Kokoxili rupture on the Xidatan Dongdatan Segment (t319)

The main section of the Kunlun Fault for this swath covers the Xidatan Dongdatan segment. As demonstrated in figure 3.10, the best fitting model for the Kunlun Pass for this track is for a locking depth of 18 km and dip of 95°. This swath covers the intersection of the Kunlun Pass Fault with the Kunlun Fault and is located 400 km east of the Kokoxili earthquake. The postseismic signal associated with the Kokoxili earthquake is clearly seen in velocity maps until mid-way across the swath. This signal is modelled and removed in chapter 4, using viscoelastic relaxation in a

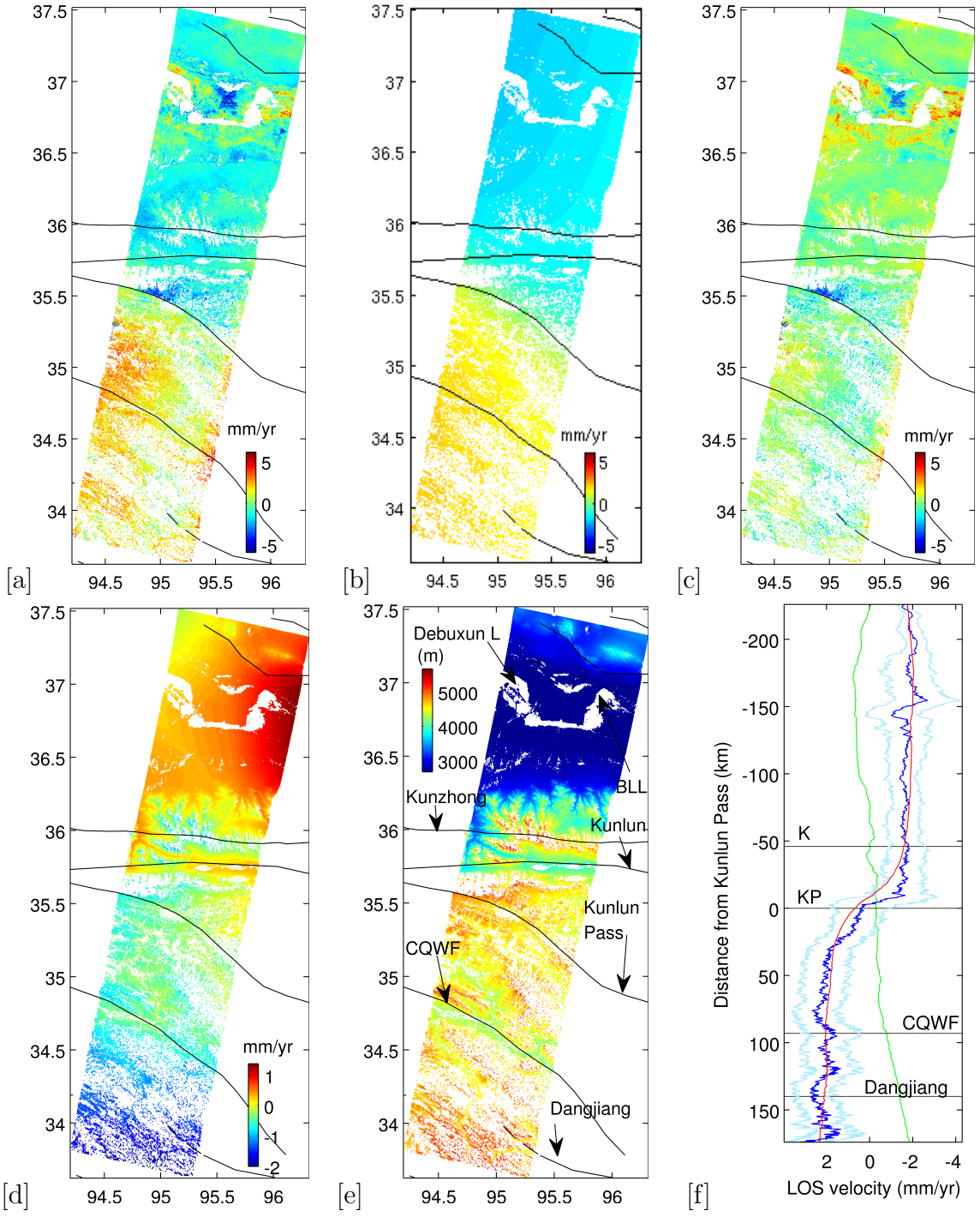

Figure 3.10: Track 319 (a) mean LOS velocity map after removing atmospheric effects, orbital errors, and the postseismic signal from the Kokoxili earthquake, (b) LOS velocity map for the best fit interseismic deformation model of 11.3 mm/yr on the Kunlun, (c) residuals between the mean LOS velocity map given in (a) and the predicted model given in (b), (d) atmospheric model from ECMWF after scaling is applied, (e) DEM, (f) average profile of the LOS velocity as for (a) in bright blue. 1 sigma error bounds in the average profile are shown in light blue, the inverted model is shown in red and atmosphere in green.

Interseismic slip rates measured using PS InSAR

Track	Fault	Slip rate (mm/yr)	Locking depth (km)	Dip (°)
319	Kunlun Pass	11.3 ±2.6	18	95
276	Kunlun	8.7 ±2.7	14	80
276	Kunlun Pass	3.7 ±2.7	18	80
462	Kunlun	9.5 ±3.2	14	80
462	Elashan	4.6 ±3.2	14	95
419	Kunlun	11.1 ±3.3	22	100
419	Dari	0.6 ±3.3	18	90
104	Riyueshan	2.6 ±1.2	14	95
104	Guanggaishan-South Dieshan	0.8 ±1.2	14	85
104	Kunlun	2.4 ±1.2	14	75

Table 3.4: Best-fitting model results for each track, showing slip rate, locking depth and dip across the Kunlun Fault and the Kunlun Pass Fault (where signals are above background noise levels).

Maxwell half-space for an elastic lid of 16 km, and a viscoelastic half space with a viscosity of $2x10^{19}$ Pa s (*Wen et al.*, 2012). Results for interseismic velocities are shown here with the postseismic signal removed.

The best-fitting model for the Kunlun Pass, of 18 km with a dip of 95°, is in agreement with *Wen et al.* (2012) and *Kidd and Molnar* (1988). This model gives a slip rate of 11.3 mm/yr. This slip rate also correlates well with GPS estimates made by *Zhang et al.* (2004) and *Wang et al.* (2001) prior to the earthquake. Residuals between the model and data have similar amplitudes on both the western and eastern sides of the swath. The postseismic signal is greater on the western side of the track than to the east, giving confidence that the postseismic signal has been accurately modelled and removed.

For this track, I masked the most northerly section of the swath when calculating orbital phase errors, to avoid biasing the results with contamination from two events occurring within the ENVISAT data time series. These events, both M 6.3, occurred on the Qaidam-Zongwulongshan Fault in 2008 and 2009, just north of the track location shown on figure 3.2. I constructed velocity maps with and without the two

satellite passes after the M 6.9 Yushu earthquake in 2010, as the southern end of the swath covers the Dangjiang segment of the Yushu-Xianshiuihe Fault. However, I observed no noticeable contamination from this event. Slightly higher amplitudes than the tectonic model to the south instead correlate with atmospheric effects, as shown in figure 3.10 [d]. Given that the edge of the swath is approximately 150 km from the epicentre of the earthquake, we would expect any postseismic signal from this event to be small.

I choose to invert for a single fault positioned according to the Kunlun Pass geometry, as signals associated with other fault locations are below background noise levels. The 1902 M 6.9 earthquake is located on the Kunzhong Fault, just to the north of the Kunlun Fault, according to the USGS catalogue (see figure 3.2). However, a number of studies (*Wen et al.*, 2007) suggest that this earthquake may have occurred on the main segment. No discernible interseismic signal is seen across the Kunzhong Fault above atmospheric noise levels. Whilst a small signal is seen across the Kunlun Fault, it is difficult to distinguish above the atmosphere, and the main interseismic signal is clearly localised across the Kunlun Pass Fault, as shown in figure 3.10 [a] and [f]. Although inversions result in a locking depth of 18 km across the Kunlun Pass Fault the average profile is noticeably sharper than for tracks further east.

The velocity map in figure 3.10 [a] shows a strong signal of ground motion, away from the satellite, at 36.9°N, 95.6°E, near the Beihuo Luxum Lake (BLL) and the Dabuxun Lake. These are in the region of the M 6.9 earthquake, occurring in 1962 (see figure3.2). However, given the time lapsed since this earthquake these signals are more likely to be from loading and unloading associated with changes in water levels, rather than a continuing postseismic signal.

3.7.2 Alan Hu Segment (t276)

For this track, the best fit model for the Kunlun Fault is shown in figure 3.11 [b] and [f] for a slip rate of 8.7 mm/yr, a locking depth of 14 km, and a dip of 80°. The best fit model for the Kunlun Pass Fault has a much lower slip rate of 3.7 mm/yr compared to the previous track. This is for a locking depth of 18 km and a dip of 80°. Whilst at the termination of the Kokoxili rupture (track 319) strain is localised predominantly on the Kunlun Pass Fault, on this track it has stepped back across onto the main strand. This occurs at the tip of the Kunlun Pass Fault (see figure 3.2).

The northern section of this swath is a region of thrust faulting. No clear localised deformation across individual thrust faults is seen in this region, suggesting low individual slip rates and more distributed deformation.

This swath is seen to have high levels of atmospheric noise particularly across the Kunzhong fault. This is clearly seen in the residuals between the best fit model and the data in figure 3.11 [c]. The predicted atmospheric effect has relatively low amplitudes compared to other tracks (see figure 3.11 [d]) in spite of the presence of localised signals in the residuals, suggesting that a global amplitude scaling factor for the ECMWF data is insufficient for this track.

A short distance west of this swath are the M 6.3 2008 and M 6.3 2003 Qaidam earthquakes located on the Da Qaidam Zongwulongshan Fault (DQZF) (*Elliott et al.*, 2011). Similarly, to the south of the swath is the M 6.9 2010 Yushu earthquake. It is difficult to be sure that there is no contamination from these events without extending the swath much further north and south. It is also possible that these events are biasing the orbital estimate and thereby influencing slip rates.

However the total LOS displacement across the entire pass of 4 mm/yr equivalent to 13.2 mm/yr of fault parallel slip over a distance of 225 km is consistent with

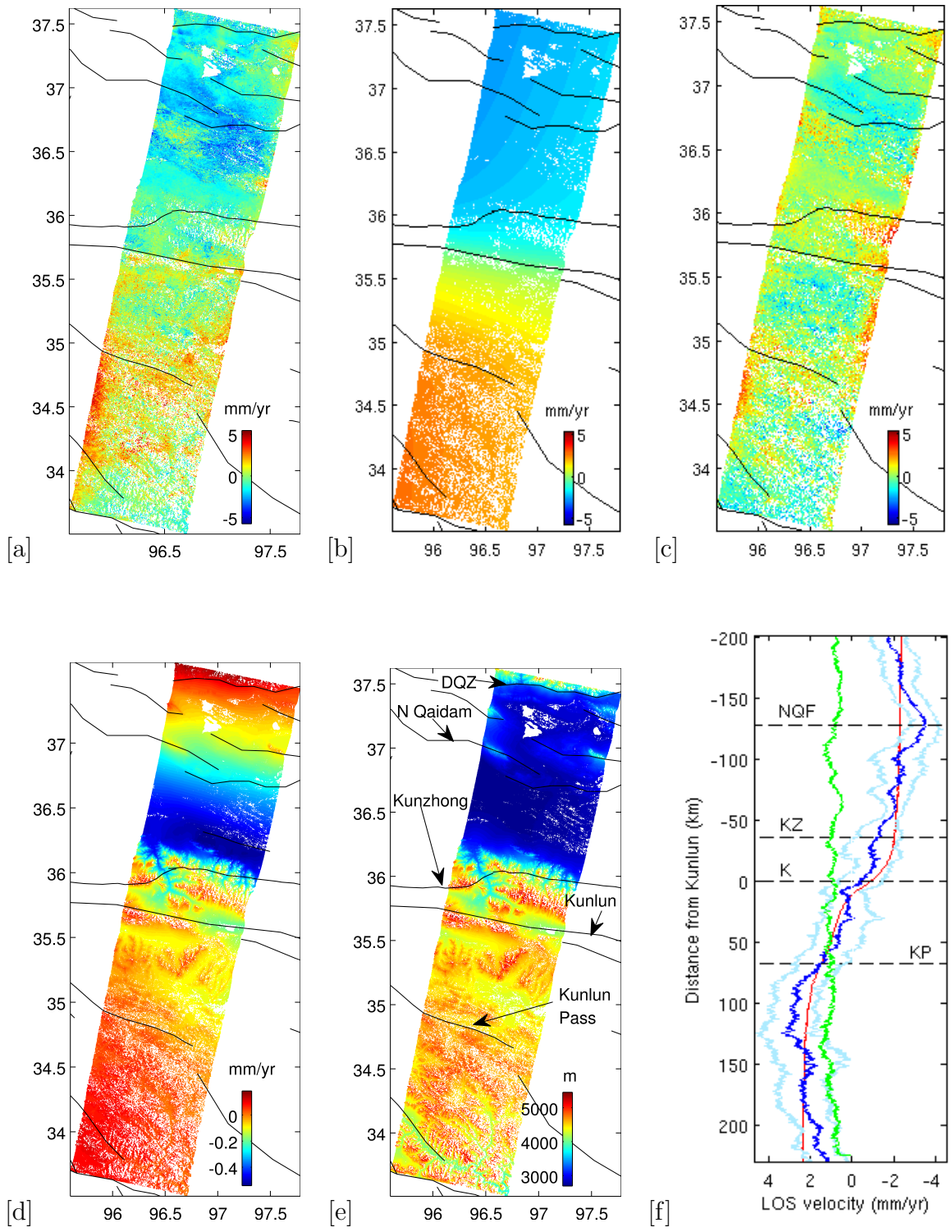

Figure 3.11: For track 276 (a) mean LOS velocity map after removing atmospheric effects and orbital errors, (b) LOS velocity map for the best fit interseismic model of 8.7 mm/yr on the Kunlun and 3.7 mm/yr on the Kunlun Pass, (c) residuals between the mean LOS velocity map and the predicted model, (d) atmospheric model from ECMWF after scaling is applied, (e) DEM, (f) average profile of the LOS velocity in bright blue. 1 sigma error bounds from the average profile are shown in light blue, the inverted model is shown in red and the scaled atmosphere in green.

GPS estimates for the region to within error (*Zhang et al.*, 2004).

3.7.3 Across the pull apart basin on the Dongxi Co Segment (t462)

This track covers the section of the Kunlun Fault that runs through a pull apart basin at the Donggei Cuona Lake and also the right lateral Elashan Fault. I use a single infinite fault to model the interseismic signal across the Kunlun Fault which is fixed to the strand running through this lake. The average profile is seen to be shifted northwards of the position of this strand suggesting a dip towards the north. This is consistent with dips of 65° and 80° previously inferred from seismic profiles in the region (*Wang et al.*, 2011). The best-fitting slip rate for the Kunlun Fault for this track is found to be 9.5 mm/yr, for a locking depth of 14 km and dip of 80°, as shown in figure 3.12 [d].

A region of decorrelation around the intersection of the Qianzhi fault with the Kunlun fault causes localised unwrapping problems. Also, a strong small-scale (∼10 km) localised signal is seen in all interferograms to the south of the Qianzhi Fault possibly due to mining at 98.67°E, 34.98°N (3.12 [a]).

A M 6.1 earthquake occurred on the right-lateral Elashan Fault in 2001. Discontinuities in early interferograms, showing offsets of the fringes across either side of the Elashan Fault and stepping across onto the South Gonge Fault suggest afterslip. However, the earthquake falls between the available data for ERS and ENVISAT, and the earthquake epicentre falls just outside this track. Therefore, for the inversion I mask the section south and east of 99.2°E, 36.1°N until the tip of the Elashan Fault, to reduce contamination from afterslip. Profiles and velocity maps are shown without this masking applied to the real data. Peak-to-peak LOS displacement of

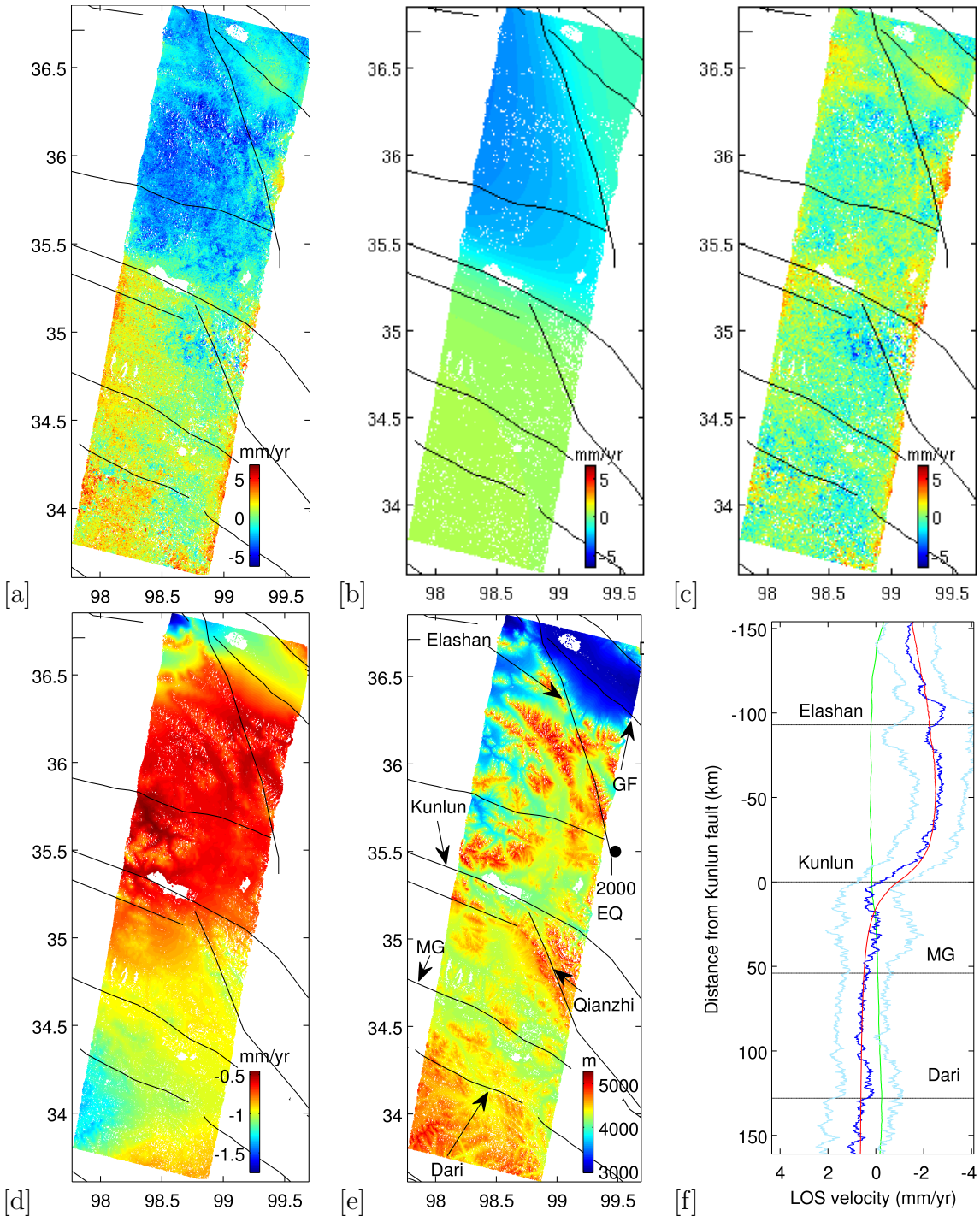

Figure 3.12: Track 462 (a) mean LOS velocity map after removing atmospheric effects and orbital errors, (b) LOS velocity map generated for the modelled interseismic deformation of 9.5 mm/yr across the Kunlun Fault and 4.6 mm/yr across the Elashan Fault, (c) residuals between the mean LOS velocity map and the predicted model, (d) inverted atmosphere, (e) DEM with the Elashan Earthquake indicated, (f) Average profile of the LOS velocity in bright blue. 1 sigma error bounds from the average profile are shown in light blue, the inverted model is shown in red, and atmosphere in green.

-1.3 mm/yr across the Elashan Fault, seen in the average profile for the best fit model in figure 3.12 [f], is consistent with right-lateral motion and is equivalent to -4.6 mm/yr of slip. The main LOS change from the atmospheric effect predicted using ECMWF data is localised across either side of the Gonghe Fault (GF) rather than across the Elashan Fault. The effect across the Elashan is therefore likely to be tectonic rather than atmospheric.

3.7.4 The intersection with the Jinguum Fault on the Maqen Segment (t419)

The last earthquake across this section of the Kunlun Fault is unknown, suggesting a possible seismic gap. Slip rates for this section are estimated by *Van Der Woerd et al.* (2002) to be 12-13 mm/yr and by *Harkins et al.* (2010) to be as low as 6 mm/yr. I obtain a best fitting slip rate of 11.2 mm/yr for a locking depth of 22 km (shown in figure 3.13 [b]). This is the highest locking depth found for the processed data. I attribute this increase in locking depth compared to more westerly sections and the tip of the fault to a localised effect related to thrust faulting across the nearby Jinguum Fault.

It is difficult to separate the slip rates for the Kunlun and the Qianzhi Fault along this section as they are relatively close together, so have overlapping signals that may trade off against one another. I therefore excluded the Qianzhi Fault from the modelling. A region of more distributed deformation could be mistaken for a higher apparent locking depth, as the deeper the locking depth, the higher the liklihood of modelling multiple faults as a single fault. However, no clear localised signal is seen across the Qianzhi Fault in the average profile for this track.

All of the inversions suggest a southwards dip for the Kunlun Fault, with the

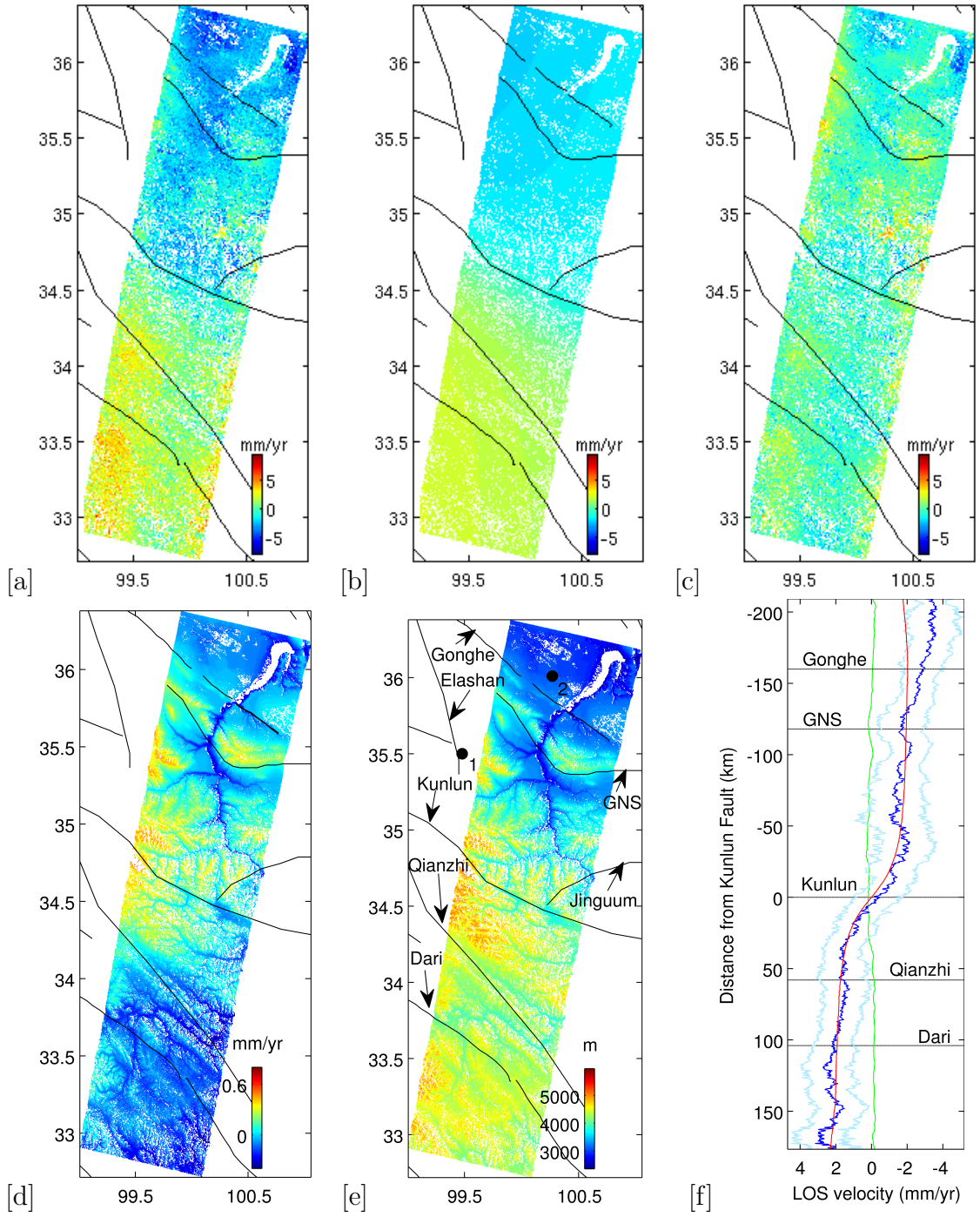

Figure 3.13: For track 419 (a) mean LOS velocity map after removing atmospheric effects and orbital errors (b) LOS velocity map generated for the modelled interseismic deformation of 11.1 mm/yr on the Kunlun Fault, (c) residuals between the mean LOS velocity map and the predicted model, (e) DEM with Elashan Earthquake (1) and Gonghe Earthquake (2) indicated, (f) average profile of the LOS velocity as for (a) in bright blue, 1 sigma error bounds from the average profile are shown in light blue, the inverted model is shown in red and atmosphere in green.

best-fitting model giving a dip of 100°. However, this could trade off against any slip that may be occurring on the Qianzhi Fault. I model using a single infinite fault, so any deviation from the strike of this idealised model will create an apparent offset, which may be fitting as a change in dip, resulting in a potential southwards bias.

This swath covers the section of the Dari Fault that ruptured in the M 6.0 1949 Banama Earthquake and the M 7.5 1947 Dari earthquake. I carried out a seperate inversion that incorporates the Dari Fault as well as the Kunlun Fault, but slip rates across the Dari Fault were found to be below background noise levels at 0.6 mm/yr, and the slip rate on the Kunlun Fault is unchanged.

Patterns of subsidence and uplift localised around the Longyangxia reservoir to the north of the swath may be a postseismic signal resulting from the M 6.5 1990 Gonge earthquake. However, no clear signal is seen across the fault location for the stacked profile in an orientation perpendicular to the Kunlun Fault, and the pattern of deformation could also be explained by changes in water levels in the reservoir. Therefore, no correction has been made. Similarly, afterslip associated with the M 6.1 2000 Elashan earthquake is considered to be small. Furthermore, the only data prior to the earthquake is ERS data; there is a strong atmospheric signal in this region, so no correction has been made for this event either.

3.7.5 The fault tip on the Maqen Segment (t104)

This track covers the tip of the Kunlun Fault, along the Maqu segment, where *Kirby et al.* (2007a) argue that slip rates are much lower than for central sections of the fault. For this track, the best fit model for the Kunlun Fault gives slip of 2.4 mm/yr (see figure 3.14 [b]) with a locking depth of 10 km and a dip of 75°N, which agrees with *Kirby et al.* (2007a) to within error. The dip also agrees with values given by *Lin and Guo* (2008) of 70-85°N.

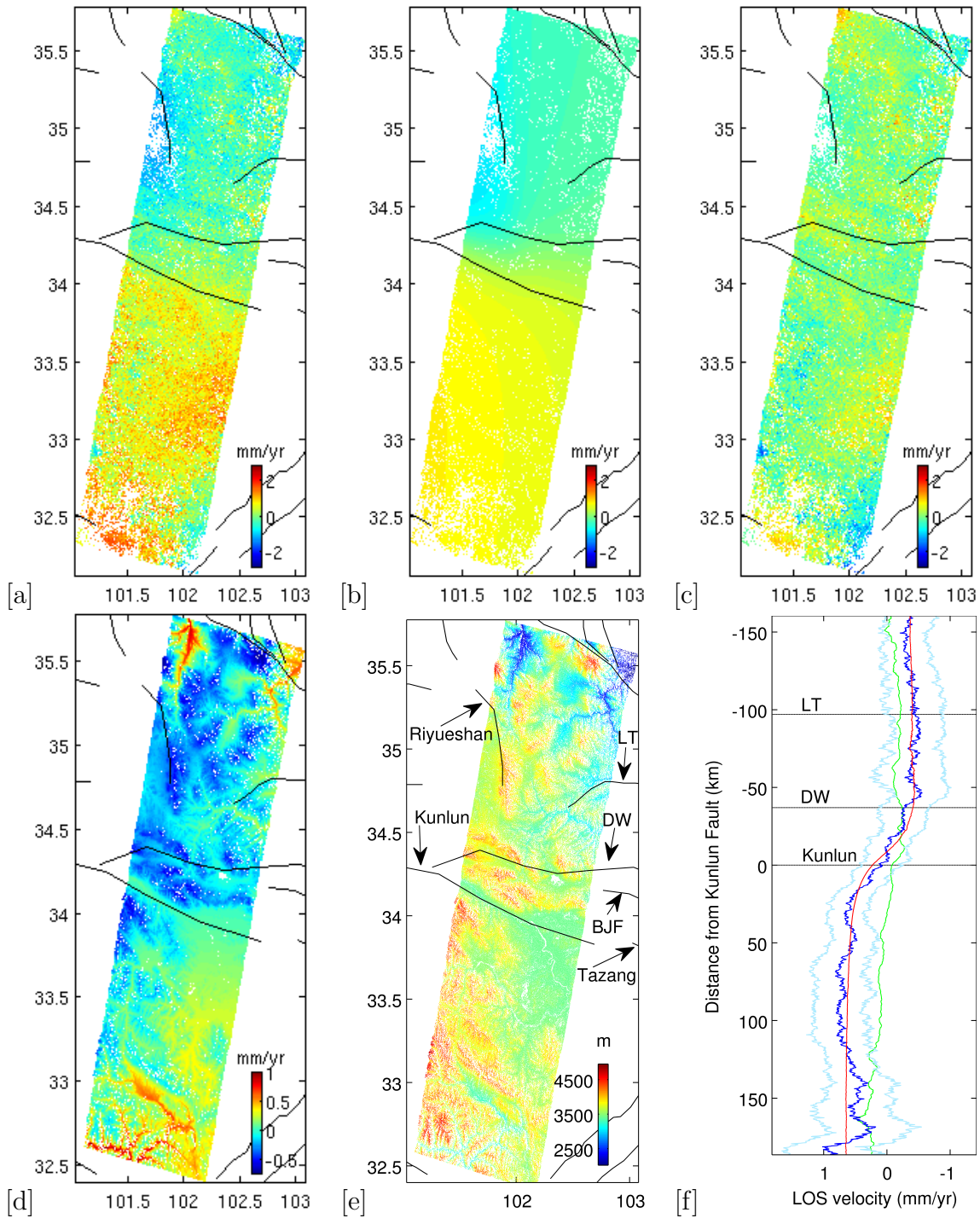

Figure 3.14: Track 104 (a) mean LOS velocity map after removing atmospheric effects and orbital errors (b) LOS velocity map generated for the modelled interseismic deformation for the Kunlun Fault of 2.4 mm/yr, Diebu-Wadu Fault (DW) of 0.8 mm/yr and the Riyueshan Fault of 2.6 mm/yr (c) residuals between the mean LOS velocity map and the predicted model,(d) inverted atmosphere (e) DEM (BJF=Bailong Jiang Fault), (f) Average profile of the LOS velocity in bright blue, 1 sigma error bounds from the average profile are shown in light blue, the inverted model is shown in red and the average profile for the scaled atmosphere in green.

The coherence was found to be much lower than tracks further eastwards due to vegetation. This resulted in the number of selected PS points being very low, leaving large regions of the track with no data and causing significant unwrapping problems. I therefore needed to use a small baseline PS approach. To do this I reduced the data set from 26 scenes to 16 by selecting the most coherent. This resulted in $\sim$ 300,000 PS being selected for the subset compared to $\sim$ 10,000 when using all scenes. The number of PS increases as points with stable phase in most scenes but not all would now be selected as PS (given the same selection criteria (e.g.**phase standard deviation**).

The Riyueshan Fault, like the Elashan Fault, is a right-lateral strike-slip fault with a similar strike direction of $\sim$170°. I modelled the Riyueshan Fault using an infinite right-lateral strike-slip fault, but tapered the signal to zero from the end of the fault over a region of 20 km; otherwise this fault would intersect with the Kunlun Fault. The Riyueshan Fault gave a slip rate of -2.6 mm/yr, much higher than suggested in previous literature. Most previous studies suggest -1 to -2 mm/yr; only a few suggest slip rates as high as -3.6 mm/yr (*Loveless and Meade*, 2011).

After removal of signals associated with the right-lateral Riyueshan Fault, north to south total LOS displacement is 1.2 mm/yr, equivalent to 4.1 mm/yr of left-lateral slip. Including an additional fault to the north of the Kunlun at the position of the Diebu-Wadu Fault (DW) gives a slip rate for the latter of 0.8 mm/yr. Nevertheless, the total north-south LOS displacement is insufficient to account for a larger number of smaller faults. This suggests that distributed deformation can not fully explain the decrease in slip rate towards the fault tip.

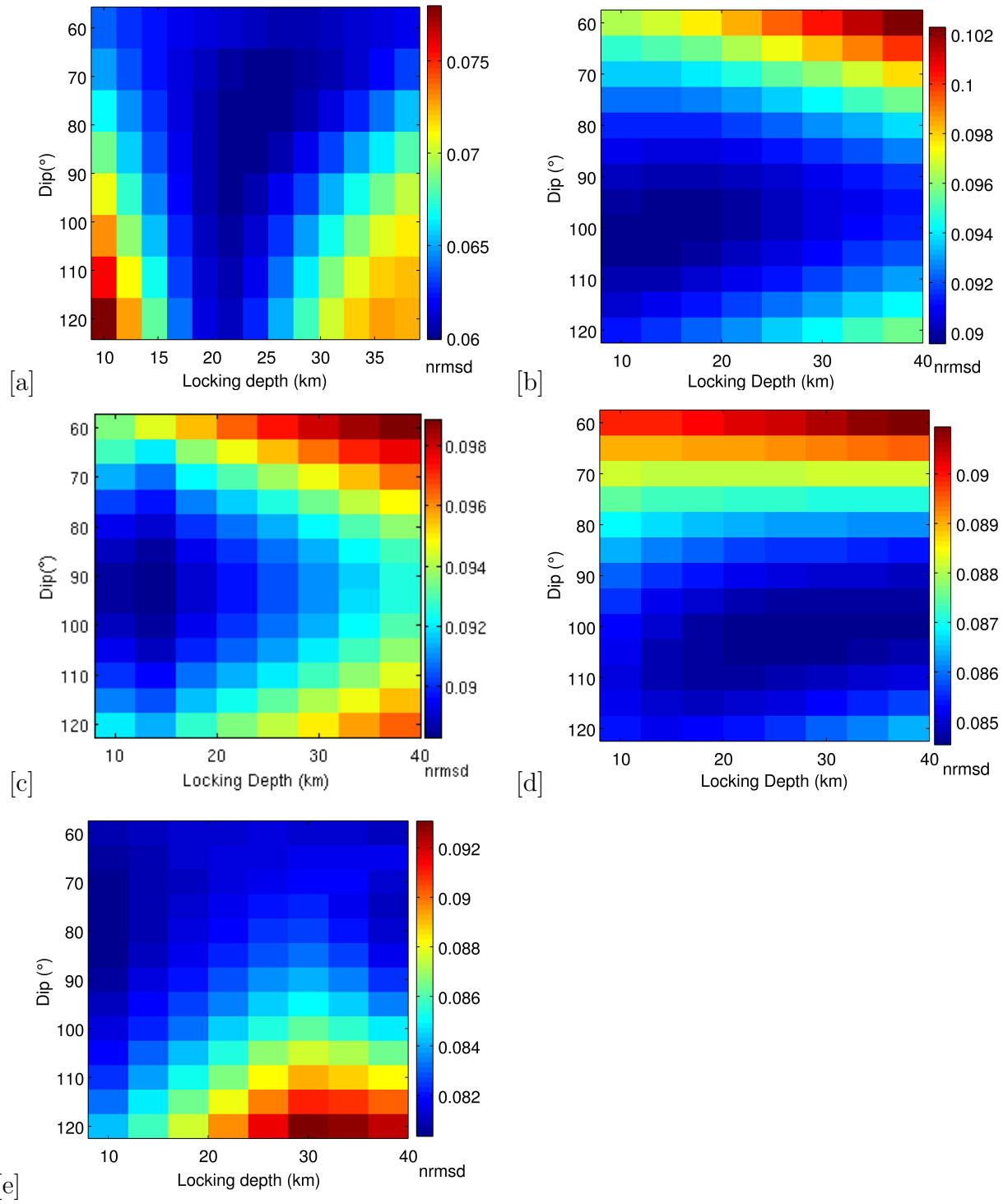

Figure 3.15: NRMSD for a suite of models for a single fault in the location of the Kunlun with variable locking depths and dips for (a) track 319, (b) track 276, (c) track 462, (d) track 419, (e) track 104.

3.7.6 Change in dip and locking depth

The largest trade-off for the fault dip is fault strike rather than locking depth. Although variations in dip are seen from the plots of Normalised Root Mean Squared Difference (NRMSD) between the data and model (see figure 3.15), I attribute these primarily to using a single fault approximation, with the exception of track 462, which covers a pull-apart basin. As a consequence of using a single infinite fault, changes in strike will appear as a shift in the fault position to the north or the south. For example, for track 419, the NRMSD flips between a dip to the north for the east side of the track, and dip to the south for the west side of the track, which reflects a change in strike of 15°. For this track, the NRMSD is shown for a middle section of the data where the strike of the fault is more accurate.

The largest trade-off for locking depth is the number of faults used to model ground motion. In Tibet, there are a significant number of mapped faults in close proximity, with little literature distinguishing those that are active. A larger number of faults with shallow locking depths and overlapping signals could result in a signal that is indistinguishable from a single fault with a much larger locking depth. The trade off with orbital tilt also has a significant impact on estimates of dip and locking depth.

Meyer et al. (1998) and *Tapponnier et al.* (2001) use the Kunlun fault as an example of large scale slip partitioning in the continental crust with normal and shear components occurring on different structures. Conversely, *Van Der Woerd et al.* (2002) characterise segments trending 105-110 °E as being pure left lateral strike slip, whereas those trending 80-105°E as showing oblique normal faulting, and those oriented 110-130°E showing components of thrust faulting.

Based on this analysis the central two tracks, 462 and 419, should have slight thrust components at strikes of 113° and 125°. The western most two tracks, 319

(Kunlun Pass) and 276 should have components of oblique normal with strikes of 95° and 100°. The easternmost track, 104, should be pure strike slip at 110°. For the purposes of this study all models have been conducted using a pure strike slip model. This is shown to give good matches to the data and slight thrusting or normal components would be indistinguishable from pure strike slip above atmospheric noise levels.

3.8 Discussion

The role that the Kunlun Fault plays in regional tectonics is determined by its relative slip rate compared to surrounding fault systems and the variability in slip along its strike. Figure 3.16 shows the best-fit slip rate for each of the tracks for PS InSAR from this study, superimposed on a plot of geological and GPS slip rates from table 3.1. This shows that at the end of the Kokoxili rupture, slip rates are localised on the Kunlun Pass Fault rather than the main strand, with rates of 11.3 mm/yr at Burdan Budai Shan (95°E, figure 3.10). It is this NNE-SSW striking offshoot of the Kunlun that was ruptured by this event, rather than the main fault. Conversely, the next track along (track 276), where there is a break in the mapped fault for the Kunlun Pass, average slip rates reduce to 3.7 mm/yr; most slip is localised back on the main strand, which accommodates 8.7 mm/yr. Then, where the Kunlun is offset by a pull apart basin (track 462), the slip rate returns to levels suggested by average geological slip rates, of 9.5 mm/yr at 98.8°E (figure 3.12).

Slip rates are found to significantly reduce from the centre of track 419 to the centre of track 104, over a region of ∼80 km, by ∼9 mm/yr. Across the intersection with the Jinguum Fault, at ∼100.16°E (track 419), slip rates are observed to be rel-

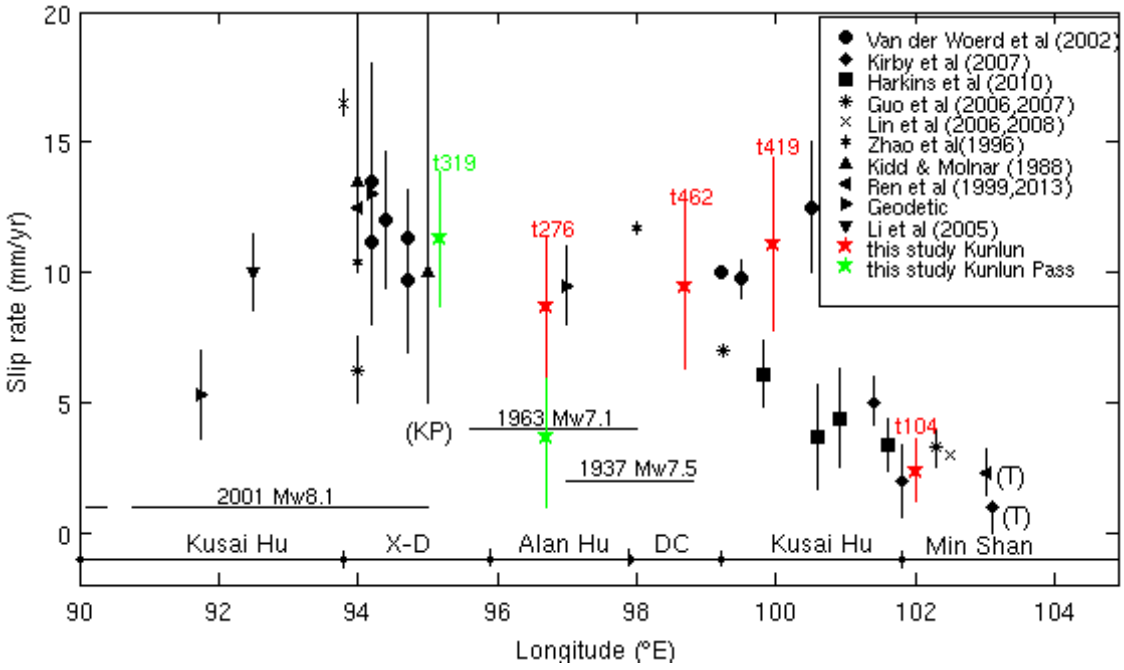

Figure 3.16: Published estimates of the slip rates on the Kunlun fault using dating, geological offsets, and geodetic techniques as per table 3.1. Measurements for offshoots and continuations of the Kunlun Fault are indicated. T and KP stand for Tazang and Kunlun Pass respectively. All other estimates are for the Kunlun. Earthquake rupture extents are shown by horizontal lines, labelled with their magnitudes. Segments are indicated at the bottom of the plot: X-D=Xidatan-Dongdatan, DC=Dongxi Co. The track numbers relating to measurement by this study are shown in red. The error bars are much smaller for track 104 as a small baseline subset was used for this track. This was possible for this track as a larger number of scenes were available with shorter perpendicular baselines, including a reasonable selection with larger temporal baselines with respect to the master.

atively high at 11.1 mm/yr. This is in agreement with *Van Der Woerd et al.* (2002), who estimate slip of 12.5 mm/yr, but significantly higher than measurements made by *Harkins et al.* (2010), of ∼4 mm/yr. Slip rates then reduce to 2.4 mm/yr towards the tip of the fault, at 102.1°E (track 104, figure 3.14), in agreement with *Harkins et al.* (2010) and *Kirby et al.* (2007a). Significant distribution of slip can not be discerned across multiple left-lateral faults running parallel to the Kunlun Fault to the north and south on track 104.

The right-lateral Elashan Fault has a higher than expected slip rate of 4.6

mm/yr. The majority of literature to date has suggested much lower slip rates; e.g., *Loveless and Meade* (2011) estimated right-lateral slip of 1.0 ± 0.8 mm/yr (north) to 4.2 ± 0.4 mm/yr (south). The Riyueshan fault has a slip rate of 2.6 mm/yr. This is in agreement with most studies which have estimated slip rates under 3 mm/yr. However, *Loveless and Meade* (2011) estimated 0.9 ± 0.8 mm/yr of left-lateral slip on the northern segment and 5.3 ± 0.5 mm/yr of right-lateral slip on the southernmost segment at latitudes south of 35.5°N. These results suggest that these right-lateral faults play a greater role in the transfer of stress than previously thought.

3.8.1 Slip rate variability

Harkins et al. (2010) summarise the four key explanations of a systematic decrease in slip rate along the Eastern Kunlun fault: (i) the transfer of left-lateral displacement from the central Kunlun Fault to adjacent faults, (ii) the absorption of deformation by crustal thickening (as explained by *England and Houseman* (1986)), (iii) continuing eastward propagation of a relatively young fault (*Cowie and Scholz*, 1992), (iv) and absorption of slip by interaction with regional clockwise rotation or distributed shear.

A number of authors have debated whether at the end of the Kunlun Fault strain is transferred beyond the plateau, or absorbed within it (with more continuous rather than localised deformation). Displacement along the Kunlun Fault could either be transferred by a series of strike-slip faults to shortening structures adjacent to and north of the Sichuan Basin in the Qinling Shan and the Longmenshan thrust belt, or to thrust faulting further northwards in the Riyue Shan, Laji Shan, Qinhai Nan Shan and Gonge Nan Shan.

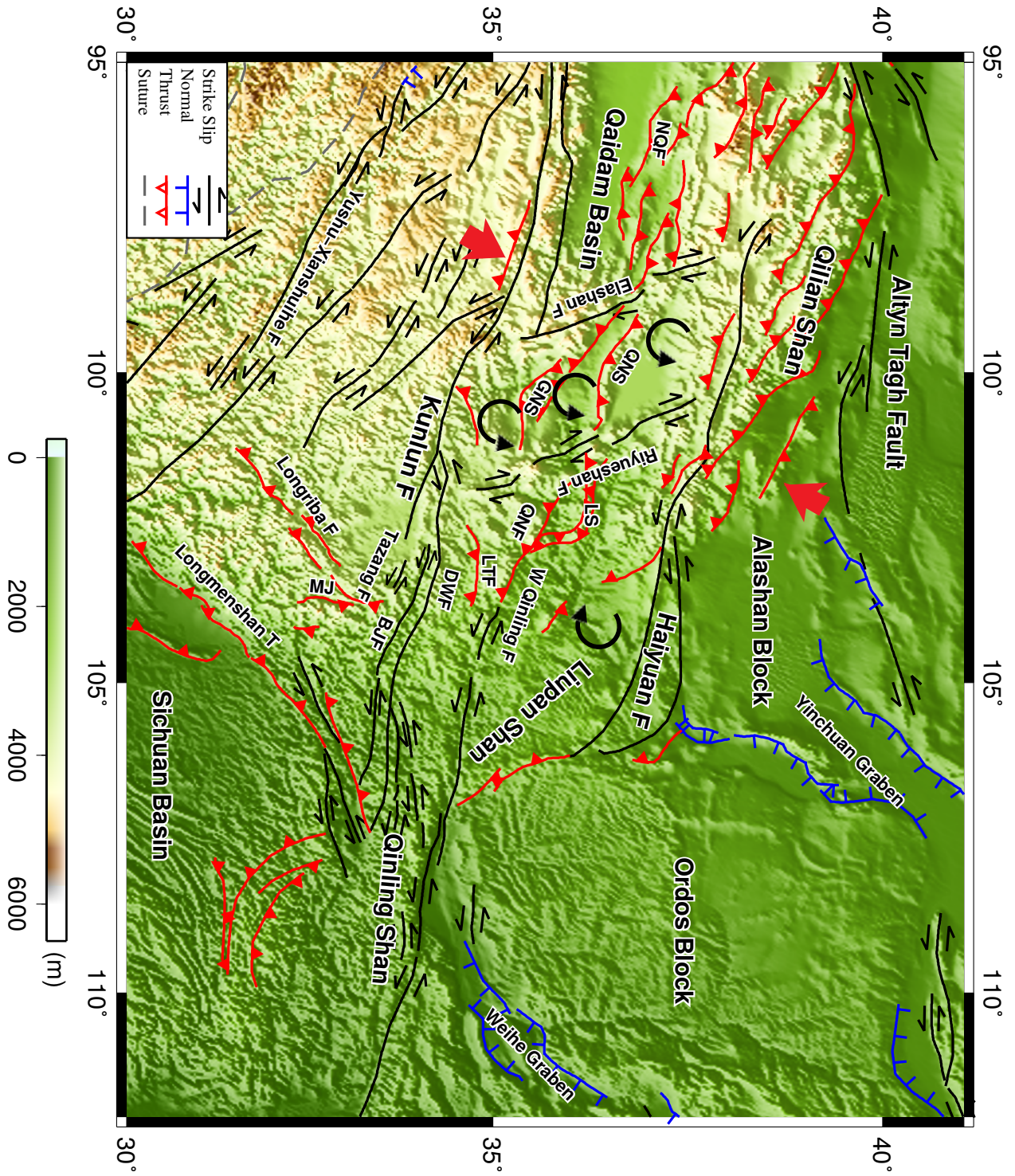

Figure 3.17: Map showing the accommodation of shear along the right-lateral Riyueshan and Elashan faults. NE-SW shortening, results in right-lateral transpression and anticlockwise rotation of crust between the Elashan and Riyueshan faults. These rotations induce left-lateral shear on the Haiyuan fault, and ultimately transfer slip on to this fault to the East. I argue that the majority of slip is transferred to the Haiyuan Fault and a compressional region north of the Kunlun in the Riyue Shan, Laji Shan, Qinhai Nan Shan and Gonge Nan Shan, via the Elashan and Riyueshan Faults. A small proportion of slip may also be transferred via the Diebu-Wadu, Bailong Jiang and Tazang faults to shortening structures adjacent to and north of the Sichuan Basin in the Qinling Shan and Longmenshan Thrust belt. NQF=North Qaidam Fault, QNS=Qinghai Nan Shan, GNS=Gonge Nan Shan, LTF=Lintan-Tangchang Fault, DWF= Diebu-Wadu Fault, BJF=Bailong Jiang Fault, MJ =Min Jiang Fault, LS=Laji Shan.

An example of the former scenario is discussed by *Van Der Woerd et al.* (2002), who argue that the left-lateral strike slip Tazang Fault could be viewed as a continuation of the Kunlun Fault to the east, in a similar way that the Manyi fault is viewed as its continuation to the west. However, *Harkins et al.* (2010) argue that no geomorphic expression of these structures is seen until 100 km east of the tip of the Kunlun fault, and that slip rates along the West Qinling Fault system are as low as 2-3 mm/yr (*Yuan et al.*, 2007). Furthermore, *Ren et al.* (2013) cite Kirby as suggesting that slip rates across the Bailong Jiang are insignificant. Slip rates across the Diebu Wadu Fault in my data are seen to be as low as 0.6 mm/yr and slip rates on the Longmenshan Fault are $\sim$ 3 mm/yr (*Ren et al.*, 2013). This suggests that for more distributed deformation to explain the reduction in slip rates, it would also need to be accommodated further northwards.

As for the latter scenario, *Burchfiel et al.* (1989), *Tapponnier et al.* (1990), and *Zhang et al.* (2004) argue that the end of the Haiyuan and Altyn Tagh faults mark the transfer of deformation into areas dominated by thrust faulting. They observe that the Altyn Tagh and Haiyuan separate an actively deforming compressional region (the Qilian Shan thrust system and the Liupin Shan thrust system, respectively) from an undeforming zone (the Tarim basin, and the Alashan and Ordos Block). Thrust faults located to the north of the Kunlun could similarly fulfil this role.

Harkins et al. (2010) note that the termination of faults further south of the Kunlun at similar longitudes supports the suggestion of *England and Molnar* (1990) that the reduction in slip rates towards the fault tip signifies the end of a broad shear zone (iv). As explained in the results section (for track 104) the total north-south LOS displacement is insufficient to account for a larger number of smaller faults. This suggests that distributed deformation can not fully account for the decrease

in slip rate towards the fault tip. Furthermore, in order for such simple clockwise rotation to fully explain slip rate variability at the tip *Harkins et al.* (2010) argue that spatial variations in regional strain patterns would drive fault slip. *Kirby et al.* (2007a) suggest that the role of a series of NNE-SSW striking right-lateral faults between the Qaidam Basin and the Kunlun Fault, including the Elashan and Riyueshan faults, may be a key component of this mechanism.

Reduction in slip rates along the Eastern Kunlun Fault towards the tip of the fault, coupled with higher than expected slip on the Elashan Fault, and significant slip on the Riyueshan Fault, suggest that slip is primarily transferred to a region of shortening to the north of the Kunlun. This results in right-lateral transpression and anticlockwise rotation of crust between the Elashan and Riyueshan faults. These rotations in turn induce left-lateral shear on the Haiyuan Fault, and ultimately the transfer of slip on to this fault to the east. This is supported by slip rates of up to 8 mm/yr (*Cavalié et al.*, 2008) on the Haiyuan Fault. This mechanism is shown in the cartographical representation in figure 3.17. Modest slip rates on strike slip faults to the south connecting the Kunlun and Qinling coupled with transferral of slip northwards suggest a wide transfer zone.

Similar mechanisms are seen in the Mongolian Altai (figure 3.18), as discussed by *Nissen* (2008), and the Gowk fault system in Iran (figure 3.19), as shown by *Funning* (2005). In the case of Mongolia the termination of the Bulnay could mark the transfer of deformation further southwards with slip transferring to the Gobi Tien Shan. Iran is a much more complicated system with no clear transferral of slip between 2 key strike slip faults.

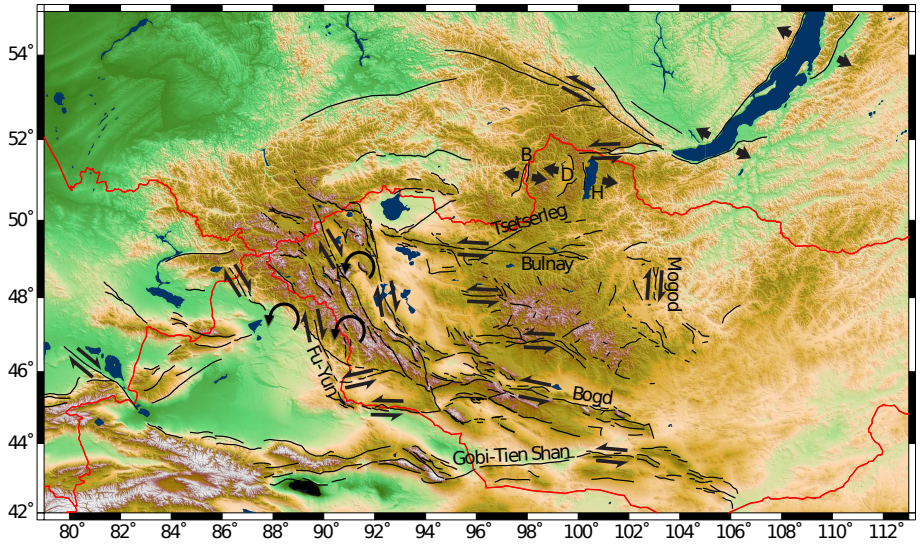

Figure 3.18: Map showing the major faults in Mongolia. India-Asia shortening results in right-lateral transpression with anticlockwise rotation of the crust in between the right-lateral faults. This results in left-lateral shear on faults to the east of the Altai. Adapted from *Nissen* (2008).

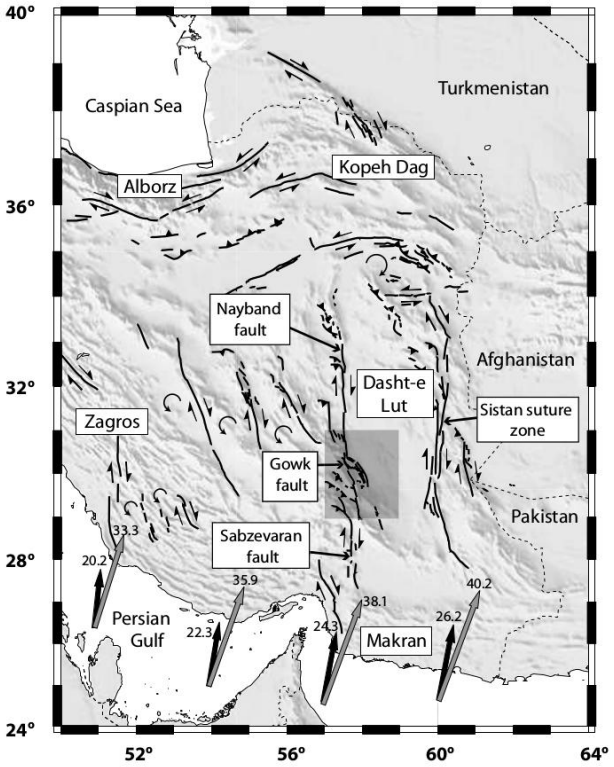

Figure 3.19: Map showing the major faults in Iran, with anticlockwise rotation seen along the Gowk fault system. Adapted from *Funning* (2005).

Chapter 4

Postseismic modelling of the Kokoxili earthquake

In this chapter, I use PS InSAR to measure surface displacements for the M_w 7.8 2001 Kokoxili earthquake, to see whether the postseismic signal towards the eastern end of the rupture is localised across: the Kunlun Fault, the Kunlun Pass Fault or a combination of both. I show whether the deformation after the earthquake is due to one or more postseismic mechanisms. To date both afterslip and viscoelastic relaxation have been proposed as plausible mechanisms (*Wen et al.*, 2012).

Previous InSAR studies all use standard InSAR rather than PS InSAR and focus on the main fault strand over the earthquakes epicentre. Here, InSAR data is incoherent along the fault and there is very little data covering the peaks of the postseismic signal. By using PS InSAR on a track at the end of the Kokoxili rupture, 380 km from the epicentre location, I show good coherence across the entire track with data connecting both sides of the fault and clearly defined peaks.

In this chapter I model afterslip using the hot-friction approximation (*Linker and Rice*, 1997) of the rate and state frictional laws (described in section 4.1.2) to create

a series of models with various preseismic slip rates and frictional parameters. I then perform a parameter space search to find the best fitting models for ENVISAT data from track 319. The data used here was processed, and the best fit interseismic model for a slip rate of 11.3 mm/yr was removed as described in chapter 3. I create here a series of viscoelastic relaxation models with a Maxwell rheology using: PSGRN to prepare the green's functions that describe the model response; and PSCMP to calculate the surface displacements, using a discrete number of rectangular fault planes (*Wang et al.*, 2006). I then compare my results for rate and state friction models for the Kokoxili earthquake to those for the 1997 M 7.6 Manyi earthquake, taken from *Bell* (2013).

4.1 Mechanisms of postseimic relaxation

Some of the earliest studies to observe continuing displacements immediately after an earthquake, with rates that decay over time, came from triangulation data collected after the 1906 San Francisco earthquake (*Segall*, 2010). *Thatcher* (1975) demonstrated that strain rates across the San Andreas Fault following this event were up to four times average rates in the region; with rates in the 30 years following the earthquake of 1.2×10^{-6} yr^{-1} and decreasing back to rates of 0.3×10^{-6} yr^{-1} thereafter. Since these initial observations, it has become widely accepted that large earthquakes are followed by transient postseismic deformation that occurs in response to stress variations resulting from coseismic stress changes.

The physical mechanisms behind these postseismic signals have primarily been modelled using: viscoelastic relaxation, transient fault slip within the rupture zone (or below it on the downdip extension of the fault) known as afterslip and poroelastic rebound (*Peltzer et al.*, 1996; *Johnson*, 2004; *Perfettini et al.*, 2005). As we

are looking at motion occurring several years after the earthquake (from 2003-2010), with a long wavelength signal (based on the study by *Ryder et al.* (2011) over the epicentre), poroelastic rebound is an unlikely mechanism. Poroelastic rebound will also have an opposite sign so if you can fit the real data with viscoelastic relaxation, poroelastic rebound is unlikely so is not considered. In the case of the Kokoxili earthquake the most likely mechanisms are therefore viscoelastic relaxation and afterslip so for the purposes of this thesis I will limit myself to exploring these two.

Models involving afterslip assume that stresses are released by sliding on a deep fault plane (or on the fault itself) whilst models of viscoelastic relaxation assume strain is distributed through a much larger volume. In spite of this distinction, *Barker* (1976) demonstrated that afterslip and distributed viscoelastic flow can be difficult to distinguish based on surface observations alone, as deformation at depth is filtered though an elastic lid which removes longer wavelength signals. Furthermore, *Savage et al.* (2005) demonstrated that they are mathematically equivalent and previous studies on the Kokoxili earthquake have found both models to fit the data similarly well (*Wen et al.*, 2012).

However these studies were done using kinematic afterslip inversion based on the peak to trough distance of InSAR data (on the order of the fault locking depth of 20-25 km) (*Wen et al.*, 2012). As a consequence of the non uniqueness of the problem without applying further constraints we can trade off the depth at which afterslip occurs against the wavelength of the output model. This raises the question of whether kinematic afterslip models are a realistic representation of deformation at depth.

I instead use a dynamical approach where the laws of rate and state friction are used to drive afterslip, starting with the known coseismic stress field. The depth at which afterslip occurs and consequently the resulting wavelength of the model

are driven by the dynamic equations. This limits our model parameter space to physically meaningful values that may help us to distinguish between afterslip and viscoelastic relaxation as plausible mechanisms.

4.1.1 Viscoelastic models

Stress exerted on a viscoelastic medium will have a time dependent relaxation. On seismic timescales the lithosphere behaves elastically, but over long enough time scales it will exhibit viscous flow in order to release stress. The timescale over which the medium relaxes depends on the viscosity and rigidity of the medium.

Viscoelastic models are thought of as combinations of elastic elements, represented by springs, and viscous elements, represented by dashpots. Springs obey Hooke's law and strain instantaneously on the application of stress and any deformation is recovered on the removal of the stress. The behaviour of a spring is represented by:

$$\sigma = \mu\epsilon \tag{4.1}$$

where σ is the stress, μ is the rigidity, and ϵ is the strain.

Conversely, a viscous medium subjected to stress will not strain instantaneously. Instead, strain will build up on a timescale dependent on the viscosity. Any deformation is permanent: once the stress is removed, strain is not recovered. The behaviour of a dashpot is represented by:

$$\sigma = \eta\dot{\epsilon} \tag{4.2}$$

where η is the viscosity, and $\dot{\epsilon}$ is the strain rate.

Lab experiments under pressures and temperatures equivalent to the upper mantle and lower crust demonstrate that rocks may deform by dislocation creep according to a Power Law rheology:

$$\dot{\epsilon} = A\sigma^n e^{\left(\frac{-Q}{RT}\right)} \tag{4.3}$$

where $\dot{\epsilon}$ is the strain rate, σ the stress, n the empirical stress (power law) exponent, A a pre-exponential factor (which depends on properties such as the grain size and activity of water), Q the activation energy, R the universal gas constant, and T the temperature. As models using Power law rheologies are still under development, and we cannot apply layered structures with nonlinear rheologies, it is more common to use rheologies where a linear relationship is applied between stress, strain and their derivatives:

$$a_0\sigma + a_1\dot{\sigma} = b_0\epsilon + b_1\dot{\epsilon} \tag{4.4}$$

We use a combination of springs and dashpots connected in series and parallel in order to represent different rheologies and to test which formulations best represent lithospheric deformation. Some of the more commonly used combinations and their equations of motion are illustrated in figure 4.1. The simplest of these models is a spring and dashpot connected in series, referred to as the Maxwell rheology, and a dashpot and spring connected in parallel, referred to as the Kelvin rheology.

In the case of the Maxwell rheology the total strain rate is the sum of the strain rate in the spring and the dashpot. Therefore, parameters a_0, a_1, b_0 and b_1 in equation 4.4 are set to give:

$$\dot{\epsilon} = \frac{\dot{\sigma}}{\mu} + \frac{\sigma}{\eta} \tag{4.5}$$

where the stress is the same in each element. A Maxwell body exhibits an instantaneous elastic strain, where the time-dependent terms dominate and linear steady

state deformation follows. If the strain remains constant, that is $\dot{\epsilon} = 0$, we can integrate the Maxwell equation, 4.5, with respect to time from 0 to t, to show that the stress will decrease exponentially as:

$$\sigma = \sigma_0 e^{\left(-\frac{\mu}{\eta}\right)t} \tag{4.6}$$

The timescale over which this relaxation occurs is referred to as the Maxwell time, $\tau = \eta/\mu$.

For a Kelvin model the stress is the sum of the stress in the spring and the dashpot, whereas the strain is the same in each element. So equation 4.4 gives:

$$\sigma = \eta\dot{\epsilon} + \mu\epsilon \tag{4.7}$$

A Kelvin body exhibits an initial time dependent strain followed by a recovery in strain on the removal of stress. We know that the earth must initally behave elastically as seismic waves propagate through the earth elastically. The Kelvin model of rheology is therefore an unrealistic approximation of the behaviour of the earth. For this reason we choose not to use a Kelvin or Standard Linear Solid to model the postseismic deformation.

A more complicated linear rheology, the Burgers rheology, combining a Maxwell and Kelvin element in series, is also commonly used. This rheology exhibits an instantaneous elastic behaviour followed by transient creep and then a long-term viscous behaviour. This model is a realistic approximation of the Earth's behaviour and has been empirically shown to give good matches to observed postseismic deformation. However, *Ryder et al.* (2011) showed that the surface deformation for the Maxwell and Burgers rheologies give similar spatial patterns of postseismic deformation for the Kokoxili earthquake. There is a lack of InSAR observations in the

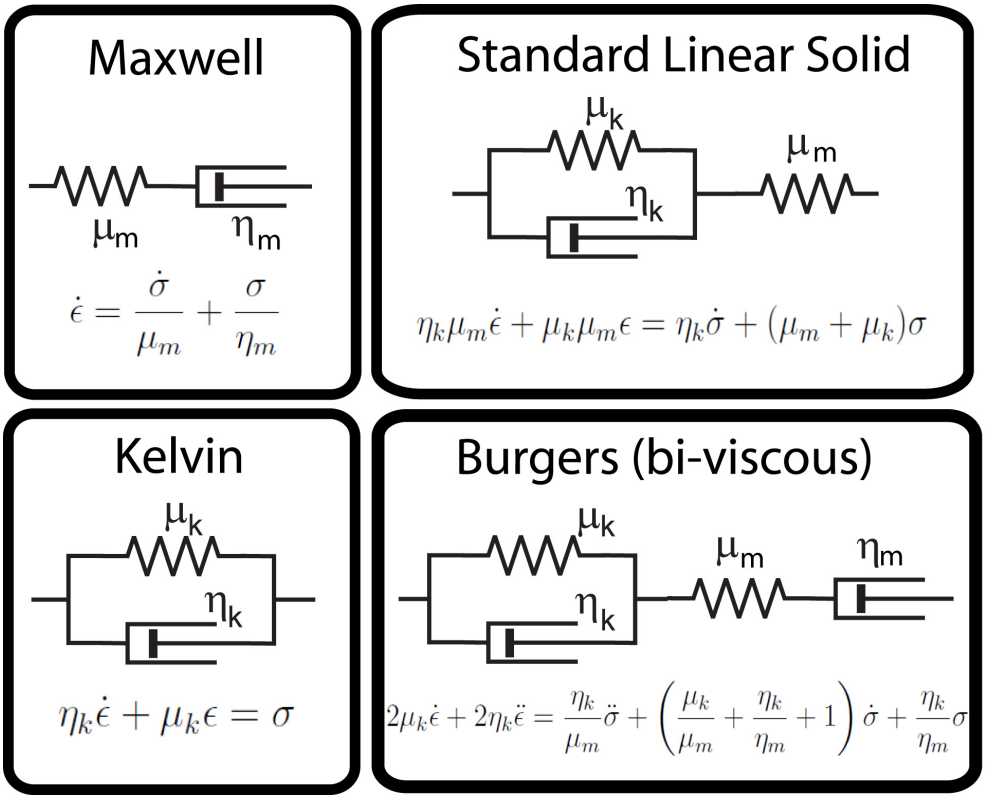

Figure 4.1: Simple mechanical analogues to linear rheologies referred to in the text. An elastic element is represented by a spring and a viscous element is represented by a dashpot. μ is the rigidity, η is the viscosity and, subscripts m and k refer to the parameters for the Maxwell and Kelvin elements respectively, and ϵ is the strain. The equations show the constitutive equation for that rheology as described in the text. Reproduced from *Bell* (2013).

early postseismic phase and atmospheric noise levels are relatively high making it difficult to generate a time series. We therefore use a Maxwell rheology to model viscoelastic postseismic deformation rather than a Burgers rheology.

4.1.2 Rate and state friction models

From our observations of faulting we observe that a range of frictional properties occur in the earth. The end members are velocity weakening behaviour, which results in earthquakes, and velocity strengthening behaviour, which results in stable sliding or creep (*Scholz*, 2002). *Brace and Byerlee* (1970) observed from a series of

rock sliding experiments that when a force is applied to a rock, periods of no motion were followed by episodes of slip. They referred to this behaviour as stick slip.

In order to describe regular stick slip behaviour of rocks in both velocity weakening and velocity strengthening zones, empirical relationships were developed from rock mechanics experiments. The most widely applied of these laws is currently the Dieterich-Ruina law (*Dieterich*, 1981; *Ruina*, 1983) where the coefficient of friction, μ, is described in terms of the instantaneous sliding velocity, V, and a state variable which characterises the state of the sliding surfaces, θ:

$$\mu\left(V,\theta\right)=\mu_0+a\ ln\left(\frac{V}{V_0}\right)+b\ ln\left(\frac{V_0\theta}{D_c}\right) \tag{4.8}$$

The state variable evolves with time or slip according to one of two possible state evolution laws, either the aging (slowness) law:

$$\dot{\theta}=1-\frac{V\theta}{D_c} \tag{4.9}$$

or the slip law, respectively:

$$\dot{\theta}=-\frac{V\theta}{D_c}ln\left(\frac{V\theta}{D_c}\right) \tag{4.10}$$

where D_c is the slip required for asperities to move past each other. *Dieterich* (1981) associated the state variable with the average contact time of asperities. This is proportional to the average asperity size and inversely proportional to the slip speed, for surfaces sliding at a constant rate. Other parameters that may be used to characterise the state of the surface include the grain size or porosity of fault gouge. Although the two state evolution laws above are mechnically different they result in the same laboratory observations. I therefore follow the example of *Bell*

(2013) and use the aging law for dynamic evolution.

By relating the shear stress change due to an earthquake, τ, to the normal stress σ_n across the fault, on which it ocurred, we can model frictionally controlled afterslip using such laws of rate and state friction as shown below:

$$\tau(t) = \sigma_n \left(\mu_0 + a \ln \left(\frac{V(t)}{V_0} \right) + b \ln \left(\frac{\theta(t) V_0}{D_c} \right) \right) \tag{4.11}$$

where the term in brackets is the frictional term, μ_0 the steady state friction at a reference velocity V_0 and a and b are material properties of the frictional surface.

The rate and state friction law predicts that slip can either be stable or unstable. The behaviour of the frictional system to an increase and subsequent decrease in velocity is represented in the figure 4.2 taken from *Scholz* (2002). Here, an increase in initial velocity results in an instantaneous increase in friction by an amount, $a \ln \left(\frac{V_1}{V_0} \right)$, which then returns to a steady state value, $(a - b) \ln \left(\frac{V_0}{V_1} \right)$. The parameters a and b control the velocity dependence of the frictional surface and relate to the resistance to an increase in velocity, and the healing term, respectively.

Velocity strengthening is stable and occurs for $\Delta\mu_{ss} \geq 0$. In this instance friction increases as slip velocity increases and retards slip acceleration. Velocity weakening is unstable and occurs for $\Delta\mu_{ss} < 0$, where normal stress is high. In this case, friction decreases as slip velocity increases and causes runaway acceleration of slip, resulting in an earthquake. Initially the coefficient of friction decreases faster than the elastic stresses resulting in run away slip. The runaway slip stops quickly because the stored elastic strain energy is depleted quickly. For a conditionally stable scenario where $\Delta\mu_{ss} < 0$, and normal stress is high, but elastic stresses decrease faster than the coefficient of friction, the system slips stably.

A more realistic picture of the behaviour of the Earth involves dividing up the

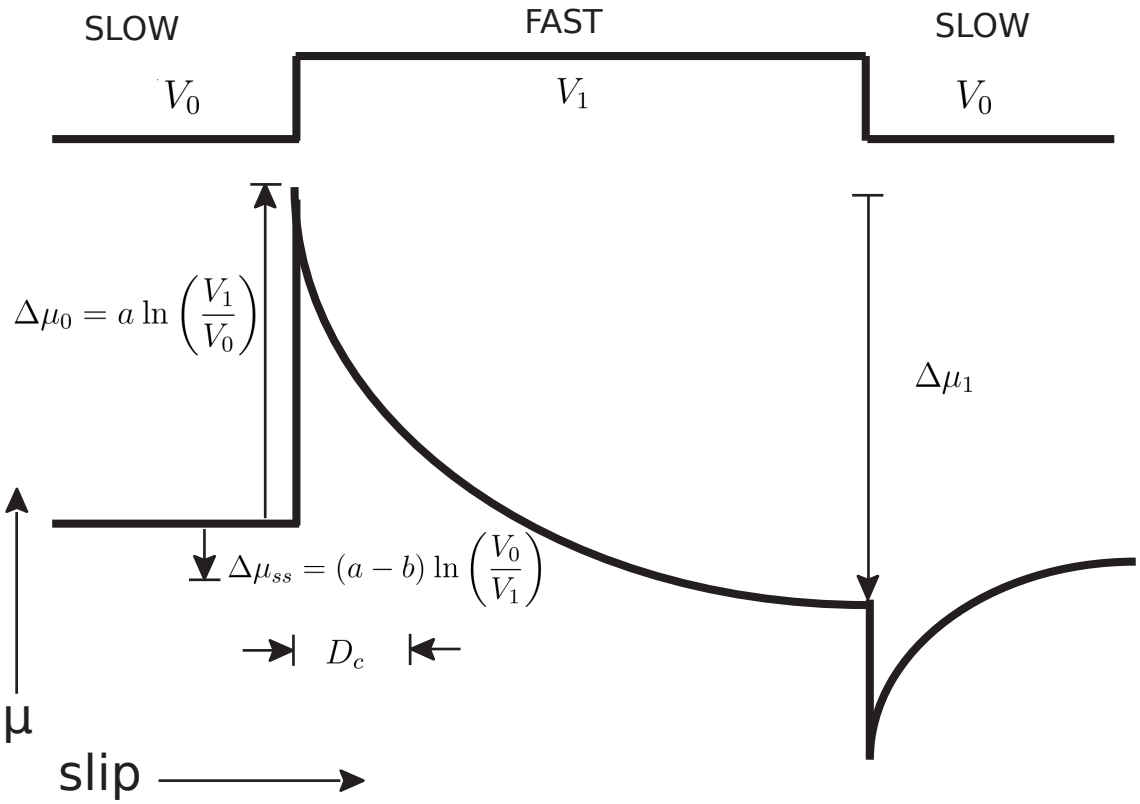

Figure 4.2: Schematic diagram taken from *Scholz* (2002) showing the frictional response to a sudden increase in sliding velocity from V_0 to V_1, followed by a sudden decrease. The frictional resistance shows a sudden increase followed by a return to a lower value (*Segall*, 2010). This figure defines the terms in the rate and state friction law, equation 4.8, where μ is the coefficient of friction and a and b are material parameters. The rapid response to the velocity step $\Delta\mu_0$ gives the parameter a. The evolution of the friction coefficent with slip $\Delta\mu_1$ gives the parameter b. Hence, the steady state change $\Delta\mu_{ss}$ is given by $(a-b)\ln\left(\frac{V_0}{V_1}\right)$. The final frictional resistance may be less than the initial friction, termed steady-state velocity weakening (as illustrated here), or greater than the initial friction, termed steady-state velocity strengthening (*Segall*, 2010).

fault zone based on how the fault slips. Seismogenic crust exhibits stick slip behaviour, whereas a transitional zone may exhibit complex behaviour, and ductile crust may exhibit stable sliding or plastic flow deformation.

To model frictional afterslip we follow the approach of *Perfettini and Avouac* (2007) and assume that brittle creep is localised on a fault obeying a pure velocity strengthening rheology. We also assume that sliding is stable, which is equivalent

to:

$$\frac{d\theta(t)}{dt} = 0 \tag{4.12}$$

If we define μ_0 as the friction at a steady-state reference velocity V_0, the friction at steady state can be written as:

$$\mu_{SS} = \mu_0 + (a-b)ln\left(\frac{V}{V_0}\right) \tag{4.13}$$

This reduces equation 4.11 to the hot friction model of *Linker and Rice* (1997):

$$\tau(V_0) = \sigma_n\left(\mu_{ss} + (a-b)ln\left(\frac{V_0}{V_{ss}}\right)\right) \tag{4.14}$$

Following the hot friction model, the frictional stress varies as the natual log of the strain, scaled by a rheolocical parameter $(a-b)\sigma$. $(a-b)\sigma$ characterises the dependency of friction on the slip rate and determines the dynamic response of the brittle creep fault zone to stress changes, *Perfettini and Avouac* (2007). Brittle creep is an exponential function of driving stress. As temperature increases with depth, fault friction changes from mostly velocity weakening at shallow depths (resulting in stick slip behaviour) to velocity strengthening at greater depths (where continuous creep occurs in response to stress). The depth of this change in regime is thought to occur at 250 $°C$ which corresponds to a depth of approximately 12 km in this region.

By imposing a static stress change at t=0 initialised by an earthquake, we can rewrite the hot friction model in terms of velocity as:

$$V = V_{pre}e^{\left(\frac{\Delta\tau}{\sigma_n(a-b)}\right)} \tag{4.15}$$

where V_{pre} is the pre-earthquake velocity which *Rice et al.* (2001) relate to the frequency of attempts to rupture asperities multiplied by the slip displacement per successful attempt. This equation was later revised by *Lapusta et al.* (2000) and *Rice et al.* (2001) to ensure that $V \to 0$ as $t \to \infty$ and to maintain continuity at $t = 0$. The adaptation takes the form:

$$V = 2V_{pre} \sinh(\frac{\Delta\tau}{\sigma_n(a-b)}) \tag{4.16}$$

4.2 The Kokoxili earthquake

The 2001 Kokoxili earthquake M_w 7.8, ruptured a 455 km section from west to east of the left lateral Taiyang Lake Fault (also known as the Heituo Fault), Kunlun and Kunlun Pass faults (see figures 4.3 and 4.4 for rupture extents. The coseismic slip distribution has been well established by InSAR (as shown in figure 4.4) and seismological methods (*Lasserre et al.*, 2005). To map the rupture geometry and surface displacements, *Lasserre et al.* (2005) used InSAR data from four adjacent descending tracks, covering almost the entire rupture, and Ikonos satellite imagery at 1 m pixel resolution. The earthquake initiated on the Taiyang Lake Fault and cut across a pull apart trough between the Taiyang Lake Fault and main Kunlun Fault. The majority of slip occurs in the upper 12 km with a maximum slip of 7.5 m occurring on the eastern end of the main Kunlun Fault (*Lasserre et al.*, 2005). The largest component of slip occurred between 0 and 5 km depth.

A simplified version of the geometry taken from *Lasserre et al.* (2005) was used for modelling afterslip, (see section 4.4). Figure 4.4 shows the fault geometry together with the distribution of aftershocks and coseismic slip distribution. Table 4.1 shows the model inputs for PSCMP of the fault geometry for viscoelastic relaxation.

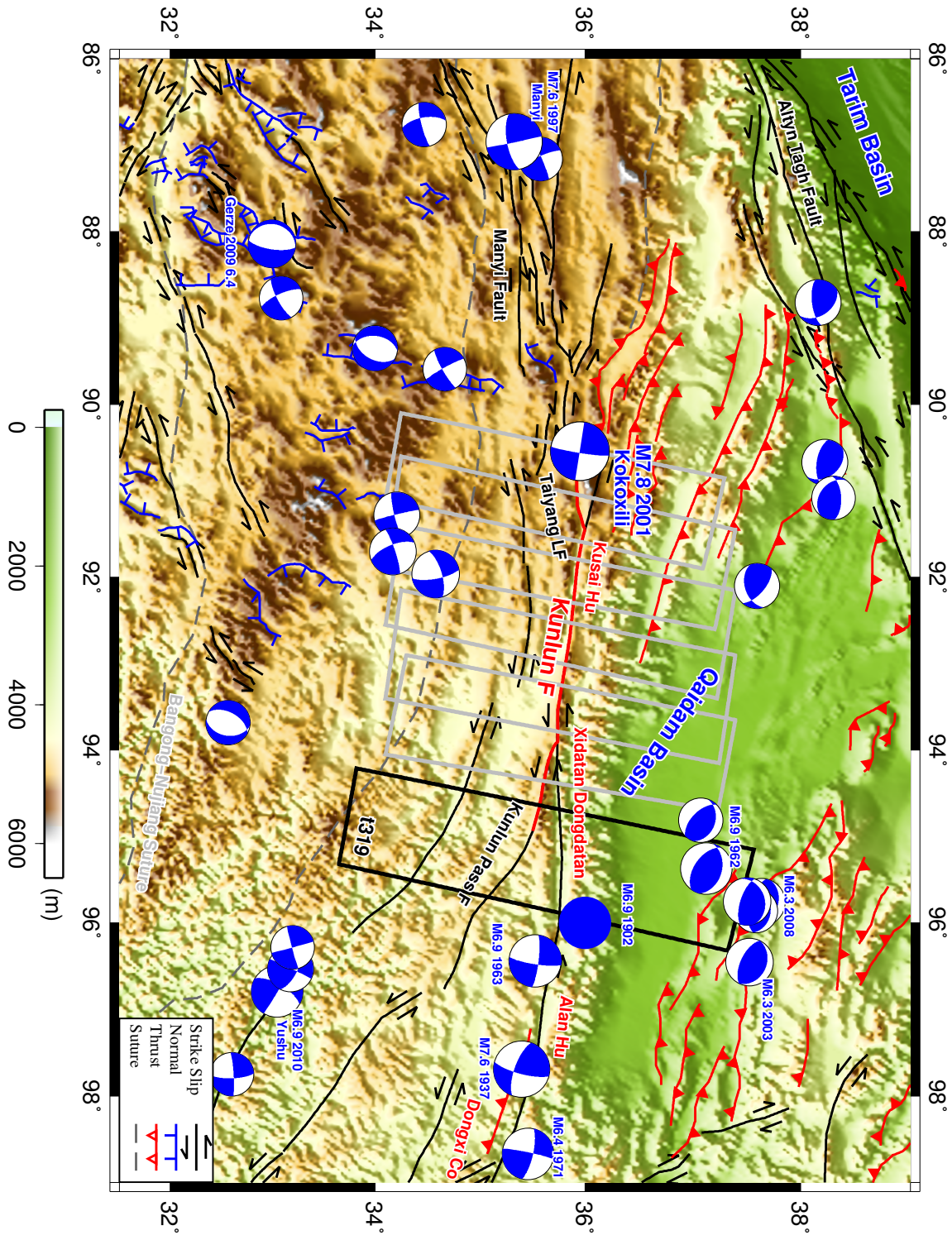

Figure 4.3: Relief map showing faults according to *Taylor and Yin* (2009) as black lines. The mapped rupture for the Kokoxili earthquake is shown in red according to *Lasserre et al.* (2005). A footprint of the processed Envisat track 319 from this study is shown as a black box and footprints for tracks used in the study by *Wen et al.* (2012) are shown as grey boxes. Earthquake focal mechanisms are taken from the USGS. Abbreviations: F=Fault, L=lake

Input fault geometry for PSCMP

Segment	Lat	Lon	L (Km)	Strike	Dip	Rake	Slip along strike (m)	Slip along dip(m)
1	35.975	90.281	28.2	254	90.0	0.0	-0.140	0.250
2	35.952	90.607	31.8	275	90.0	0.0	-2.050	0.190
3	35.992	91.034	45.6	278	90.0	0.0	-2.610	0.670
4	35.994	91.448	30.0	260	90.0	0.0	-1.540	0.000
5	35.945	91.754	26.1	260	90.0	0.0	-1.800	0.040
6	35.904	92.054	28.7	261	90.0	0.0	-2.120	0.140
7	35.877	92.291	14.6	264	90.0	0.0	-2.290	-0.070
8	35.857	92.478	19.3	262	90.0	0.0	-3.780	0.040
9	35.832	92.748	29.7	265	90.0	0.0	-5.210	0.160
10	35.797	93.094	33.3	261	90.0	0.0	-3.890	-0.520
11	35.750	93.469	35.0	261	90.0	0.0	-5.350	0.460
12	35.709	93.804	26.0	261	90.0	0.0	-3.230	-0.250
13	35.669	94.057	20.6	258	90.0	0.0	-3.120	-1.140
14	35.622	94.313	26.9	261	90.0	0.0	-2.470	-1.070
15	35.577	94.627	30.7	261	90.0	0.0	-2.490	-0.370
16	35.523	94.958	30.3	258	90.0	0.0	-1.340	0.040

Table 4.1: Earthquake fault parameters for the 16 segment model of *Wen et al.* (2012) based on the inversion of InSAR data. Segments are numbered from west to east and correspond to the faults in figure 4.4. Lat and lon are the latitude and longitude of each fault patch respectively of the centre and top. L is the lateral fault extent and the maximum depth of the fault segment (D) is set to 16.5 km for all segments

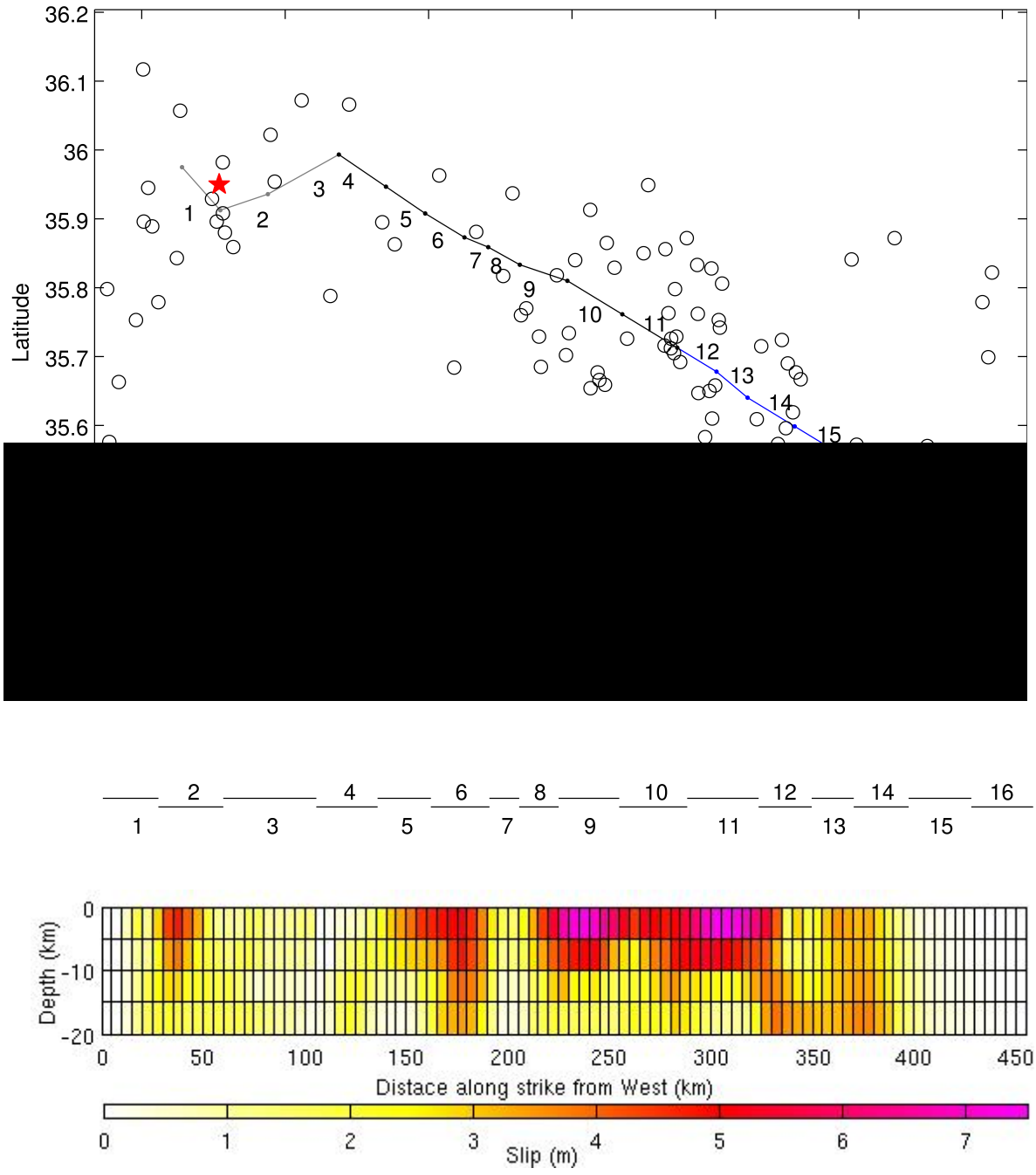

Figure 4.4: The surface location of the Kokoxili rupture along the Taiyang Lake Fault (segments 1-3, grey), the Main Kunlun Fault (segments 4-11, black) and the Kunlun Pass Fault (segments 12-16, blue). The lower part of the figure shows the slip distribution on the faults based on *Lasserre et al.* (2005). Open circles denote the aftershocks and the red star the epicentre taken from the USGS NEIC catalogue.The majority of slip occurs in the upper 12 km with maximum slip of 7.5 m ocurring on the Eastern end of the Main Kunlun Fault, refer to *Lasserre et al.* (2005) for more details.

4.3 Measuring postseismic deformation

To obtain an initial estimate of the intersismic signal I first removed a preliminary estimate of the postseismic signal presented by *Wen et al.* (2012). This postseismic model was for their best fit viscoelastic solution, for a Maxwell rheology with an elastic lid of 16 km, over a viscolelastic half space, with a viscosity of 2×10^{19} Pa s. I forward modelled this for the inputs shown in table 4.1 using PSGRN to prepare the greens functions that describe the model response; and PSCMP to calculate the surface displacements, using a discrete number of rectangular fault planes (refer to *Wang et al.* (2006) for an explanation of these codes).

This viscoelastic postseismic model was then removed from the real data and a least squares inversion was carried out to give an interseismic rate of 11.3 mm/yr, as explained in chapter 3. The obtained interseismic model for the best fit solution of 11.3 mm/yr and scaled atmospheric model were then removed from the original data. The postseimic signal is then remodelled and reinverted for a range of parameters and the results are shown here in section 4.5. A map of the region indicating the track processed for this study and those used for previous InSAR studies is shown in figure 4.3.

4.4 Numerical implementation of afterslip

I use the fault geometry and coseismic slip distribution of *Lasserre et al.* (2005) as the inputs to the afterslip models. I simplified the geometry to make three vertical and straight faults based on the strike of the Taiyang Lake Fault, the main Kunlun Fault and the Kunlun Pass Fault. As we would expect longer wavelengths, related to any afterslip deeper than 40 km, to be removed from the real data when we remove orbital phase errors (*Biggs*, 2007b), I only extend the fault plane in the model down

to a depth of 40 km. The shallowest depth of afterslip on the fault plane is set to 10 km as the crust is assumed to be velocity weakening above this depth (*Scholz*, 2002). The Parkfield earthquake (*Freed*, 2007) which is an example of asperities surrounded by creeping areas and the central section of the North Anatolian Fault (*Kaneko et al.*, 2013) are notable exceptions, where shallow afterslip is observed on the main fault. The validity of this assumption for the Kokoxili earthquake is discussed further in section 4.6.

The fault plane is discretised into 5 km × 5 km patches resulting in a total of N=546 fault patches. The stress τ on each fault patch i at time t is given by:

$$\tau(i,t) = \tau_{pre}(i) + \tau_0(i) + \tau_{aft}(i,t) \tag{4.17}$$

where τ_{pre} is the preseismic stress, τ_0 is the stress due to the earthquake and τ_{aft} is the stress induced on the plane after the earthquake from afterslip on all of the fault patches. As τ_{aft} is a result of slip on all the surrounding patches as well as patch i it can be rewritten in terms of an elastic kernel K, the components of which represent the horizontal stress change on patch i due to a unit of horizontal slip at patch q, (*Bell*, 2013).

$$\tau_{aft}(i,t) = \sum_{q=1}^{N} K(i,q)s(q,t) \tag{4.18}$$

where s is the afterslip at patch q at time t.

I initialise the model by combining equations 4.16 and 4.17 at the time of the earthquake to obtain the afterslip velocity at any time step t after this (*Bell*, 2013):

$$V(i,t) = 2V_{pre}(i)sinh\left(\frac{\tau_0(i) + \tau_{aft}(i,t)}{(a-b)\sigma_n(i)}\right) \tag{4.19}$$

We can calculate the afterslip velocities at any point after the earthquake, using the coseismic slip distribution to calculate the stress change from the earthquake at each patch location, assuming that at the time of the earthquake $\tau_{aft}(i,0) = 0$. The dynamic evolution of the stress field through time is then given by discretising the velocity into the change in slip that occurs over a given time $\frac{\Delta s}{\Delta t}$. So equation 4.19 becomes:

$$\Delta s(i,\Delta t) = 2\Delta t V_{pre}(i) sinh\left(\frac{\tau_0(i)}{(a-b)\sigma_n(i)}\right) \tag{4.20}$$

In implementing these dynamic equations, for slip evolution with time, I use the same five assumptions as *Bell* (2013): no afterslip occurs on patches where stress change from the earthquake is negative, the velocity is constant over the calculated time interval dt, I ignore change in normal stress due to afterslip, I clip velocities to 0.3 m/s to avoid instabilities, and I only use the horizontal component of shear parallel to the fault trace. Refer to *Bell* (2013) for a more detailed explanation of the reasons for these assumptions.

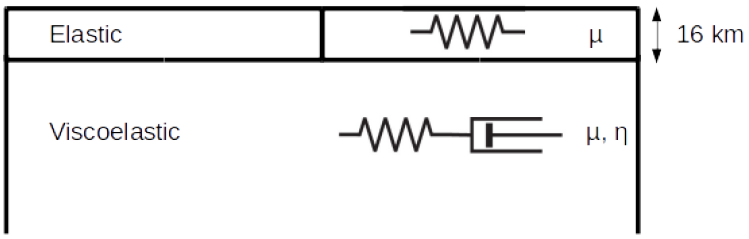

Figure 4.5: Cross section through the earth model used in modelling viscoelastic deformation. A 16km thick elastic layer at the surface (in which the coseismic fault dislocations are located) overlies a viscoelastic halfspace, with a Maxwell rheology. The viscosity of the half space is varied from 1×10^{18} Pa s to 9×10^{20} Pa s.

4.5 Viscoelastic results for a Maxwell rheology

I use the PSGRN and PSCMP codes developed by *Wang et al.* (2006) to generate a series of viscoelastic models. PSGRN creates the Green's functions used to describe the response of the model to a dislocation source, in this case a strike-slip. PSCMP then calculates the surface displacements. All of the forward models have a Maxwell rheology with an elastic lid of 16 km and a viscoelastic half space as shown in figure 4.5. I use the coseismic input model of *Lasserre et al.* (2005), shown in figure 4.4. For each time step available in the processed ENVISAT data (26 dates in total, refer to section 3.2 for details), I generate forward models for a range of viscosities, from 1×10^{18} Pa s to 9×10^{20} Pa s. To define μ, for all models, I use an average crustal density of 2.7 g/cm^3 and seismic velocities from *Steck et al.* (2009).

I combine the forward models for a single viscosity, for each time step, to produce an average line-of-sight velocity covering the entire period from 2003-2010. This is done using the same methodology applied to the real data, described in section 3.3. I then spatially sample this at the same locations as the real data, and generate an average profile perpendicular to the fault strike (as described in section 3.5.2). I show the real data for the average velocity only, rather than a timeseries, as the level of incoherence and noise is relatively high. I ran a series of models for different viscosities and found the smallest RMS misfit for a viscosity of 2×10^{19} Pa s. A timeseries showing the evolution of surface displacements for the best fit viscoelastic model is shown later, in section 4.7, alongside the best fit afterslip model.

The average LOS velocity for the real data and best fit model are shown in figure 4.7. A good fit to the real data is seen for this simple model, with a maximum peak-to-trough LOS velocity change of 4.9 mm/yr. The wavelength of the average profile for the model is seen to give a good fit to the real data; the estimated peak to trough distances are 91 km and 88 km for the real data and model, respectively.

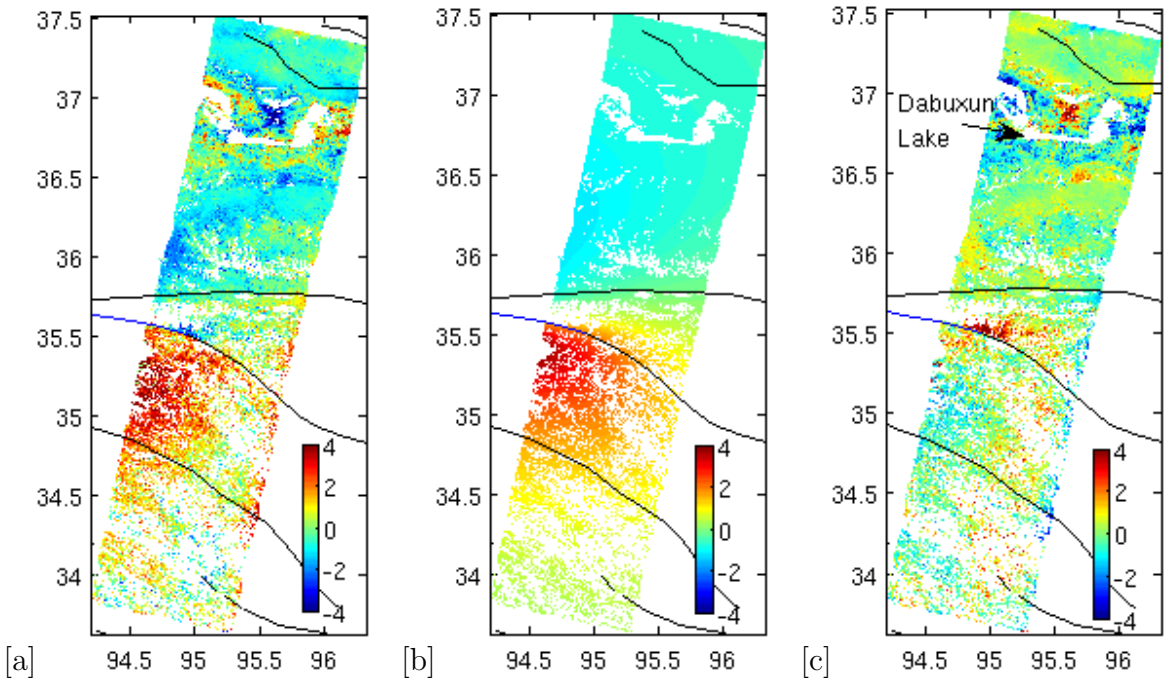

Figure 4.6: Line of sight deformation in mm/yr for [a] real data, [b] postseismic model for a Maxwell rheology with an elastic lid of 16 km, over a viscolelastic half space with a viscosity of 2×10^{19} Pa s and [c] residuals (rupture extent from the Kokoxili earthquake is indicated in blue)

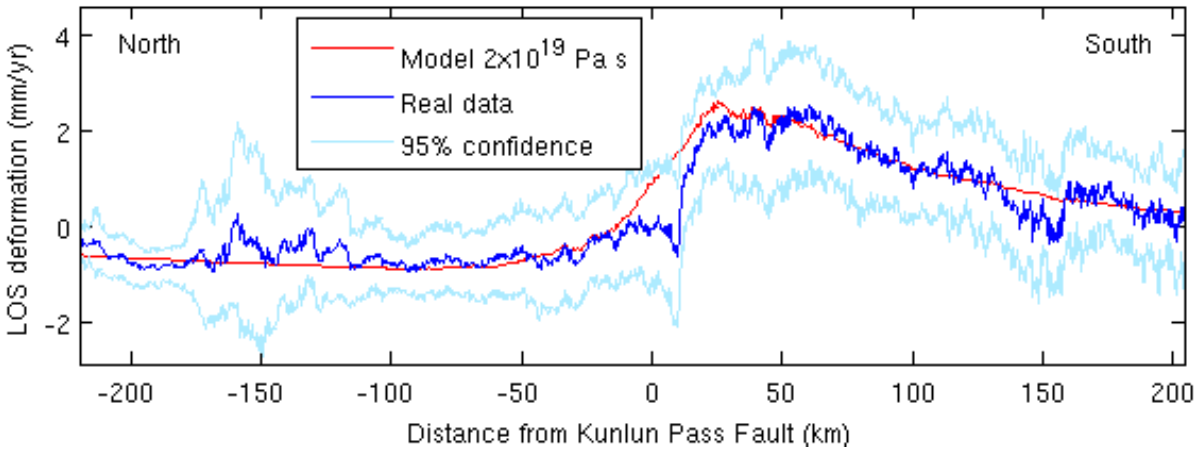

Figure 4.7: Average profile for line of sight deformation for the best fit viscoelastic model with a Maxwell rheology of viscosity 2×10^{19} Pa s generated using PSGRN and PSCMP (*Wang et al.*, 2006), and coseismic inputs from *Lasserre et al.* (2005) is shown in red. The real data for the average profile is shown in blue and the corresponding upper and lower bounds for the 95 percent confidence interval are shown in light blue. Profiles are shown here perpendicular to the orientation of the Kunlun Pass Fault rather than the Kunlun Fault as shown in chapter 3.

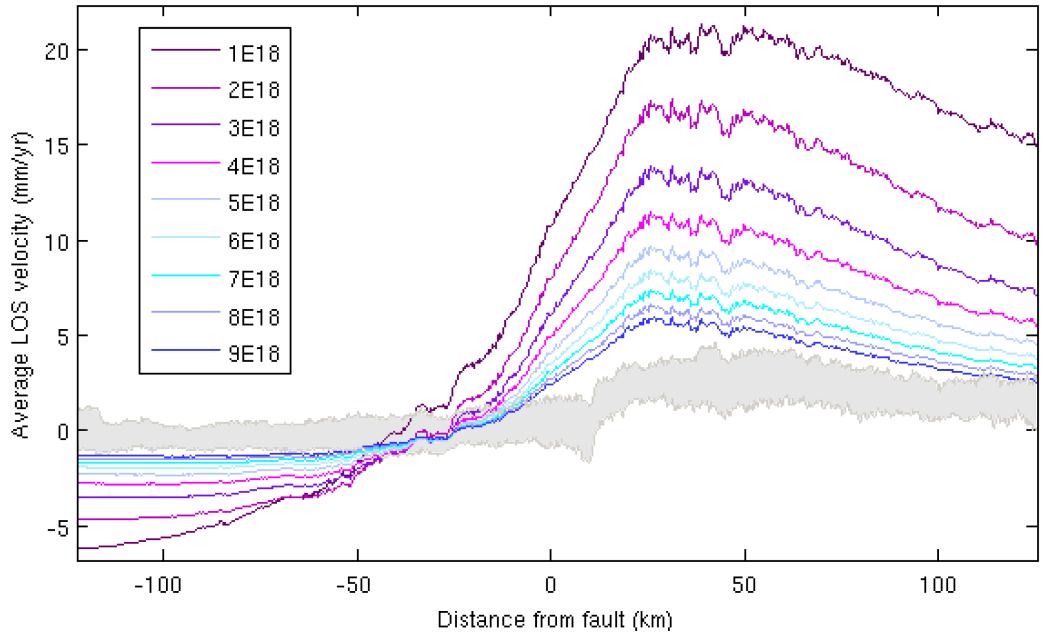

Figure 4.8: Average LOS velocity for a maxwell rheology with a viscosity of $1 \times 10^{18} - 9 \times 10^{18}$ Pa s. 1 sigma error bounds for the average profile of the real data are indicated in grey.

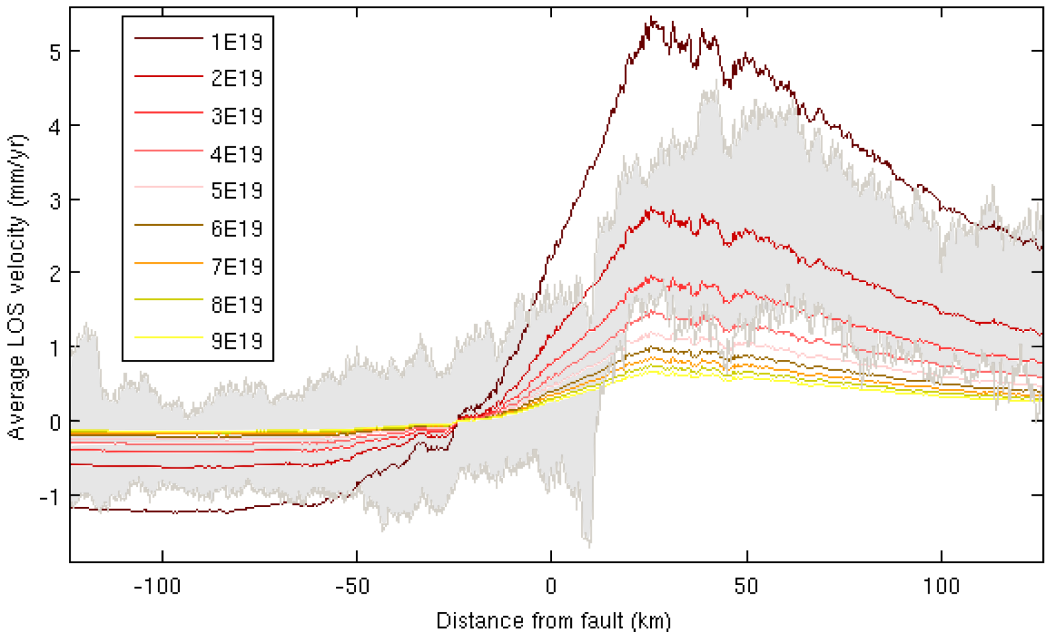

Figure 4.9: Average LOS velocity for a maxwell rheology with a viscosity of $1 \times 10^{19} - 9 \times 10^{19}$ Pa s. 1 sigma error bounds for the average profile of the real data are indicated in grey.

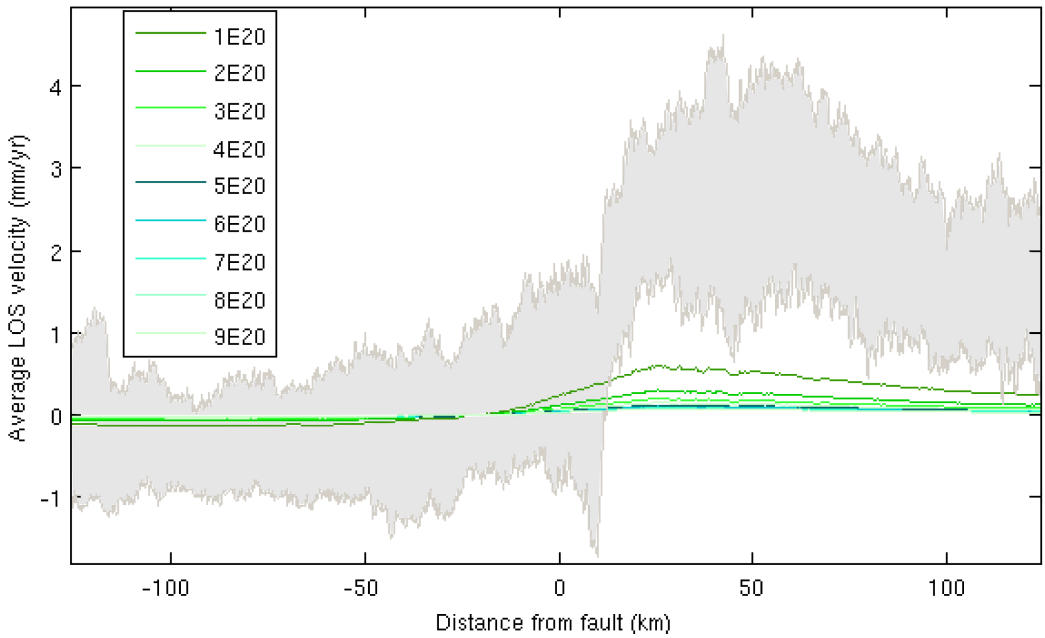

Figure 4.10: Average LOS velocity for a maxwell rheology with a viscosity of $1 \times 10^{20} - 9 \times 10^{20}$ Pa s. 1 sigma error bounds for the average profile of the real data are indicated in grey.

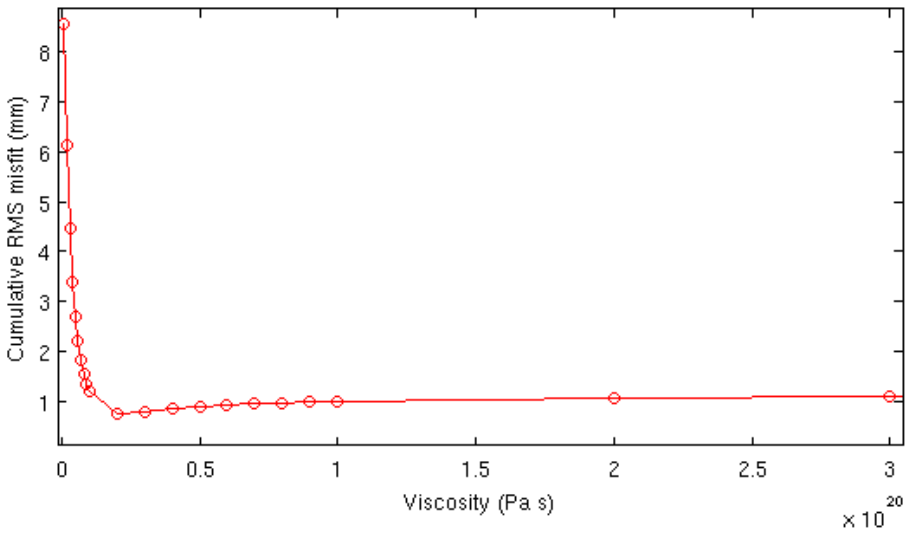

Figure 4.11: Cumulative RMS misfit curves as a function of Maxwell viscosity for the average line of sight deformation.

There is a clear distinction between models, with the only two models sitting within the 95 percent confidence intervals of the real data being for viscosities of 2×10^{19} Pa s and 3×10^{19} Pa s, as shown in figures 4.8, 4.9 and 4.10. All models with higher viscosities have peak to trough amplitudes that are too small, to match the real data, and those with lower viscosities have amplitudes that are too great.

A clear minimum is seen for the cumulative RMS misfit at a viscosity of 2×10^{19} Pa s as seen in figure 4.11. The largest residuals are near the fault and to the North on the Dabuxun Lake in figure 4.6. These effects are attributed to inaccuracies due to rapid changes in the strike of the fault which are not accounted for in the model, errors in dip in the initial coseismic model and subsidence around the lake.

4.6 Frictional afterslip results

Immediately after the earthquake afterslip velocities rapidly vary, so I change the time step over which afterslip is calculated, dt. For the first minute, I run the models using a time step of every second, then for every minute for the rest of the hour, and then every day. I generate afterslip models for each available date of the ENVISAT data, and obtain an average velocity, using the same methodolgy as for the viscoelastic models and real data (see section 4.5).

I run rate and state frictional afterslip models for a range of frictional parameters $(a - b)$ from 6×10^{-4} to 4.5×10^{-3} and for four preseismic velocities: 11.3 mm/yr (interseismic rate), 20 mm/yr, 40 mm/yr and 60 mm/yr. A minimum preseismic velocity of the interseismic rate is expected so I exclude lower velocities and this is justified by the results which show only slight changes in the amplitudes of the profile for 11.3 mm/yr and 20 mm/yr.

The best fit afterslip models are for a preseismic velocity of 20 mm/yr and

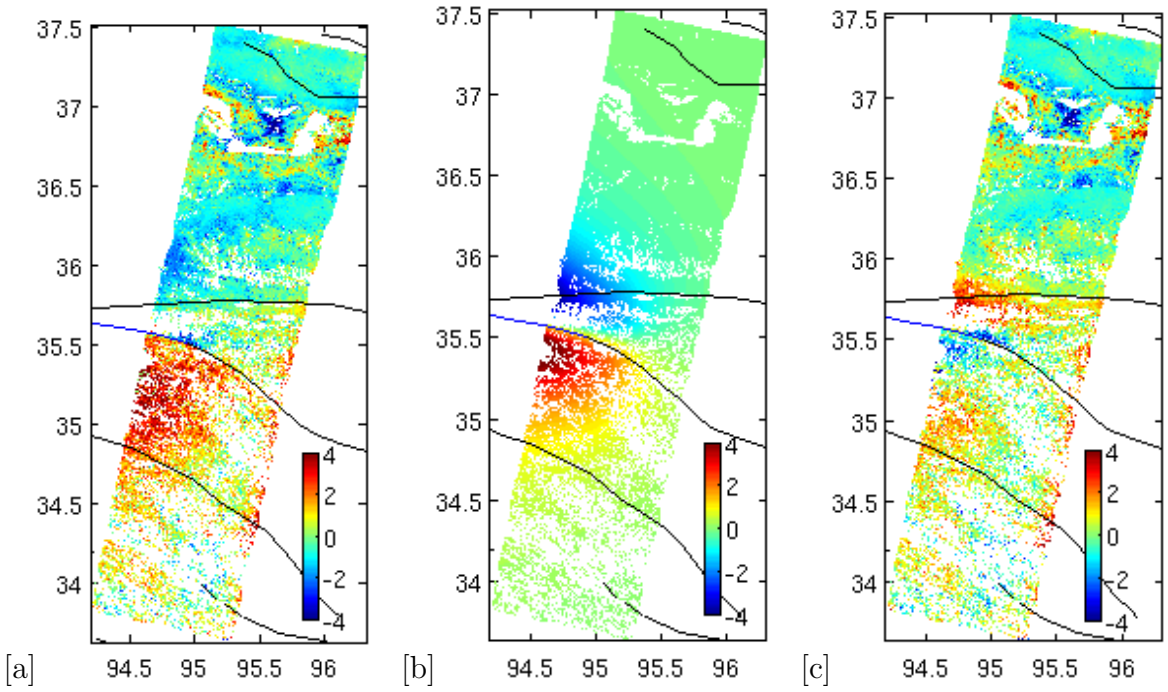

Figure 4.12: Average Line of sight deformation in mm/yr for [a] real data stacked for 24 scenes from 20030625 to 20100623 (rupture extent for the Kokoxili earthquake is indicated in blue), [b] best fit rate and state friction model with a preseismic velocity of 20 mm/yr and (a-b) frictional parameter of 2.5×10^{-3}, and [c] corresponding residuals

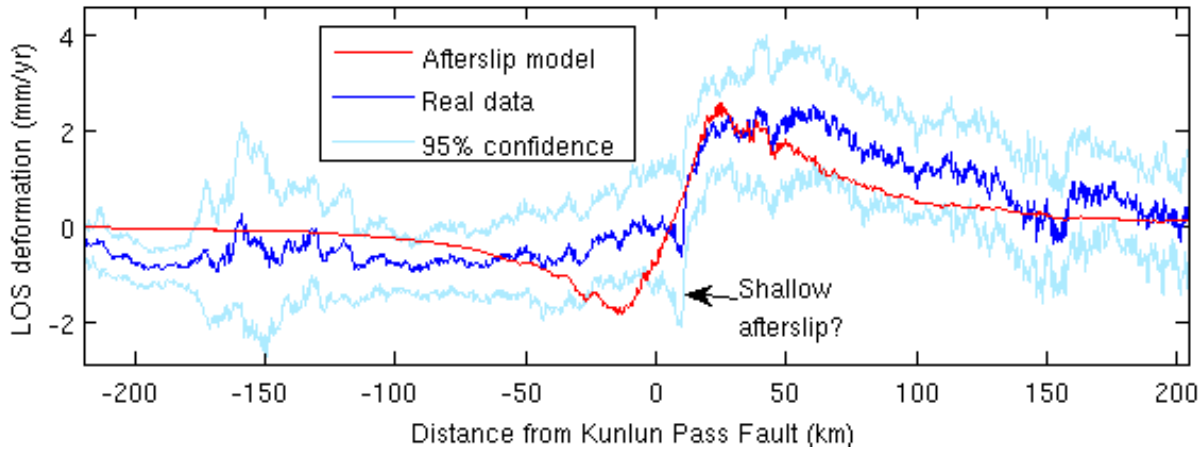

Figure 4.13: Average profile for LOS deformation in mm/yr for the real data with atmospheric effects, interseismic velocity and orbital errors removed in blue, the upper and lower bounds of the 95 percent confidence interval for the real data in light blue and the best fit rate and state friction model with a preseismic velocity of 20 mm/yr and (a-b) frictional parameter of 2.5×10^{-3} in red.

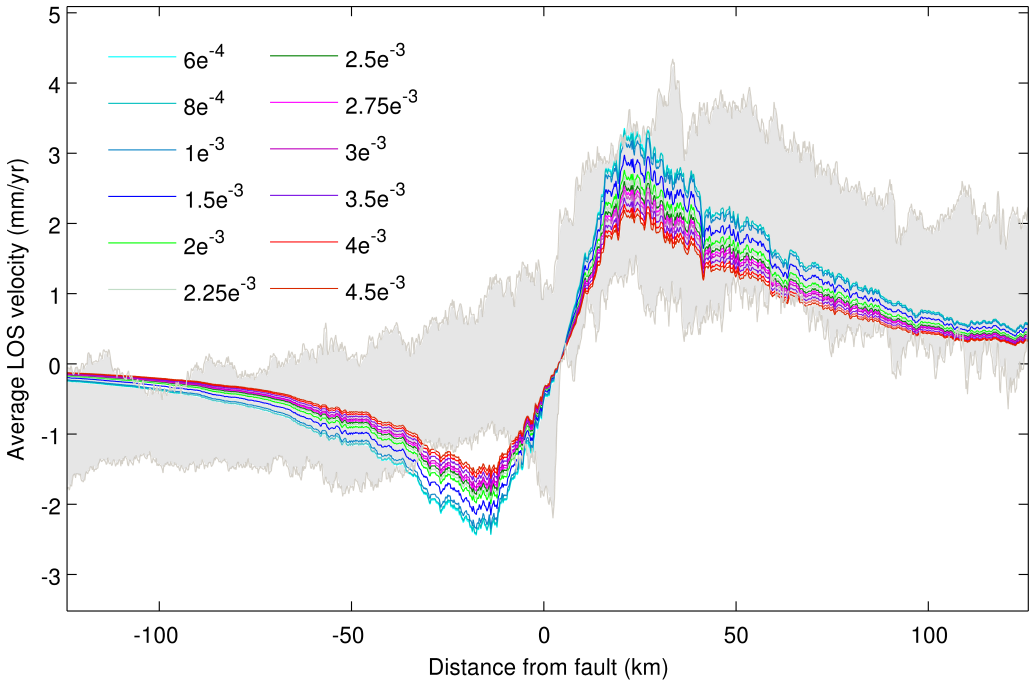

Figure 4.14: Average LOS velocity from rate and state friction models for a preseismic velocity of 20 mm/yr with a range of frictional parameters (a-b). 1 sigma error bounds for the average profile of the real data are indicated in grey.

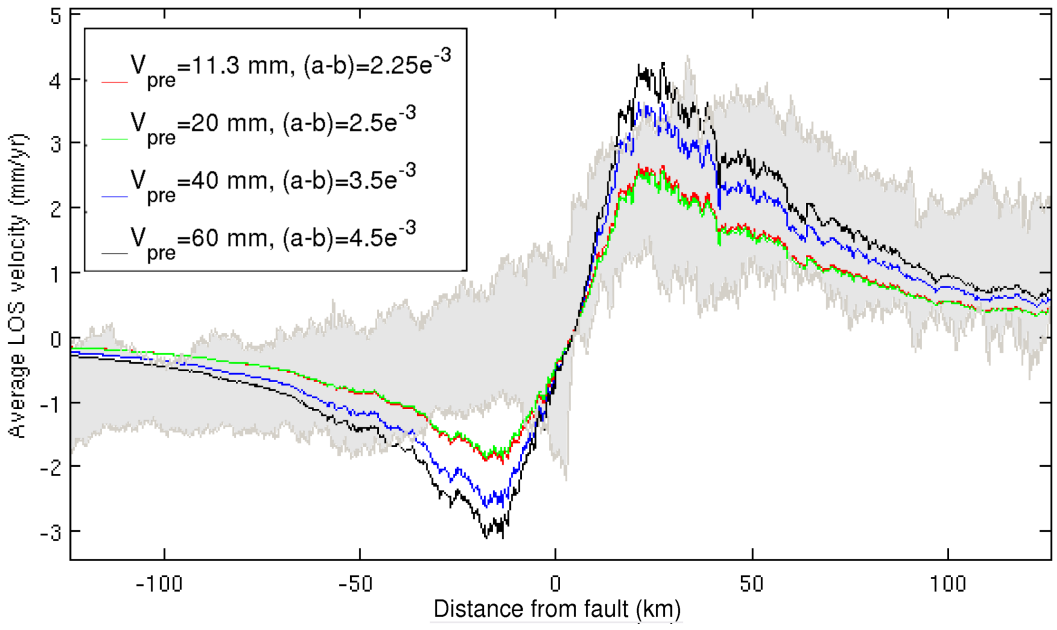

Figure 4.15: Average LOS velocity from rate and state friction models for a range of preseismic velocities. 1 sigma error bounds for the average profile of the real data are indicated in grey.

$(a-b)$ of 2.5×10^{-3}, and a preseismic velocity of 11.3 mm/yr and $(a-b)$ of 2.25×10^{-3}. Both of these models give very similar patterns for LOS deformation as seen in figures 4.15 and 4.16. Figure 4.12 shows the LOS velocity for the best fit model, together with the real data, and residuals for a preseismic velocity of 20 mm/yr and $(a-b)$ of 2.5×10^{-3}. Figure 4.13 shows the corresponding average profiles and 95 percent confidence intervals. Figure 4.16 [a] shows the LOS deformation for a preseismic velocity of 11.3 mm/yr and $(a-b)$ of 2.25×10^{-3}. The peak to trough distance for this model is 37 km, much shorter than the 88 km given for the best fit viscoelastic model. However, compared to previous postseismic studies, modelling motions so long after an earthquake, the fit to the real data is still reasonably good, as discussed later. The largest residuals are to the north of the fault within 15 km of the fault location.

In order for afterslip to be the primary mechanism of stress relaxation following the Kokoxili earthquake the longer wavelength signals present in the data need to be matched. This requires deeper afterslip than is obtained using rate and state friction (initialising the model with coseismic stresses). Nevertheless, the shape of average profiles together with large residuals within 15 km of the fault location suggest the presence of afterslip shallower than 10 km.

Figure 4.14 shows the average profiles for each of the frictional parameters for a preseismic velocity of 20 mm/yr. As we would expect from equation 4.20 the amplitude is seen to decrease for increasing $(a-b)$, as there is greater resistance to an increase in velocity so less afterslip.

Figure 4.15 shows the average profiles for each of the preseismic velocities: 11.3 mm/yr, 20 mm/yr, 40 mm/yr, and 60 mm/yr, for the best fit (a-b) parameter for that velocity. Figure 4.16 shows the LOS velocity for each of these models in 2D together with residuals. The amplitudes are much higher for the best fit models for

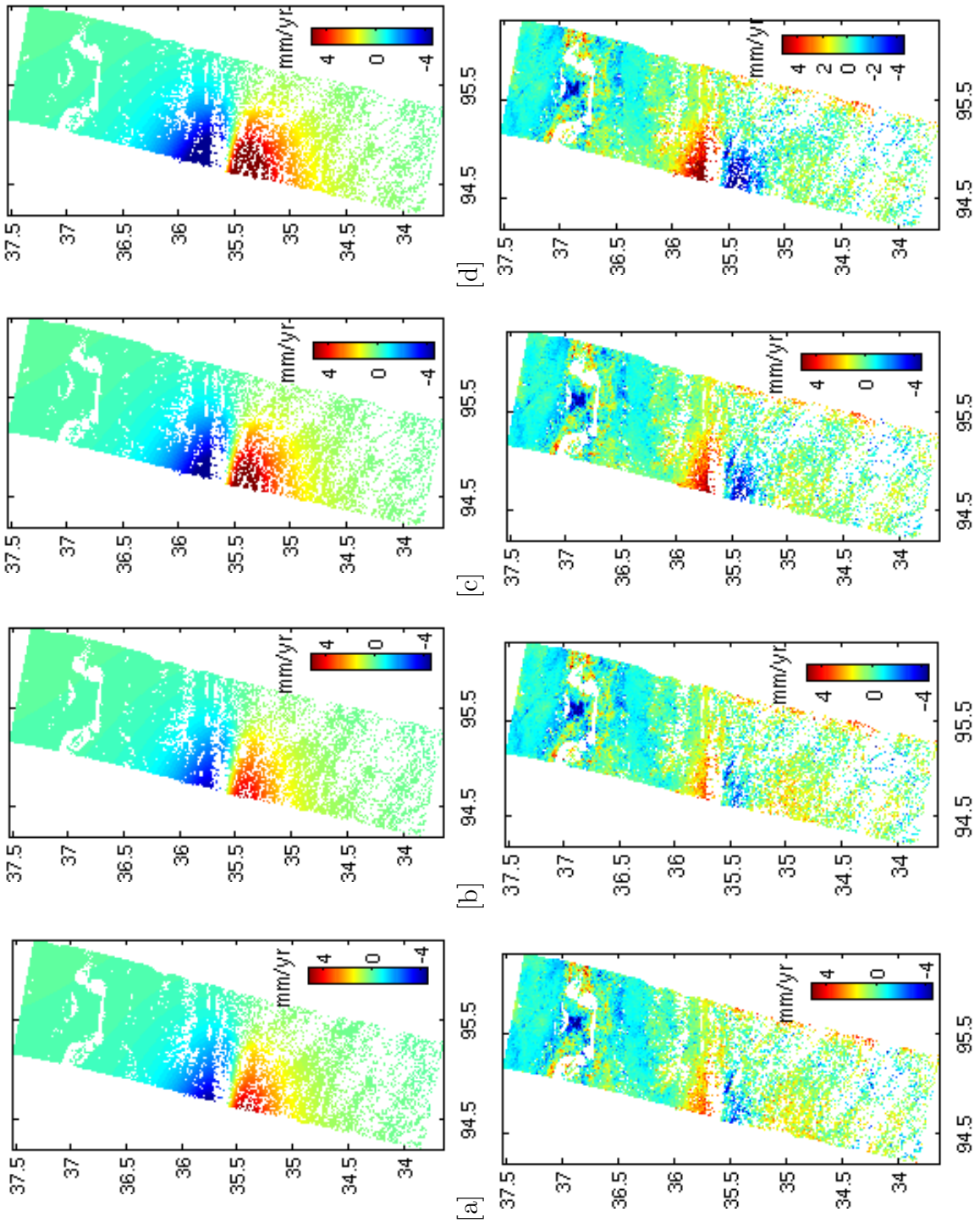

Figure 4.16: The top panel shows modelled line of sight deformation for four rate and state friction models that lie within the minimum of the RMS plot in figure 4.17: [a] V_{pre} 11.3 mm/yr, and (a-b) 2.25×10^{-3}, [b] V_{pre} 20 mm/yr, and (a-b) 2.5×10^{-3}, [c] V_{pre} 40 mm/yr, and (a-b) 3.5×10^{-3} and [d] V_{pre} 60 mm/yr, and (a-b) 4.5×10^{-3}. The bottom panel shows their corresponding residuals.

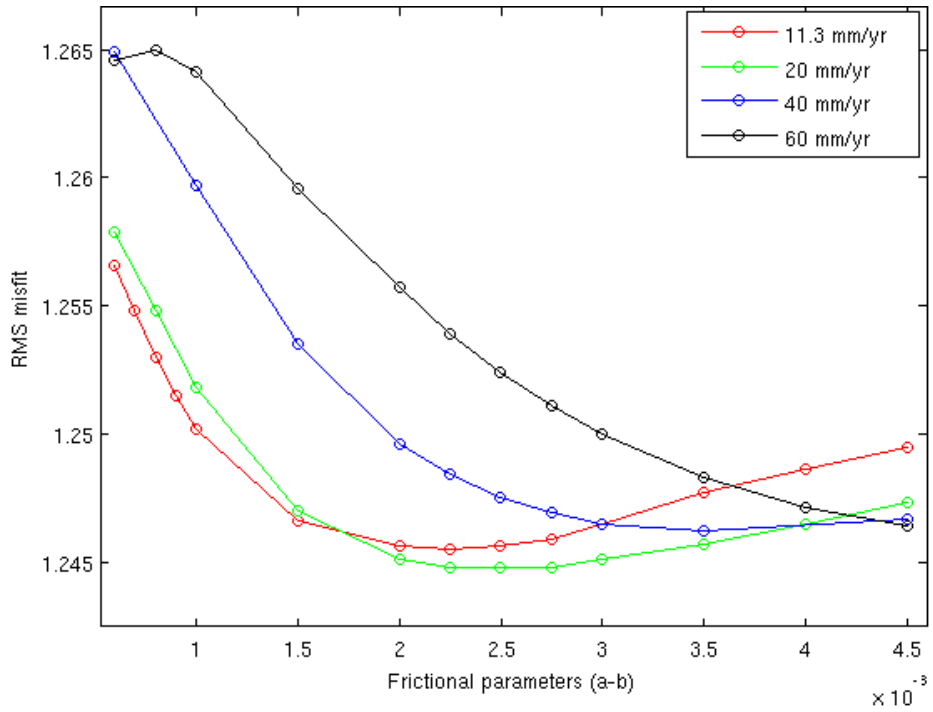

Figure 4.17: RMS misfit between the real data and the predicted LOS deformation for rate and state friction afterslip models for a range of frictional parameters $(a - b)$ and preseismic velocities.

preseismic velocities of 40 mm/yr and 60 mm/yr. Very similar amplitudes are seen for the best fit models for 11.3 mm/yr and 20 mm/yr. For all (a-b) frictional parameters and preseismic velocities, the model velocities are too high in the nearfield and too low in the farfield.

Curves showing the RMS misfit against frictional parameter (a-b) are shown in figure 4.17. For higher preseismic velocity the RMS minimum for the (a-b) frictional parameter increases. The RMS minimum for a preseismic velocity of 11.3 mm/yr is at an (a-b) frictional parameter of 2.5×10^{-3} and for a preseismic velocity of 60 mm/yr at 4.5×10^{-3}. Friction needs to be higher for higher levels of preseismic velocity to be reached before onset of afterslip. A larger proportion of the slip is occuring later after the earthquake for higher preseismic velocities; whereas the majority of slip is occurring earlier for smaller preseismic velocities.

Figure 4.18 shows, at various time points, the modelled afterslip with depth for the best fit model for a v_{pre} of 20 mm/yr and $(a-b)$ of 2.5×10^{-3}. Regions where there was high slip for the coseismic are shown to be surrounded by regions of high afterslip below and around. There is little afterslip in the deepest section of the model due to relatively small stress changes at those depths. The majority of the afterslip is constrained to a depth of 20-25 km. The shear stress change at various time points is shown in figure 4.19. Regions of high slip for the coseismic are shown to correlate with regions of high shear stress change. Regions with highest shear stress change result in patches with the highest slip rates. With time the stress change progresses deeper and decreases in amplitude. This can be seen in figure 4.19 where at 340 km along the profile at a depth of 24 km the shear stress change is 5.9 MPa after 130 days and 2.7 MPa after 3145 days. The same distance along the profile at a depth of 28 km the shear stress change is 1.9 MPa after 130 days and 2.3 MPa after 3145 days. The stress has not been fully relieved so slip will continue until it has been dissipated.

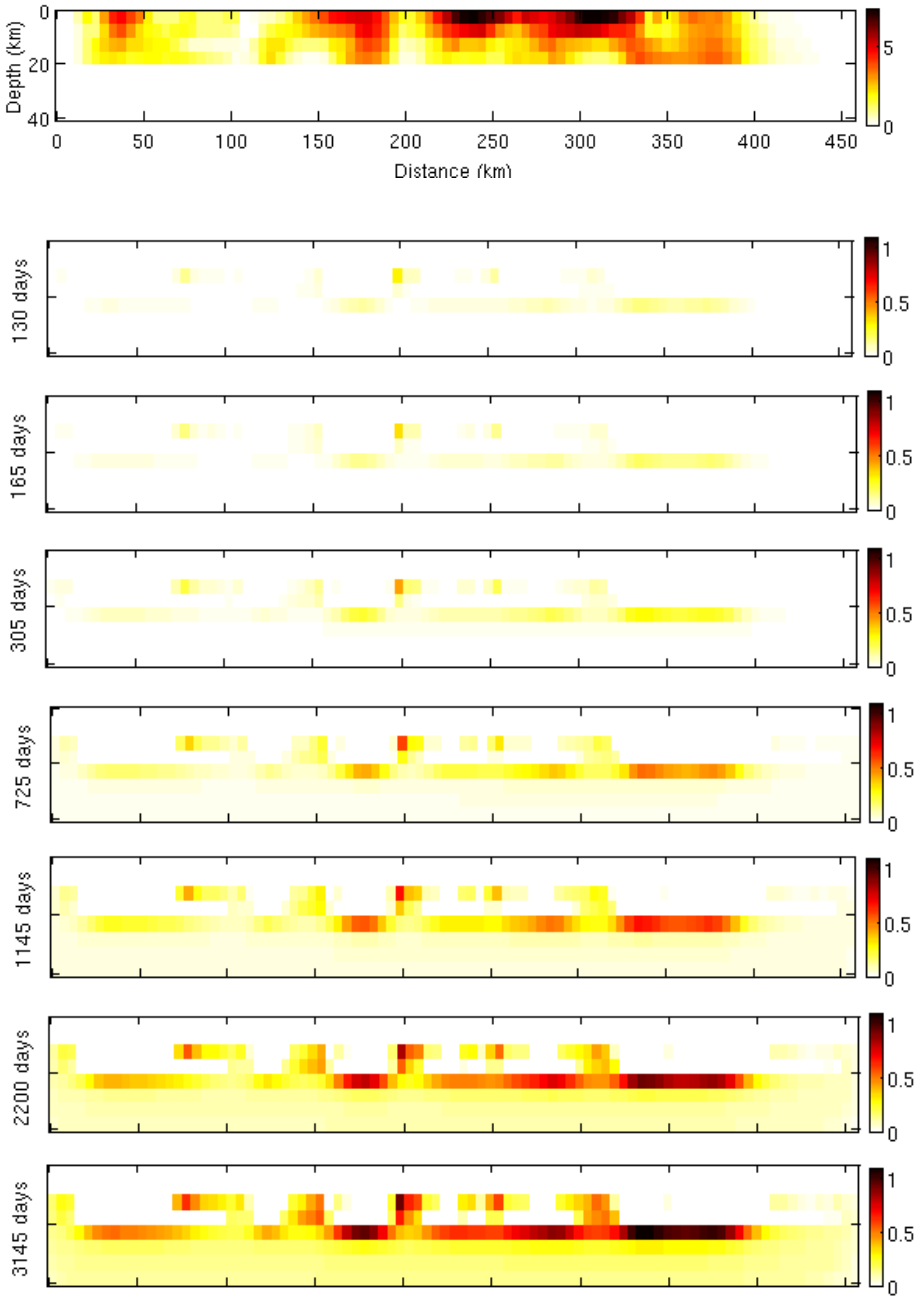

Figure 4.18: For track 319 Modelled afterslip in metres at various timepoints for a $v_{pre} = 20$ mm/yr and $a - b = 2.5 \times 10^{-3}$. The top panel denotes the coseismic distribution of *Lasserre et al.* (2005). Regions of high slip for the coseismic are shown to correlate with regions of high afterslip below and around, and high shear stress change as shown in figure 4.19.

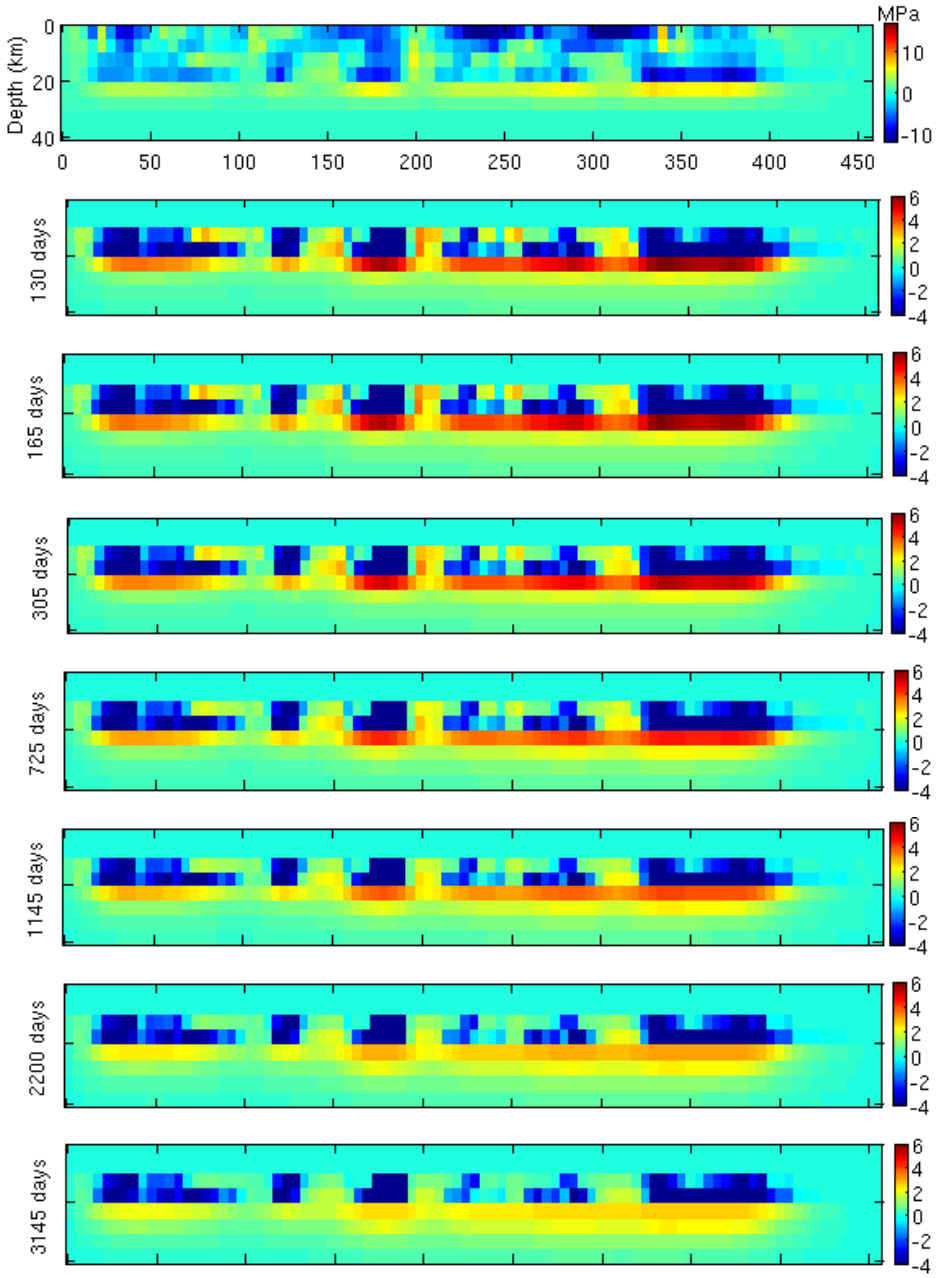

Figure 4.19: For track 319 Modelled afterslip shear stress change in MPa at various timepoints for a v_{pre} = 20 mm/yr and $a - b = 2.5 \times 10^{-3}$. The top panel denotes the coseismic stress change *Lasserre et al.* (2005). Blue regions indicate a stress drop so no slip occurs for these patches. Regions with highest shear stress change result in patches with the highest slip rates. With time the stress change progresses deeper and decreases in amplitude.

4.7 Comparison between afterslip and viscoelastic relaxation

The time evolution for afterslip and viscoelastic relaxation are seen to be very different. Figures 4.20 and 4.21 show the cumulative line of sight velocity for a subset of the available scenes, for the best fit models for viscoelastic relaxation and afterslip. The amplitude is seen to increase much faster for afterslip than for linear viscoelastic relaxation. This is seen in figure 4.22, where the amplitude of LOS velocity for two PS points (one in the peak to the north and one in the trough to the south of the fault) is shown for each of the models. High amplitudes are restricted to within 100 km of the fault location for all afterslip models; whereas much higher amplitudes are seen in the farfield for all viscoelastic models. These trends can be seen more clearly by looking at the corresponding 2D models shown in figure 4.23.

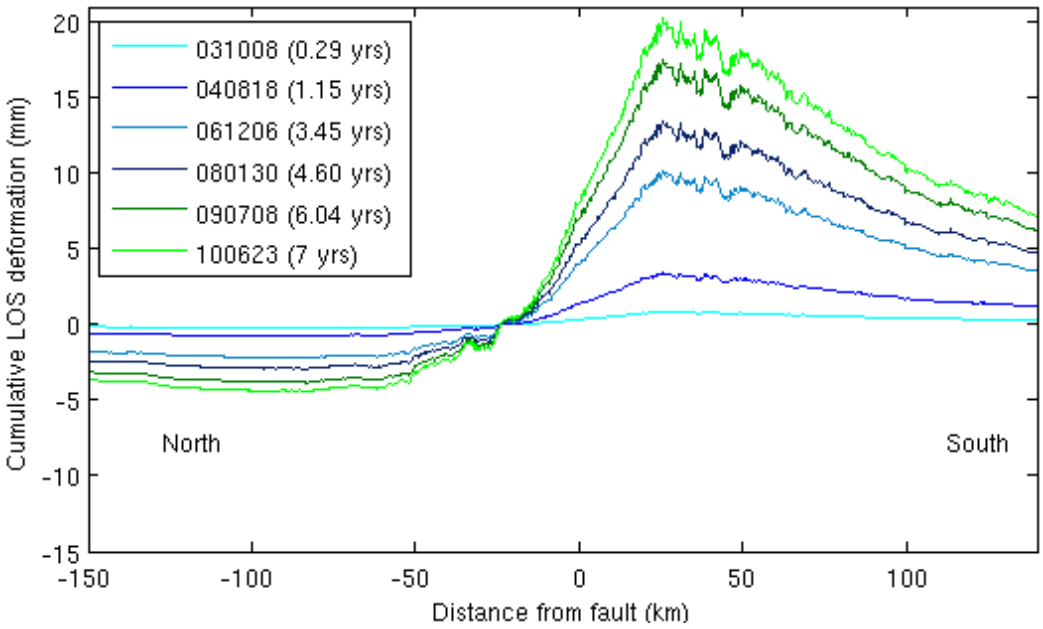

Figure 4.20: Cumulative LOS deformation in mm with respect to scene 030625 (1.61 yrs after the earthquake) for time points as shown for a maxwell rheology with a viscosity of 2×10^{19} Pa s

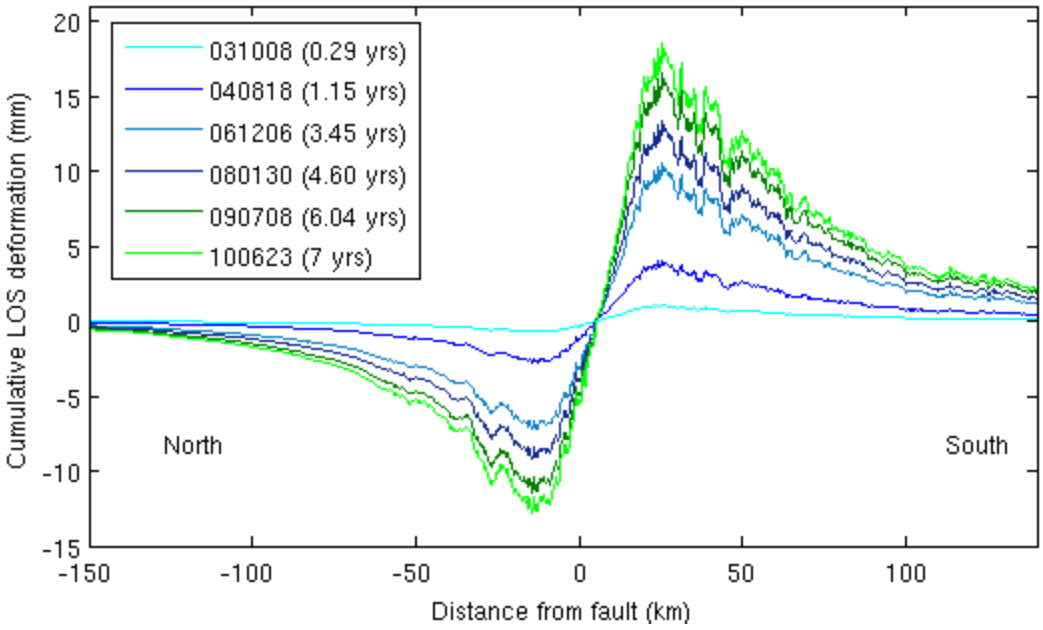

Figure 4.21: Cumulative LOS deformation in mm with respect to scene 030625 (1.61 yrs after the earthquake) for time points as shown for a rate and state friction afterslip with a preseismic velocity of 20 mm/yr and a-b frictional parameter of 2.5×10^{-3}

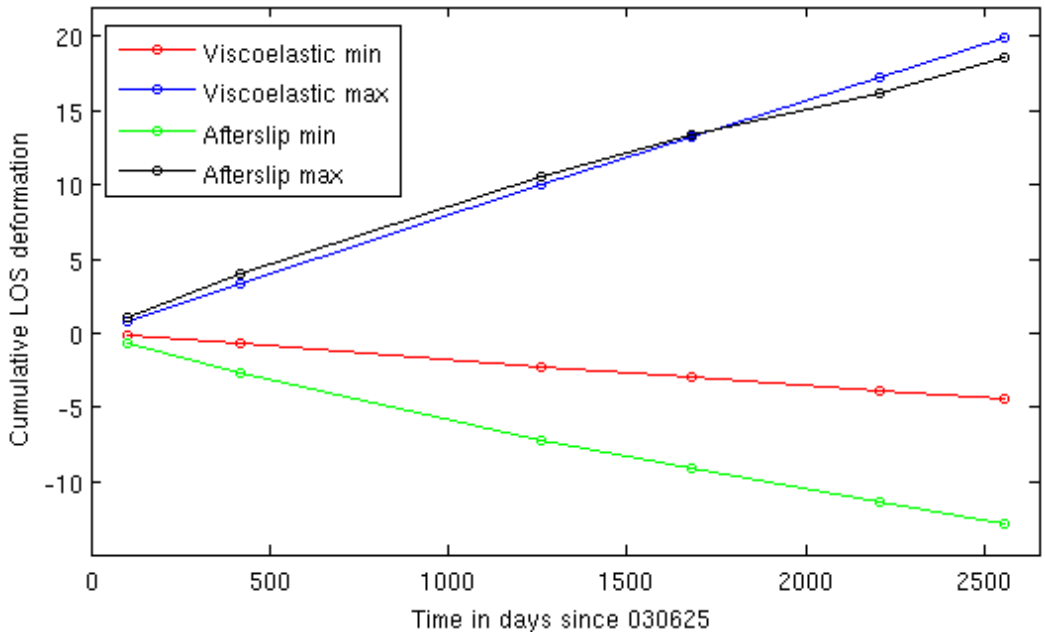

Figure 4.22: Cumulative LOS deformation in mm with respect to scene 030625 (1.61 yrs after the earthquake) for time points as shown: for a maxwell rheology with a viscosity of 2×10^{19} Pa s, and for afterslip with a preseismic velocity of 20 mm/yr and $a-b = 2.5\times10^{-3}$. For viscoelastic relaxation the minimum is for the average profile at a distance -84 km north of the fault, and the maximum is for the average profile at a distance 26 km south of the fault. For afterslip the minimum is at a distance 14 km north of the fault and the maximum is at a distance 26 km south of the fault.

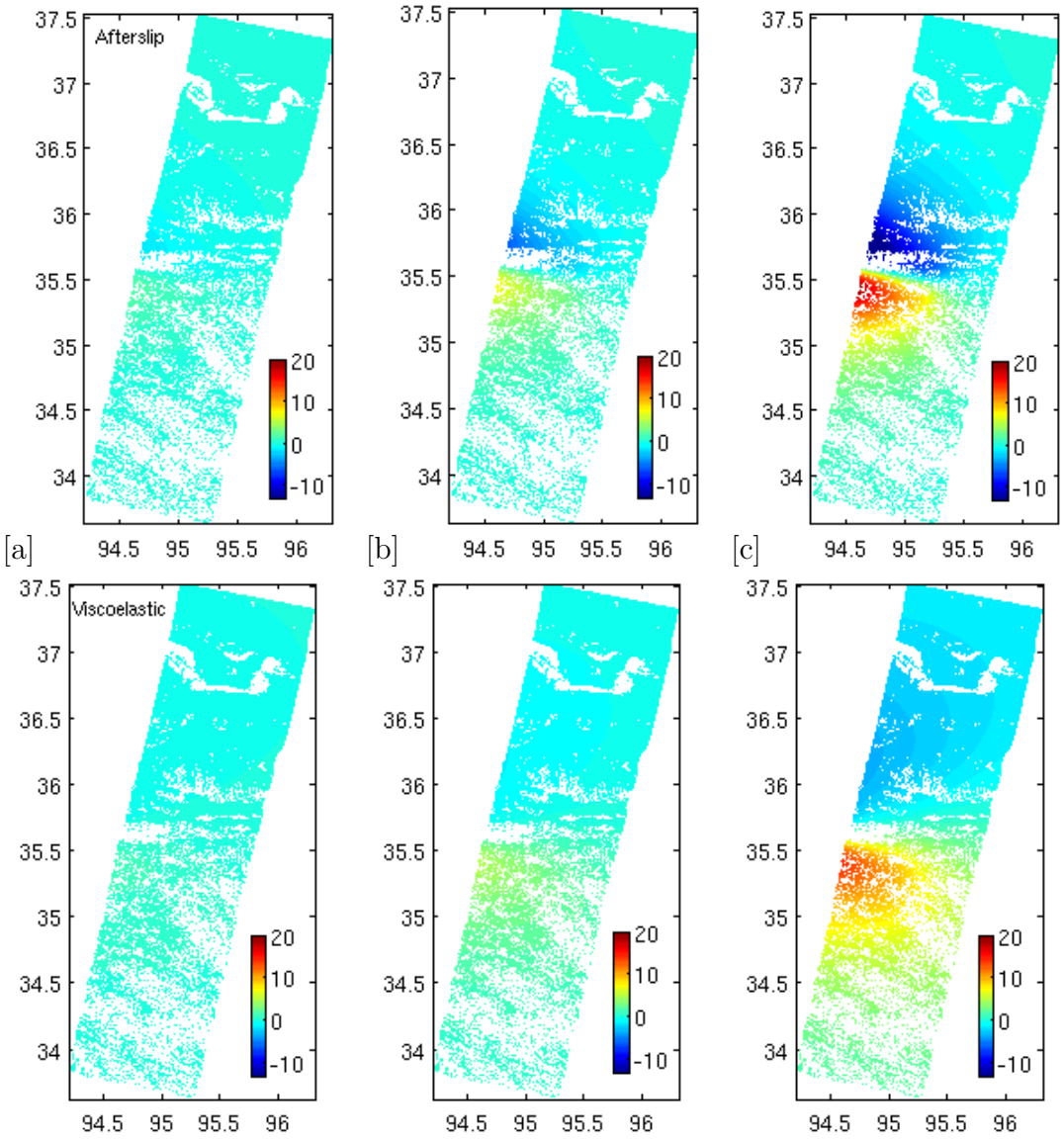

Figure 4.23: Modelled line of sight deformation in mm for (above) rate and state friction afterslip model with a preseismic velocity of 20 mm/yr and $(a - b) = 2.5 \times 10^{-3}$, and (below) viscoelastic relaxation with a viscosity of 2×10^{19} Pa s for: (on this page) [a] 0.29 yrs (030625-031008), [b] 1.15 yrs (030625-040818), [c] 3.45 yrs (030625-061206), and (over the page) [d] 4.6 yrs (030625-080130), [e] 6.04 yrs (030625-090708), and [f] 7 yrs (030625-100623)

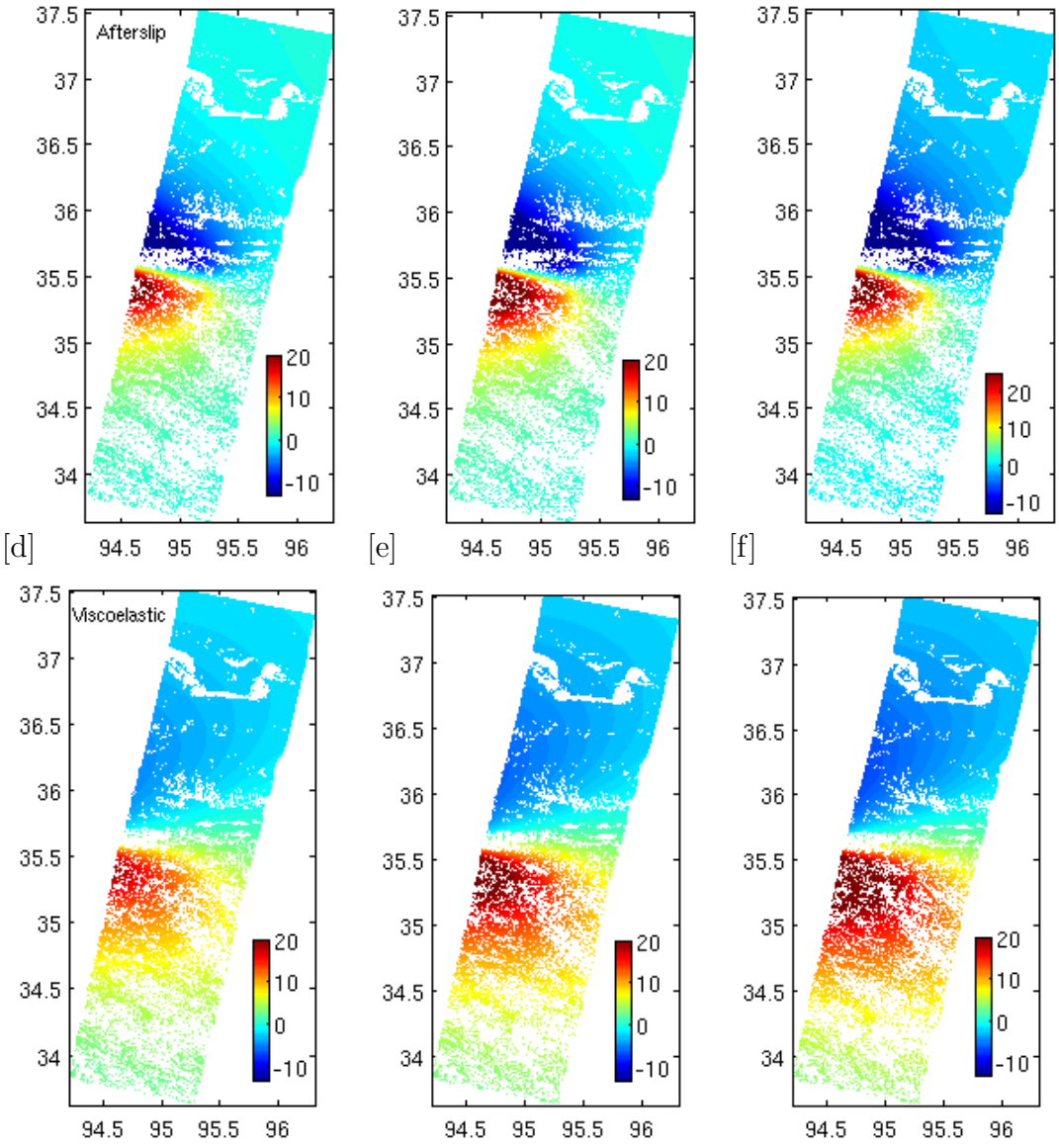

4.8 Discussion

4.8.1 Previous postseismic studies

Afterslip has been proposed as a likely mechanism for postseismic deformation by various authors for a number of earthquakes. $(a - b)$ values for rate and state frictional afterslip studies to date suggest similar values for a range of tectonic

Earthquake	Author(s)	(a-b)σ (MPa)
1992 Landers	*Perfettini and Avouac* (2007)	0.48-0.53
1999 Izmit	*Hearn et al.* (2002, 2009)	0.4
1999 Chi-Chi	*Perfettini and Avouac* (2004)	0.3-1.5
2001 Peru	*Perfettini et al.* (2005)	0.26
2002 Denali	*Johnson et al.* (2009)	0.5
2003 Tokachi-oki	*Fukuda et al.* (2009)	0.29-0.43
	Miyazaki et al. (2004)	0.2
2004 Parkfield	*Barbot et al.* (2009)	0.7
	Johnson (2006)	0.05-0.1
2005 Nias Simeulue	*Hsu et al.* (2006)	0.2-0.7
1997 Manyi	*Bell* (2013)	0.6-1.5*
2001 Kokoxili	This study	0.8-1.8*

Table 4.2: Review of Afterslip Studies that use geodetic data taken from *Bell* (2013). * indicates an average depth value was used to calculate σ of 26km for Manyi and 22.5km for this study.

settings. Table 4.2 reviews results from such studies to date. Similar $(a - b)$ values are seen for the Kokoxili earthquake as the Manyi earthquake. A table comparing the range of models lying in the RMS well for these two studies is shown in Table 4.4.

4.8.2 Comparison with Manyi results

Although *Bell* (2013) argued that his afterslip model for the Manyi Earthquake provides good fits to the real data, I suggest that his peak-to-trough wavelengths are also too small and that viscoelastic relaxation provides much better fits to the real data for later times as shown in figure 4.24.

The wavelength of the afterslip signal reflects the depth at which afterslip occurs. The deeper the afterslip the longer the wavelength of the signal. The short wavelength given by the model reflects the fact that afterslip occurs relatively shal-

Input fault geometry for PSCMP for the Manyi earthquake

$V_{pre}(mm/yr)$	(a-b)
8	$8X10^{-4}$
20	$1X10^{-3}$
30	$1.5X10^{-3}$
50	$2X10^{-3}$
120	$3X10^{-3}$

Table 4.3: Preseismic velocities and (a-b) frictional parameters of the range of rate and state friction models that lie in the RMS well for the Manyi earthquake taken from *Bell* (2013).

Input fault geometry for PSCMP for the Kokoxili earthquake

$V_{pre}(mm/yr)$	(a-b)
11.3	$2.25X10^{-3}$
20	$2.5X10^{-3}$
40	$3.5X10^{-3}$
60	$4.5X10^{-3}$

Table 4.4: Preseismic velocities and (a-b) frictional parameters of the range of rate and state friction models that lie in the RMS well for the Kokoxili earthquake.

low close to the original fault slip. For a viscoelastic model consisting of an elastic lid and a viscoelastic half space we are seeing deeper longer wavelength motion. The viscoelastic model matches the real data much better for later times. Although afterslip would migrate downwards with time it fails to match the signal suggested by real data for the timespan of the data.

We see a clear distinction between the wavelength of signals generated using dynamic rate and state friction models of afterslip and those using viscoelastic relaxation. Peak to peak wavelengths of profiles 1.6-8.6 years after the earthquake for rate and state afterslip are 40km whereas those for viscoelastic relaxation are 90km. We find a best fitting model of viscoelastic relaxation with a viscosity of $2X10^{19}$ Pa s which is in agreement with values along the main fault strand from

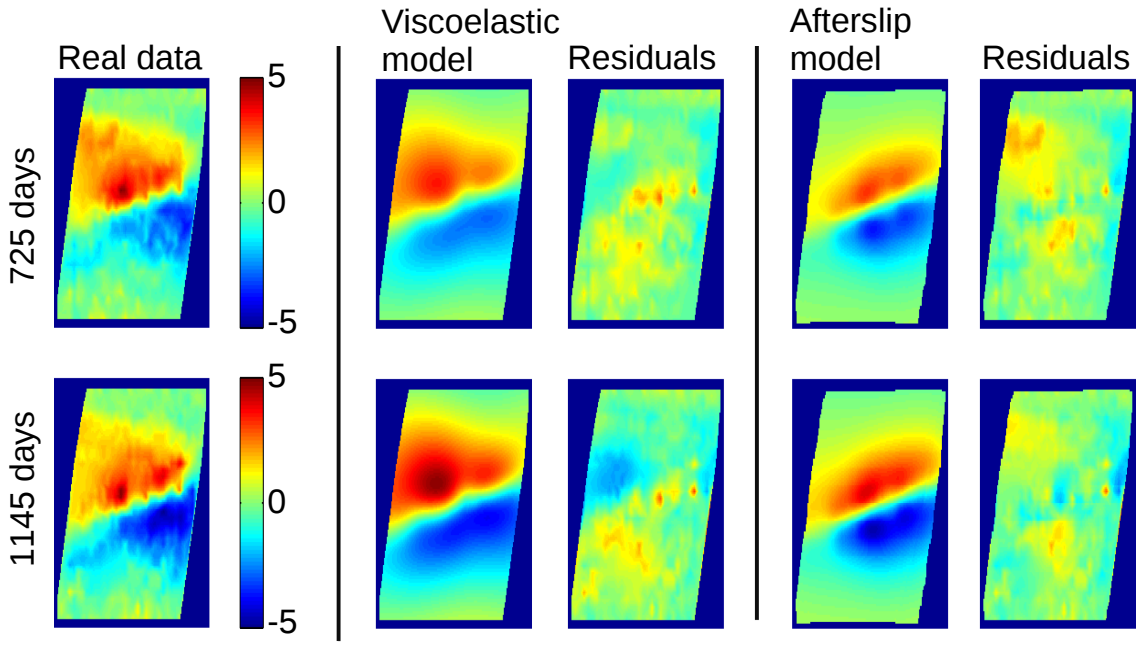

Figure 4.24: Cumulative LOS deformation in cm at 725 days and 1145 days for the Manyi earthquake: (left panel) real data, (centre panel) best fit viscoelastic model and residuals from *Ryder et al.* (2007), (right panel) afterslip model and residuals from *Bell* (2013). The longer wavelengths of the viscoelastic model are seen to reflect the real data much better than the afterslip model. Taken from *Bell* (2013)

Ryder et al. (2011). A strong post seismic signal is seen across the Kunlun Pass fault whereas any signal across the main fault strand must be below background noise levels. This correlates both with our knowledge of the continuation of the rupture along this offshoot of the Kunlun fault, rather than along the main strand, and with the measured interseismic signal shown in the previous chapter.

Chapter 5

A velocity map for Western Turkey

5.1 Introduction

A number of studies have looked at interseismic strain accumulation across the North Anatolian and East Anatolian faults, e.g. *Cavalié and Jónsson* (2014); *Cetin et al.* (2014); *Cakir et al.* (2014); *Walters et al.* (2014); *Yamasaki et al.* (2013), but relatively little work has been done on a fault scale across the grabens in Western Turkey. I use PS InSAR to look at this problem both due to the interest in regional tectonics and as a consequence of questions that have been raised by continous GPS monitoring. *Aktug et al.* (2009) argue that GPS results show largely uniform strain accumulation across the region. The aim of this chapter is to see whether GPS data are too sparsely located to measure strain localisation or if the GPS data accurately show tectonic deformation in the region.

Using PS InSAR I cover a region approximately 300 km by 400 km using a combination of ascending and descending data from the ENVISAT satellite. I compare

this with GPS data in the region, to see whether the spatial resolution of the GPS is too low to resolve strain localisation across the grabens, or whether deformation is more distributed. I then combine the two data sets to generate high resolution velocity and strain rate maps, which can be used for seismic hazard assessment and to distinguish between different dynamic models of continental deformation.

5.2 Tectonic setting

The pattern of deformation in Western Turkey is due to both the movement of material laterally away from Eastern Turkey, and the south westward motion of the southern Aegean relative to Eurasia (see figure 5.1 showing a map of the region with major faults indicated, and figure 5.2 showing GPS velocities). Turkey is driven westwards with respect to Arabia by the gravitational potential energy from thickened crust in Eastern Turkey (*Taymaz et al.*, 1991), push from Arabia, and pull from the trench (*Jackson and McKenzie*, 1988). This anti-clockwise rotation of the Anatolian Plateau with respect to Eurasia is being accomodated along the right-lateral North Anatolian Fault and by left-lateral slip on the East Anatolian Fault (*McKenzie*, 1972). The North Anatolian Fault (NAF) runs east-west for an extent of 1200 km, from its intersection with the East Anatolian Fault in the east to the Aegean Sea in the west. At its western end the fault splits into a number of splays.

From GPS measurements the slip rate on the NAF is estimated to be 24±1 mm/yr by *McClusky et al.* (2000), and 24.5 to 27.5 mm/yr by *Aktug et al.* (2009), the latter incorporating small components of shortening on the northern segment. On the southern segment, *Aktug et al.* (2009) estimate 3.2 to 5.3 mm/yr of lateral motion. From InSAR, in the east the NAF is estimated to have 19±2 mm/yr of

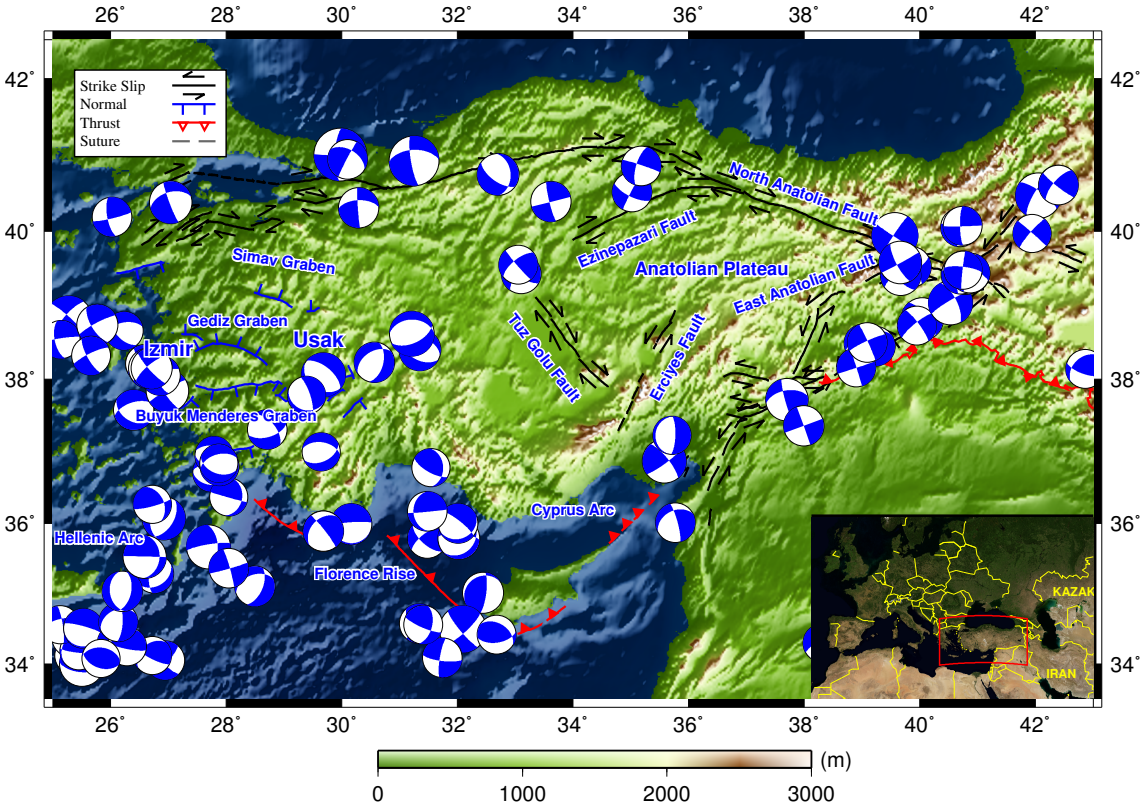

Figure 5.1: SRTM topography of Turkey and seismicity for events greater than M_w 5.6 taken from the global CMT catalogue (1976-2011) with beach balls indicating normal, thrust and stike slip events. Major faults in the region are indicated with strike slip faults in black, normal faults in blue and thrust faults in red taken from *Saroglu et al.* (1992).

right-lateral slip with a locking depth of 17±9 km (*Walters et al.*, 2014). The northern and southern segments are shown in figure 5.3.

The East Anatolian Fault runs for 400 km north-east to south-west from its intersection with the NAF to the Mediterranean Sea. From GPS it has an estimated slip rate of 9±1 mm/yr (*McClusky et al.*, 2000) and from InSAR 10±2 mm/yr with a locking depth of 12±4 km (*Walters et al.*, 2014).

Aktug et al. (2009) showed that extension in Western Anatolia increases in magnitude from the Anatolian Plateau to the Aegean coast. The East Anatolian Plateau is a region of relatively slow rates of deformation. The lower lying regions of Western Turkey, eastern and northern Greece, and the north Aegean Sea have

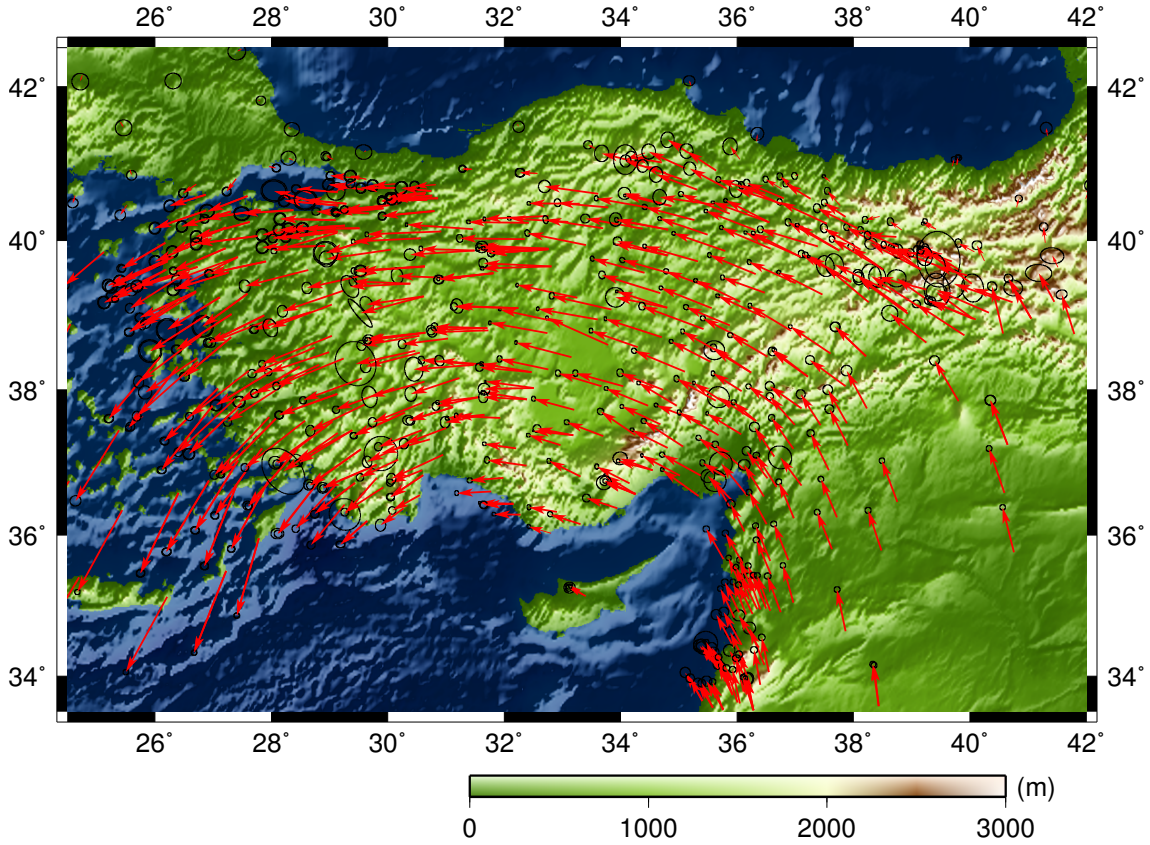

Figure 5.2: Map showing GPS velocities for Turkey as vectors in red together with their 95 percent error ellipses shown in black. The velocites are rotated into a Eurasia fixed plate as per *Reilinger et al.* (2006) using stations in common with the exception of data from *Yavasoglu et al.* (2011). Data are taken from *Reilinger et al.* (2006); *Gomez et al.* (2007); *Le Beon et al.* (2008); *Aktug et al.* (2009); *Ozener et al.* (2010); *Alchalbi et al.* (2010); *Al Tarazi et al.* (2011); *Tatar et al.* (2012); *Aktug et al.* (2009).

thinner crust and are dominated by extension. This extension is accomodated by normal faulting earthquakes across five main grabens: the Bakirçay Graben, Simav Graben, Gediz Graben, Büyük Menderes Graben and Küyük Menderes Graben. A map showing the major earthquakes and faults in the region is shown in figure 5.3.

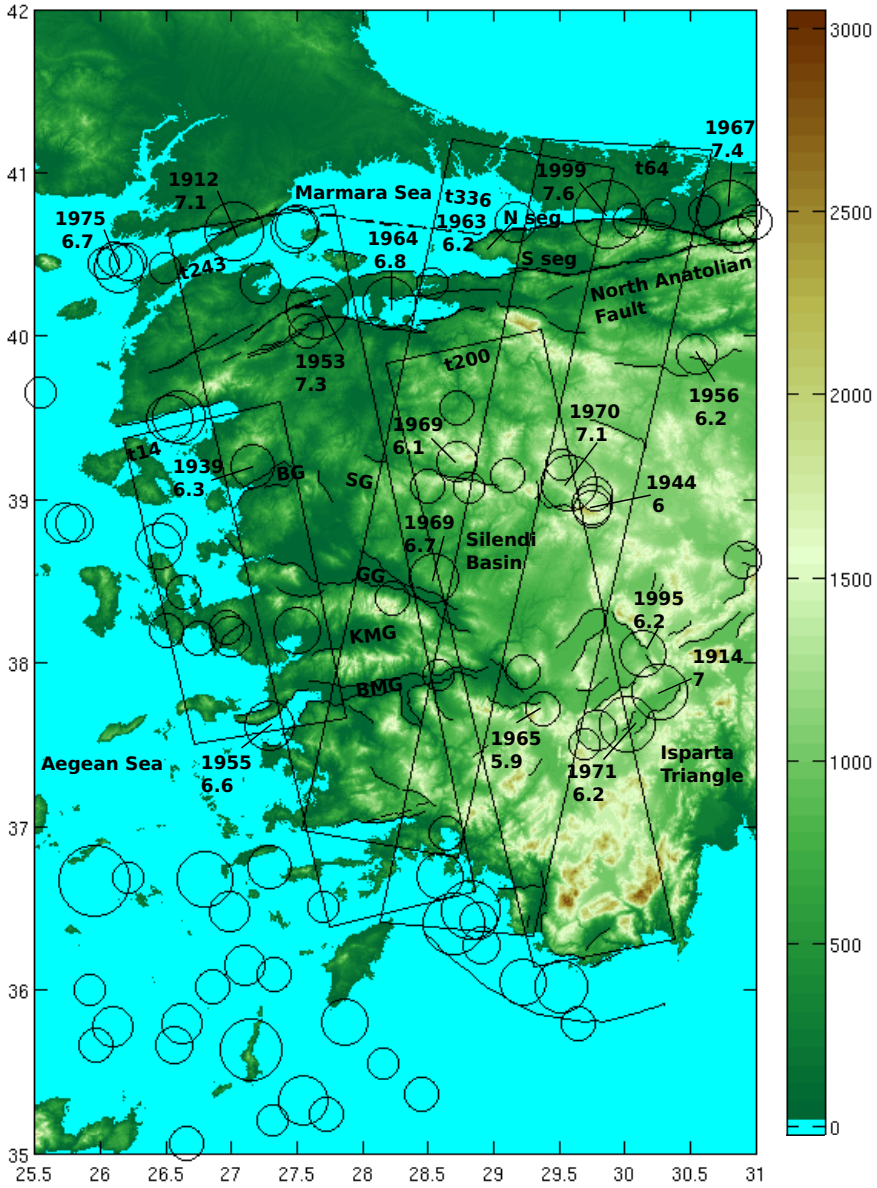

Figure 5.3: Map showing the location of the five processed InSAR tracks for ascending data numbers 14, 243, 200 and for descending data numbers 336 and 64 indicated by the black boxes. Mapped faults according to *Saroglu et al.* (1992) are shown as black lines and the major events across the grabens for Western Turkey are labelled with the year and magnitude of the event shown. Earthquakes scaled according to their magnitude taken from the NEIC catalogue for events greater than 5.6 are shown as black circles. The five main grabens that are the focus of this study are the Bakirçay Graben (BG), Simav Graben (SG), Gediz Graben (GG), Büyük Menderes Graben (BMG), and Küyük Menderes Graben (KMG). N seg=north segment of NAF, S seg=south segment of NAF.

5.3 Data availability and processing

Following the procedure outlined in chapter 2, using StAMPS I processed data from the ENVISAT satellite for three ascending tracks (from west to east): 14, 243, and 200, and two descending tracks: 336, and 64. This data covers the period from 2002-2010 and consists of 134 scenes, covering a region of Western Turkey that is 300 km by 400 km in extent. Figure 5.3 shows the location of each of the InSAR tracks overlaid on a fault map of the region. I generate a ratemap for each of the five tracks as outlined in section 3.3.

To make corrections for orbital phase errors, I first make an initial estimate of deformation using the GPS velocities. The GPS data are taken from a combination of studies, listed in the caption to figure 5.2, given in the fixed Eurasia reference frame of *Reilinger et al.* (2006). In instances where more than one set of data are available, for an individual site, I combine the velocities using the inverse of the variances to weight the data. To make a velocity map from the GPS data I interpolate the east and north components of the velocities, separately using Delauny triangulation. I then use bilinear interpolation within each triangle from the velocities at the vertices. I filter these gridded velocities using a 50 km diameter Gaussian filter and project them into the LOS of the satellite, using the incidence angle of the satellite. I subtract the result from the stacked, processed PS InSAR data. I then invert for an orbital plane, as described in section 2.5, on the difference between the LOS velocity estimated from GPS and that measured using PS InSAR.

I find many of the tracks have high levels of incoherence compared with Tibet, and significant atmospheric effects correlated with coastal proximity, so I choose a subset of the data with smaller perpendicular baselines for PS selection. The temporal and perpendicular baselines for each of the tracks is shown in figure 5.4 with the chosen subset of data indicated.

PS selection criteria for each track

Track No	density rand	merge resamp size	unwrap grid size	unwrap time win	weed σ	weed time win
14	30	30	200	750	0.9	750
243	30	200	1000	750	0.8	750
200	30	200	1000	750	0.8	750
336	30	200	1000	750	0.8	750
64	20	300	1000	365	0.7	365

Table 5.1: PS parameter selection criteria for each track where different values are used. Refer back to the text for parameters that were consistent for all tracks. PS selection was performed using StAMPS with the same PS being used for each interferogram in the time series. Abbreviations: window (win), resample (resamp), random (rand), standard deviation(σ)

Number of PS points selected for each track

Track Number	Number of PS points
14	777536
243	247698
200	240821
336	320577
64	293500

Table 5.2: PS selection was performed using StAMPS with the same PS being used for each interferogram in a time series.

I use ECMWF ERA interim re-analysis data to correct for atmospheric effects as described in section 2.4.2, as less than 40 % of MERIS scenes were useable due to cloud cover. As discussed in section 2.4.3 an amplitude scaling factor is applied to the total ECMWF correction. In this case, as GPS data in the region is abundant, I perform a least squares fit for an amplitude scaling factor on the residuals between the GPS LOS velocities and the PS InSAR data (after correcting for orbital phase errors).

I processed all five InSAR tracks with: a **clapeyron low pass wavelength** of 800 m, **clapeyron window** of 64, a **filter grid size** of 50 m, a **maximum topographic error** of 5 m, **scn time window** of 365 days, **scn wavelength** of 100 m

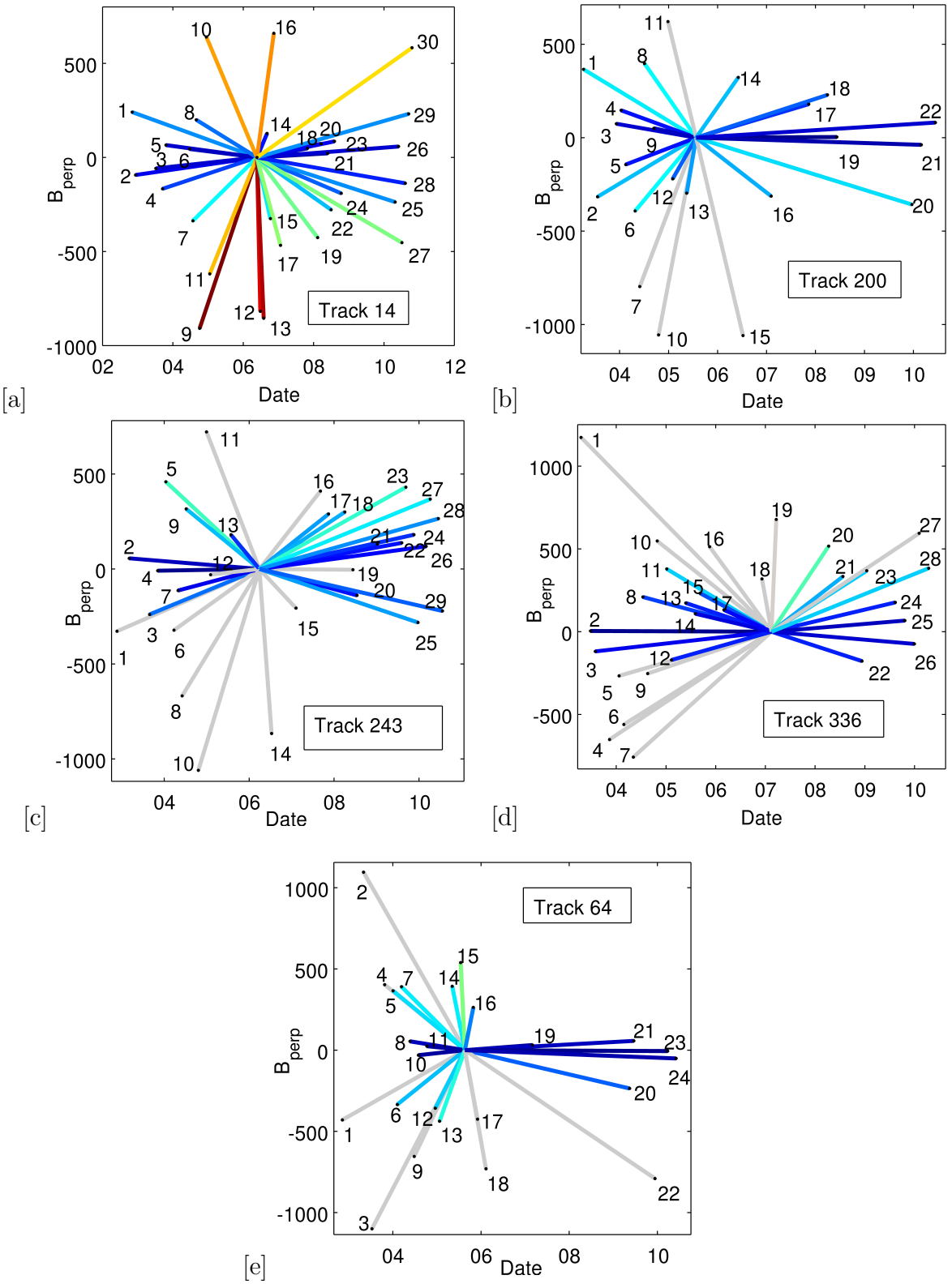

Figure 5.4: Perpendicular baselines in meters are shown for tracks [a] 14, [b] 200, [c] 243, [d] 336, and [e] 34. Lines are colour coded according to the perpendicular distance between each satellite pass and the master date is shown in table 5.3. Grey lines indicate those dates excluded from PS selection and stacking to improve signal to noise ratio.

Key showing the dates of satellite passes represented by the numbers in figure 5.4

No	Track 14	Track 200	Track 243	Track 336	Track 64
1	20021105	20030407	20021121	20030417	20021109
2	20021210	20030721	20030306	20030626	20030503
3	20030708	20031208	20030828	20030731	20030712
4	20030916	20040112	20031106	20031113	20031025
5	20031021	20040216	20040115	20040122	20040103
6	20040622	20040426	20040325	20040226	20040207
7	20040727	20040531	20040429	20040506	20040313
8	20040831	20040705	20040603	20040715	20040522
9	20041005	20040913	20040708	20040819	20040626
10	20041214	20041018	20041021	20041028	20040731
11	20050118	20041227	20041230	20050106	20041009
12	20060627	20050131	20050203	20050210	20041218
13	20060801	20050516	20050728	20050526	20050122
14	20060905	20060605	20060713	20050804	20050507
15	20061010	20060710	20070208	20050908	20050716
16	20061114	20070205	20070906	20051117	20050820
17	20070123	20071112	20071115	20060302	20051029
18	20071030	20080331	20080403	20061207	20051203
19	20080212	20080609	20080612	20070322	20060211
20	20080318	20091221	20080717	20080410	20070303
21	20080527	20100301	20090108	20080724	20090516
22	20080701	20100614	20090806	20081211	20090620
23	20080805		20090910	20090115	20091212
24	20081014		20091119	20090813	20100327
25	20100427		20091224	20091022	20100605
26	20100601		20100304	20091231	
27	20100706		20100408	20100204	
28	20100810		20100617	20100415	
29	20100914		20100722		
30	20101019				
master	**20060523**	**20050725**	**20060330**	**20070215**	**20050820**

Table 5.3: Key showing the dates of satellite passes represented by the numbers in perpendicular baseline plots for Western Turkey.

and with **weed zero elevation** set to yes (refer back to chapter 2 for a summary of the meaning of each of the parameters). Where I have chosen different values for selection parameters to process different tracks, these parameters are shown in table 5.1. In Tibet the PS selection was changed between tracks mainly by altering the **density random** to enable more points to be selected south of the Kunlun Fault, which was generally more incoherent than to the north. However, in Western Turkey incoherence was not shown to be limited to particular regions. Because there are also more scenes available for most tracks, instead I could address incoherence by using a subset of the data with shorter perpendicular baselines. As a consequence,

the main variation in selection criteria is for the **weed phase standard deviation**, which varies from 0.7 to 0.9. The greatest difference in parameters is for track 14, in order to account for the large proportion of sea contained within that track. The number of PS selected for each track is shown in table 5.2.

5.4 PS InSAR ratemaps for Western Turkey

Figures 5.5-5.9 show ratemaps generated using the procedures outlined in sections, 2, 2.5, 3.3, and 5.3, for each of the five tracks. I generated average profiles for each track, which are shown in figures 5.5-5.9 [d] for the LOS velocity from GPS, and PS InSAR. This was done by projecting the LOS velocities onto a profile running parallel to the track heading direction, as shown earlier in section 3.5.2. For all five tracks good agreement is shown with the GPS (in the top middle panel and for the profile in the bottom panel). The magnitude of the atmospheric signal (top right panel) is seen to be small compared to the tectonic signal.

Change in relative LOS velocity across the North Anatolian Fault (NAF) consistent with right-lateral strike-slip motion is observed in both the GPS and InSAR data for track 336. Track 64 shows motion consistent with right lateral interseismic strain accumulation in the GPS. However in the InSAR overlap between strain accumulation for the northern and southern strands of the NAF results in a gentler slope and larger apparent locking depth. Without data further northwards we miss the flattening of the arctan function. For tracks 64 and 336 the signal is dominated by motion on the north section of the fault with any motion across the southern section approximately a fifth of the magnitude. For track 243 from 200 km southwards on the profile we observe change in LOS velocity consistent with right lateral

motion. In the proximity of the Marmara Sea on track 243 the interseismic signal is complicated by coastal subsidence and uplift. Tracks 200 and 14 do not extend sufficiently far north to cover the NAF.

For track 64, the slip rate appears to be much lower for the NAF than is indicated by the GPS data. This can be explained by the fact that track 64 covers the 1999 Izmit earthquake, and the GPS data covers the period 1997-2005 (mostly after 1999) whereas the InSAR data spans 2003-2010. We would therefore expect the InSAR to have a lower component of postseismic signal, as we would expect this to decay with time after the earthquake. Furthermore, track 336, which is further from the earthquake epicentre, matches the GPS to within error. Similarly, track 243, which covers the Ms 7.3 1953 earthquake, on the western end of the NAF, also gives good agreement with the GPS data.

Based on the 95 % confidence interval of the data, any interseismic signal localised across individual grabens would need to be greater than 2 mm/yr, in the satellite LOS, to be reliably modelled. Nevertheless, in the central section of the tracks, there is approximately 2 mm/yr change in satellite LOS velocity, associated with extension across the grabens; this is equivalent to ∼6 mm/yr of ground motion. This localised signal is seen to be strongest for track 243 shown in figure 5.7. The InSAR data covering the five main grabens all agree with the GPS to within error (actual locations of GPS data points are indicated later in figure 5.16). Furthermore, by combining the GPS and InSAR data to generate a velocity map (as shown later in section 5.7) we can reduce these errors.

Towards the south, for each of the descending tracks (200, 243, 14), anti-clockwise rotational motion results in a greater component of the velocity projected in LOS away from the satellite. This is observed, in figures 5.5, 5.7, and 5.9 as a downward trend (north to south). Conversely an upward trend is seen in figures 5.6 and 5.8 for

ascending profiles (tracks 64, 336). These trends relating to anti-clockwise rotation are approximately 5 mm in the LOS of the satellite over a region of ∼100-150 km.

For track 14 we see the coseismic signal associated with the 2005 Izmir earthquakes. I show results for this track with these earthquakes included in figure 5.9 (d) and then an additional profile with these events masked in figure 5.9 (e). This masked profile results in much better agreement with the GPS data.

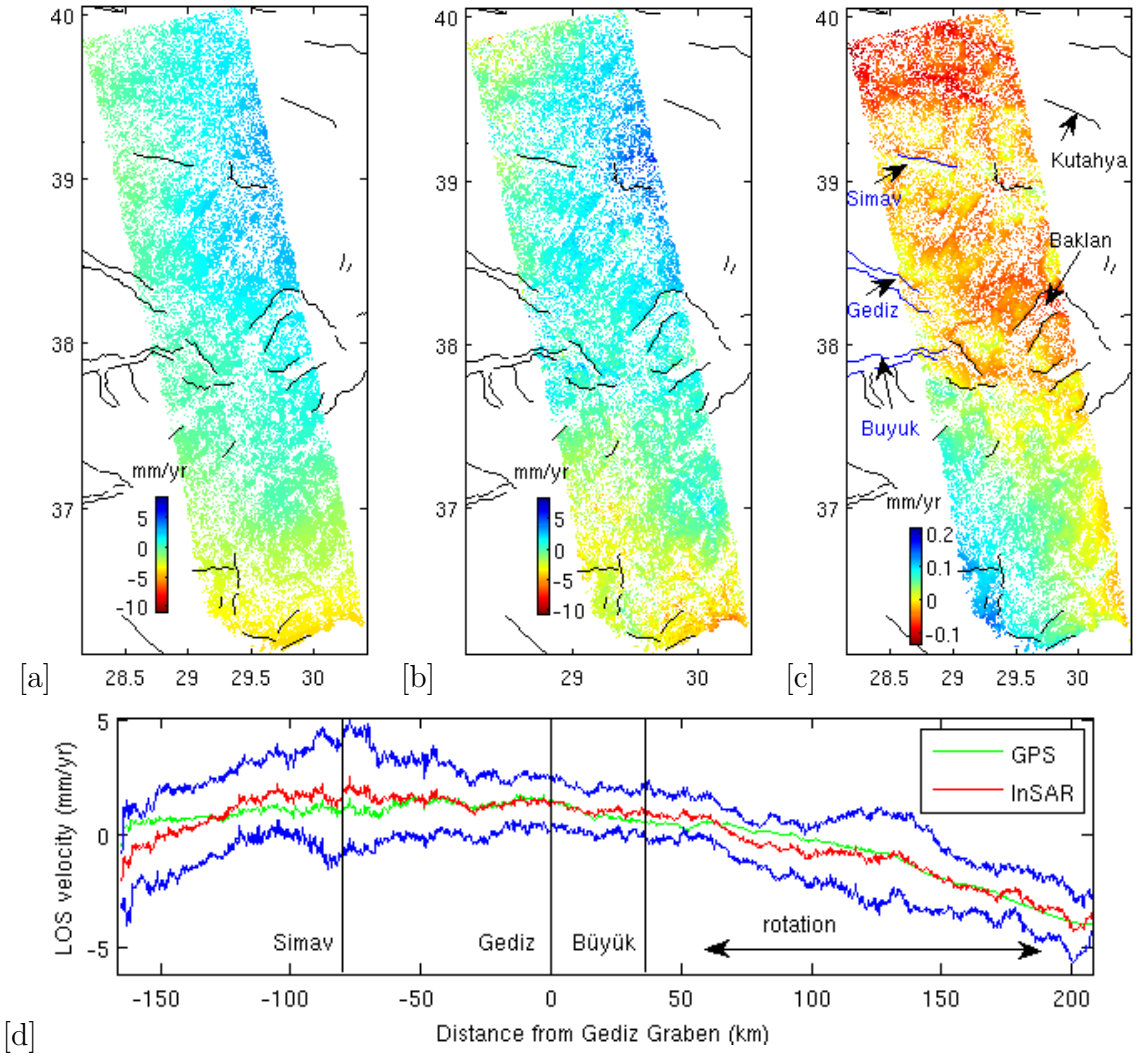

Figure 5.5: Track 200 (a)LOS velocity for GPS data (b) LOS velocity map after removing atmospheric effects and orbital errors for PS InSAR (c) scaled LOS velocity for atmospheric effects modelled using ECMWF data (d) Average profile of velocity map for the GPS data projected into LOS is shown in green, the PS InSAR LOS velocity as for (b) is shown in red and 1 sigma error bounds from the average profile are shown in blue. RL=right lateral.

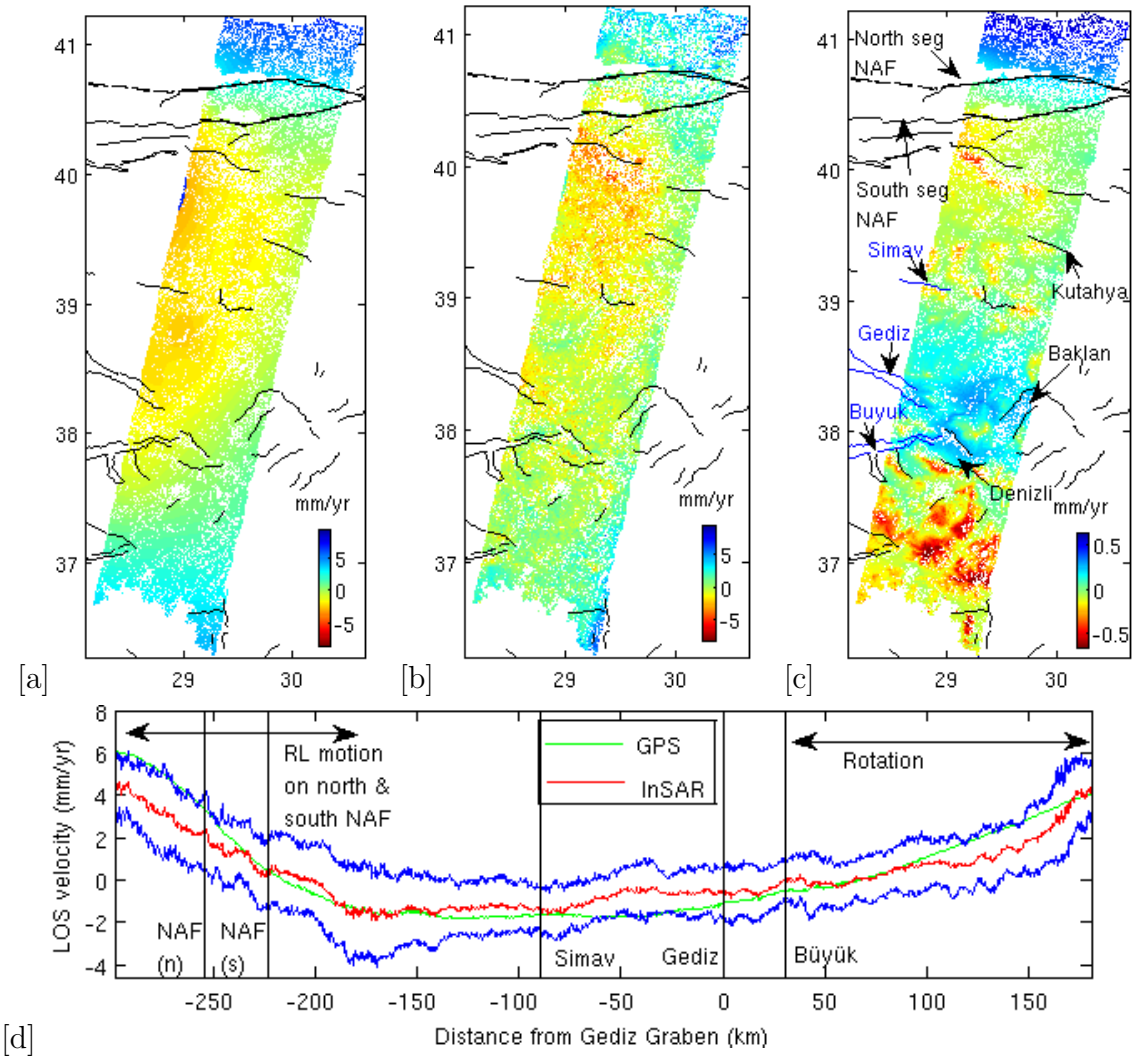

Figure 5.6: Track 64 (a)LOS velocity for GPS data (b) LOS velocity map after removing atmospheric effects and orbital errors for PS InSAR (c) scaled LOS velocity for atmospheric effects modelled using ECMWF data (d) Average profile of velocity map for the GPS data projected into LOS is shown in green, the PS InSAR LOS velocity as for (b) is shown in red and 1 sigma error bounds from the average profile are shown in blue. RL=right lateral.

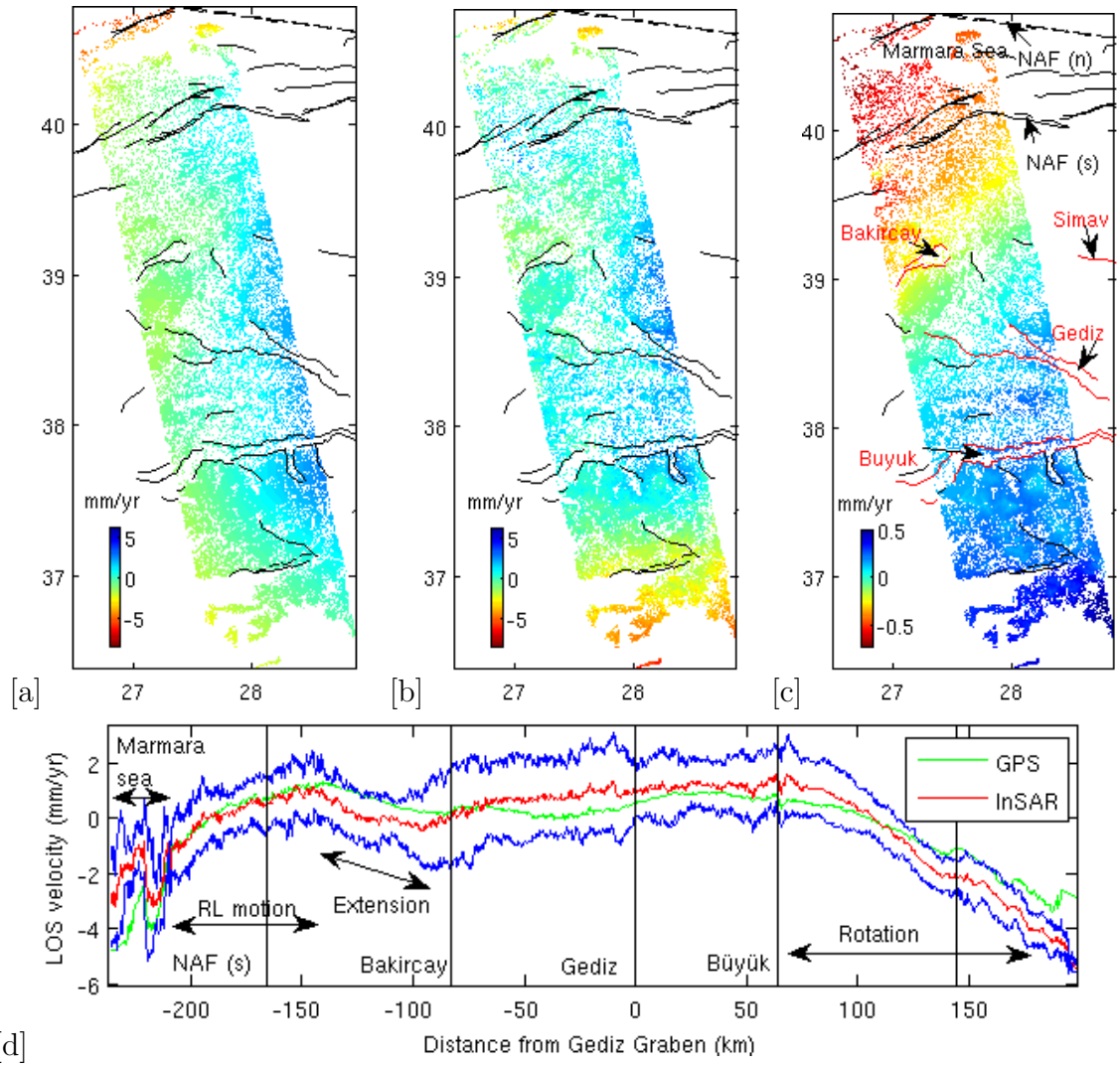

Figure 5.7: Track 243 (a)LOS velocity for GPS data (b) LOS velocity map after removing atmospheric effects and orbital errors for PS InSAR (c) scaled LOS velocity for atmospheric effects modelled using ECMWF data (d) Average profile of velocity map for the GPS data projected into LOS is shown in green, the PS InSAR LOS velocity as for (b) is shown in red and 1 sigma error bounds from the average profile are shown in blue. RL=right lateral.

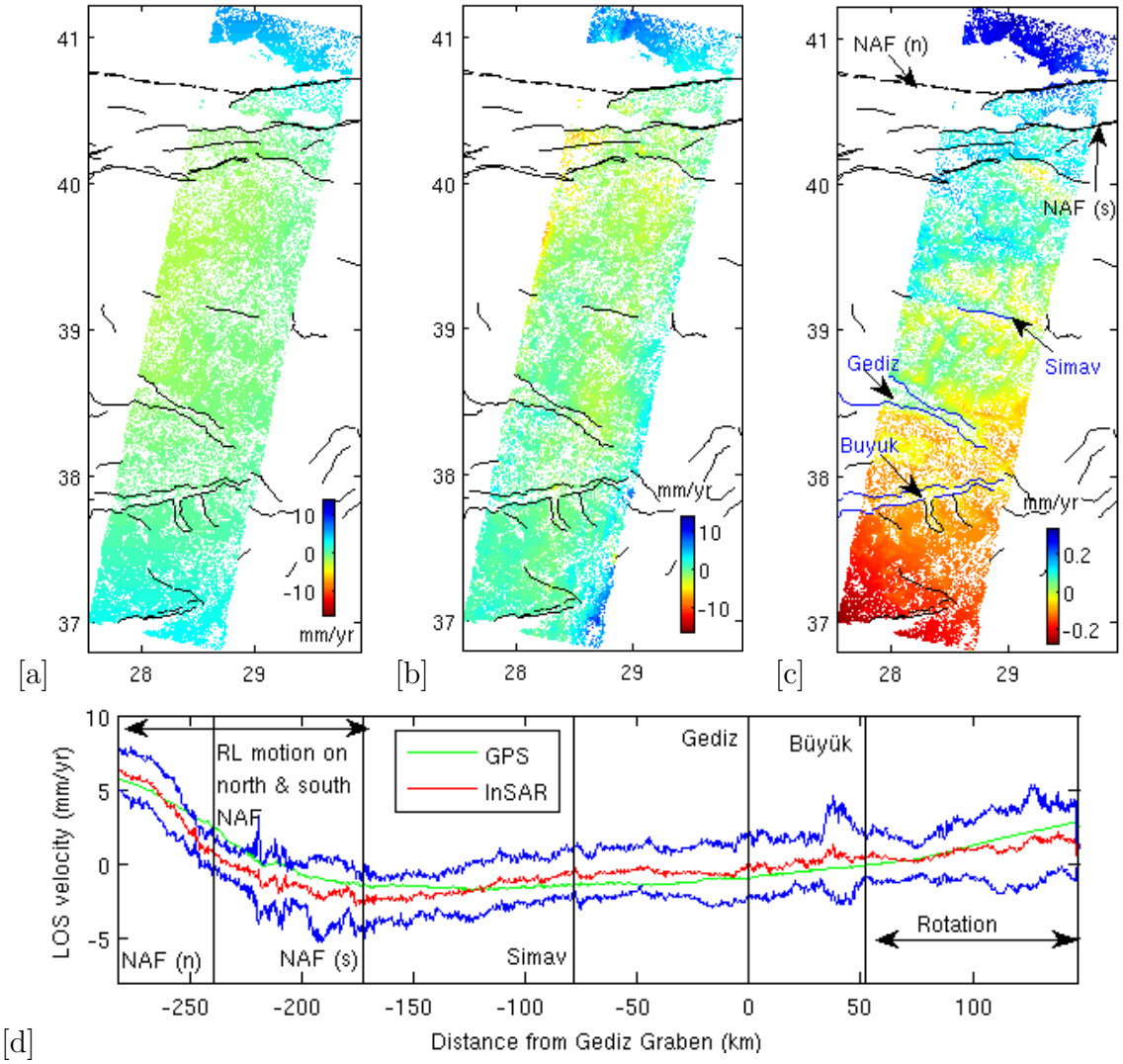

Figure 5.8: Track 336 (a)LOS velocity for GPS data (b) LOS velocity map after removing atmospheric effects and orbital errors for PS InSAR (c) scaled LOS velocity for atmospheric effects modelled using ECMWF data (d) Average profile of velocity map for the GPS data projected into LOS is shown in green, the PS InSAR LOS velocity as for (b) is shown in red and 1 sigma error bounds from the average profile are shown in blue.

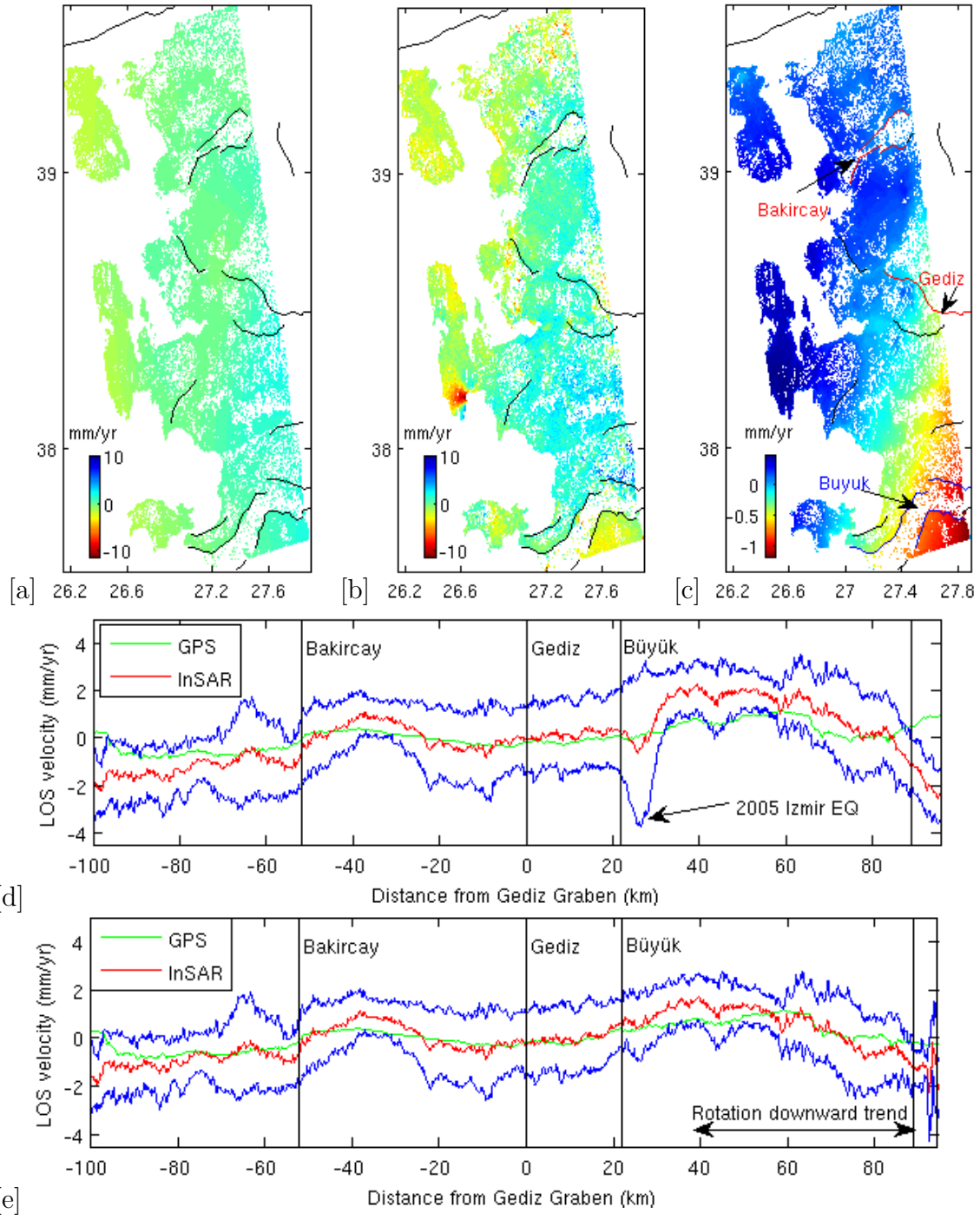

Figure 5.9: Track 14 (a)LOS velocity for GPS data (b) LOS velocity map after removing atmospheric effects and orbital errors for PS InSAR (c) scaled LOS velocity for atmospheric effects modelled using ECMWF data (d) Average profile of velocity map for the GPS data projected into LOS is shown in green, the PS InSAR LOS velocity as for (b) is shown in red and 1 sigma error bounds from the average profile are shown in blue. (e) Average profile of velocity map for track 14 as for (d) but with the 2005 Izmir earthquakes masked. RL=right lateral.

5.5 Constructing a velocity field using both GPS and PS InSAR

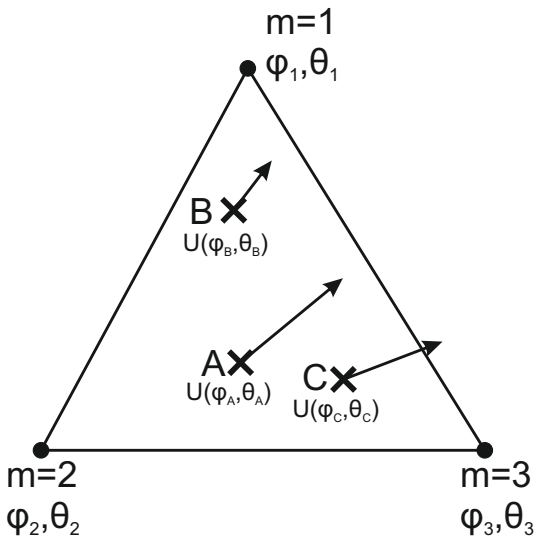

Figure 5.10: Definition sketch for velocity field inversion taken from *Walters* (2012). m=1, 2 and 3 are the three vertices of the triangle, moving at velocities $\mathbf{u}_1$, $\mathbf{u}_2$ and $\mathbf{u}_3$. A, B and C are three points within the triangle where horizontal GPS velocities have been measured.

The PS InSAR line of sight velocity is combined with existing GPS measurements in order to construct a velocity field for Western Turkey. I use the approach of *Haines* (1982) to relate the observed strain rate to a continuous velocity field. I adapt this method as per *England and Molnar* (1997) to apply this technique to an arbitrary triangular mesh (shown in figure 5.11) solving for the velocities at each node. This assumes a homogeneous strain rate within each triangle so velocity varies linearly with latitude and longitude within each triangle. I then combine GPS and InSAR data using the Laplacian smoothing approach of *Wang and Wright* (2012).

Following *England and Molnar* (1997), the velocity at any point within a triangle **U** can be related to the velocities at its vertices, assuming a homogeneous strain

rate by:

$$\mathbf{U}(\phi,\theta) = \sum_{m=1}^{3} N_m \mathbf{u}_m \tag{5.1}$$

where θ and ϕ are the latitude and longitude, N_m is the interpolation or shape function and $\mathbf{u}_m$ is the velocity at vertex m. The shape function defines the relationship that interpolates the solution at any point in the triangle to the discrete values obtained at the mesh nodes and is given by:

$$N_m = a_m + b_m\phi + c_m\theta \tag{5.2}$$

where a_m are the coefficients for each of the vertices of the triangle m. For the vertex $m = 1$, the coefficients of the shape function are given by:

$$a_1 = (\phi_2\theta_3 - \phi_3\theta_2)/\Delta \tag{5.3}$$

$$b_1 = (\theta_2 - \theta_3)/\Delta \tag{5.4}$$

$$c_1 = (\phi_3 - \phi_2)/\Delta \tag{5.5}$$

where

$$\Delta = \phi_1(\theta_2 - \theta_3) + \phi_2(\theta_3 - \theta_1) + \phi_3(\theta_1 - \theta_2) \tag{5.6}$$

Likewise, the shape function for vertices 2 and 3 are given by cyclic permutation of the subscripts 1, 2 and 3 respectively. The design matrix for the inversion $\mathbf{A_{gps}}$ consists of these shape functions (*Walters*, 2012).

Figure 5.10 defines each of the parameters for a velocity field inversion using GPS data. For a velocity map of GPS data the equation 5.1 can be re-written so $\mathbf{U}$ are the observed GPS velocities, $\mathbf{d}_{gps}$, and $\mathbf{u}_m$ are the model parameters which are solved for using the design matrix $\mathbf{A}_{gps}$ (*Walters*, 2012):

$$\mathbf{A}_{gps}\mathbf{m}_{vel} = \mathbf{d}_{gps} \tag{5.7}$$

I then combine the GPS and InSAR velocities and apply a Laplacian smoothing constraint to regularise the observations using the approach of *Wang and Wright* (2012). The InSAR LOS velocities, $\mathbf{X}_{LOS}$ are related to the velocity at a given vertex by:

$$\mathbf{X}_{LOS}(\phi,\theta) = \sum_{m=1}^{3} N_m \mathbf{u}_m \cdot \mathbf{Z}_{LOS} \tag{5.8}$$

where $\mathbf{Z_{LOS}}$ is the vector joining the satellite to a point on the ground in latitude and longitude. The formulation of the inverse problem combining our observations is then given by:

$$\begin{pmatrix} \mathbf{A}_{gps} & 0 \\ \mathbf{A}_{sar} & \mathbf{A}_{orb} \\ \kappa^2\nabla^2 & 0 \end{pmatrix} \begin{pmatrix} \mathbf{m}_{vel} \\ \mathbf{m}_{orb} \end{pmatrix} = \begin{pmatrix} \mathbf{d}_{gps} \\ \mathbf{d}_{sar} \\ 0 \end{pmatrix} \tag{5.9}$$

where $\mathbf{d}_{sar}$ is the observation vector consisting of the PS InSAR LOS velocities ($\mathbf{X}_{LOS}$), $\mathbf{A}_{sar}$ is the design matrix made up of the shape functions and local LOS unit vectors, $\mathbf{A}_{orb}$ is the orbital design matrix to solve for orbital phase errors in the PS InSAR data and $\mathbf{m}_{orb}$ are the orbital parameters for each PS InSAR observation (*Walters*, 2012).

I correct for any orbital errors using the GPS data when generating the InSAR rate maps. I therefore just solve for a static offset for each ratemap, $\mathbf{m}_{orb}$, and $\mathbf{A}_{orb}$ in 5.9 is given by:

$$\begin{pmatrix} A^1_{orb} & 0 & \dots & 0 \\ 0 & A^2_{orb} & \dots & 0 \\ \vdots & \vdots & \vdots & \vdots \\ 0 & 0 & \dots & A^n_{orb} \end{pmatrix} \tag{5.10}$$

where A^i_{orb} is a column vector of ones for the ith of n ratemaps.

I solve the system of equations in 5.9 using a weighted least squares inversion:

$$\mathbf{m} = \underbrace{[\mathbf{A}^T\mathbf{\Sigma}_d^{-1}\mathbf{A}]^{-1}}_{\mathbf{\Sigma}_m} \mathbf{A}^T\mathbf{\Sigma}_d^{-1}\mathbf{d} \tag{5.11}$$

where $\mathbf{\Sigma}_d$ is the full variance-covariance matrix for the observations, formed from the formal uncertainties of the GPS data and the full covariance matrix of InSAR data.

To account for the velocities of some vertices being overdetermined and those of others being underdetermined we regularise our data using Laplacian smoothing; here κ^2 is a smoothing factor that determines the strength of the smoothing, and $\bigtriangledown^2$ is a discretised approximation of the Laplacian smoothing operator, given by, (*Desbrun et al.*, 1999):

$$L(x_i) = \frac{2}{\sum_{j\in N_1(i)} |e_{ij}|} \sum_{j\in N_1(i)} \frac{x_j - x_i}{|e_{ij}|} \tag{5.12}$$

where x_i and x_j are components of velocities at vertices i and j, $|e_{ij}|$ is the length of the edge e_{ij} joining the two vertices, and $N_1(i)$ is the number of vertices neighbouring vertex i. A comparison of the results for a range of smoothing factors is given in the next section.

5.6 A velocity field for Western Turkey

I performed a velocity field inversion as described above using the VELMAP package developed by *Wang and Wright* (2012), adapting the front end to take PS InSAR data from StAMPS. I combined the PS InSAR ratemaps presented earlier in section 5.4 with the GPS data vectors shown in figure 5.2. Inputs for the velocity field

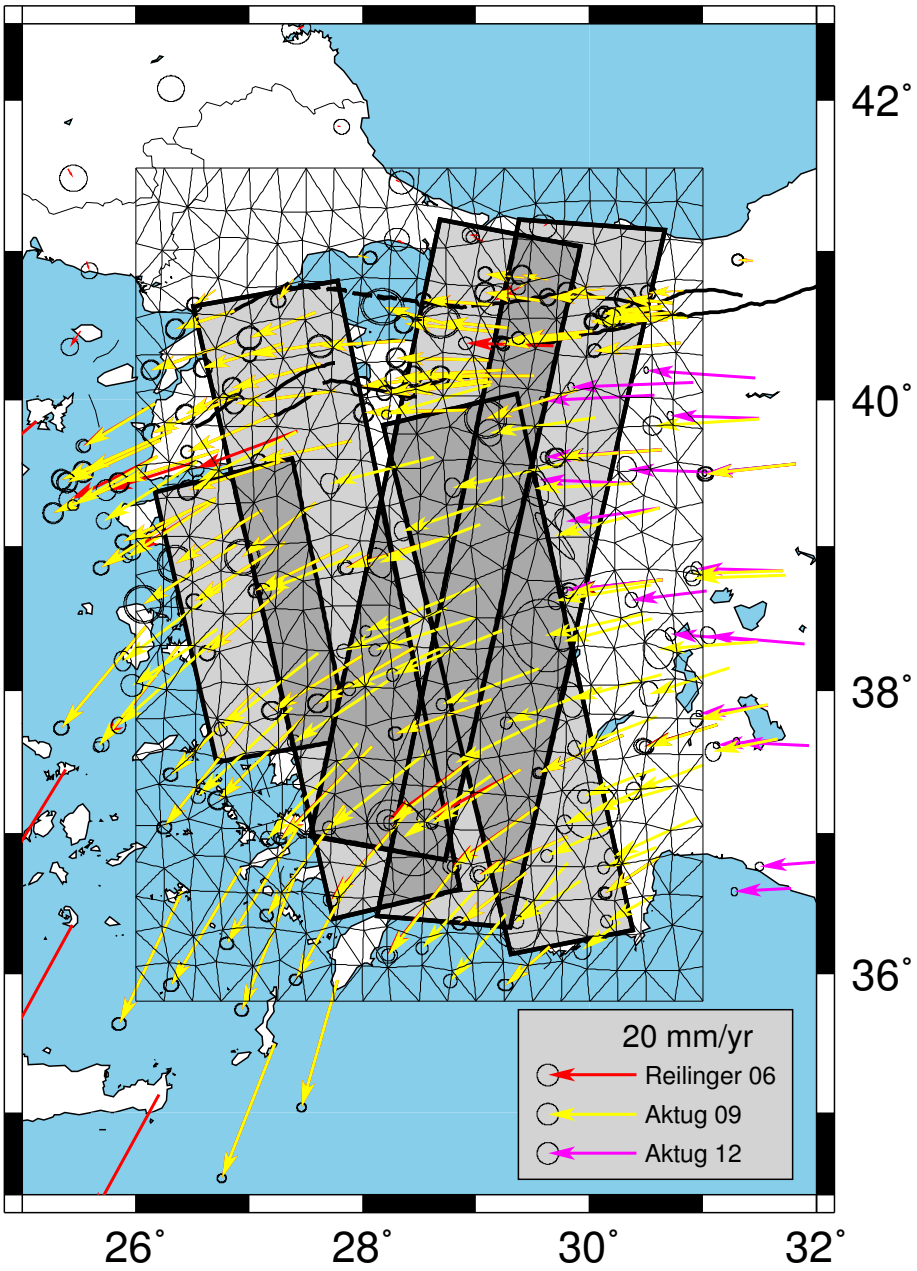

Figure 5.11: Map showing the velocity field inversion inputs. The input triangular mesh is indicated with black lines. The InSAR footprints for each of the five tracks are indicated in light grey with overlapping regions between tracks shown by the darker grey polygons. GPS vectors are shown in red for *Reilinger et al.* (2006), yellow for *Aktug et al.* (2009) and magenta for *Aktug et al.* (2012). The 95 percent error ellipses are shown by black circles.

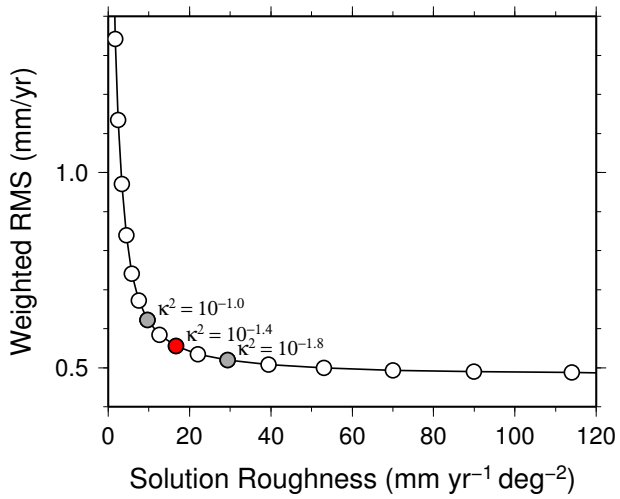

Figure 5.12: Plot showing the lcurve for the RMS misfit for a range of κ values trading off against solution roughness. The preferred smoothing factor is shown in red for $\kappa^2 = 10^{-1.4}$ with the oversmoothed and undersmoothed solution shown in figure 5.13 [a] and [d] , and [c] and [f], respectively indicated in grey.

inversion are shown in figure 5.11. I assumed that any vertical motion is below background noise levels and inverted for a 2D velocity field. This seems reasonable given that *Walters* (2012) showed vertical motions to be below background noise levels for Eastern Turkey. Furthermore, based on the GPS data, horizontal velocities are much greater than vertical velocities (*Aktug et al.*, 2009). As horizontal velocities were already difficult to detect across the grabens, vertical velocities would be negligible.

I test a range of Laplacian smoothing parameters for κ^2 from 1 to 0.001 to explore the trade off between the RMS misfit and the roughness of the solution. Figure 5.12 shows this trade off, and figure 5.13 compares the velocity fields and strain rates for three solutions that lie near the maximum point of curvature. My preferred solution is for $\kappa^2 = 10^{-1.4}$. This is equivalent to a solution roughness of 17 mm yr^{-1} deg^{-1} (over a region of approximately 100 km). This gives an RMS misfit of $\sim$0.55 mm/yr. Smoother solutions localise strain on the north segment of the

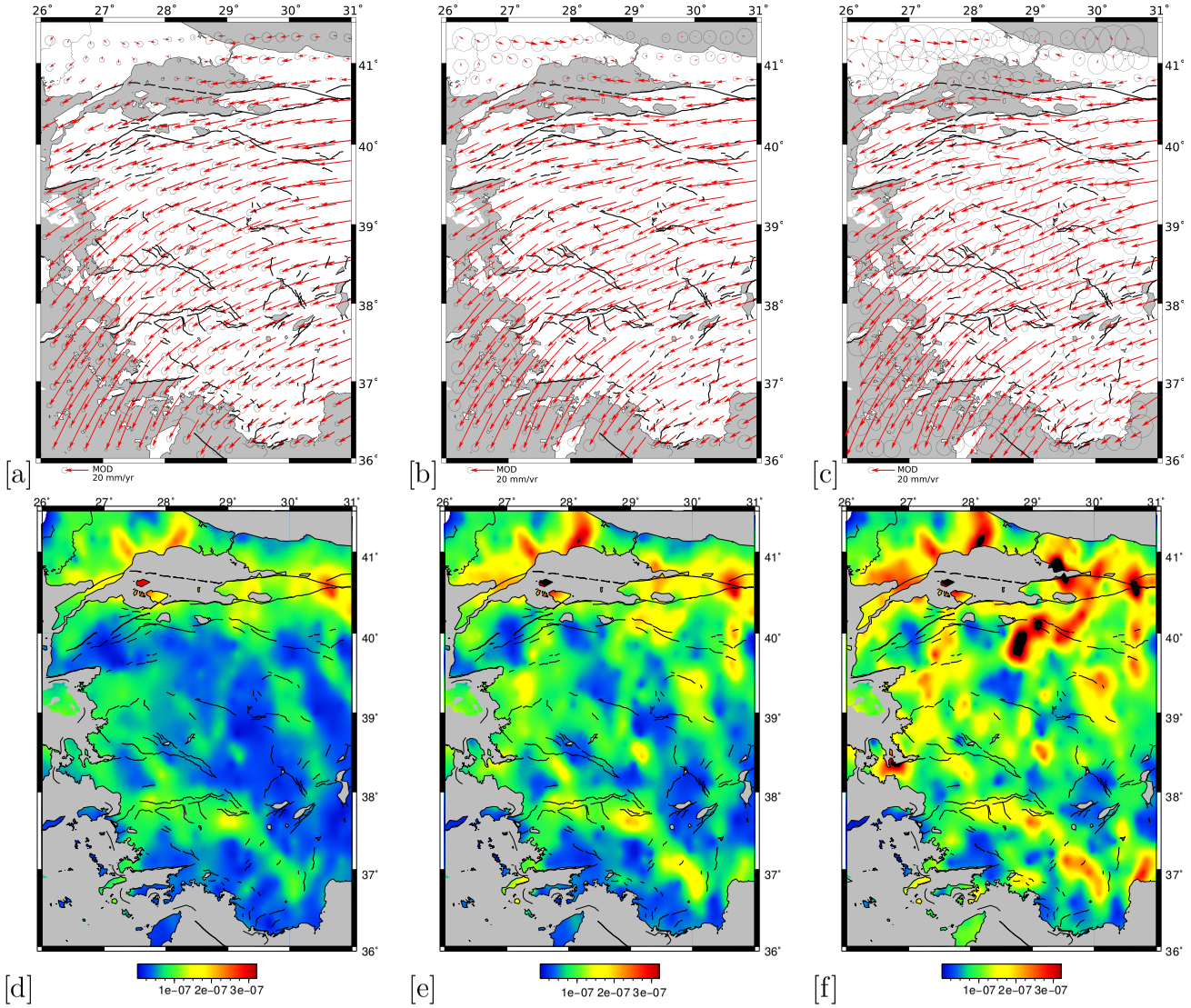

Figure 5.13: Comparison of different smoothing factors for a joint inversion of GPS and PS InSAR data. Top panel shows velocity field and the bottom panel shows the strain for κ values from left to right of $10^{1.0}$, $10^{1.4}$, $10^{1.8}$. Error ellipses are shown at the 2σ level shown as black circles.

NAF with some strain localised on the southern segment and the Büyük Menderes graben. However, for smoother solutions, the magnitude of these signals is not significantly greater than background levels, such as those seen in the relatively non deforming region further east towards the Anatolian Plateau. Rougher solutions result in little difference in strain rates across the northern section of the NAF and the southern segment. My preferred solution shows strain localised in the regions of known earthquakes and across some of the major grabens, and higher strain rates across the northern segment of the NAF compared to the southern segment.

The solution for the preferred smoothing factor has GPS residuals that are small as shown in figure 5.15. The largest residuals are in the region of the 1999 Izmit earthquake and the 2005 Izmir earthquakes where there may be mismatches and disagreement between the different datasets due to the amount of postseismic and coseismic signal that is included. Also larger residuals are seen just to the west of the Isparta traingle.

The enlarged figure, 5.14, shows the velocity field and strain rates for the preferred solution together with the principal strain rates for compression and extension. There are five major grabens in western Turkey across which we are looking for localised strain: the Bakirçay Graben, the Simav Graben, the Gediz Graben, the Büyük Menderes Graben, and the Küyük Menderes Graben. Strain rates of 80 nstrain/yr are found throughout Western Turkey, with strain rates of up to 150 nstrain/yr across small sections of some of the major grabens. In general, fairly uniform strain rates are seen across western Turkey, with any strain localisation being of short wavelengths on the order of 10-30 km.

Strain rates of 300 nstrain/yr are seen on the NAF, either side of the Izmit earthquake, to the west where the Ms 6.2 1963 earthquake occurred at point d, and to the east where the Ms 7.4 1967 earthquake occurred at point e, where the northern

and southern strands converge. Similar strain rates are seen to the west of Istanbul, north of the Marmara Sea at points a, b, and c. North-south extension is observed with strain rates of 150 to 200 nstrain/yr in the seismic gap marked f, between the Ms 6.8 1964 earthquake on the NAF, and the Ms 6.2 1956 earthquake (marked g) on an offshoot from the main fault strand, further east.

The highest rate of strain near the Bakirçay Graben is at point h, north of the mapped fault where the Ms 6.3 1939 earthquake occurred. The Gediz Graben and the Büyük Menderes Graben have highest strain rates at the point of maximum curvature of the faults (at points l, m, and n) but offset from the fault location to the south. Any curvature in the fault is likely to be associated with vertical motion which might explain the stronger signals in these areas. In the case of the Büyük Menderes Graben this offset of strain southwards may be due to grabens running perpendicular to the main graben on the southern side of the fault. At the easternmost tip of the Büyük Menderes Graben at point o where the Ms 5.9 1965 earthquake occurred strain rates are also relatively high at 140 nstrain/year.

The Gediz Graben generally has strain rates that are indistinguishable from background levels, with maximum strain rates of 100 nstrain/yr at its western end at point q, near Izmir. Similarly, strain rates across the Simav Graben are comparatively low with higher strain rates seen further south across the Selendi Basin at point r, in a region of NE-SW compression. Whilst there are no major faults in this region included in the Fault map of *Saroglu et al.* (1992) the $\sim$ 50 km wide region of the Selendi basin which lies between the Gediz Graben and the Simav Graben has been mapped by *Ciftci and Bozkurt* (2010) as having a series of NNE-SSW oriented normal faults. Further north and east at points i and j, in a region of NE-SW extension, high strain rates are also observed near the Ms 7.1 1970 earthquake and the Ms 6 1944 earthquake. The Isparta triangle is a relatively non deforming region,

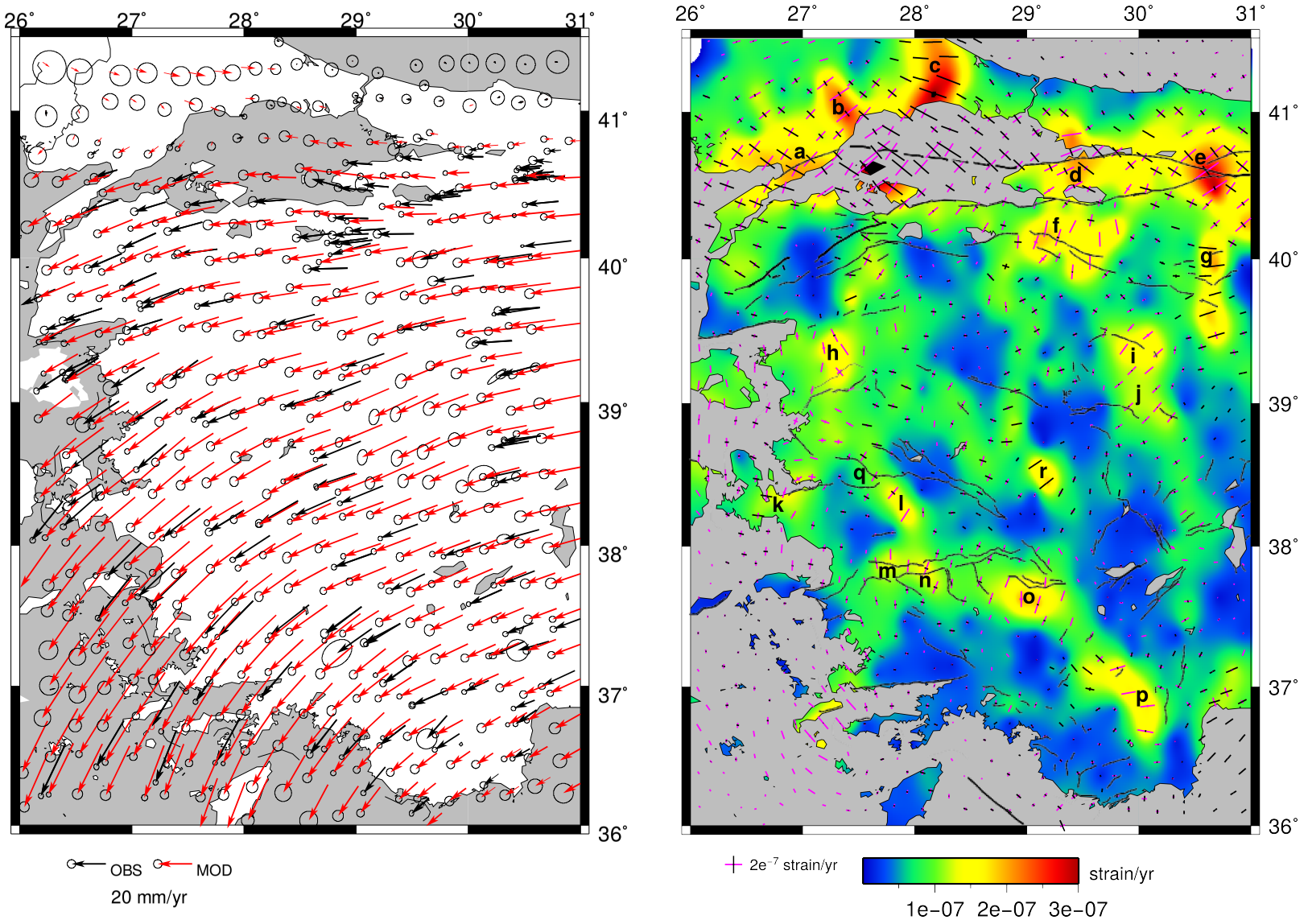

Figure 5.14: Map showing the best velocity field inversion results for a joint inversion with GPS and InSAR for $\kappa^2 = 10^{-1.4}$. The left hand panel shows the modelled velocity field in red with observed data shown in black and error ellipses at the 2σ level shown as black circles. The right hand panel shows the magnitude of the second invariant of the strain rate tensor derived from the velocities at the mesh vertices. The principal strain rates for compression are shown as black bars and for extension as magenta bars.

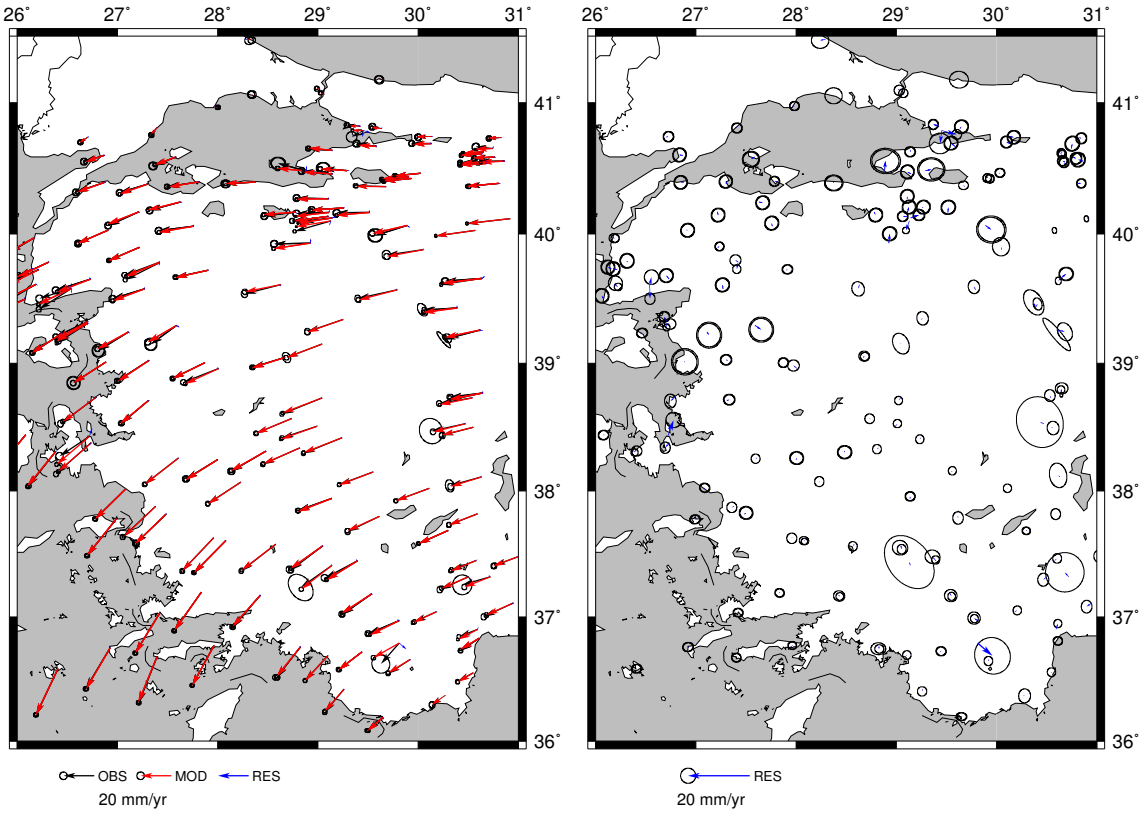

Figure 5.15: GPS data (black), models (red) and residuals (blue) for the velocity field. Error ellipses for the data and model velocity vectors are shown at the 2 σ level. Residual vectors alone are shown to the right with a scale twice that on the left.

but strain is also localised just west of here at point p where east-west extension is observed. However, large residuals are also seen here (see figure 5.15) so localised strain in this region may be an artifact due to discrepencies in the data.

5.7 Comparison between GPS and PS InSAR velocity and strain rate maps

I ran a series of experiments, in order to assess the information gain from measuring ground motion using PS InSAR, over sparsely located GPS data. I generated velocity maps and strain rate maps for 4 different scenarios as shown in figure 5.16 using: (i) all the available GPS data and PS InSAR data, (ii) only GPS data (marked as blue and red circles), (iii) only PS INSAR data in the region covered by each of the 5 tracks, with GPS data only outside this region (marked as blue circles), (iv) only a reduced set of the GPS data marked by the blue circles and no PS InSAR data (i.e. no data in the box covered by the 5 tracks).

The results of these experiments are shown in figures 5.17 and 5.18. I found that the velocity fields and strain rate maps for GPS and PS InSAR (figure 5.17 [a]) are largely the same as those for GPS only (figure 5.17 [b]). Only minor differences are seen with slightly higher strain rates for the joint inversion, north of the Selendi Basin, in the region of the 1944 and 1970 earthquakes (i and j in figure 5.14). Slightly higher strain rates are also seen on the eastern offshoot to the southern segment of the NAF, in the seismic gap between the 1964 earthquake and the 1956 earthquake (marked f in the enlarged figure 5.14). Marginally lower strain rates are seen for the joint inversion at the site of the 1965 earthquake (marked o in figure 5.14).

The greatest gain from adding PS InSAR data in a region such as Western Turkey which has a dense GPS network is in reducing errors, particularly in the east component. Adding the PS InSAR data reduces the uncertainty in the east-west component from 1.7 mm/yr to 1.3 mm/yr as seen in figure 5.19. This reduction in errors is particularly noticeable where there are few GPS observations near the 1970 earthquake (i and j in figure 5.14).

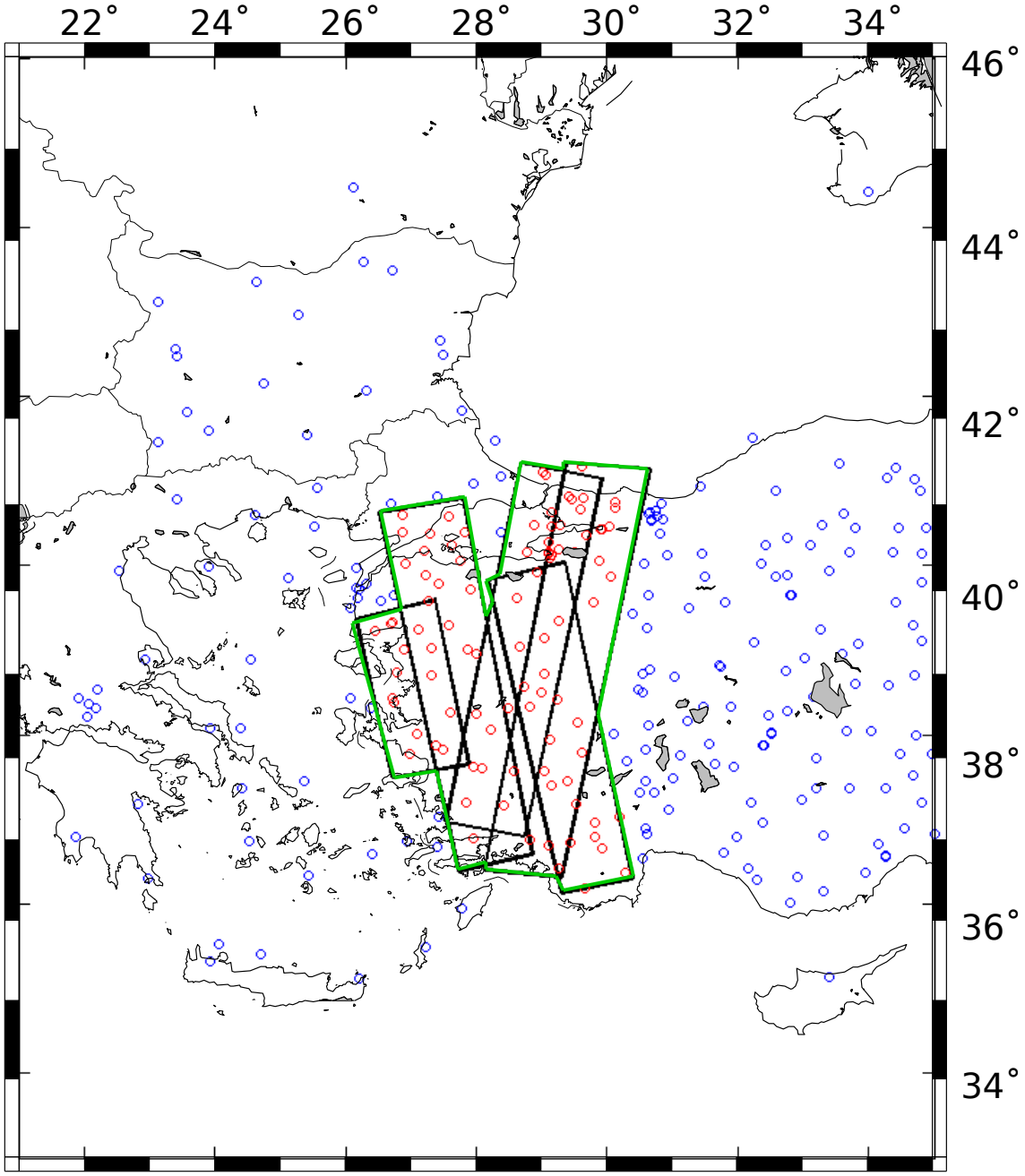

Figure 5.16: Plot showing the data used in test experiments for each of the scenarios described in the text. GPS data locations are indicated by circles and PS INSAR tracks by black boxes. Excluded GPS points are shown in red for scenarios (iii) PS InSAR data only and (iv) no data in the box (marked in green). All inversions use the GPS data indicated by the blue dots.

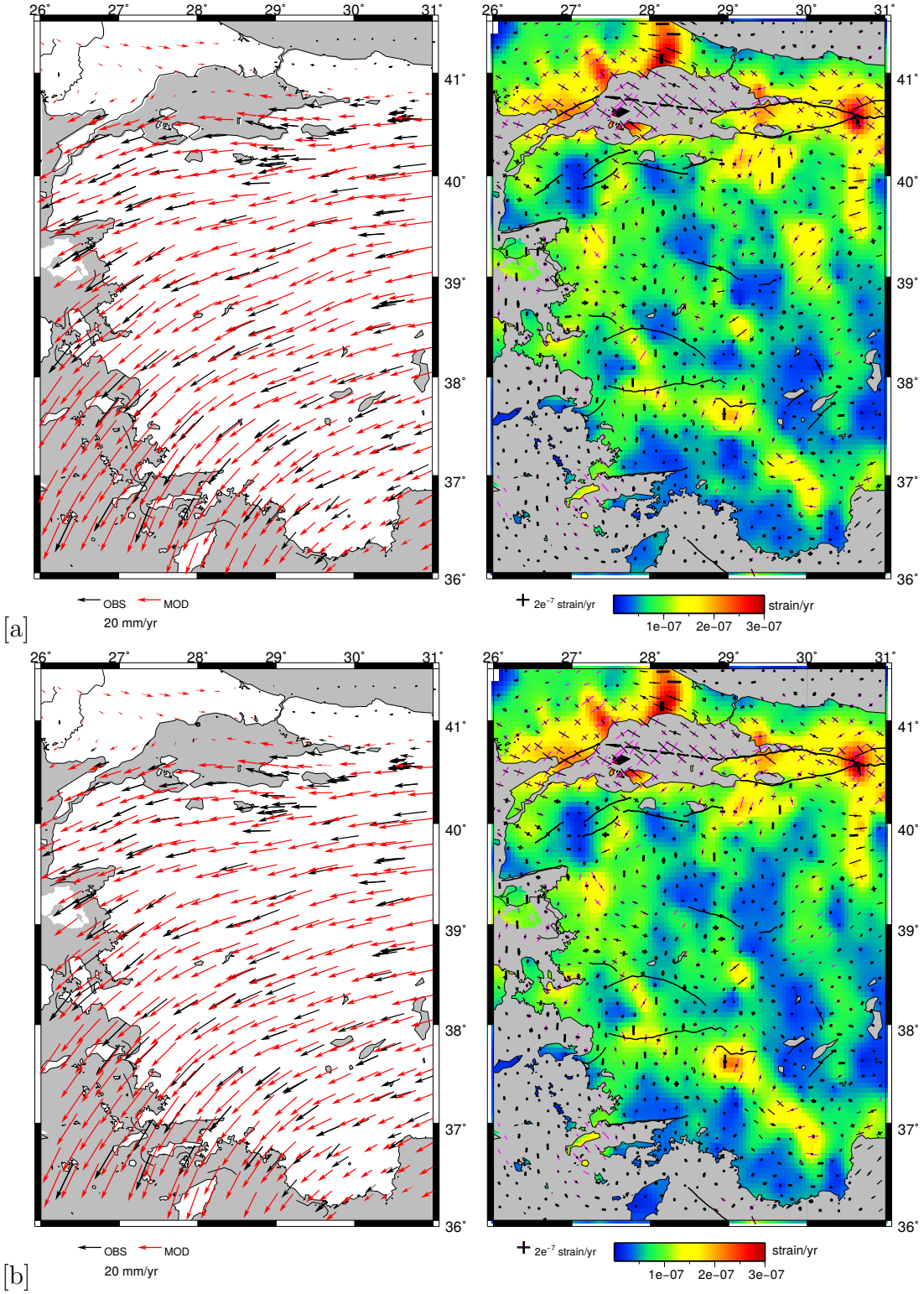

Figure 5.17: Comparison between velocity fields (left hand panel) and strain rates (right hand panel) for GPS and PS InSAR data (a) for all available GPS data and all five PS InSAR tracks (scenario (i) in the text), (b) for GPS data only (scenario (ii)), indicated by the blue and red circles in figure 5.16. Continued in figure 5.18

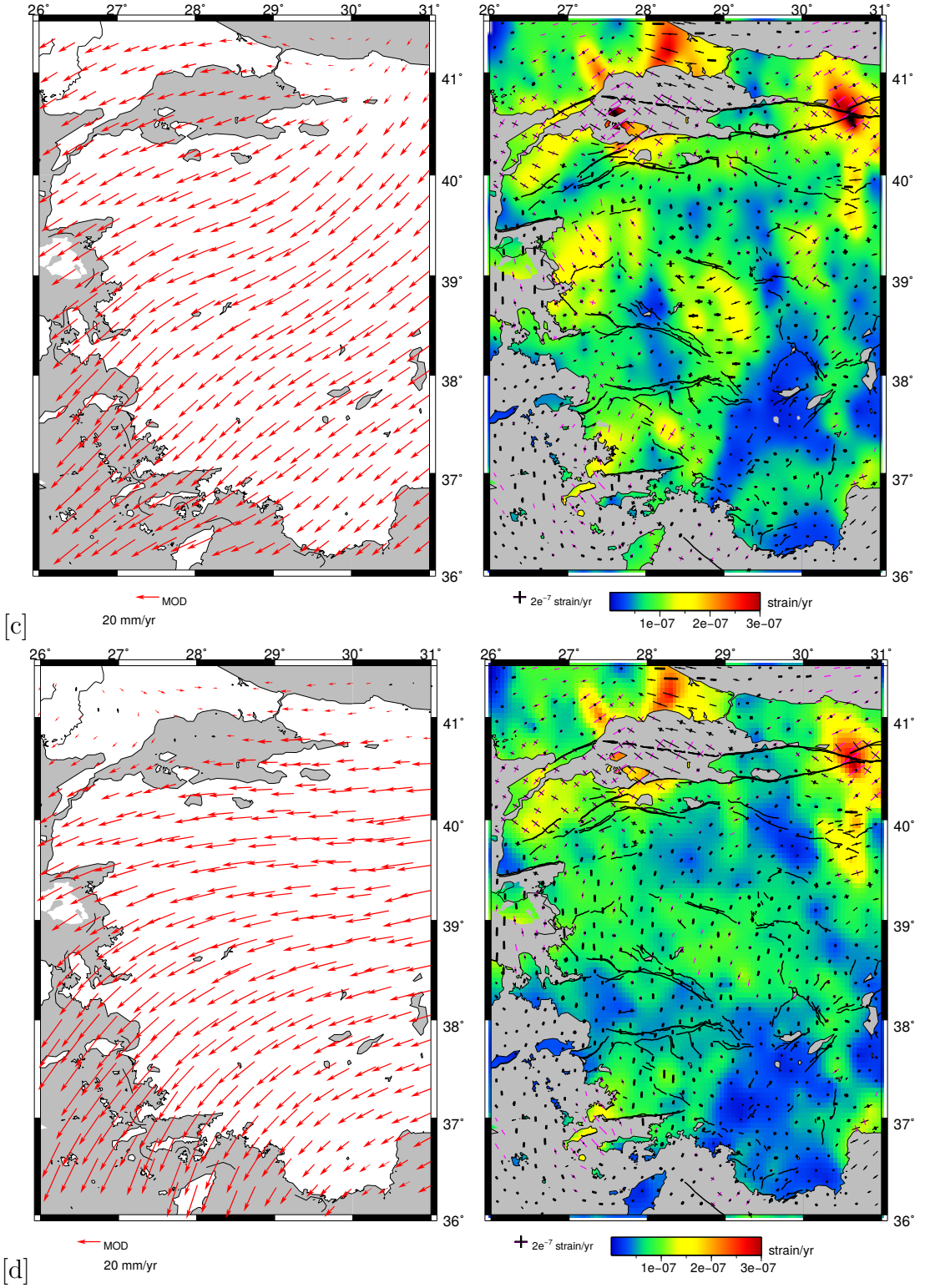

Figure 5.18: Continuation of figure 5.17, comparison between velocity fields (left hand panel) and strain rates (right hand panel) for GPS and PS InSAR data (c) for only GPS data outside the box (blue circles in figure 5.16) and only PS InSAR data inside the box (scenario (iii)), (d) using only GPS data outside the box (blue circles in figure 5.16) and no data inside the box (scenario (iv).

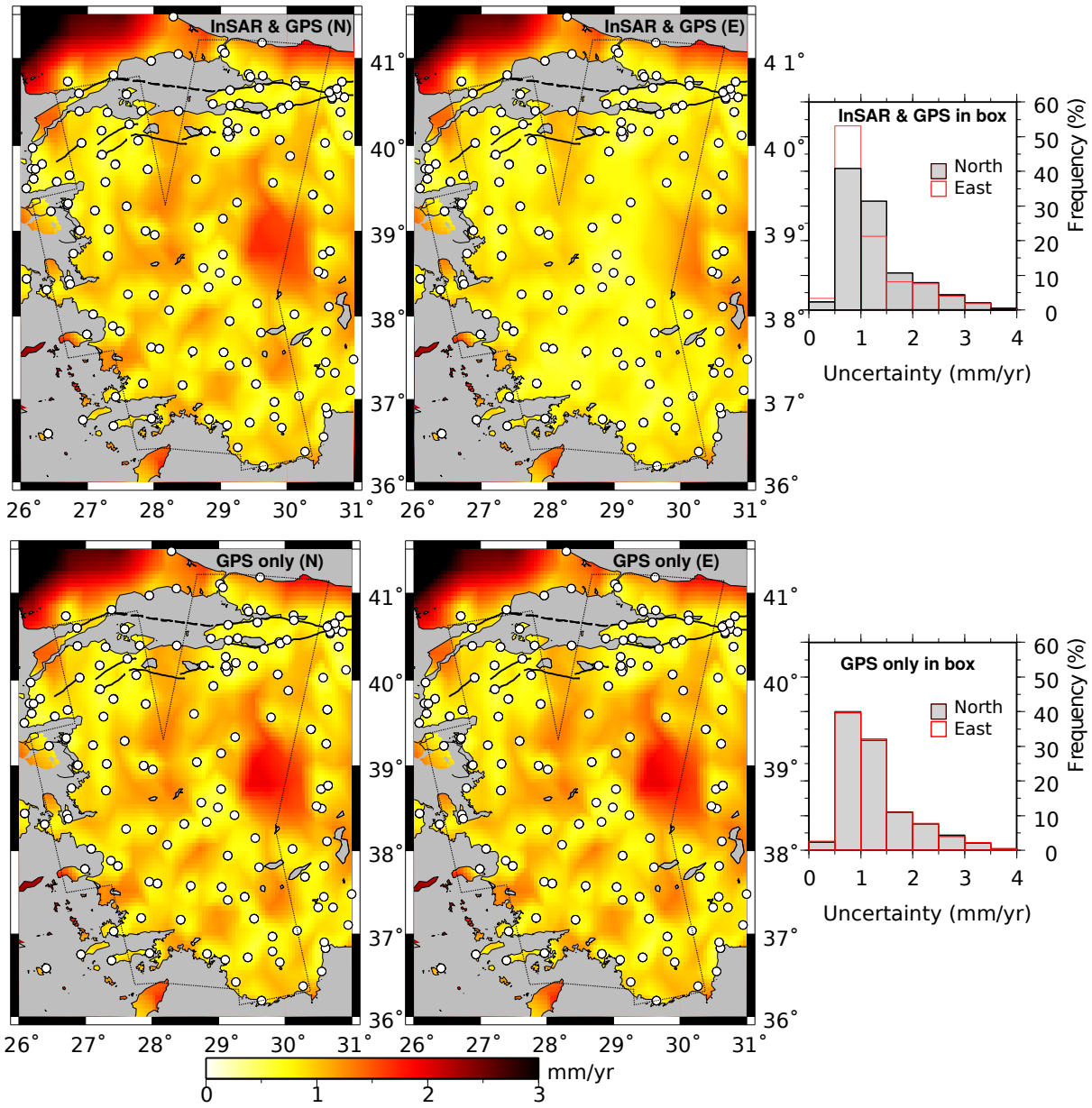

Figure 5.19: Histogram and spatial distribution of the uncertainties in the velocity field for a joint inversion of GPS and PS InSAR data (top panel) and for GPS data alone (bottom panel). GPS site locations are shown by the white circles.

I ran experiment (iv) to test how good a job the PS InSAR does in regions where only very sparse GPS data are available, for example in Tibet. I compare this to strain rate maps and velocity maps generated using no data in the box covered by

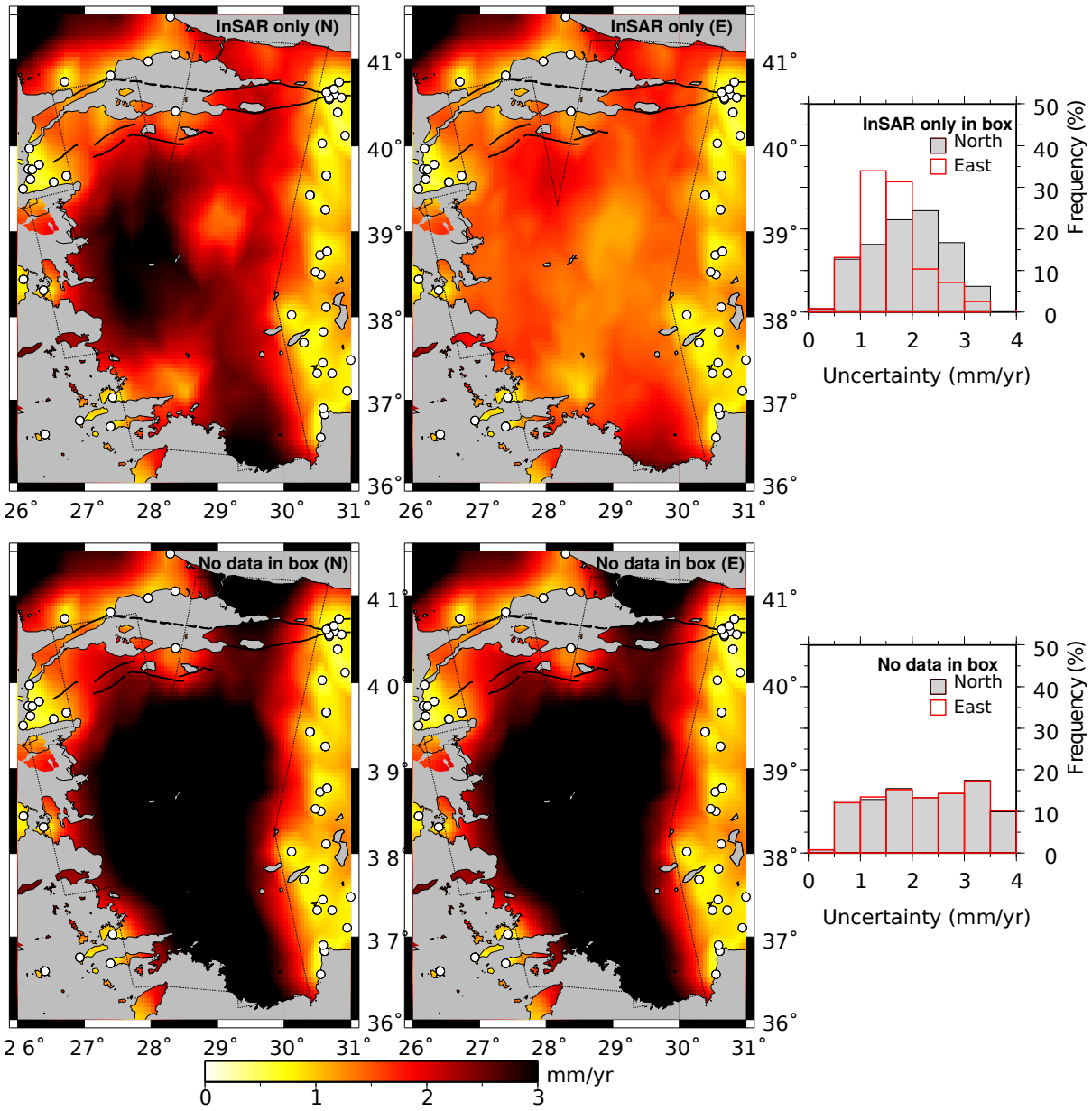

Figure 5.20: Histogram and spatial distribution of the uncertainties in the velocity field for inversions done using: PS InSAR data only in the box, and GPS outside this region, as shown in blue in figure 5.16 (top panel); no data in the box and solely GPS outside this region (bottom panel). GPS site locations are shown by the white circles.

the tracks and only GPS outside as shown in figure 5.16. Having PS InSAR data reduces the uncertainties notably by approximately 1.5 mm/yr in the east-west component as shown in figure 5.20. These improvements are greatest around Istanbul on the NAF and across the Gediz and Küyük Menderes Grabens.

5.8 Discussion

I find in agreement with *Aktug et al.* (2009) that the strain rate increases from 40 nstrain/yr on the Western Anatolian Plateau to 160 nstrain/yr towards the Aegean coast. The deformation is shown to be largely extensional with regions north of latitude 38.5 exhibiting NE-SW to NNE-SSW extension. This rotates anti-clockwise towards the south-west where the principal direction of extension is seen to be NNW-SSE. Towards the south-west the change in velocity is due to a combination of extension and anti-clockwise rotation with respect to Eurasia.

The largest strain rates are observed across the Gediz graben and the Büyük Menderes graben. Rates of extension are shown to be up to 140 nstrain/yr on the Büyük Menderes Graben and 100 nstrain/yr on the Gediz graben. If this strain is localised on the grabens this is equivalent to extension of 6 mm/yr for the Büyük Menderes graben and 4.5 mm/yr for the Gediz graben. A component of right lateral motion is also observed across the Eastern end of the Büyük Menderes graben and a component of left lateral motion is observed on the western end of the Gediz graben as shown by the bars for principal strain rate for compression and tension in figure 5.14. The velocity gradients to the north are dominated by right lateral motion on the North Anatolian Fault where discrepencies between the GPS and InSAR can be attributed to transient processes following the 1999 Izmit earthquake.

In general we see distributed deformation with small regions of localisation as-

sociated with known grabens. Although we do see small regions of localised strain on the major grabens, the rates are in many cases not that much higher than rates away from known fault locations. Indeed these changes are so small that average profiles for GPS and InSAR show uniform velocity gradients for tracks 200 and 64 with subtle interseismic signals seen only for track 243 (see figure 5.7) and in this case primarily in the GPS. This smooth variation in velocity field is in contrast to Eastern Turkey where *Walters et al.* (2014) find strain to be focused on the major fault boundaries. The principal strain rates derived from InSAR and GPS are in agreement with the sense of faulting derived from the CMT catalogue. InSAR primarily adds value in regions where there is insufficient GPS data available and to measure variability in slip rates in regions where contiuous data is not available. The InSAR data highlights a gap in the GPS network at 29.9°E, 39°N in the region of the 1970 and 1944 earthquakes.

Chapter 6

Conclusions and Discussion

In this chapter I summarise the results from chapters 2-5, and discuss the implications of these results. I finish by discussing opportunities for further research with the recently launched Sentinel-1A satellite. I suggest further areas of research in the field under four main categories: areas that can benefit most from the higher spatial and temporal resolution of Sentinel-1, developments in the modelling of tectonic processes, improvements to noise removal algorithms (in particular atmospheric noise), and generation of global strain rate maps.

6.1 Summary of results and implications

Chapter 2

The StAMPS software has a range of parameter options for the filtering of data, the selection of PS candidates, the weeding of noisy candidates and the unwrapping of data. In chapter 2 I explained how these parameters control each aspect of the processing chain and showed results comparing PS selection using the GAMMA and StAMPS software: in Izmir, Turkey and across the Kunlun Fault, in Tibet.

I demonstrated that StAMPS, which assesses the likelihood of a pixel being a PS using a probabilistic approach based on phase stability rather than amplitude, works much better in non-urban environments. I then showed how to use ECMWF data for the removal of atmospheric noise. I demonstrated that it performed better when a scaling correction was applied to account for inaccuracies in the amplitude of the signal.

Chapter 3

In chapter 3 I compared a rate map for a single track generated across the Kunlun fault using standard DifSAR with that generated using PS InSAR. The two techniques were shown to be in agreement to within error with slip rates of 10.5 $\pm$2.1 mm/yr and 9.5 $\pm$3.2 mm/yr for DifSAR and PSInSAR respectively. PS InSAR was shown to produce valuable data in regions that were previously found to be incoherent using DifSAR. I generated velocity maps in the LOS of the satellite for 5 tracks covering the Eastern Kunlun Fault using PS InSAR. I modelled slip rates and locking depths for the five tracks and found variability in slip rate towards the tip of the fault and increased locking depth coincident with a transition towards a region right lateral faulting and thrust faulting.

For the westernmost of the tracks, at the end of the Kokoxili rupture, interseismic slip rates were shown to be localised on the Kunlun Pass Fault rather than the main strand with rates of 11.3 mm/yr. This is in agreement with the coseismic fault rupture mapped for the Kokoxili earthquake, which follows along this offshoot rather than continuing along the main fault strand.

The next track along, where a break in the mapped fault for the Kunlun Pass is seen, average slip rates across the Kunlun Pass reduce to 3.7 mm/yr and most slip is localised back on the main strand, with this accommodating 8.7 mm/yr of

slip. Where the Kunlun Fault is offset by a pull apart basin, the slip rate returns to levels suggested by average geological slip rates of 9.5 mm/yr. Further east, slip rates are seen to be relatively high at 11.1 mm/yr. This is in agreement with *Van Der Woerd et al.* (2002) who estimate slip of 12.5 mm/yr but is significantly higher than measurements made by *Harkins et al.* (2010) of 4 mm/yr. Slip rates then significantly reduce towards the fault tip by ∼9 mm/yr over a region of 80 km down to a slip rate of 2.4 mm/yr, in agreement with *Harkins et al.* (2010) and *Kirby et al.* (2007a).

Although some slip was seen across the Guanggaishan-South Dieshan Fault the combined LOS displacement across the entire swath was shown to be insufficient to explain decreases along the Kunlun Fault as more distributed deformation. Furthermore, any slip across the Tangchang (Tazang) Fault was seen to be below background noise levels. My results showed that reduction in slip rates along the Eastern Kunlun Fault towards the tip of the fault were coupled with higher than expected slip on the Riyueshan and Elashan faults. I argued that slip is being transferred to a region of shortening to the North of the Kunlun Fault and subsequently onto the Haiyuan Fault.

Chapter 4

In chapter 4 I used PS InSAR to measure surface displacements for the Mw 7.8 2001 Kokoxili earthquake towards the end of the coseismic rupture. The postseismic signal was shown to coincide with the Kunlun Pass Fault with no discernible signal associated with the Kunlun Fault. This is in agreement both with the coseismic rupture mapped by *Lasserre et al.* (2005) and with the interseismic signal, which was shown in chapter 3 to be localised on this offshoot from the main fault strand.

I modelled the postseismic signal using a viscoelastic mechanism with a Maxwell

rheology and an afterslip model generated from dynamic rate and state friction laws. The best fitting model for viscoelastic relaxation, with an elastic lid of 16 km and a viscoelastic halfspace, was for a viscosity of 2×10^{19} Pa s. This was shown to be in agreement with the viscosity found by *Ryder et al.* (2011) from DifSAR tracks further west covering the earthquakes epicenter across the Kunlun Fault. The best fitting model for frictional afterslip was for a preseismic velocity of 20 mm/yr and $(a - b)$ frictional parameters of 2.5×10^{-3}. Regions of high slip for the coseismic were shown to correlate with regions of high afterslip below. The majority of the afterslip for this model was constrained to a depth of 20-25 km.

The peak to peak wavelength of 37 km for the frictional afterslip model was shown to be a worse fit than the viscoelastic model which had a wavelength of 90 km. I compared my results for afterslip with those shown by *Bell* (2013) for the Manyi earthquake and argued that his wavelengths are also too short.

Chapter 5

In chapter 5 I generated velocity maps for five overlapping tracks using PS InSAR. I found that the rates across the major grabens and the North Anatolian Fault were in good agreement with GPS data. Discrepencies across the NAF in the region of the Izmit earthquake can be explained by time varying postseismic signals. I combined the PS InSAR and GPS data to generate high resolution strain rate maps. Strain rates of 80 nstrain/yr are found throughout Western Turkey, with strain rates of up to 150 nstrain/yr across small sections of some of the major grabens. In general, fairly uniform strain rates are seen across western Turkey, with any strain localisation being of short wavelengths on the order of 10-30 km.

6.2 Future Opportunities

With the recent launch of the Sentinel 1a satellite and the anticipated launch of the Sentinel 1b satellite next year the resulting datasets should contribute significantly towards answering many interesting tectonic questions. Its main advantages are high temporal and spatial resolution, high precision, increased sensitivity to vertical motions, high precision, and good global coverage. The resulting data will contribute to both the need for global strain rate maps for seismic hazard assessment purposes and the measurement of time varying deformation processes.

In terms of temporal resolution, this study has highlighted the need to better understand how we can integrate the short-term earthquake cycle with long term deformation modelling and move from geodetic to geologic time scales. Western Turkey and Tibet are just two examples of regions exhibiting very different rheological processes. Although tectonic deformation has shown to be largely explained by gravitational potential energy in both regions, the build up of strain between earthquakes and postseismic processes after earthquakes are very different. Whilst postseismic relaxation is shown to be rapid in a regime where a low viscosity layer drives temporal evolution of tectonic stresses in Western Turkey, slow relaxation is seen to be the case in Tibet where postseismic signals continue to be observed decades later. The results in chapter 4 showed that strong postseismic signals were seen over a decade after the Kokoxili earthquake. Similarly, further east near Beijing, the M 1976 Tangshan earthquake is another example of relaxation processes on the order of decades, as aftershocks continue to be observed today. Improved temporal resolution will contribute to our understanding of postseismic processes. Some key questions for future work are: how can we explain such diverse behaviour and what does this mean for earthquake prediction?

In terms of spatial resolution, understanding continental deformation processes

on different lengthscales will come a step closer with the availability of much higher resolution velocity measurements than existing global GPS data and the relatively small number of InSAR studies. On spatial scales of 10 km the crust behaves as rigid blocks separated by individual faults whereas on much larger lengthscales, on the order of 100 km, actively deforming regions behave more like a continuum. The results in chapter 5 showed that in the case of Western Turkey, small regions of localised strain were observed across a few of the grabens on short wavelengths on the order of 10-30 km, but strain was uniform on wavelengths on the order of 100 km. InSAR studies will provide a data-driven approach to determining the lengthscales at which it is appropriate to describe deformation as multiple rigid blocks, and those at which it is more appropriately described as a continuum.

Improved spatial and temporal resolution will see a move towards dynamical models of the earthquake cycle, constrained by observations of different parts of faults at different stages in the cycle. It will help us to investigate how faults interact and improve our understanding of the transfer of stress. We will continue to identify areas where creep is occurring and regions where faults are locked. Future work should investigate the variability in properties across a fault zone and seek to better understand the role of fault segmentation. In the generation of global velocity maps, image alignment across tracks will begin to become important.

The greater precision of data from this next generation of satellites will require more sophisticated models than screw dislocation. Whilst a number of studies using this model address the trade off between slip rate, locking depth and dip, the variation in fault strike is typically ignored. Furthermore, in regions where there are several faults in close proximity and fault maps are incomplete we may be modelling several faults with smaller slip rates as a single fault with a much larger locking depth and slip rate. This has important implications for earthquake hazard assessment.

High resolution maps of vertical motion will help to model across normal and thrust faults, including those in western Turkey and north of the Kunlun Fault in Tibet, respectively. The M 8 1556 Shaanxi earthquake, which occured on the Ordos Block, near the city of Xian, killed approximately 830,000 people. It is thought to have occurred in a region of extension on one or a combination of the North Huashan, Piedmont and Weihe Faults (*Hou et al.*, 1998), all of which have slip rates which are currently below background noise levels. A number of faults that currently have slip rates that are too low to observe (both those incorporating vertical components and pure strike-slip faults) will begin to become measureable with Sentinel-1. This will be aided by the identification of previously unknown faults with high-resolution imagery and DEMs. In addition to decoupling horizontal and vertical motions due to both regular ascending and descending satellite passes we should begin to decouple rotations from LOS velocities. This need was highlighted in chapter 5 by the velocity maps and corresponding profiles for Western Turkey.

6.3 Future Limitations

The major limitations to generating accurate global velocity maps using Sentinel 1 are DEM errors, orbital phase errors, unwrapping errors and perhaps most importantly (in terms of contribution to phase delay) atmospheric noise. Using higher resolution topography such as that from Pleiades should significantly reduce DEM errors. Existing algorithms for unwrapping data such as the branch cut algorithm (*Goldstein et al.*, 1988) and the Minimum Cost Flow algorithm (*Costantini*, 1998) are already fairly effective. It is therefore anticipated that the greatest contribution to reducing unwrapping errors will come from a combination of the removal of dom-

inant signals in our data prior to unwrapping, and improving coherence.

If we can minimise phase jumps between neighbouring PS (or pixels in DifSAR) prior to unwrapping our data then we reduce the chances of introducing unwrapping errors. This was illustrated by *Jolivet et al.* (2011) across the Himalayan arc by removing atmospheric noise prior to unwrapping. Incorporating atmospheric estimates using ECMWF data earlier in the processing chain may have more far-reaching benefits than just for the unwrapping of data. In StAMPS the atmospheric signal is currently estimated by filtering only, we could instead incorporate ECMWF data earlier in order to improve our atmospheric estmate at the PS selection stage.

6.3.1 Coherence

Interferograms generated from 12 day Sentinel 1 data are already proving to have significantly better coherence than the standard 35 and 70 day interferograms of ENVISAT data. Sentinel-1 is also planned to have much tighter orbital constraints than ENVISAT with an orbital tube of ∼100 m. This should result in improved coherence in regions with steep topography. Nevertheless, it is anticipated that coherence will continue to be problematic in highly vegetated and snow-covered regions. In this study I have shown PS InSAR to significantly improve coherence in Tibet. It is also anticipated that advances in atmospheric noise removal techniques and the development of new filtering algorithms will reduce incoherence.

6.3.2 Atmospheric corrections

Unfortunately Sentinel-1 does not have any atmospheric sensors such as MERIS on-board. However, the Jet Propulsion Laboratory, in their online services for correcting atmosphere in radar (OSCAR), is combining ∼25 km resolution ECMWF data

with MODIS estimates of water vapour to generate phase delay maps at the times of image acquistion for INSAR missions (*VonAllmen et al.*, 2011). In this study the spatial resolution of the ECMWF ERA-I delay maps was 75 km so it is anticipated that these higher-resolution phase delay maps will significantly reduce inaccuracies in the spatial patterns of the signal. Inaccuracies in the amplitude of the signal are largely attributed to widely-publicised errors in water vapour concentrations (*Bao and Zhang*, 2013; *Oikonomou and O'Neill*, 2006) in the lower troposphere, which are used to calculate the water vapour partial pressure, e, in equation 2.29.

The correction that I have made to ECMWF data that scales the amplitude of the LOS phase delay is rather crude as it applies a single scaling factor to the entire scene. Machine learning techniques could be applied to make more sophisticated adjustments for systematic inaccuracies in water vapour content values and temporal interpolation errors.

The spatial characteristics of atmospheric noise in Tibet were observed to have similar spatial patterns for different dates in the time series. Therefore, instead of limiting ourselves to using only the data for timestamps matching our satellite passes I suggest we employ datamining and machine learning techniques to characterise atmospheric signals for a given region using all available ECMWF time stamps. One such technique involves using neural networks (e.g. mixture density networks or expectation maximisation) to find gaussian mixture models that characterise spatial characteristics in the ECMWF data. Neural networks are statistical models that provide a mapping from a vector of inputs $\mathbf{d}$ to a vector of outputs $\mathbf{m}$ where the relationship between these variables is unknown and possibly nonlinear. In this instance the unknown relationship is between the ECMWF data and our phase delay maps.

6.3.3 Global strain rate maps

The technique employed for combining GPS data and PS InSAR data to generate strain rate maps of Western Turkey, showed that different smoothing factors (used for regularising the data) can significantly change the strain rates. The choice of smoothing factor is essentially arbitrary. I chose a smoothing factor that resulted in higher strain localisation on the northern than on the southern strand of the NAF based on prior knowledge of higher slip rates on the northern strand. However I argue that it is more appropriate to use smoother solutions in low velocity regions and rougher solutions in high velocity regions.

An alternative approach is to use an adaptive mesh with varying grid size based on the availability of data. Smoothing could also be applied only to those nodes that are underconstrained in the inversion. A more robust technique would be to use a Bayesian approach that optimises the trade-off between model resolution and solution accuracy.

6.4 Outlook

In this thesis I have:

- measured slip rate variability across one of the longest faults in the world, the Kunlun Fault using PS InSAR. This is the first time that this has been measured geodetically and the first time that PS INSAR has been used to measure tectonic deformation in Tibet.

- showed that the postseismic signal at the end of the rupture for the Kokoxili earthquake is localised on the Kunlun Pass Fault rather than the Kunlun Fault, which has potential implications for seismic hazard.

- showed that viscoelastic relaxation is a more appropriate mechanism than afterslip for modelling the postseismic signal associated with the Kokoxili earthquake; whereas previous authors have suggested either mechanism is equally plausible.

- showed using PS InSAR data that Western Turkey has largely uniform deformation on lengthscales of ∼100 km with any strain localisation of small wavelengths on the order of 10-30 km across a few of the grabens, in agreement with GPS data. This has important implications in terms of the rheology of the region.

The much shorter revisit times of 6-12 days, reduced orbital tube, and regular ascending and descending passes for Sentinel-1 will all contribute to: reducing uncertainties, improving coherence, and helping to decouple vertical and horizontal ground motions. Nevertheless, it is anticipated that measuring interseismic slip rates less than 5 mm/yr or postseismic signals more than a decade after an earthquake (even for those events as high in magnitude as the Kokoxili earthquake) will continue to be challenging. Atmospheric noise will arguably pose the greatest challenge. Added to this will be the greater need for techniques and technologies that can manage big data in terms of supercomputing, parallelisation of code, automated processing, big data analysis and data storage.

Bibliography

Agram, P. S. (2010), *Persistent Scatterer Interferometry in Natural Terrain*, 127-128 pp., Dphil thesis: University of Stanford.

Aktug, B., J. Nocquet, A. Cingoz, B. Parsons, Y. Erkan, P. England, O. Lenk, M. Gurdal, A. Kilicoglu, H. Akdeniz, and A. Tekgul (2009), Deformation of western turkey from a combination of permanent and campaign gps data: Limits to block-like behavior, *Journal of Geophysical Research (Solid Earth)*, *114*.

Aktug, B., E. Parmaksiz, M. Kurt, O. Lenk, A. Kilicoglu, M. Gurdal, and S. Ozdemir (2012), Deformation of central anatolia: Gps implications, *Journal of Geodynamics*, *1.4.1*.

Al Tarazi, E., J. Abu Rajab, F. Gomez, W. Cochran, R. Jaafar, and M. Ferry (2011), Gps measurements of near-field deformation along the southern dead sea fault system, *Geo-chemistry, Geophysics, and Geosystems*, *12*.

Alchalbi, A., M. Daoud, F. Gomez, S. McClusky, R. Reilinger, M. Romeyeh, A. Alsouod, R. Yassminh, B. Ballani, R. Darawcheh, R. Sbeinati, Y. Radwan, R. A. Masri, M. Bayerly, R. A. Ghazzi, and M. Barazangi (2010), Crustal deformation in northwestern arabia from gps measurements in syria: Slow slip rate along the northern dead sea fault, *Geophysical Journal International*, *180*, 125135.

Avouac, J., and P. Tapponier (1993), Kinematic model of active deformation in central asia, *Geophysical Research Letters*, *20*, 895–898.

Baby, B., P. Gole, and J. Lavergnat (1988), A model for the tropospheric excess pathlength of radio waves from surface meteorological measurements, *Radio Science*, *23*, 1023–1038, doi:10.1029/RS023i006p01023.

Bao, X., and F. Zhang (2013), Evaluation of ncepcfsr, ncepncar, era-interim, and era-40 reanalysis datasets against independent sounding observations over the tibetan plateau, *Journal of Climate*, *26*.

Barbot, S., Y. Fialko, and Y. Bock (2009), Postseismic deformation due to the m 6.0 2004 parkfield earthquake: Stress-driven creep on a fault with spatially variable rate-and-state friction parameters, *Journal of Geophysical Research*, *114*.

Barker, T. (1976), Quasi-static motions near the san andreas fault zone, *Geophysical Journal of the Royal Society*, *45*, 689–705.

Bell, M. (2013), *The earthquake cycle of the Manyi Fault, Tibet*, 127-128 pp., Dphil thesis: University of Oxford.

Bell, M. a., J. R. Elliott, and B. E. Parsons (2011), Interseismic strain accumulation across the Manyi fault (Tibet) prior to the 1997 M w 7.6 earthquake, *Geophysical Research Letters*, *38*(24), doi:10.1029/2011GL049762.

Biggs, J. (2007b), *InSAR Observations of the Earthquake Cycle on the Denali Fault, Alaska*, University of Oxford DPhil thesis.

Biggs, J., T. Wright, Z. Lu, and B. Parsons (2007), Multi-interferogram method for measuring interseismic deformation: Denali fault, Alaska, , *170*(3), 1165–1179.

Brace, W. F., and J. Byerlee (1970), California earthquakes: Why only shallow focus?, *Science*, *168*, 1573–1575.

Brown, E., R. Bendick, D. Bourles, V. Gaur, P. Molnar, G. Raisbeck, and F. Yiou (2002), Slip rates of the karakoram fault, ladakh, india, determined using cosmic ray exposure dating of debris flows and moraines, *J. Geophys. Res.*, *107*, 2192, doi:10.1029/2000JB000100.

Buck, A. L. (1981), New equations for computing vapor pressure and enhancement factor, *Journal of Atmospheric and Oceanic Technology*, *20*, 15271532.

Buckley, S. (1998), *Slip along the Hayward fault, California estimated from space-based SAR interferometry*, Ph.D. thesis, University of Texas, Austin, Texas.

Burchfiel, B., Q. Deng, P. Molnar, L. Royden, L. Wang, P. Zhang, and W. Zhang (1989), Intracrustal detachments within zones of intracontinental deformation, *Geology*, *17*, 748–752.

Bürgmann, R., and G. Dresen (2008), Rheology of the lower crust and upper mantle: Evidence from rock mechanics, geodesy, and field observations, *Annual Review of Earth and Planetary Sciences*, *36*, 531567.

Byerlee, J. (1978), Friction of rocks, *Pure and Applied Geophysics*, *116*, 615626, doi:10.1007/BF00876528.

Cakir, Z., S. Ergintav, A. Akoglu, R. Cakmak, O. Tatar, and M. Meghraoui (2014), Insar velocity field across the north anatolian fault (eastern turkey): Implications for the loading and release of interseismic strain accumulation, *J. Geophys. Res. Solid Earth*, *119*, 79347943.

Cavalié, O., and S. Jónsson (2014), Block-like plate movements in eastern anatolia observed by insar, *Geophysical Research Letters*, *41*, doi:10.1002/2013GL058170.

Cavalié, O., C. Lasserre, M.-P. Doin, G. Peltzer, J. Sun, X. Xu, and Z.-K. Shen (2008), Measurement of interseismic strain across the Haiyuan fault (Gansu, China), by InSAR, *Earth and Planetary Science Letters*, *275*(3-4), 246–257, doi:10.1016/j.epsl.2008.07.057.

Cetin, E., Z. Cakir, M. Meghraoui, S. Ergintav, and A. Akoglu (2014), Extent and distribution of aseismic slip on the ismetpaa segment of the north anatolian fault (turkey) from persistent scatterer insar, *Geochemistry, Geophysics, Geosystems*, *15*, 2883–2894.

Chen, C., and H. Zebker (2002), Phase unwrapping for large sar interferograms: Statistical segmentation and generalised network models, *IEEE Trans. Geosci. Remote Sens*, *40*, 109–1719, doi:10.1109/TGRS.2002.802453.

Chen, W.-P., and P. Molnar (1983), Focal depths of intracontinental and intraplate earthquakes and their implications for the thermal and mechanical properties of the lithosphere, *Journal of Geophysical Research*, *88*, 41834214, doi:10.1029/JB088iB05p04183.

Chen, Z., B. C. Burchfiel, Y. Liu, R. W. King, L. H. Royden, W. Tang, E. Wang, J. Zhao, and X. Zhang (2000), Global positioning system measurements from eastern tibet and their implications for india/eurasia intercontinental deformation, *Journal of Geophysical Research*, *105*(B7), doi:10.1029/2000JB900092.

Chevalier, M. L., F. Ryerson, P. Tapponnier, R. Finkel, J. Van der Woerd, H. Li, and Q. Liu (2005), Slip-rate measurements on the karakorum fault may imply secular variations in fault motion, *Science*, *307*, 411414, doi:10.1126/science.1105466.

Ciftci, N., and E. Bozkurt (2010), Structural evolution of the gediz graben, sw turkey: temporal and spatial variation of the graben basin, *Basin Research*, *22*, 846–873.

Colesanti, C., A. Ferretti, F. Novali, C. Prati, and F. Rocca (2003), Sar monitoring of progressive and seasonal ground deformation using the permanent scatterers technique, *IEEE Trans. on Geosci. Remote Sensing*, *41*, 16851701.

Copley, A., and D. McKenzie (2007), Models of crustal flow in the India-Asia collision zone, *Geophysical Journal International*, *169*, 683–698.

Costantini, M. (1998), A novel phase unwrapping method based on network programming, *IEEE Transactions on Geoscience and Remote Sensing*, *36*, 813–821, doi:10.1109/36.673674.7.2.2.

Cowie, P. A., and C. Scholz (1992), Displacement length scaling relationship for faults: Data synthesis and discussion, *J. Struct. Geol.*, *14*, 1149–1156.

Craddock, W., and E. Kirby (2014), Rates and style of cenozoic deformation around the gonghe basin, northeastern tibetan plateau, *Geosphere*, *10*, 1255–1282.

Curlander, J. C., and N. McDonough (1991), *Synthetic aperture radar Systems and signal processing*, John Wiley and Sons.

de Michele, M., D. Raucoules, F. Rolandone, P. Briole, J. Slichon, A. Lemoine, and H. Aochi (2011), Spatiotemporal evolution of surface creep in the parkfield region of the san andreas fault (1993-2004 from synthetic aperture radar, *Earth and Planetary Science Letters*, *308*, 141–150.

Deng, Q., Y. Ran, X. Yang, and et al. (2007), Map of active tectonics in china (in chinese), *Beijing: Seismological Press*.

Desbrun, M., M. Meyer, and A. Schroder, P. Barr (1999), Implicit fairing of irregular meshes using diffusion and curvature flow, in proceedings of the 26th annual conference on computer graphics and interactive techniques, p. 317324.

Dieterich, J. H. (1981), *Constitutive properties of faults with simulated gouge: Mechanical Behaviour of Crustal Rocks*, 103-120 pp., AGU.

Doin, M. P., C. Lasserre, G. Peltzer, O. Cavalie, and C. Doubre (2009), Corrections of stratified tropospheric delays in sar interferometry: Validation with global atmospheric models, *J. Appl. Geophys.*, *69*.

Ekström, G., and P. England (1989), Seismic strain rates in regions of distributed continental deformation, *Journal of Geophysical Research*, *94*, 23110.

Elliott, J. (2008b), *Strain accumulation release on the Tibetan Plateau measured using InSAR*, University of Oxford DPhil thesis.

Elliott, J., J. Biggs, B. Parsons, and T. Wright (2008a), Insar slip rate determination on the altyn tagh fault, n. tibet, in the presence of topographically correlated atmospheric delays, *Geophysical Research Letters*, *35*, doi:10.1029/2009GL039337.

Elliott, J., R. Walters, P. England, J. Jackson, Z. Li, and B. Parsons (2010), Extension on the tibetan plateau: recent normal faulting measured by insar and body wave seismology, *Geophysical Journal International*, *183*(2), 503–535.

Elliott, J., B. Parsons, J. Jackson, X. Shan, R. Sloan, and R. Walker (2011), Depth segmentation of the seismogenic continental crust: The 2008 and 2009 qaidam earthquakes, *Geophysical Research Letters*, *38*.

Elliott, J. R., A. Copley, R. Holley, K. Scharer, and B. Parsons (2013), The 2011 mw 7.1 van (eastern turkey) earthquake, *Journal Geophysical Research*, doi:10.1002/jgrb.50117.

England, P., and G. Houseman (1986), Finite strain calculations of continental deformation 2. comparison with the india-asia collision zone, *Journal of Geophysical Research*, *91*, 3664–3676.

England, P., and D. McKenzie (1982), A thin viscous sheet model for continental deformation, *Geophysics Journal International*, *70*, 295321, doi:10.1111/j.1365-246X.1982.tb04969.x.

England, P., and P. Molnar (1990), Right-lateral shear and rotation as the explanation for strike-slip faulting in eastern tibet, *Nature*, *344*, 140–142.

England, P., and P. Molnar (1997), The field of crustal velocity in asia calculated from quaternary rates of slip on faults, *Geophysical Journal International*, *130*, 551–582.

Ferretti, A., C. Prati, and F. Rocca (2000), Nonlinear subsidence rate estimation using permanent scatterers in differential sar interferometry, *IEEE Trans. on Geosci. Remote Sensing*, *38*.

Ferretti, A., C. Prati, and F. Rocca (2001), Permanent scatterers in sar interferometry, *IEEE Trans. on Geosci. Remote Sensing*, *39*, 8–20.

Freed, A. (2007), Afterslip (and only afterslip) following the 2004 parkfield, california, earthquake, *Geophysical Research Letters*, *34*.

Fukuda, J., K. Johnson, K. Larson, and S. Miyazaki (2009), Fault friction parameters inferred from the early stages of afterslip following the 2003 tokachi-oki earthquake, *Journal of Geophysical Research: Solid Earth*, *114*, 4412.

Funning, G. (2005), Source Parameters of large shallow earthquakes in the Alpine-Himalayan belt from InSAR and waveform modelling, D.Phil. thesis, Earth Sciences, University of Oxford, Oxford, U.K., p. 66.

Funning, G., B. Parsons, and T. Wright (2007), Fault slip in the 1997 Manyi, Tibet earthquake from linear elastic modelling of InSAR displacements, *Geophysics Journal International*, *169*, 988–1008.

Garthwaite, M. (2011), *Deformation of Tibet: InSAR analysis and viscous flow models, Ph.D. thesis, School of Earth and Environment, University of Leeds, Leeds, U.K.*, 136 pp.

Geller, R. (2011), Shake up time for japanese seismology, *Nature*, *472*, 407–409.

Goldstein, R., and C. Werner (1998), Radar interferogram filtering for geophysical applications, *Geophysical Research Letters*, *25*, 4035–4038.

Goldstein, R., H. Zebker, and C. Werner (1988), Satellite radar interferometry: Two dimensional phase unwrapping, *Radio Science*, *23*, 713720.

Goldsworthy, M., and J. Jackson (2001), Migration of activity within normal fault systems: Examples from the quaternary of mainland greece, *J. Struct. Geol.*, *23*, 489–506.

Gomez, F., G. Karam, M. Khawlie, S. McClusky, P. Vernant, R. Reilinger, R. Jaafar, C. Tabet, K. Khair, and M. Barazangi (2007), Global positioning system measurements of strain accumulation and slip transfer through the restraining bend along the dead sea fault system in lebanon, *Geophysical Journal International*, *168*, 10211028.

Guo, J. (2006), New constraints on recent large earthquakes along the xidatan-dongdatan segment of the kunlun fault, western china, *Bulletin of the Seismological Society of America*, *96*(1), 48–58, doi:10.1785/0120040176.

Guo, J., a. Lin, G. Sun, and J. Zheng (2007), Surface ruptures associated with the 1937 m 7.5 tuosuo lake and the 1963 m 7.0 alake lake earthquakes and the paleoseismicity along the tuosuo lake segment of the kunlun fault, northern tibet, *Bulletin of the Seismological Society of America*, *97*, 474–496, doi:10.1785/0120050103.

Haines, A. J. (1982), Calculating velocity fields across plate boundaries from observed shear rates, *Geophysical Journal International*, *68*, 203209.

Hanssen, R. F. (2001), *Radar Interferometry: Data Interpretation and Analysis*, Kluwer Acad., Norwell, Mass.

Harkins, N., E. Kirby, X. Shi, E. Wang, D. Burbank, and F. Chun (2010), Millennial slip rates along the eastern kunlun fault: Implications for the dynamics of intracontinental deformation in asia, *Lithosphere*, *2*(4), 247–266, doi:10.1130/L85.1.

Hearn, E., R. Burgmann, and R. Reilinger (2002), Dynamics of izmit earthquake postseismic deformation and loading of the duzce earthquake hypocenter, *Bulletin of the Seismological Society of America*, *92*(1), 172–193, doi:10.1785/0120000832.

Hearn, E., S. McClusky, S. Ergintav, and R. Reilinger (2009), Izmit earthquake postseismic deformation and dynamics of the north anatolian fault zone, *Journal of Geophysical Research (Solid Earth)*, *114*, 8405.

Hooper, A. (2006), *Persistent scatterer radar interferometry for crustal deformation studies and modeling of volcanic deformation*, Ph.D. thesis, Stanford University.

Hooper, A., and H. Zebker (2007b), Phase unwrapping in three dimensions, with applications to insar time series, *J. Opt. Soc. Am. A*, *24*, 27372747.

Hooper, A., H. Zebker, P. Segall, and B. Kampes (2004), A New Method for Measuring Deformation on Volcanoes and Other Natural Terrains Using InSAR Persistent Scatterers, *Geophys. Res. Letters*, *31*, doi:10.1029/2004GL021737.

Hooper, A., P. Segall, and H. Zebker (2007), Persistent scatterer interferometric synthetic aperture radar for crustal deformation analysis, with application to Volcan Alcedo, Galapagos, *Journal of Geophysical Research*, *112*, doi:10.1029/2006JB004763.

Hooper, A., D. Bekaert, K. Spaans, and M. Arikan (2012), Recent advance in SAR interferometry time series analysis for measuring crustal deformation, *Tectonophysics*, *514-517*, 1–13, doi:10.1016/j.tecto.2011.10.013.

Hou, J., M. Han, B. Chai, and H. Han (1998), Geomorphological observations of active faults in the epicentral region of the huaxian large earthquake in 1556 in shaanxi province, china, *Journal of Structural Geology*, *20*, 549557, doi:10.1016/S0191-8141(97)00112-0. 1.1.1.

Hsu, Y.-J., M. Simons, J.-P. Avouac, J. Galetzka, K. Sieh, M. Chlieh, D. Natawidjaja, L. Prawirodirdjo, and Y. Bock (2006), Frictional afterslip following the 2005 nias-simeulue earthquake, sumatra, *Science*, *312*, 1921–1926, doi:10.1126/science.1126960.

Jackson, J. (2006), Fatal attraction: living with earthquakes, the growth of villages into megacities, and earthquake vulnerability in the modern world, *Philosophical Transactions of the Royal Society of London, Series A*, *364*, 19111925, doi:10.1098/rsta.2006.1805.

Jackson, J., and D. McKenzie (1988), The relationship between plate motions and seismic moment tensors, and the rates of active deformation in the mediterranean and middle east, *Geophysical Journal International*, *93*, 4573, doi:10.1111/j.1365-246X.1988.tb01387.x.

Johnson, K. M. (2004), Viscoelastic earthquake cycle models with deep stress-driven creep along the san andreas fault system, *Journal of Geophysical Research*, *109*(B10), B10,403, doi:10.1029/2004JB003096.

Johnson, K. M. (2006), Frictional properties on the san andreas fault near parkfield, california, inferred from models of afterlip following the 2004 earthquake, *The Bulletin of the Seismological Society of America*, *96*, 670–682.

Johnson, K. M., R. Bürgmann, and J. Freymueller (2009), Coupled afterslip and viscoelastic flow following the 2002 denali fault alaska earthquake, *Geophysical Journal International*, *176*, 670–682.

Jolivet, R., R. Cattin, N. Chamot-Rooke, C. Lasserre, and G. Peltzer (2008), Thin-plate modeling of interseismic deformation and asymmetry across the Altyn Tagh fault zone, *Geophysical Research Letters*, *35*(2), L02,309, doi:10.1029/2007GL031511.

Jolivet, R., R. Grandin, C. Lasserre, M.-P. Doin, and G. Peltzer (2011), Systematic insar tropospheric phase delay corrections from global meteorological reanalysis data, *Geophysical Research Letters*, *38*, doi:10.1029/2011GL048757.

Jolivet, R., C. Lasserre, M.-P. Doin, S. Guillaso, G. Peltzer, R. Dailu, J. Sun, Z.-K. Shen, and X. Xu (2012), Shallow creep on the haiyuan fault (gansu, china) revealed by sar interferometry, *Journal of Geophysical Research*, *117*, doi:10.1029/2011JB008732.

Jolivet, R., M. Simons, P. Agram, Z. Duputel, and Z.-K. Shen (2014), Aseismic slip and seismogenic coupling along the central san andreas fault, *Geophysical Research Letters*, *42*.

Kampes, B. M. (2006), *Radar Interferometry: Persistent Scatterer Technique. First edn.*, Springer, P. O. Box 17, 3300 AA, Dordrecht, The Netherlands.

Kampes, B. M., and N. Adam (2005), Stun algorithm for persistent scatterer interferometry, *FRINGE 2005 Workshop. European Space Agency*.

Kaneko, Y., Y. Fialko, D. Sandwell, X. Tong, and M. Furuya (2013), Interseismic deformation and creep along the central section of the north anatolian fault (turkey): Insar observations and implications for rate-and-state friction properties, *Journal of Geophysical Research*, *118*.

Khoshmanesh, M., Shirzaei, and R. Nadeau (2015), Time-dependent model of aseismic slip on the central san andreas fault from insar time series and repeating earthquakes, *Journal of Geophysical Research*, *120*, 6658–6679.

Kidd, W., and P. Molnar (1988), Quaternary and active faulting observed on the 1985 academia sinica royal society geotraverse of tibet, *Phil. Trans. R. Soc. Lond.*, *327*, 337–363.

Kirby, E., N. Harkins, E. Wang, X. Shi, C. Fan, and D. Burbank (2007), Slip rate gradients along the eastern kunlun fault, *Tectonics*, *26*(2), doi:10.1029/2006TC002033.

Kostrov, V. V. (1974), Seismic moment and energy of earthquakes and seismic flow of rock, *Izv. Acad. Sci. USSR Phys. Earth Physics*, *1*, 2340.

Kursinski, E., G. Haji, J. Schofield, and R. Linfield (1997), Observing earth's atmosphere with radio occultation measurements using the global positioning system, *Journal of Geophysical Research*, *102*(D19), 23,429 – 23,465.

Lapusta, N., J. R. Rice, Y. Ben-Zion, and G. Zheng (2000), Elastodynamic analysis for slow tectonic loading with spontaneous rupture episodes on faults with rate and state dependent friction, *Journal of Geophysical Research (Solid Earth)*, *105*, 23,765–23,789, doi:10.1029/2000JB900250.

Lasserre, C., G. Peltzer, F. Crampé, Y. Klinger, J. Van der Woerd, and P. Tapponnier (2005), Coseismic deformation of the 2001 M w = 7.8 Kokoxili earthquake in Tibet, measured by synthetic aperture radar interferometry, *Journal of Geophysical Research*, *110*(B12), B12,408, doi:10.1029/2004JB003500.

Le Beon, M., Y. Klinger, A. Q. Amrat, A. Agnon, L. Dorbath, G. Baer, J. Ruegg, O. Charade, and O. Mayyas (2008), Slip rate and locking depth from gps profiles across the southern dead sea transform, *Journal of Geophysical Research*, *113*.

Li, H., J. Van der Woerd, P. Tapponnier, Y. Klinger, Q. Xuexiang, Y. Jingsui, and Z. Yintang (2005), Slip rate on the Kunlun fault at Hongshui Gou, and recurrence time of great events comparable to the 14/11/2001, Mw7.9 Kokoxili earthquake, *Earth and Planetary Science Letters*, *237*(1-2), 285–299, doi:10.1016/j.epsl.2005.05.041.

Li, Z., J. R. Elliott, W. Feng, J. a. Jackson, B. E. Parsons, and R. J. Walters (2011), The 2010 M W 6.8 Yushu (Qinghai, China) earthquake: Constraints provided by InSAR and body wave seismology, *Journal of Geophysical Research*, *116*(B10), B10,302, doi:10.1029/2011JB008358.

Lin, a., and J. Guo (2008), Nonuniform slip rate and millennial recurrence interval of large earthquakes along the eastern segment of the kunlun fault, northern tibet, *Bulletin of the Seismological Society of America*, *98*(6), 2866–2878, doi:10.1785/0120070193.

Lin, a., J. Guo, K.-i. Kano, and Y. Awata (2006), Average Slip Rate and Recurrence Interval of Large-Magnitude Earthquakes on the Western Segment of the Strike-Slip Kunlun Fault, Northern Tibet, *Bulletin of the Seismological Society of America*, *96*(5), 1597–1611, doi:10.1785/0120050051.

Linker, M., and J. Rice (1997), Models of postseismic deformation and stress transfer assoiciated with the loma prieta earthquake, *USGS Professional Paper*, *1550*, 253–275.

Loveless, J., and B. Meade (2011), Partitioning of localized and diffuse deformation in the Tibetan Plateau from joint inversions of geologic and geodetic observations, *Earth and Planetary Science Letters*, *303*(1-2), 11–24, doi:10.1016/j.epsl.2010.12.014.

Massonnet, D., M. Rossi, C. Carmona, F. Adragna, G. Peltzer, K. Feigl, and R. T. (1993), The displacement field of the landers earthquake mapped by radar interferometry, *Nature*, *364*, doi:10.1038/364138a0.

McClusky, S., S. Balassanian, A. Barka, C. Demir, S. Ergintav, I. Georgiev, O. Gurkan, M. Hamburger, K. Hurst, H. Kahle, K. Kastens, G. Kekelidze, R. King, V. Kotzev, O. Lenk, S. Mahmoud, A. Mishin, M. Nadariya, A. Ouzounis,

D. Paradissis, Y. Peter, M. Prilepin, R. Reilinger, I. Sanli, H. Seeger, A. Tealeb, M. Toksoz, and G. Veis (2000), Global positioning system constraints on plate kinematics and dynamics in the eastern mediterranean and caucasus, *Journal of Geophysical Research*, *105*, 5695–5720.

McKenzie, D. (1972), Active tectonics of the mediterranean region, *Geophys. J. R. astr. Soc.*, *30*, 109–185.

McKenzie, D. P., and R. Parker (1967), The north pacific: an example of tectonics on a sphere, *Nature*, *216*, 12761280, doi:10.1038/2161276a0.

Meade, B. J., and B. Hager (2005), Block models of crustal motion in southern california constrained by gps measurements, *Journal of Geophysical Research*, *110*.

Meyer, B., P. Tapponnier, L. Bourjot, F. Mdtivier, Y. Gaudemer, G. Peltzer, S. Guo, and Z. Chen (1998), Crustal thickening in gansu-qinghai, lithospheric mantle subduction, and oblique, strike-slip controlled growth of the tibet plateau, *Geophysical Journal International*, *135*(1), 1–47, doi:10.1046/j.1365-246X.1998.00567.x.

Miyazaki, S., P. Segall, J. Fukuda, and T. Kato (2004), Space time distribution of afterslip following the 2003 tokachi-oki earthquake: Implications for variations in fault zone frictional properties, *Geophysical Research Letters*, *31*, 6623, doi:10.1029/2003GL019410.

Molnar, P., H. J. Anderson, E. Audoine, D. Eberhart-Phillips, K. Gledhill, E. Klosko, T. McEvilly, D. Okaya, M. Savage, T. Stern, and F. Wu (1999), Continuous deformation versus faulting through the continental lithosphere of new zealand, *Science*, *286*, 516519, doi:10.1126/science.286.5439.516. 1.3.2, 1.12.

Morgan, W. J. (1968), Rises, trenches, great faults, and crustal blocks, *Journal of Geophysical Research*, *73*, 19591982, doi:10.1029/JB073i006p01959.

Nissen, E. (2008), Active Mountain-building in Mongolia and Iran, D.Phil. thesis, Earth Sciences, University of Oxford, Oxford, U.K., p. 11.

Oikonomou, E., and A. O'Neill (2006), Evaluation of ozone and water vapor fields from the ecmwf reanalysis era-40 during 19911999 in comparison with uars satellite and mozaic aircraft observations, *Jounal of Geophysical Research*, *111*, 11.

Okada, Y. (1985), Surface deformation due to shear and tensile faults in a half-space, *Bulletin of Seismological Society of America*, *75*(4), 1135–1154.

Okada, Y. (1992), Internal deformation due to shear and tensile faults in a half-space, , *82*(2), 1018–1040.

Ozener, H., E. Arpat, S. Ergintav, A. Dogru, R. Cakmak, B. Turgut, and U. Dogan (2010), Kinematics of the eastern part of the north anatolian fault zone, journal of geodynamics, *Journal of Geodynamics*, *49*, 141150.

Parsons, B., T. Wright, P. Rowe, J. Andrews, J. Jackson, R. Walker, M. Khatib, M. Talebian, E. Bergman, and E. R. Engdahl (2006), The 1994 Sefidabeh (eastern Iran) earthquakes revisited: new evidence from satellite radar interferometry and carbonate dating about the growth of an active fold above a blind thrust fault, , *164*, 202–217, doi:10.1111/j.1365-246X.2005.02655.x.

Peltzer, P., G.and Rosen, F. Rogez, and K. Hudnut (1996), Postseismic rebound in fault step overs caused by pore fluid flow, *Science*, *273*, 1202–1204.

Perfettini, H., and J.-P. Avouac (2004), Postseismic relaxation driven by brittle creep: A possible mechanism to reconcile geodetic measurements and the decay rate of aftershocks, application to the chi-chi earthquake, taiwan, *Journal of Geophysical Research (Solid Earth)*, *109*, doi:10.1029/2003JB002488.

Perfettini, H., and J.-P. Avouac (2007), Modeling afterslip and aftershocks following the 1992 landers earthquake, *Journal of Geophysical Research (Solid Earth)*, *112*.

Perfettini, H., J.-P. Avouac, and J.-C. Ruegg (2005), Geodetic displacements and aftershocks following the 2001 $M_w = 8.4$ Peru earthquake: Implications for the mechanics of the earthquake cycle along subduction zones, *Journal of Geophysical Research (Solid Earth)*, *110*, 9404, doi:10.1029/2004JB003522.

Prescott, W. H., and A. Nur (1981), The accommodation of relative motion at depth on the San Andreas fault system in California, , *86*, 999–1004, doi:10.1029/JB086iB02p00999.

Reid, H. F. (1910), The mechanics of the earthquake, in the california earthquake of april 18, 1906: Report of the state earthquake investigation commission, *Carnegie Institution of Washington Publication 87*, *2*, 1628.

Reilinger, R., S. McClusky, P. Vernant, S. Lawrence, S. Ergintav, R. Cakmak, H. Ozener, F. Kadirov, I. Guliev, R. Stepanyan, M. Nadariya, G. Hahubia, S. Mahmoud, K. Sakr, A. ArRajehi, D. Paradissis, A. Al-Aydrus, M. Prilepin, T. Guseva, E. Evren, A. Dmitrotsa, S. Filikov, F. Gomez, R. Al-Ghazzi, and G. Karam (2006), Gps constraints on continental deformation in the africa-arabia-eurasia continental collision zone and implications for the dynamics of plate interactions, *Journal of Geophysical Research*, *111*.

Ren, J., Y. Wang, Z. Wu, and J. Ye (1999), Quaternary faulting of eastern kunlun fault(xidatan-dongdatan), northern tibetan plateau, *Research on Active fault*, *7*, 147–164.

Ren, J., X. Xu, R. Yeats, and S. Zhang (2013), Millennial slip rates of the tazang fault, the eastern termination of kunlun fault: Implications for strain partitioning in eastern tibet, *Tectonophysics*, *608*, 1180–1200.

Rice, J., N. Lapusta, and K. Ranjith (2001), Rate and state dependent friction and the stability of sliding between elastically deformable solids, *Journal of Mechanics Physics of Solids*, *49*, 1865–1898, doi:10.1016/S0022-5096(01)00042-4.

Rogers, G., and H. Dragert (2003), Episodic tremor and slip on the cascadia subduction zone: The chatter of slient slip, *Science*, *300*, 19421943.

Rosen, P., S. Hensley, G. Peltzer, and M. Simons (2004), Updated repeat orbit interferometry package released., *eos*, *85*(35).

Rosen, P. A., S. Hensley, I. R. Joughin, F. K. Li, S. N. Madsen, E. Rodriguez, and R. M. Goldstein (2000), Synthetic aperture radar interferometry, *Proc. IEEE*, *88*, 333382.

Ruina, A. (1983), Slip instability and state variable friction laws, , *88*, 10,359–10,370.

Ryder, I., B. Parsons, T. J. Wright, and G. J. Funning (2007), Post-seismic motion following the 1997 manyi (tibet) earthquake: Insar observations and modelling, *Geophysical Journal International*, *169*(3), 1009–1027, doi:10.1111/j.1365-246X.2006.03312.x.

Ryder, I., R. Bürgmann, and F. Pollitz (2011), Lower crustal relaxation beneath the Tibetan Plateau and Qaidam Basin following the 2001 Kokoxili earthquake, *Geophysical Journal International*, *187*(2), 613–630, doi:10.1111/j.1365-246X.2011.05179.x.

Ryerson, F., M. Caffee, and R. Finkel (1998), Holocene left-slip rate determined by cosmogenic surface dating on the xidatan segment of the kunlun fault (qinghai, china), *International Conference and Sino-American Symposium on Tectonics of East Asia Chungli, Taiwan*, *26*.

Saroglu, F., I. Emre, O.and Kuscu, A. Boray, A. Barka, S. Ozer, and S. Sirin (1992), Active fault map of turkey, *Gen. Dir. of Miner. Res. and Explor., Ankara, Turkey*.

Savage, J. C., and R. O. Burford (1973), Geodetic Determination of Relative Plate Motion in Central California, , *78*, 832–845.

Savage, J. C., J. L. Svarc, and S.-B. Yu (2005), Postseismic relaxation and transient creep, *Journal of Geophysical Research (Solid Earth)*, *110*, B11402, doi:10.1029/2005JB003687.

Scharroo, R., and P. Visser (1998), Precise orbit determination and gravity field improvement for the ers satellites, *Journal of Geophysical Research*, *103*, 8113–8127, doi:10.1029/97JC03179.

Scholz, C. H. (1982), Scaling laws for large earthquakes: Consequences for physical models, *Bulletin of the Seismological Society of America*, *72*, 114.

Scholz, C. H. (2002), *The Mechanics of Earthquakes and Faulting*, Cambridge University Press, Cambridge.

Segall, P. (2010), *Earthquake and Volcano Deformation*, Oxford University Press.

Shankar, P. (2010), Persistent scatterer interferometry in natural terrain, Ph.D. thesis, Stanford University.

Shankar, P., and H. Zebker (2011), Persistent scatterer selection using maximum likelihood estimation, *Geophysical Research Letters*, *34*.

Smith, E. K., and S. Weintraub (1953), The constants in the equation for atmospheric refractive index at radio frequencies, *Journal of research of the National Bureau of Standards*, *50*(1).

Socquet, A., G. Peltzer, and C. Lasserre (2005), Interseismic deformation along the central segment of the altyn tagh fault (tibet, china) determined by sar interferometry, *Eos Trans. AGU*, *86*(52).

Steck, L. K., W. S. Phillips, K. Mackey, M. L. Begnaud, R. J. Stead, and C. A. Rowe (2009), Seismic tomography of crustal P and S across Eurasia, , *177*, 81–92, doi:10.1111/j.1365-246X.2009.04109.x.

Tapponnier, P., and P. Molnar (1977), Active faulting and tectonics of China, *Journal of Geophysical Research*, *82*, 2905–2930.

Tapponnier, P., G. Peltzer, and R. Armijo (1986), On the mechanics of the collision between india and asia, geological society special publications, p. 115157.

Tapponnier, P., B. Meyer, J. Avouac, G. Peltzer, Y. Gaudemer, G. Shunmin, X. Hongfa, Y. Kelun, C. Zhitai, C. Shuahua, and D. Huagang (1990), Active thrusting and folding in the Qilian Shan and decoupling between upper crust and mantle in northeastern Tibet, *Earth and Planetary Science Letters*, *97*, 382–403.

Tapponnier, P., F. J. Ryerson, J. Van der Woerd, A.-S. Mériaux, and C. Lasserre (2001), Long-term slip rates and characteristic slip: keys to active fault behaviour and earthquake hazard, *Comptes Rendus de l'Académie des Sciences - Series IIA - Earth and Planetary Science*, *333*(9), 483–494, doi:10.1016/S1251-8050(01)01668-8.

Tatar, O., F. Poyraz, H. Gursoy, Z. Cakir, S. Ergintav, Z. Akpnar, F. Kocbulut, F. Sezen, T. Turk, K. . Hastaoglu, A. Polat, B. Mesci, . Gursoy, I. Ayazh, R. Cakmak, A. Belgen, and H. Yavasoglu (2012), Crustal deformation and kinematics of the eastern part of the north anatolian fault zone (turkey) from gps measurements, *Tectonophysics*, *518*, 5562.

Taylor, M., and G. Peltzer (2006), Current slip rates on conjugate strike-slip faults in central tibet using synthetic aperture radar interferometry, *J. Geophys. Res.*, *111*.

Taylor, M., and A. Yin (2009), Active structures of the himalayan-tibetan orogen and their relationships to earthquake distribution, contemporary strain field, and cenozoic volcanism, *Geosphere*, *5*, doi:10.1130/GES00217.1.

Taymaz, T., J. Jackson, and D. McKenzie (1991), Active tectonics of the north and central aegean sea, *Geophysical Journal International*, *106*, 433–490.

Thatcher, W. (1975), Strain accumulation and release mechanism of the 1906 san francisco earthquake, *Journal of Geophysical Research*, *80*, 4862–4872.

Thatcher, W. (2009), How the continents deform: The evidence from tectonic geodesy, *Annual Review of Earth and Planetary Sciences*, *37*, 237262.

Thomas, M., J. Avouac, J. Champenois, J. Lee, and L. Kuo (2014), Spatiotemporal evolution of seismic and aseismic slip on the longitudinal valley fault, taiwan, *Journal of Geophysical Research*, *119*, 5114–5139.

Turner, R., M. Shirzaei, R. Nadeau, and R. Burgmann (2015), Slow and go: Pulsing slip rates on the creeping section of the san andreas fault, *J. Geophys. Res.*, *120*, doi:10.1002/2015JB011998.

Van Der Woerd, J., P. Tapponnier, F. J. Ryerson, A.-s. Meriaux, B. Meyer, Y. Gaudemer, R. C. Finkel, M. W. Caffee, Z. Guoguang, and X. Zhiqin (2002), Uniform postglacial slip-rate along the central 600 km of the Kunlun Fault (Tibet), from 26Al, 10Be, and 14C dating of riser offsets, and climatic origin of the regional morphology, *Geophysical Journal International*, *148*(3), 356–388.

VonAllmen, P., E. Fielding, Z. Xing, L. Pan, and E. Fishbein (2011), Web service infrastructure for correcting insar imaging, *AGU Fall Meeting Abstracts*, *B1440*.

Walters, R. (2012), *Geodetic observation and modelling of continental deformation in Iran and Turkey*, University of Oxford, DPhil.

Walters, R., B. Parsons, and T. Wright (2014), Constraining crustal velocity fields with insar for eastern turkey: Limits to the block-like behavior of eastern anatolia, *Journal of Geophysical Research*, *119*, 5215–5234.

Wang, C., R. Gao, A. Yin, H. Wang, Y. Zhang, T. Guo, and Y. Li, Q.and Li (2011), A mid-crustal strain-transfer model for continental deformation: A new perspective from high-resolution deep seismic-reflection profiling across ne tibet, *Earth and Planetary Science Letters*, *306*, 279–288.

Wang, H., and T. Wright (2012), Satellite geodetic imaging reveals internal deformation of western tibet, *Geophysical Research Letters*, *39*.

Wang, H., T. Wright, and J. Biggs (2009), Interseismic slip rate of the northwestern xianshuihe fault from insar data, *Geophysical Research Letters*, *36*, doi:10.1029/2008GL036560.

Wang, K., R. Wells, S. Mazzotti, R. Hyndman, and T. Sagiya (2003), A revised dislocation model of interseismic deformation of the cascadia subduction zone, *Journal of Geophysical Research*, *108*, doi:10.1029/2001JB001227.

Wang, Q., P. Z. Zhang, J. T. Freymueller, R. Bilham, K. M. Larson, X. Lai, X. You, Z. Niu, J. Wu, Y. Li, J. Liu, Z. Yang, and Q. Chen (2001), Present-day crustal deformation in China constrained by global positioning system measurements., *Science (New York, N.Y.)*, *294*(5542), 574–7.

Wang, R., F. Lorenzo-Martín, and F. Roth (2006), PSGRN/PSCMP a new code for calculating co- and post-seismic deformation, geoid and gravity changes based on the viscoelastic-gravitational dislocation theory, *Computers and Geosciences*, *32*, 527–541, doi:10.1016/j.cageo.2005.08.006.

Wang, S., C. Fan, and E. Wang (2008), Late cenozoic deformation along the northwestern continuation of the xianshuihe fault system, eastern tibetan plateau, *GSA Bulletin*, *120*, 312–327.

Wen, X., G. Yi, and X. Xu (2007), Background and precursory seismicities along and surrounding the Kunlun fault before the Ms8.1, 2001, Kokoxili earthquake, China, *Journal of Asian Earth Sciences*, *30*(1), 63–72, doi:10.1016/j.jseaes.2006.07.008.

Wen, Y., Z. Li, C. Xu, I. Ryder, and R. Bürgmann (2012), Postseismic motion after the 2001 M W 7.8 Kokoxili earthquake in Tibet observed by InSAR time series, *Journal of Geophysical Research*, *117*(B8), B08,405, doi:10.1029/2011JB009043.

Wiens, D. A., and S. Stein (1983), Age dependence of oceanic intraplate seismicity and implications for lithospheric evolution, *Journal of Geophysical Research*, *88*, 64556468, doi:10.1029/JB088iB08p06455.

Wright, T. (2002), Remote monitoring of the earthquake cycle using satellite radar interferometry, *Philosophical Transactions of the Royal Society of London, Series A*, *360*, 28732888, doi:10.1098/rsta.2002.1094.

Wright, T., B. Parsons, and E. Fielding (2001), Measurement of interseismic strain accumulation across the North Anatolian Fault by satellite radar interferometry, , *28*, 2117–2120, doi:10.1029/2000GL012850.

Wright, T., B. Parsons, and P. England (2004), Insar observations of low slip rates on the major faults of western tibet, *Science*, *305*, 236–239.

Yamasaki, T., T. Wright, and G. Houseman (2013), Weak ductile shear zone beneath a major strike-slip fault:inferences from earthquake cycle model constrained by geodetic observations of the western north anatolian fault zone, *Journal of Geophysical Research*, *114*.

Yavasoglu, H., E. Tar, O. Tuysuz, Z. Cakr, and S. Ergintav (2011), Determining and modeling tectonic movements along the central part of the north anatolian fault (turkey) using geodetic measurements, *Journal of Geodynamics*, *51*, 339343.

Yuan, D., Z.-S. Lei, H. Wen-Gui, Z. Xiong, W.-P. Ge, X.-W. Liu, and B.-C. Liu (2007), Textural research of the wudu earthquake in 186 b.c. in gansu province, china, and discussion on its causative structure, *Acta Seismologic Sinica*, *20*, 696707, doi:10.1007/s11589-007-0696-5.

Zebker, H., P. Shankar, and A. Hooper (2007), Insar remote sensing over decorrelating terrains: Persistent scattering methods, *IEEE, Radar Conference*, doi:10.1109/RADAR.2007.374307.

Zebker, H. A., P. A. Rosen, R. M. Goldstein, A. Gabriel, and C. Werner (1994), On the derivation of coseismic displacement field using differential radar interferometry : The landers earthquake, *J. Geophys. Res.*, *99*.

Zhang, P.-Z., Z. Shen, M. Wang, W. Gan, R. Bürgmann, P. Molnar, Q. Wang, Z. Niu, J. Sun, J. Wu, S. Hanrong, and Y. Xinzhao (2004), Continuous deformation of the Tibetan Plateau from global positioning system data, *Geology*, *32*(9), 809.

Zhao, G. (1996), Quaternary faulting in north qinghai-tibet plateau, *Earthquake Research in China*, *12*, 107–118.